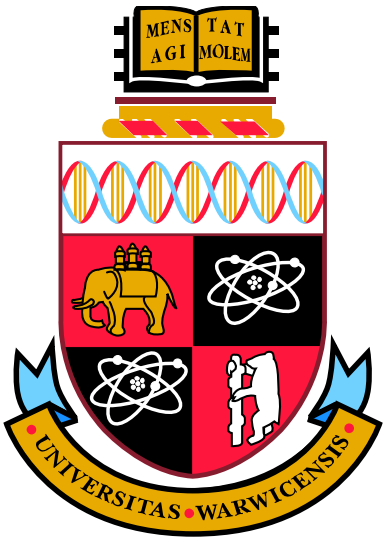

Exploring new emission line diagnostics for accreting compact objects

by

Lieke van Spaandonk, MSc

Thesis

Submitted to the University of Warwick

for the degree of

Doctor of Philosophy

Department of Physics

March 2011

THE UNIVERSITY OF WARWICK

Contents

List of Tables

List of Figures

Acknowledgments

Twinkle, twinkle, little star,
How I wonder what you are!

I would like to take this opportunity to wholeheartedly thank Danny Steeghs for his supervision, guidance and scientific support during the past three and a half years. The Astronomy and Astrophysics group at the University of Warwick provided a comfortable and stimulating environment for me to do my work and for that, I want to thank all academic staff, post-docs and PhD students. Extra gratitude goes to Tom Marsh, for the additional supervision. I would like to thank Joao, Jon and Simon for the endless provision of chocolate, coffee, programming support, inappropriate conversation and general distraction throughout the years, and Sandra for the, sometimes, much needed girly talk about dresses and shoes.

A great thanks to my social 'support' group, for providing me with friendship throughout the years, independent of distance. In no particular order[1]: Dean, Ulrika, Solveig, José, Lisa, Stephanie and Ruth.

Als laatste, maar zeker niet als minste, wil ik graag mijn familie bedanken. Vaders en moeders, ik kan jullie niet dankbaar genoeg zijn voor de onophoudelijke steun en toeverlaat tijdens mijn ontdekkingsreis naar de wonderen van de natuur. Thijs, Koen en Guus, ik zal jullie gezichten tijdens mijn Masters uitreiking nooit vergeten en het zet me regelmatig weer met beide beentjes stevig terug op aarde. Oma, dank je wel voor alle koffie, kapsels en planten, maar vooral voor de Brabantse gezelligheid. Ik kom snel weer 'blieken en gebruiken' op de boulevard. En Andrew, ook al heb je me laten zien dat wonderen heel dicht bij huis gevonden kunnen worden en hou ik heel veel van je, ik ben je niet dankbaar voor het onophoudelijk neuriën van 'Twinkle, twinkle, little star', hoe toepasselijk ook het ook mag zijn.

Twinkle, twinkle, little star,
How I still wonder what you are...

[1] OK, maybe in height, but with astronomy error bars.

Declaration and published work

I declare that the work presented in this thesis is my own except where stated otherwise, and was carried out entirely at the University of Warwick, during the period October 2007 to March 2011, under the supervision of Dr. D.T.H. Steeghs. The research reported here has not been submitted, either wholly or in part, in this or any other academic institution for admission to a higher degree.

The following Chapters of this thesis are based on refereed publications:

- Chapter 3 is based on van Spaandonk, L., Steeghs, D., Marsh, T. R., Torres, M. A. P. *Time-resolved spectroscopy of the pulsating CV GW Lib*, 2010, Monthly Notices of the Royal Astronomical Society, **401**, 1857
- Chapter 4 is based on van Spaandonk, L., Steeghs, D., Marsh, T. R., Parsons, S.G. *The mass of the white dwarf in GW Libra*, 2010, Astrophysical Journal Letters, **715**, L109

Conference contributions based on this thesis are:

- NAM, Belfast, 2008. Poster: *Time-resolved spectroscopy of the pulsating CV GW Lib.*
- Wild Stars in the Old West II, Tucson Arizona, USA 2009. Oral Presentation: *Ca II Spectroscopy of Short Orbital Period CVs.*
- IAC Winterschool, Tenerife 2009. Poster: *Mapping Emission Line Features in CVs.*
- NAM, Glasgow, 2010. Poster: *Binary populations in* SDSS*: A new diagnostic for system parameters of evolved white dwarf binaries.*

I acknowledge with thanks the variable star observations from the AAVSO International Data base contributed by observers worldwide and used in this work.

Abstract

Theory predicts that a large fraction of CVs should have passed through the minimum period. The Sloan Digital Sky Survey (SDSS) sample is finally unearthing these systems in large numbers. But due to their faint donor stars, the orbital period is often the only measurable system parameter for most CVs. The indirect measurable of the superhump period, and hence superhump excess, could potentially provide an indication of the mass ratio of the systems via the empirical relation between the two observables. While this relation is potentially very useful for the determination of mass ratios, the large scatter in the calibrators, especially at the low mass ratio end, prohibits a direct conversion between easy to measure light curve variability and the much sought after mass ratio. To place a short period CV firmly on the evolutionary track (e.g pre- or post bounce systems), more direct methods to determine the mass ratio are required, as well as a better calibration and validation of the relation between the superhump excess and mass ratio.

We can achieve this, by constraining the mass ratios of short period CVs using dynamical constraints on the radial velocities of the binary components. The radial velocity of the WD (K_1) is only occasionally directly measurable as the WD features are typically swamped by the strong disc features. As the disc is centred on the WD, measuring the disc radial velocity can give an indication of the WD radial velocity, but these measures tend to be biased by hotspots and other asymmetries in the disc.

Measuring the radial velocity of the donor star (K_2) is less straightforward and normally performed by either measuring the radial velocity of the donor absorption lines for earlier type donor stars, or via emission lines associated with the donor star, if irradiated by the disc and WD. The first method fails in short period CVs as the faint features from the late type donors in these systems are concealed in the accretion and WD dominated optical spectrum, even at very low mass loss rates. The second method comes with tight timing constraints as the irradiated donor is generally only visible on top of the double peaked disc emission shortly after outburst and data needs to be obtained via target of opportunity programs.

In this thesis, we present a spectroscopic survey of short periods CVs and explore new techniques in addition to the traditional methods for the determination of the radial velocity components. We combine these new methods with the exploitation of the more 'exotic' Ca II triplet lines in the I-band in addition to the commonly used Balmer lines.

We will show that, while it suffers from some of the same systematics as the Balmer lines, we can measure K_1 better in Ca II than in Balmer, especially when exploiting Doppler maps for these measures. More importantly for many systems, donor emission is visible in the Ca II lines, which provides us with measures for the radial velocity amplitude of this feature ($K_{\rm em}$). These, combined with K-correction models, yield a good measure of K_2. We find that the determination of $K_{\rm em}$ is easy in Doppler maps, and that the K-correction, via irradiation methods, is fairly solid. We use these values to dynamically constrain the mass ratios for 13 CVs, including several eclipsing systems to test the validity of our method. The survey includes well known systems such as GW Lib, WZ Sge, OY Car and IP Peg.

Glossary and abbreviations

WD white dwarf

CV cataclysmic variable

DN dwarf nova

FWHM full width at half maximum

EW equivalent width

FWZI full width at zero intensity

RLOF Roche lobe over flow

MB magnetic braking

GWR gravitational wave radiation

LMXB low mass X-ray binary

CCD charge coupled device

RMS root mean square

RV radial velocity

MEM maximum entropy map

COS centre of symmetry

DD diagnostic diagram

S/N signal to noise

RON read out noise

VLT Very Large telescope

WHT William Herschel telescope

SED spectral energy distribution

Chapter 1

Cataclysmic Variables

1.1 Binaries

Roughly half of the stars visible at night are multiple systems containing two or more stars orbiting around a common centre of mass due to their mutual gravitational attraction. The diversity of binary systems is explained by a broad range of initial parameters: e.g. initial masses of the individual components, age and hence evolution, the separation, the influence of the individual evolution on the system etcetera. Understanding these parameters provides crucial information about binary and stellar evolution since all stellar population models are affected by binary interactions.

1.1.1 Nomenclature

Out of the many different binary configurations, this thesis only concerns the eclipsing and the spectroscopic binaries at short orbital periods containing an evolved compact object.

- **Eclipsing binaries** are those binaries that have their orbital plane orientated along our line of sight, showing periodic dips in brightness as one of the components passes in front of the other, hence blocking its light. These eclipses in the light curves do not only reveal the presence of the secondary star but also contain information on the relative effective temperatures and radii of both stars, as they are a function the eclipse width and depth (e.g. Parsons et al. 2010, Littlefair et al. 2008).

- **Spectroscopic binaries** show periodic Doppler shifts in their emission and/or absorption features due to the orbital motion along the line of sight. This periodic motion is used in radial velocity studies, and at a bare minimum, provides a measure of the orbital period of the binary (e.g. Gänsicke et al. 2009 and references therein). Two classes of spectroscopic binaries exist:

– **Single line binaries** only display the spectral features of one binary component. Single lined binaries also include planetary systems, as the presence of the (undetectable) planet is revealed by the periodical wobble of the central star.

– **Double line binaries** show the spectral features of both components, with their respective Doppler shifts out of phase by $\Delta\phi = 0.5$. The ratio of the radial velocities is a measure of the mass ratio of the components, see next section (1.1.2).

1.1.2 Binary geometry

Kepler's third law states that the orbital period squared ($P_{\rm orb}^2$) of a body around its centre of mass, is directly proportional to the semi-major axis of the orbit cubed (a^3; Kepler et al. 1619). In this scenario, gravity provides the centripetal force required to keep the system im circular motion. The relation for two bodies around a common centre of mass, is given by:

$$P_{\rm orb}^2 = \frac{4\pi^2}{G(M_1 + M_2)} a^3 \tag{1-1}$$

with M_1 the primary mass, M_2 the secondary mass and $M_2 < M_1$ for the systems concerned in this thesis. We can draw up the next set of equations for the components as they rotate around their common centre of mass:

$$a = a_1 + a_2, \tag{1-2}$$

$$M_1 a_1 = M_2 a_2, \tag{1-3}$$

$$\tag{1-4}$$

with a_1 and a_2 the distance from the primary and secondary to the centre of mass. The true circular velocities for the components are given by

$$v_1 = \frac{2\pi a_1}{P_{\rm orb}}, \tag{1-5}$$

$$v_2 = \frac{2\pi a_2}{P_{\rm orb}}. \tag{1-6}$$

Solving the latter two for a_1 and a_2 and substituting into the mass ratio $q \equiv M_2/M_1$, gives the relation between the mass ratio and the velocities: $q = v_1/v_2$. The velocity is projected along the line of sight, with the measured radial velocity $K_{1,2} = v_{1,2} \sin i$, with i the inclination angle of the system. Thus, we can express the mass ratio as the ratio of the observed velocities:

$$q = \frac{M_2}{M_1} = \frac{K_1}{K_2} \tag{1-7}$$

with $q < 1$ for the systems in this thesis. For single lined systems, when only the radial velocity of one component is measurable, the mass function is defined as:

$$f(M) = \frac{M_1 \sin^3 i}{(1+q)^2} = \frac{P_{\rm orb} K_2^3}{2\pi G} \tag{1-8}$$

which, as $\sin^3 i \leqslant 1$ and $(1+q)^2 \geqslant 1$, sets a lower limit for the mass of the primary component.

1.1.3 Roche lobe geometry

The geometry of close binaries is generally talked about in terms of the Roche geometry. For a Cartesian coordinate frame co-rotating with the binary, the origin at the primary and the x-axis aligned with the centres of the components, the y-axis in the direction of the orbital motion and the z-axis perpendicular to the orbital plane, the total potential can be expressed as the sum of the gravitational potential of the individual stars and the effective potential of the centrifugal force. This is known as the Roche potential (Frank et al., 1992):

$$\Phi_R = -\frac{GM_1}{(x^2+y^2+z^2)^{1/2}} - \frac{GM_2}{((x-a)^2+y^2+z^2)^{1/2}} - \frac{1}{2}\Omega_{\rm orb}^2 \left[(x-\mu a)^2 + y^2\right]. \tag{1-9}$$

This equation is solely determined by the binary separation and the component masses, with $\mu = M_2/(M_1+M_2)$ and the orbital period via $\Omega_{\rm orb} = 2\pi/P_{\rm orb}$. The Roche equipotentials ($\Phi_R = \text{const}$), are set by the mass ratio, relative to the binary separation (Figure 1-1). Close to the components, these potentials are nearly circular as they are mostly governed by the component's mass, but further outwards the gravitational potential of the second mass distorts this shape. The inner most equipotential, where the surfaces of the two individual stars just touch as the forces cancel in the inner Lagrangian point (L_1), is known as the Roche Lobe and only within this equipotential material is gravitationally bound to the parent star.

If the surface of a star expands beyond its Roche lobe, material is no longer gravitationally bound to that star and when entering the lobe of the companion star, material will be gravitationally bound to the latter instead. The net result is a flow of material from lobe to lobe, through L_1, called Roche lobe over flow (RLOF).

1.2 Binary evolution

All binaries can be separated into three distinct groups depending on the relative sizes of the stellar radii (R_*) compared to their Roche lobe radii ($R_{\rm L}$):

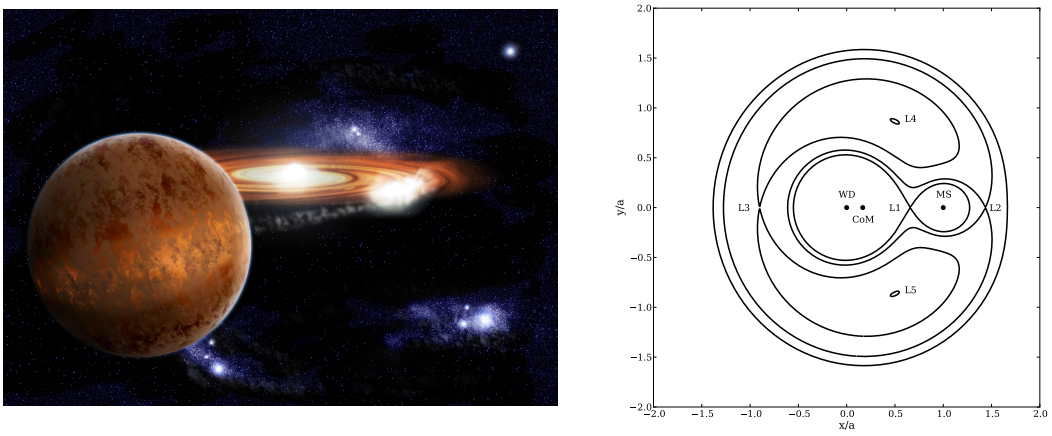

Figure 1-1: **Left:** Artist's impression of the CV SDSS 1035+055 showing the donor star (in this case a brown dwarf), the mass transfer stream, the disc around the WD and the hotspot - where the stream impacts the disc (Courtesy Stuart Littlefair). **Right:** Roche Equipotentials for a system with mass ratio $q = 0.2$. Indicated are the positions of the primary and secondary star and the centre of mass. Also indicated are the 5 Lagrangian points. The Inner Lagrangian point L_1 lies between the two masses. For the two outer Lagrangian points, L_2 lies behind the smaller mass, on the line determined by the two masses, and L_3 lies behind the larger mass. L_4 and L_5 are positioned at the vertical corners of the two equilateral triangles with as shared base the line between the centres of the two stars, with L_4 leading the motion of the orbit and L_5 laging behind.

- **Detached binary** if both components have $R_* < R_{\rm L}$.
- **Contact binary** if both components have $R_* = R_{\rm L}$.
- **Semi-detached binary** if one component has $R_* < R_{\rm L}$ and the other $R_* > R_{\rm L}$. In these cases RLOF normally occurs.

Throughout its evolution, a binary can transform through these stages, depending on the initial masses and separation.

This thesis concerns the semi-detached binaries which contain accretion discs, a result of the mass transfer through L_1. The Roche geometry is too difficult to solve analytically, hence approximations for numerous parameters have been derived which are generally accurate to $\sim 1\%$. Various approximations using the observables of the binary (K_1, K_2 and $q = K_1/K_2$) are given in chapter 2 in Warner (1995). For example, the distance from L_1 to the centre of the primary, R_{L_1}, is given by:

$$\frac{R_{L_1}}{a} = 0.500 - 0.227 \log q, \tag{1-10}$$

valid for $0.1 \leq q \leq 10$ (equation 2.4b) and the volume radius of the secondary star R_2, which can be approximated for $0 < q < \infty$ (equation 2.5c):

$$\frac{R_2}{a} = \frac{0.49q^{2/3}}{0.6a^{2/3} + \ln(1 + q^{1/3})}. \tag{1-11}$$

1.2.1 Accretion and disc formation

The donor star loses gas from its Roche lobe, as it flows through L_1 into the Roche lobe of the primary at roughly the sound speed in the gas, which is set by the temperature of the donor's atmosphere. The Coriolis force deflects the now free falling steam line and the material cannot fall straight onto the primary but sweeps past. As the particles in the stream do not have enough energy to escape the Roche lobe, they will be deflected close to the lobe surface and close in on themselves (top line, Figure 1-2). The material will settle into a Keplerian orbit around the primary, with the same angular momentum as the initial angular momentum of the material at the L_1 point: at the circularisation radius. The Keplerian orbital velocity is given by:

$$\Omega_{\rm orb}(r) = \left[\frac{GM}{r^3}\right]^{1/2}, \tag{1-12}$$

and, for mass ratios between $0.05 < q < 1$, the circularisation radius can be approximated by:

$$\frac{r_{\rm circ}}{a} = 0.0488q^{-0.464} \tag{1-13}$$

(equation 2.14 from Warner 1995; second line, Figure 1-2). Different Keplerian radii have different Kepler velocities, hence the ring will experience friction between material at slightly different radii, which heats the gas. Radiation carries away the released potential energy, which causes the material to move to smaller radii. To conserve angular momentum, material also has to move towards larger radii, spreading the ring into a disc (third line, Figure 1-2). As angular momentum flows outwards through the disc, material can flow inwards and ultimately accrete onto the primary. The maximum disc radius is determined by tidal interactions with the secondary as it soaks up angular momentum. This radius is given by equation 2.61 from Warner (1995):

$$\frac{r_{\rm tidal}}{a} = \frac{0.60}{1 + q} \tag{1-14}$$

and is valid for $0.03 < q < 1$. See bottom two lines in Figure 1-2.

1.2.2 CV evolution

Cataclysmic Variables (CVs) are semi-detached interacting binary systems containing a white dwarf (WD) primary and secondary which transfers mass onto the WD through

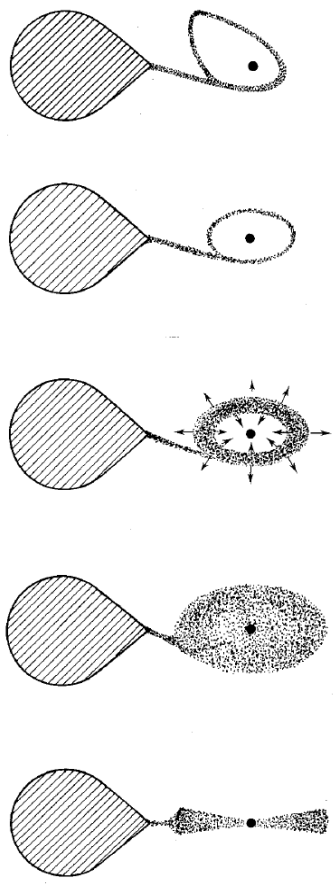

Figure 1-2: Schematic illustration of the formation of an accretion disc (Figure 1 from Verbunt 1982). From top to bottom:
Top line: Initial stream trajectory due to Coriolis forces and the gravitational field.
Second line: Formation of a ring at the circularisation radius.
Third line: Due to viscosity the disc spreads into a ring.
Fourth line: Disc forms with the outer radius set by tidal interactions with the secondary.
Bottom line: Side view.

Roche lobe overflow. The secondary star is typically a main sequence star.

CVs are formed through the evolutionary channel depicted in Figure 1-3, starting with a binary containing one massive ($\gtrsim 1M_\odot$ for existing CVs) main-sequence star and one less massive star ($\lesssim 1M_\odot$) at a binary separation of a few hundred solar radii and with an orbital period of roughly 10 years (Figure 1-3, top line). Evolution on the main sequence is faster for more massive stars and thus the more massive binary component expands first to become a red giant. Its envelope will encompass the secondary during the common envelope phase when $R_* >> R_\mathrm{L}$ (Figure 1-3, second line, Iben & Livio 1993). Friction causes the core of the more massive star and the secondary to spiral inwards, simultaneously expelling the outer layers. The end product of this phase is a stellar remnant, in this case a WD, and a low mass main sequence star, with $M_2 < M_\mathrm{WD} < 1.44\mathrm{M}_\odot$ for CVs (Figure 1-3, 3rd line). See Iben (1991) for a detailed description of binary evolution, and Ritter (2008) for a detailed summary of CV evolution in particular.

The now formed CV can come in two flavours depending on the magnetic field strength of the WD:

- **Magnetic WDs** cannot form a full accretion disc due to the strong magnetic field. Infalling charged material is forced to move along the field lines and the

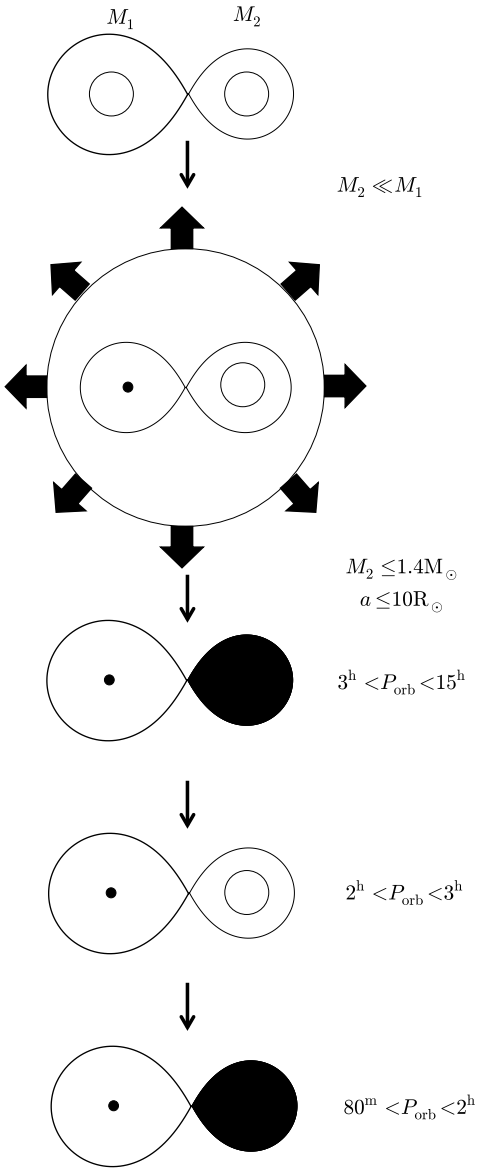

Figure 1-3: CV evolution channel. Indicated are the Roche lobes (tear drop shapes). When Roche lobe filling, these are solid. Compact stars are indicated with a black dot. Starting with a detached binary with one massive and one lighter star (top). The more massive star evolves faster, becoming a red giant and the envelope encompasses the entire binary (second line). When the outer layers are expelled, and angular momentum loss brings the less massive star into contact with its Roche Lobe. The end product is a WD with a Roche lobe overflowing secondary star and orbital period of less than 15 hours: a CV (3rd line). Continued angular momentum loss will decrease the period through the period gap (4th line) towards the short period CVs (bottom line). Based on figure 14 from Iben (1991), not to scale.

material can only accrete onto the magnetic poles. Depending on the field strength these CVs are subdivided into polars (with strong magnetic fields at 1000 to 8000 Tesla and no disc) and intermediate polars with weaker fields (100-1000 Tesla and truncated discs, Hellier 2001).

- **Non-magnetic WDs** can form accretion discs and accretion happens around the equator of the WD. This thesis is only concerned with these disc driven CVs.

1.2.3 Angular momentum loss

During the periods of RLOF, transferring mass from the low mass companion is a complex balance between loss of angular momentum, response of the secondary to mass loss, changes of separation and the influence of the mass ratio on the Roche lobe geometry. The main two mechanisms behind angular momentum loss in CVs are magnetic braking and gravitational wave radiation. The total orbital angular momentum can be expressed as:

$$J = \frac{M_1 M_2}{M} a^2 \Omega_{\rm orb} \tag{1-15}$$

with M the total mass of the system and any eccentricity of the orbit is neglected. The rate of change in the orbital separation (and hence period via Equation 1-1) is given by:

$$\frac{\dot{a}}{a} = 2\frac{\dot{J}}{J} - 2\frac{\dot{M}_1}{M_1} - 2\frac{\dot{M}_2}{M_2} + \dot{M}M. \tag{1-16}$$

Here, the angular momentum component is the total loss in angular momentum due to both gravitational wave radiation and magnetic braking. The period evolution as a function of the mass transfer rate is given in Figure 1-4 for a typical CV.

Magnetic braking

CVs which orbital periods above 3 hours, lose angular momentum chiefly through magnetic braking (MB; Spruit & Ritter 1983). The rotation of the secondary is tidally locked to the orbital period due to the strong tidal forces in the close binary which forces co-rotation. Charged particles are attached to the field lines, and forced to co-rotate with the secondary out to large radii. When these particles are released, they are removed from the system with large velocities, draining the angular momentum of the orbit. For periods below 3 days, the angular momentum loss due to magnetic braking is proportional to:

$$\frac{\dot{J}_{\rm MB}}{J} \propto -f_{\rm MB}^{-2} \frac{k^2 R_2^4}{a^2} \frac{M^2}{M_1 M_2} \Omega_{\rm orb}^2 \tag{1-17}$$

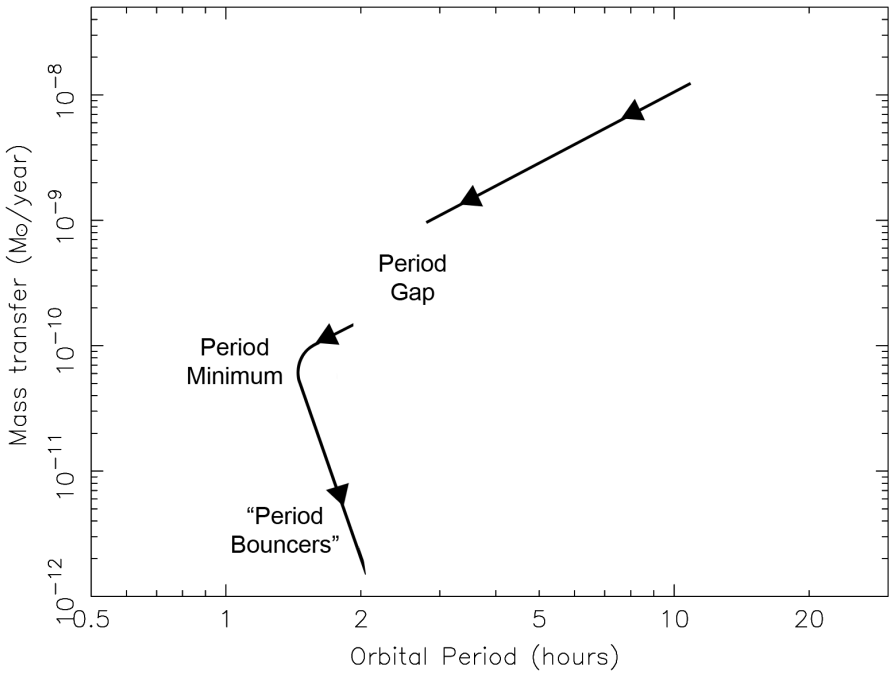

Figure 1-4: Period evolution versus accretion rate. Indicated is the general evolution of a CV from a long period, through the period gap at 2-3 hours, towards the minimum period at around 70 minutes. At this point, more mass transfer results in an increase of the orbital period (Figure based on figure 4.2 from Hellier 2001).

with $f_{\rm MB}$ varying between $f_{\rm MB} = 0.73$ (Skumanich, 1972) and $f_{\rm MB} = 1.78$ (Smith, 1979) and $k^2 = 0.1$, the gyration radius of the secondary star (derived from equation 3 of Verbunt & Zwaan 1981). In better understandable units, this amounts to mass loss rates between $\dot{M} \sim 10^{-9} - 10^{-8} M_{\odot}\,{\rm yr}^{-1}$ for CVs (Figure 1-4).

Gravitational radiation

According to general relativity, matter curves space and the orbital motion of a binary system causes ripples to arise in this space fabric. The energy and angular momentum propagating outwards in these ripples is extracted from the binary orbit, causing the stars to spiral inwards, decreasing the orbital separation and hence the period. This process dominates the period evolution for CVs with orbital periods below 2 hours as magnetic braking is ad hoc disrupted at orbital periods of around 3 hours (Rappaport et al., 1983). General relativity predicts (Landau & Lifshitz, 1975) that the rate of angular momentum loss due to gravitational radiation is given by:

$$\frac{\dot{J}_{\rm GR}}{J} = -\frac{32G^3}{5c^5}\frac{M_1 M_2 M}{a^4} \qquad (1\text{-}18)$$

and results in rates of $\dot{M} \sim 10^{-10} M_\odot \, \mathrm{yr}^{-1}$ for compact binaries, Figure 1-4 (Rappaport et al., 1982).

1.2.4 Mass transfer

We now consider a binary which consists of a WD and a low mass main sequence donor star. To initiate mass transfer (a characteristic of CVs), the secondary star radius must reach its Roche limit. To understand the reaction of the binary on the mass transfer, we need to understand the subtle interplay between $q, a, \dot{M}$ and $\dot{R}_2$ and on what timescales these processes take place. Three time scales are important for stellar structure and evolution. Firstly, the dynamical time scale on which the star reacts to departures from hydrostatic equilibrium:

$$t_{\mathrm{dyn}} = \sqrt{\frac{2R^3}{GM}} \simeq 40 \left[\left(\frac{R}{R_\odot} \right)^3 \frac{M_\odot}{M} \right] \text{ minutes.} \tag{1-19}$$

Secondly, the thermal time scale (or Kelvin Helmholtz time scale), which measures the time to react to departures from thermal equilibrium:

$$t_{\mathrm{th}} = \frac{GM^2}{RL} \simeq (3.0 \times 10^7) \left(\frac{M}{M_\odot} \right)^2 \frac{R_\odot}{R} \frac{L_\odot}{L} \text{ years,} \tag{1-20}$$

with L the luminosity of the star. Hence the donor is always in hydrostatic equilibrium, but not necessarily in thermal equilibrium. The third time scale is the nuclear time scale, which is the characteristic main-sequence lifetime of a star:

$$t_{\mathrm{nuc}} \simeq (7 \times 10^9) \frac{M}{M_\odot} \frac{L_\odot}{L} \text{ years.} \tag{1-21}$$

Transferring mass from the less massive star to the more massive star results in an increase of separation to conserve angular momentum. As the mass ratio also changes, the Roche geometry adjusts to the new system parameters. The change of secondary radius in comparison to this new Roche lobe boundary determines the nature of the mass transfer.

The rate of change of the secondary radius is a combination of the change due to evolutionary changes (on nuclear timescales) and due to mass loss:

$$\frac{\dot{R}_2}{R_2} = \left(\frac{\dot{R}_2}{R_2} \right)_{\dot{M}_2} + \left(\frac{\dot{R}_2}{R_2} \right)_{\mathrm{nuc}}. \tag{1-22}$$

As we can express the radius of a star in terms of its mass using a power law

$$R_2 \propto M_2^{\xi}, \tag{1-23}$$

with the mass radius exponent denoted by ξ, we can describe the change in radius due to mass loss using the logarithmic derivative of the above equation:

$$\left(\frac{\dot{R}_2}{R_2}\right)_{\dot{M}_2} = \xi \left(\frac{\dot{M}_2}{M_2}\right). \tag{1-24}$$

For the Roche lobe radius, we can find a similar expression

$$\left(\frac{\dot{R}_L}{R_L}\right) = 2\left(\frac{\dot{J}}{J}\right) + \xi_L \left(\frac{\dot{M}_2}{M_2}\right). \tag{1-25}$$

The change in radius can now be expressed solely in terms of the mass loss rate and the two exponents:

$$\frac{\dot{R}_2}{R_2} - \frac{\dot{R}_L}{R_L} \simeq \frac{\Delta\dot{R}}{R_2} = (\xi - \xi_L)\frac{\dot{M}_2}{M_2} \tag{1-26}$$

with $\Delta\dot{R} = \dot{R}_2 - \dot{R}_L$. As $\frac{\dot{M}_2}{M_2}$ is negative, $\xi - \xi_L < 0$ leads to an unstable situation as the stellar radius is always larger than the Roche lobe radius, which leads to an increase in mass loss, and an unstable mass transfer situation. In this situation, the mass transfer rate is on a quicker time scale than the star can contract, the mass transfer will be enhanced, which results in runaway mass transfer (on dynamical or thermal timescales).

If $\xi - \xi_L > 0$, the difference in radius is negative, and the Roche lobe expands with respect to the stellar radius, which will decrease the mass transfer rate. To maintain stable mass transfer, an additional driving mechanism is needed to keep increasing the difference between the stellar radius and its Roche lobe radius. In CVs this occurs via angular momentum loss via either magnetic breaking or gravitational radiation.

For conservative mass transfer, and the standard situation with $\xi = 1$, the change in radius depends only the mass ratio of the system as $\xi_L = 2q - 5/3$ (Kolb 2010; Frank et al. 1992). If $q \gtrsim \frac{4}{3}$, the mass transfer is unstable, and stable mass transfer can only happen in systems with $q \lesssim \frac{4}{3}$.

1.2.5 Period distribution

The orbital period of a CV is the most accessible binary parameter and hence often the main focus of binary evolution models. The observed orbital period distribution for a total of $\sim$ 800 sources (Ritter & Kolb, 2003) is show in Figure 1-5. This distribution has three pronounced features, namely the diminishing number of CVs at long orbital periods, a drop of system numbers in the 2-3h orbital period range and a sharp cut-off at $\sim$80 minutes. All these features can be explained within the binary evolution models for CVs.

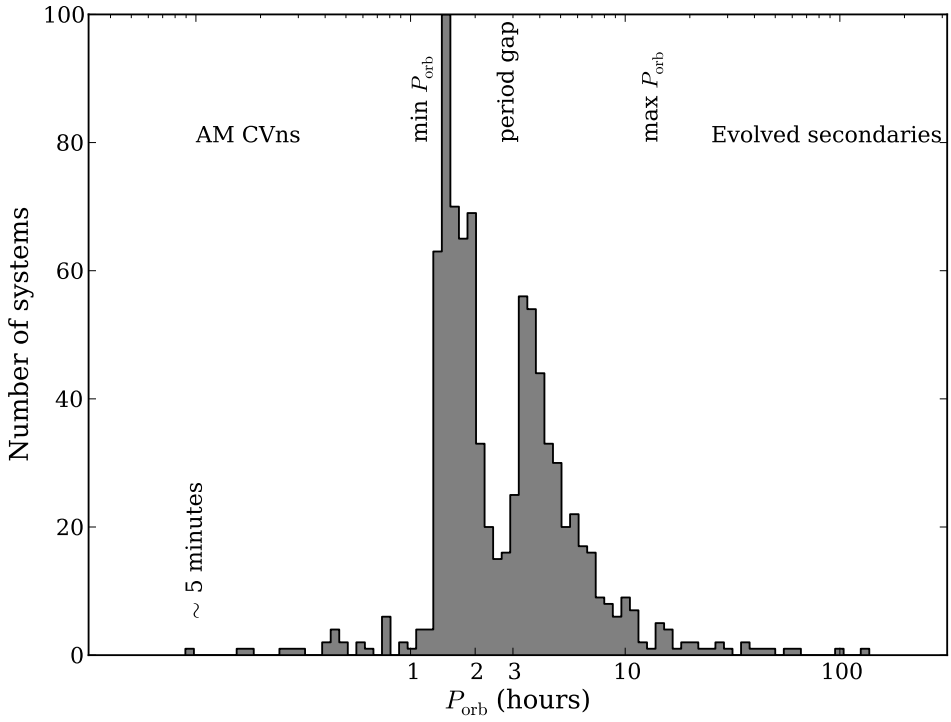

Figure 1-5: Period distribution of CVs. Data from Ritter & Kolb (2003). Distinct features are the diminishing numbers with periods above 12 hours, the drop of numbers in the 2-3 hour period range and the sharp cut-off for periods below $\sim$ 80 minutes. Those systems with orbital periods longer than 12 hours contain an evolved secondary star, and systems with a period shorter than the minimum period contain degenerate, hydrogen deficient components.

In CVs, the orbital period is closely related to the mass and radius of the secondary via

$$P_{\rm orb} \propto \left(\frac{R_2^3}{M_2}\right)^{1/2} \tag{1-27}$$

hence changes in period can be explained by comparing the change of the radius and mass of the secondary via the exponent ξ.

Maximum orbital period

The maximum period for a CV is set by requiring a slower evolution for the secondary star than for the primary: e.g. $q < 1$, with $M_{1,\rm max} = M_{\rm WD,max} < 1.4 M_\odot$. A longer orbital period gives a larger Roche lobe radius, hence a larger and more massive secondary is needed to establish mass transfer. Using the approximation

$$M_2 \approx 0.065 P_{\rm orb}^{5/4} M_\odot \tag{1-28}$$

with $P_{\rm orb}$ in hours (equation 2.100; Warner 1995), this gives a maximum period of ~ 12 hours for $M_2 \sim 1.4 M_\odot$. As only few WDs are at the Chandrashekar limit, a smooth decrease of systems from ~ 6 hours onwards (equivalent to $M_2 \sim 0.6 M_\odot$) is seen in Figure 1-5.

Period gap

The transition from magnetic braking towards gravitational radiation as the main source for the loss of angular momentum is governed by a change of mass transfer rate, from $\dot{M} \sim 10^{-9} - 10^{-8} M_\odot\,{\rm yr}^{-1}$ (magnetic braking) to $\dot{M} \sim 10^{-10} M_\odot\,{\rm yr}^{-1}$ (gravitational radiation, Figure 1-4). This is not an instantaneous transition, as the secondary's response to the change of mass is on a longer time scale than the change in mass loss rate occurs. Mass loss results in a drop in weight on the core, this decreases the number of nuclear reactions, dropping the outward pressure and as a result the star contracts. During magnetic braking, this process happens on a long time scale and hence the star is always slightly too large for its mass. When magnetic braking ceases (disruptive magnetic braking, Rappaport et al. 1983) at the upper edge of the gap (observationally determined at $P_{\rm gap,+} = 3.18 \pm 0.04$ hr, Knigge 2006), mass transfer ceases and the secondary can contract to its correct size, detaching from the Roche lobe. Gravitational radiation decreases the period, and the Roche lobes, till at the lower edge of the gap (observationally determined at $P_{\rm gap,-} = 2.15 \pm 0.03$ hr, Knigge 2006), when the secondary and the Roche lobe come into contact again and mass transfer is resumed. In terms of period changes during both pre- and post-period gap, the mass-radius exponent $\xi = 1$, which means that R^3 decreases quicker than M_2, and hence the period will evolve towards shorter periods due to the drive of mass loss via the loss of angular momentum.

Minimum period

After reattachment, the mass transfer will decrease the period until the minimum period, at ∼70 minutes (e.g. Paczyński 1971, Kolb & Baraffe 1999, Barker & Kolb 2003) has been reached. This point is defined by the secondary reaching a mass of $\sim 0.08 {\rm M}_\odot$. Now the $t_{\rm th}$ exceeds the mass transfer time scale, which is only driven by gravitational radiation, hence the star contacts slower. If R_2 decreases more slowly than $M_2^{1/2}$, this results in an increase in orbital period. For CVs this point coincides with the donor becoming degenerate and further mass loss results in an increase in radius and hence in period.

The observationally determined orbital period minimum happens at $P_{\rm min} = 76.2 \pm 1.0$ minutes (Knigge, 2006), which is close to the theoretically determined value ($P_{\rm min} \approx$ 77min, see Barker & Kolb 2003 for a discussion).

AM CVn

The AM CVs systems contain two hydrogen deficient, degenerate stars and have very short orbital periods (below the period minimum) while sustaining mass transfer via RLOF. There are three proposed routes for the formation of an AM CVn system. The first route has an initial system containing two WDs, with gravitational radiation shortening the period until mass transfer starts at which point the system will evolve towards longer periods. The second route contains a low mass, non-degenerate helium star transferring mass onto a WD. At a period of $\sim$ 10minutes, the helium star will become semi-degenerate and the period will increase with further mass loss. The last route states that the AM CVn is born from a CV containing an evolved secondary star which uncovers a He-rich core after mass loss, causing the period to increase. For a recent review of these evolution channels, see Solheim (2010).

Evolved secondaries

Several systems exist with an orbital period above $\sim$ 12 hours. These contain a secondary star evolving towards the red giant phase (low density). As the secondary is expanding in these systems, independently of mass loss, the orbital period will evolve towards even longer periods.

1.3 Dwarf Novae

Non-magnetic CVs are further classified into several subgroups, of which the Dwarf Novae (DNe) systems are a subclass and of interest for this thesis. They are characterised by semi periodic outbursts of typically 2-5 magnitudes, which is the origin of the name 'Cataclysmic Variable'. The interval between outbursts varies between several days to tens of years. The duration of an outburst is from two to twenty days and this length is correlated with the interval between the outbursts. The recurrence time is correlated with the length of the outburst and is a well defined timescale for most DNe. Depending on their outburst behaviour, the DNe are subdivided into three main classes:

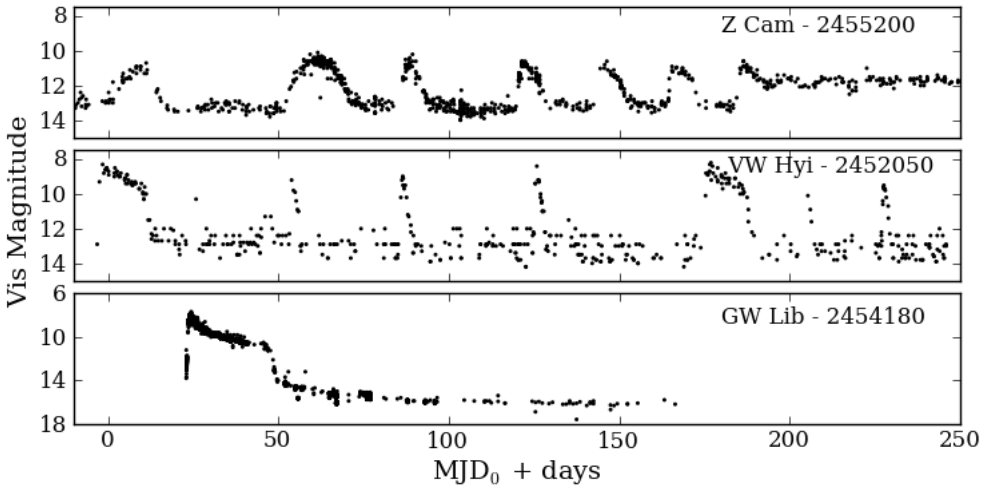

Figure 1-6: **Top:** Lightcurve of Z Cam, the prototype system of those DNe that show prolonged standstills. **Middle:** Lightcurve of the SU UMa type DN VW Hyi showing both regular and superoutbursts. **Bottom:** Lightcurve of the WZ Sge type system GW Lib during its most recent superoutburst in 2007. Note the difference in magnitude scaling. Constructed from observations made by the AASVO.

- **Z Cam** systems show prolonged standstills at ~ 0.7 mag below maximum brightness as the outburst ceases for periods of days to years (top panel, Figure 1-6).
- **SU UMa** have occasional super-outbursts. These bursts achieve a brighter state (by ~ 0.7 mag) and remain in outburst for ~ 5 times longer than normal outbursts (middle panel, Figure 1-6).
  - **WZ Sge** type systems are a sub-class of the SU UMa type, but are characterised by having short orbital periods and very low accretion rates ($\sim 10^{-11} M_{\odot} \mathrm{yr}^{-1}$) resulting in the display of only very rare but extremely bright outbursts on recurrence time scales of 10-20 years (bottom panel Figure 1-6).
- **U Gem** systems are those DNe that neither show standstills nor super-outbursts.

1.3.1 Disc outburst

The sudden brightening of CVs are associated with an increase in luminosity arising from the accretion disc. However, steady state accretion flows cannot describe time-dependent phenomena such as these semi-regular outbursts. Osaki (1974) and Hōshi (1979) proposed a disc instability model to explain the outbursts seen in DNe. Between outbursts (in quiescence), the viscosity in the disc is low. For accretion discs, with disc

height H and local sound speed c_s, the viscosity can be expressed in terms of the α-parameter: $\nu = \alpha c_s H$ with $\alpha \lesssim 1$ (Shakura & Sunyaev, 1973). Due to the long viscous time scale, mass transfer through the disc onto the WD, is slower than mass transfer into the disc from the donor, and hence material accumulates. At the onset of the outburst, the disc will become unstable, increasing the viscosity and the transport of material both inwards and outwards, increasing the size of the disc as well as the accretion rate of material onto the WD. This increase in accretion and viscosity enhances the luminosity of the system and drains the material from the disc. Once drained, the disc will return to its low-viscosity, low-luminosity state. After outburst, interaction between the mass transfer stream and the disc will decrease the disc size as in-falling material has angular momentum corresponding to the circularisation radius and this cycle can then repeat itself.

Disc instability

The disc instability model for DNe is based on the limit-cycle between the effective temperature ($T_{\rm eff}$) and the surface density (Σ) for an annulus of the disc at radius R. The turning points on the equilibrium curve between the surface density and the effective temperature (and indirectly mass transfer rate) of a disc annulus, are defined by $\Sigma_{\rm min}$ at $T_{\rm crit,2}$, $\dot{M}_{\rm crit,2}$ and by $\Sigma_{\rm max}$ at $T_{\rm crit,1}$, $\dot{M}_{\rm crit,1}$, with $T_{\rm crit,1} < T_{\rm crit,2}$ and $\dot{M}_{\rm crit,1} < \dot{M}_{\rm crit,2}$, see Figure 1-7. The curve indicates thermal equilibrium, that is, when the viscous heating balances the radiation from the surface. Any annulus with Σ, T to the right of the curve will heat up as the heating exceeds the cooling and move upwards in the diagram till it reaches the top of the S-curve. Whereas an annulus with Σ, T to the left of the curve will cool down till it reaches equilibrium on the lower branch of the curve.

Stable configurations are on those branches when $\mathrm{d}T_{\rm eff}/\mathrm{d}\Sigma > 0$, while the branch with $\mathrm{d}T_{\rm eff}/\mathrm{d}\Sigma < 0$ is unstable. A positive perturbation on this branch causes Σ to rise and hence a larger T is needed which causes a movement away from the curve. For a negative perturbation, Σ decreases, which requires a cooler T.

The cycle between quiescence and outburst in DNe can be seen as a cycle through the curve. During quiescence an annulus of the disc lies on the lower branch but with $\dot{M}_{\rm crit,1} < \dot{M} < \dot{M}_{\rm crit,2}$, this results in an increase of Σ as the mass cannot pass through the ring at the same rate as it comes into it. Σ will increase till it reaches the maximum surface density possible on the lower branch, $\Sigma_{\rm max}$, when more mass accumulates, the ring will heat on the thermal time scale until it reaches equilibrium on the top branch of

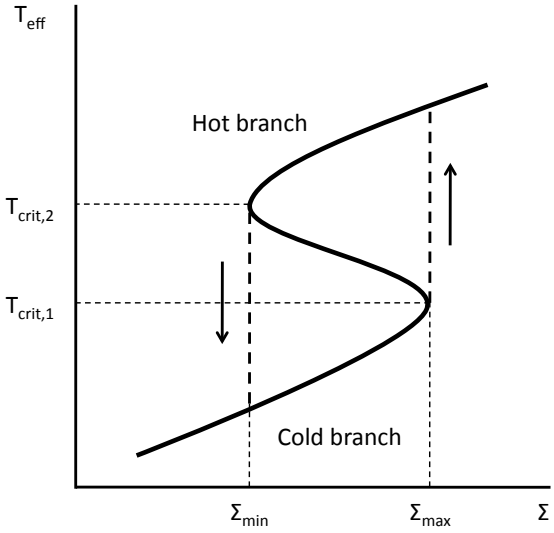

Figure 1-7: Disc instability plot. A schematic S-shaped thermal equilibrium curve showing the two critical surface densities. Based on figure 3.25 from Warner (1995).

the S-curve. As now, $\dot{M} < \dot{M}_{\rm crit,2}$, the surface density decreases until it reaches the left turning point. Decreasing Σ further results in a cooling of the ring towards the lower branch.

An outburst in the disc of a DN is initiated in the annulus which is first pushed over its critical surface density. This causes instability in the neighbouring annuli, sending heat waves through the disc until most of the disc is on the upper branch. The reverse happens for the return to quiescence, as cooling waves propagate through the disc once an annulus returns to the lower branch.

1.3.2 Superhumps

During super-outbursts, low mass ratio DNe show large amplitude variations in their light curves at periods slightly longer than the orbital period of the system, see Figure 1-8 for the September 2007 superoutburst of V455 And. These are called superhumps after the super orbital humps in the light curve.

Theory

Superhumps are believed to come from an eccentric instability at the 3:1 resonance between the disc and the secondary which causes the eccentric disc to precess in low mass ratio systems (Whitehurst 1988; Hirose & Osaki 1990; Lubow 1991b). This model is supported by the presence of superhumps in other low mass ratio systems harbouring an accretion disc, including LMXB's and AM CVn systems (Zurita et al. 2002; Skillman et al. 1999). The origin of the light increase is associated with the extra heating due to periodic deformations of the disc shape (Lubow 1992; Murray 1996, 2000; Kunze et al.

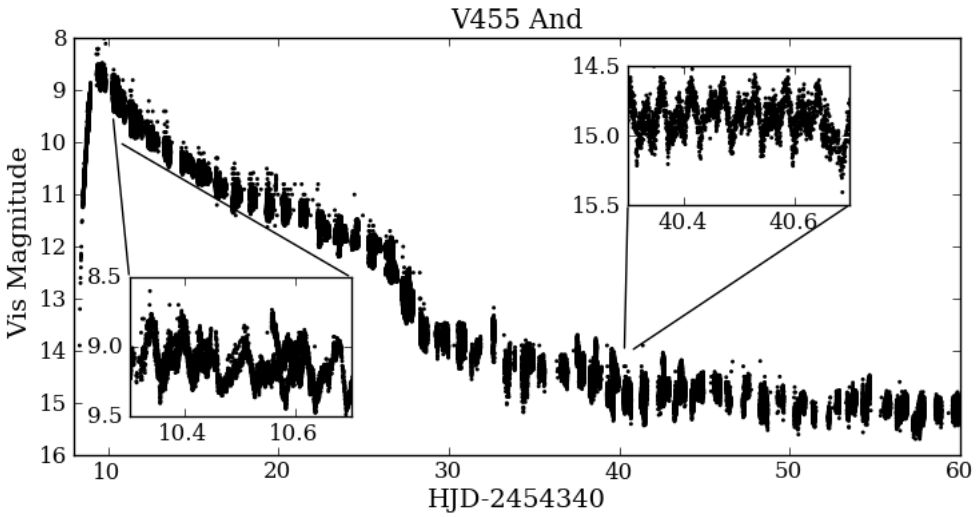

Figure 1-8: Lightcurve of the 2007 superoutburst of V455 And. The insets show a close up of the curve during the plateau phase (bottom left) and the general decline (top right), displaying the superhumps: variations in the brightness of around one magnitude, and with a period slightly longer than the orbital period. Constructed from observations made by AASVO.

1997; Simpson & Wood 1998; Wood et al. 2000). These studies also find a critical mass ratio at which superhumps cease to happen, $q_{\rm crit} \sim 0.3$, this limit is mainly set by the maximum mass ratio in which the 3:1 tidal interaction point is still placed inside the maximum extent of the disc.

Smoothed particle hydrodynamics (SPH) is a Lagrangian method, which models the flow of a fluid as a set of moving particles (Monaghan, 1992). SPH simulations by Murray (1998) show that the energy released from a disc that has become tidally unstable is sufficient to account for the excess luminosity of a superoutburst, and produces superhumps in the integrated light curve of the disc. Foulkes et al. (2004) show 2-D SPH simulations for a system with $q = 0.01$ that reveal an eccentric, non-axisymmetric precessing disc of changing density, which is continuously stretching and relaxing on the superhump period. Figure 1-9 shows the surface density maps, which display tightly wrapped spiral density waves that extend from the outermost regions to small radii. These produce shear and dissipation in the outer disc, and propagate angular momentum outwards, allowing disc gas to move inward.

Lubow (1991a, 1991b, 1992) shows that the final precession rate ω for an eccentric disc can be split into three terms:

$$\omega = \omega_{\rm dyn} + \omega_{\rm press} + \omega_{\rm tran} \tag{1-29}$$

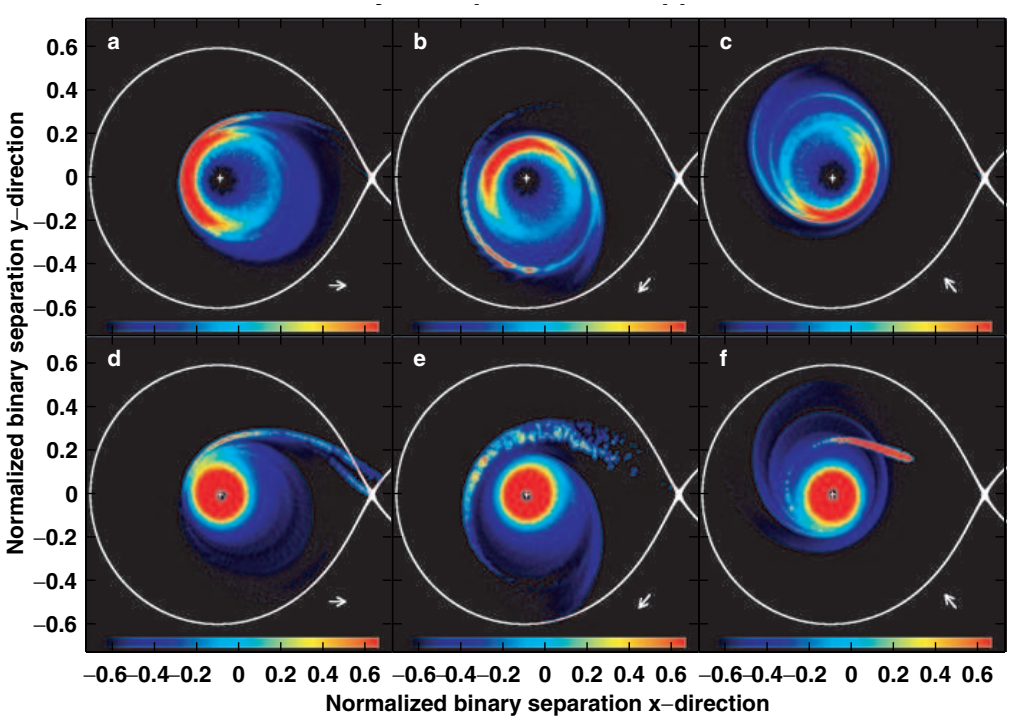

Figure 1-9: Example of SPH simulations. **Top:** (a, b, c) shows accretion disc surface density maps using a logarithmic colour-scale for binary phases 0.00, 0.36, and 0.64, respectively. The secondary orbits anticlockwise with respect to the inertial frame, with mass being added from the L 1 point at the right of each map. The solid curve is the Roche lobe of the primary, plotted in a frame that co-rotates with the binary. The arrow in the lower right-hand corner of each map indicates a fixed direction to an observer. The bottom row (d, e, f) shows the corresponding dissipation maps plotted with a logarithmic colour-scale. Figure 1 from Foulkes et al. (2004).

where $\omega_{\rm dyn}$ is the dynamical precession frequency arising from the resonance, $\omega_{\rm press}$ is a pressure-related term acting to slow the precession and $\omega_{\rm tran}$ is a transient term. This latter contribution is related to the time-derivative of the mode giving rise to the dynamical precession.

Observations

Observers express the amount of precession as the fractional difference between the observed superhump period and the orbital period:

$$\epsilon = \frac{P_{\rm sh} - P_{\rm orb}}{P_{\rm orb}}. \tag{1-30}$$

For $\omega_{\rm press,dyn} \ll \omega_{\rm orb}$, this can be expressed in precession terms, and hence linked to theory, via:

$$\epsilon \approx \frac{\omega_{\rm dyn} + \omega_{\rm press}}{\omega_{\rm orb}}, \tag{1-31}$$

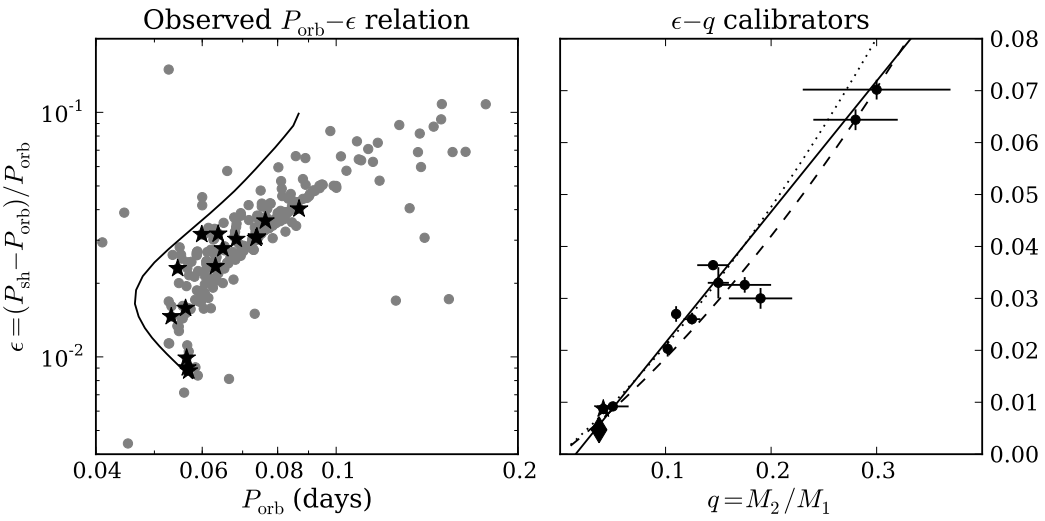

Figure 1-10: **Left:** $P_{\rm orb}$ versus the superhump period excess ϵ (based on data from Ritter & Kolb 2003. The *black stars* indicate those systems that are part of the survey conducted in this thesis. The *black* line indicates the predicted trend for the mass loss rate if the angular momentum loss is solely governed by gravitational radiation (data from Kolb & Baraffe 1999). **Right:** Mass ratio q versus the superhump period excess, note the differently scaled y-axis. The *black dots* are Patterson's calibrators. The lines represent the different relations: Patterson's empirical relation (*dotted line*; 2005), Knigge's relation (*solid*; 2006) and Kato's relation (*dashed*; 2009). Also indicated in respectively *black diamond* and *black star* are the LMXB KV UMa and the eclipsing AM CVn system SDSS J0926+3624.

(equation 25, Pearson 2006). Figure 1-10 shows the orbital period versus observed superhump excess for all CVs in the catalogue of Ritter & Kolb (2003). The red line indicates the predicted period evolution if the angular momentum loss is solely governed by gravitational radiation and an assumed empirical relation of $\epsilon(q)$, which underestimates the mass loss rate. A better fit is found when assuming $\dot{J} \sim 3\dot{J}_{\rm GR}$ (Townsley & Bildsten, 2003).

Several observational studies have been carried out to find a relation between superhump period and the system parameters of the binary. To date, the best determined relation is found between the mass ratio and the superhump excess (Patterson et al., 2005), following the theoretical prediction by Mineshige et al. (1992) of $\epsilon = 0.34q$. Based on twelve systems (10 eclipsing systems, 1 assumed upper limit to the period and one eclipsing Low Mass X-ray binary (LMXB) with an extremely low mass ratio; see table 7, Patterson et al. 2005) they fix the relation to:

$$\epsilon = 0.18q + 0.29q^2 \tag{1-32}$$

with the assumption that $\epsilon = 0$ when $q = 0$. Knigge (2006) re-analyses the system

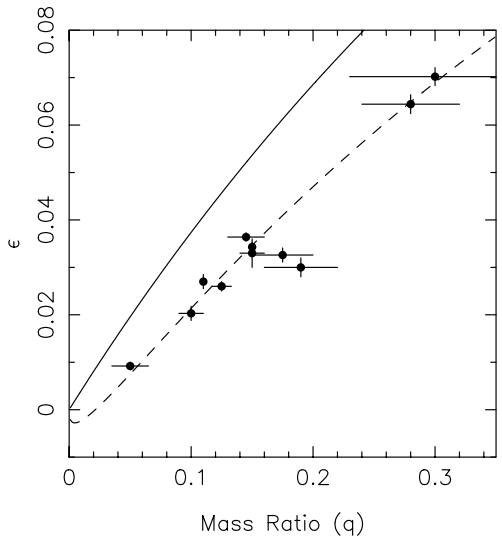

Figure 1-11: Comparison of the calibration systems from Patterson et al. (2005) with a model with purely dynamical precession (*solid*) and including the pressure term (*dashed*; figure 5 from Pearson 2006).

parameters of Patterson's calibrators with no fixed origin assumptions:

$$q(\epsilon) = (0.114 \pm 0.005) + (3.97 \pm 0.41) \times (\epsilon - 0.025). \tag{1-33}$$

A final relation is presented by Kato et al. (2009) based on a large scale observational campaign of superhumping CVs:

$$\epsilon = 0.16q + 0.25q^2. \tag{1-34}$$

All these relations and the initial set of calibrator systems are plotted in Figure 1-10.

The tie between observations and theory is investigated by Pearson (2006). He shows that the pressure term is needed to fit the list of $\epsilon(q)$ calibrators as given by Patterson et al. (2005), see Figure 1-11. His best relation is derived from theory, by generating $\epsilon(q)$ predictions from the formula numerically and then finding the best-fitting polynomial to these values:

$$\epsilon = 3.5 \times 10^{-4} + 0.24q - 0.12q^2 \tag{1-35}$$

and is valid for $0.01 < q < 0.4$.

1.4 Setting the scene

Theory predicts that a large fraction (roughly 70%) of CVs should have passed through the minimum period. The Sloan Digital Sky Survey (SDSS) sample is finally unearthing these systems in large numbers (Figure 1-5 shows a spike at short orbital periods,

Gänsicke et al. 2009). But due to their faint donor stars, the orbital period is often the only measurable system parameter for most candidate post-period minimum CVs. The indirect measurable of the superhump period, and hence superhump excess could potentially provide an indication of the mass ratio of the systems via the empirical relation between the two observables. While this relation is potentially very useful for the determination of mass ratios, the large scatter in the calibrators, especially at the low mass ratio end, prohibits a direct conversion between easy to measure light curve variability and the much sought after mass ratio.

To place a short period CV firmly on the evolutionary track (e.g pre- or post bounce), more direct methods to determine the mass ratio are required. But also a better calibration and validation of this above relation is needed. In this thesis, we will explore new emission line diagnostics for accreting compact objects using traditional emission line features and the more 'exotic' calcium II lines in the *I*-band. The direct aim is to determine the system parameters using these new tools, for a hand full of short period, superhumping CVs. Indirectly we aim to provide new calibrators for the empirical relation between $\epsilon(q)$. In the next Chapter, we will explore all diagnostics, techniques and data analysis tools applicable for binaries that are used in this thesis to determine dynamical mass ratios for DNe.

Chapter 2

Methods

CVs display spectral features originating from a range of system components. The typical temperatures of the components results that CVs are good sources over a range of wavelengths, from X-ray and UV to optical to infra-red (IR). This, combined with their relative brightness and short orbital periods, makes CVs excellent objects to pursue with time-resolved optical spectroscopy. Studying the spectral features from the different components throughout the orbital period provides us with measures for their radial velocities (K_1 and K_2) which dynamically constrain the system parameters (e.g. $q = K_1/K_2$). These are of extreme importance for binary evolution tests, as we saw in Chapter 1.

For this thesis, we acquired a considerable amount of time-resolved spectroscopic data. This Chapter covers the reduction and analysis steps we followed for all observed CVs.

2.1 Spectral features in CVs

White Dwarf

A hydrogen dominated WD (type DA) spectrum shows mainly broad Balmer absorption lines due to the high pressure in its atmosphere. The shape of these lines is a direct function of the temperature and $\log g$, and can be used to determine these parameters in single WDs. In accreting WDs, narrow metal lines from freshly accreted gas can be seen in absorption. As the WD is heated by accretion, temperatures are generally $\gtrsim 10\,000$K, thus their continuum emission peaks in the blue (Figure 2-1). In a binary, the radial velocity curve of the WD as a function of the orbital period gives K_1.

Donor star

The donor stars in DNe are low mass main sequence stars with K and later spectral type features. These stars have a typical surface temperature in the range $1\,600 - 5\,000$K and therefore their continuum emission peaks at (infra-) red wavelengths (Figure 2-1).

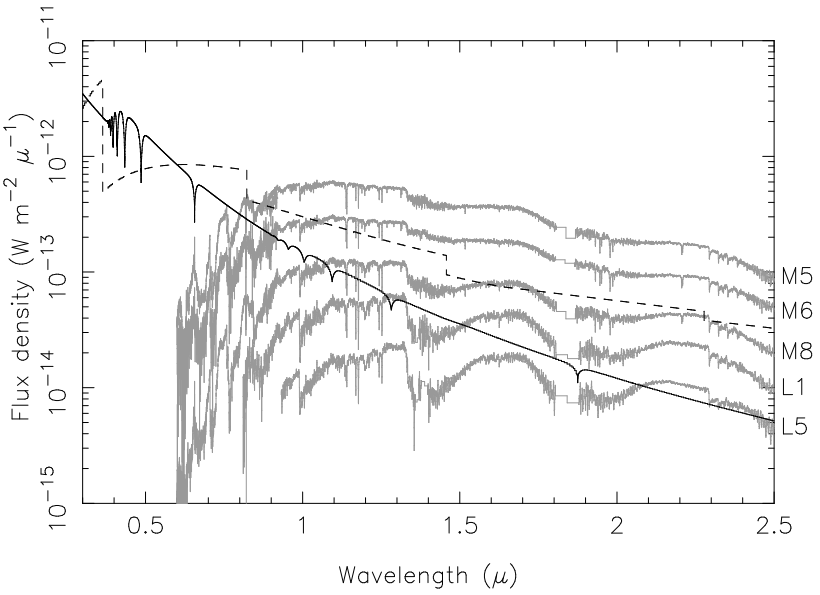

Figure 2-1: Spectrum displaying the principal components of a cataclysmic variable. Fluxes are scaled to a nominal system at 10pc and show the contributions from the accreting white dwarf (solid curve: $T = 15\,000$K) dominating at short wavelengths, the accretion disc (dashed curve: optically thin continuum model appropriate for low mass transfer rates) and the donor star. Shown is a sequence of late-type donors scaled to their approximate contribution to the SED going from M to L type (spectra from the Cushing et al. (2005) and Hawley et al. (2002) atlases). Courtesy Tom Marsh.

Single low mass, main sequence stars display spectral features due to absorption by a broad range of metals at these wavelengths. In CVs, these absorption features can be suppressed by irradiation on the inner hemisphere of the donor, and hence are primarily visible on the cool backside of the donor. When present, we can use these lines to determine the projected radial velocity ($K_{\rm abs} \gtrsim K_2$). However, in DNe systems the donor stars are faint compared to the accretion disc continuum and direct detection of these absorption lines is often very difficult, in the optical range.

Irradiation of the inner hemisphere of the donor can give rise to emission lines if enough energy is available to excite hydrogen and helium. This is normally only the case just after a disc outburst. The emission will have a radial velocity of $K_{\rm em} \leq K_2$ as only the front is irradiated.

Accretion Disc

As the temperature in the accretion disc is dependent on the radius (equation 5.43, Frank et al. 1992), its total spectrum cannot be described by a single black body but

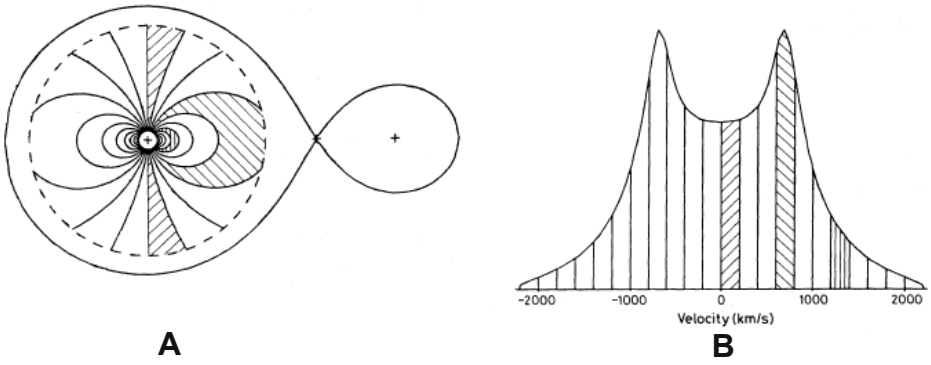

Figure 2-2: Double peaked profile (**B**) formation from the accretion disc (**A**). Regions of constant radial velocity in the disc are shown as hatched areas on the left. The corresponding velocity bins are indicated by the same hatched pattern, in the line profile on the right. Figure from Horne & Marsh (1986).

must be seen as the sum of black bodies with temperatures appropriate for each radius in the disc. For discs around CVs, the emission peaks in the UV and optical as the disc is constrained in size (Figure 2-1). The overall luminosity is set by the accretion rate, and in high rate cases the luminous disc can obscure both the donor and WD features.

The accretion disc in quiescent DNe is optically thin and reveals itself as double peaked hydrogen emission lines due to the range of velocities in the rotating disc and their projection along our line of sight (Figure 2-2). In outburst, the disc manifests itself as a more luminous continuum as it transforms into a hot, optically thick disc and the spectral features can become dominated by strong and single peaked absorption lines. However, some optically thick discs display emission line regions as well and hence the line profiles from the disc are not always a clear indication of the state of the disc. By tracing the radial velocity of the disc ($K_{\rm disc}$) we can indirectly trace K_1, as the disc is centred on the WD and thus should track its radial velocity curve.

Total DNe spectrum

As a DN contains a WD, a mass donor star and an accretion disc, a DN spectrum is a superposition of the individual spectra of each component (Figure 2-1). In high accretion rate systems, the luminous disc dominates the spectrum and obscures the WD and donor features. In low accretion rate systems, the WD and donor features can be strong enough in respectively the UV and the IR to be visible on top of the disc's

spectrum and allow K_1 and K_2 to be measured. Unfortunately, the donor becomes intrinsically faint just at those short periods when the mass accretion rate decreases.

2.2 Time-resolved spectroscopy

2.2.1 Spectroscopy

Using a spectrograph, the light emitted by a source can be dispersed as a function of wavelength. Using a long-slit at the focus of the collimator, the parallel light rays from a distant star are directed as a parallel beam towards a diffraction grating (either transmissive or reflective). The grating diffracts wavelengths at different angles, perpendicular to the slit direction. Finally, the camera focuses all light travelling at any given angle onto a unique point on the detector.

The resolving power of the spectrograph is normally quoted as $R = \lambda/\Delta\lambda$, with $\Delta\lambda$ the smallest difference in wavelength to be measurable at a wavelength λ (e.g. VLT/UVES has a resolving power of $R \sim 80\,000$, whereas WHT/ISIS has $R \sim 800 - 7000$). The actual resolution is a function of the number of lines on the diffraction grating, and the width of the slit and order, as a narrower slit can provide a higher resolution as can using a higher order, but both at the cost of loss of light.

The wavelength range of the observed spectrum is dependent on the diffraction grating, angle, size of the Charge-Coupled Device (CCD, Boyle & Smith 1970) and the observed order, hence a wavelength calibration is required for every set-up change. A flux calibration is also needed along the wavelength axis, as the optics throughput and the response of the detector are wavelength dependent.

CVs have orbital periods between 80 minutes and several hours. Sampling the orbit and measuring the shifts of the lines as a function of time, provides measures of the period, phase and velocity semi amplitude of the components. On one hand, a maximum exposure time is set by our wish to minimise smearing and broadening of features. The amount of smearing depends on the K-amplitude of the line features as the radial velocity changes during the exposure, and long exposures naturally broaden all features. On the other hand, the minimum exposure time is set by the requirement of a S/N > 6 to avoid read out noise domination on the CCD used for astronomical observations in the optical wavelength range ($3\,000$Å $- 10\,000$Å, Howell 2000). Thus exposure times often need to be a suitable compromise between time resolution and S/N.

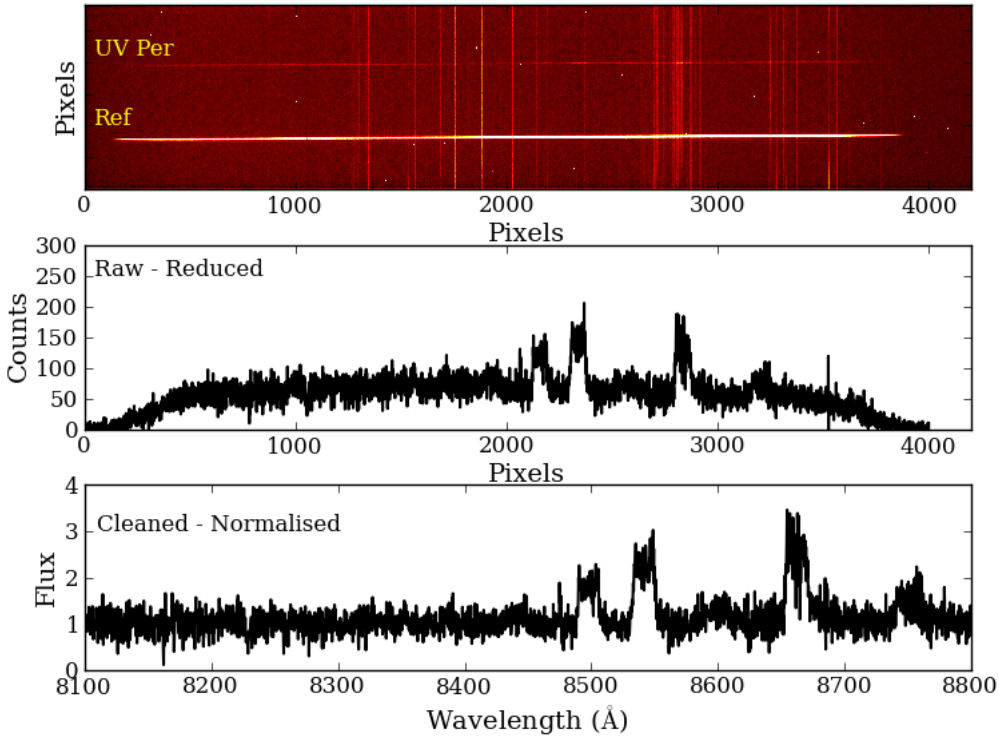

Figure 2-3: Top to bottom: Raw data frame for UV Per (WHT August 2009 run) showing both the object spectrum along the x-direction as well as the spectrum of a nearby reference star. Also visible are the multiple sky lines present in this wavelength range (vertical lines) and cosmic rays (white dots). After bias and flat field correction and optimal extraction of the spectrum along the dispersion direction, the second panel shows the reduced spectrum of UV Per. The bottom panel shows the final product: a normalised and wavelength calibrated spectrum.

2.2.2 Data reduction

CCD data requires a set of calibrations to reduce the raw 2-D images (Figure 2-3, top panel) into 1-D spectra (bottom panel). The three sources of noise contributing to a CCD image are the read out noise, the thermal noise and the fixed pattern noise. To correct for these features bias, dark and flat field frames are needed. This is followed by the extraction of the spectra and, finally, the conversion from CCD-pixels into wavelength units and from CCD-counts into flux units.

Bias correction

Read out noise (RON) is introduced by the error in the charge measurement process and is an intrinsic property of the device used. To avoid a negative value of an unexposed

pixel after read out (as the storage of the sign requires an extra data bit) a bias level of order 100 - 1000 electrons is added to each pixel. We can correct for this level in two ways. The first way is to add an 'overscan' region on each frame. These pseudo-pixels are not exposed to light and can be averaged to find the bias level and RON of the frame in question. The second method is to obtain frames with a zero exposure time and the shutter closed to avoid incident light. To reveal any static 2-D bias structure, these frames are stacked, averaged and subtracted from each science frame. For this work, the 2-dimensional bias frames are first median stacked and then subtracted. Any remaining small deviations are corrected for using the overscan region.

Dark correction

Thermal excitation of electrons give rise to an additional source of noise in the frame which builds up over time. To correct for this effect one can take dark frames, which are frames with the same exposure time and settings as the science frame but with the shutter closed. However, most modern detectors have a negligible dark current when cooled with liquid nitrogen to reduce the thermal excitation, a method commonly used at telescopes as it makes dark frames redundant, reducing overhead times. All data taken for this work comes from such cooled CCDs, voiding dark current correction.

Flat field correction

The fixed pattern noise, or pixel-to-pixel variation of the CCD can be corrected for with flat fields. Uniformly illuminating the CCD using bright, featureless lamps reveals the response of the individual pixels. This includes small variations of up to 1% but also the more problematic features like non-responsive (or dead) pixels. Again, several frames are averaged to find the static flat field. For spectroscopy, the flat fields are not flat as the spectral shape of any flat field source is dependent on the wavelength. Hence, the science frames are not divided directly by the flat field, as is done in photometry, but by a frame that is created by fitting the flat field shape along the wavelength axis and dividing the flat field by this. The result is a normalised 2-D image with variations of up to a few percent which all science frames are divided by.

Both the bias and flat field corrections for spectroscopy in this work are done using the STARLINK package FIGARO[1]. I have written several C-shell scripts to automate the

[1]See `http://www.starlink.rl.ac.uk/` for more information.

reduction of the data presented in this thesis.

Spectral extraction

The optimal extraction method, as presented by Marsh (1989), is commonly used for the extraction of distorted and tilted spectra. The extraction procedure is a succession of several (dependent) steps, and assumes that the image of the slit lies roughly parallel to the rows of the CCD and the dispersion is roughly parallel to the columns. The first step is fitting a low order polynomial to the spectrum along the dispersion direction to track curvature and tilt introduced by the spectrograph optics. On a line perpendicular to this track, a low order polynomial is fitted to sky background regions. For the object region a profile is fitted, again perpendicular to the track, to calculate the contributing pixels and their weight. In a final step both the background subtraction is performed as well as the final extraction of the spectrum using the optimal weights estimated in the previous steps, while cosmic outliers are identified and removed. The final product is a 1-D spectrum in pixels versus counts (Figure 2-3, middle panel).

We controlled the spectral extraction using the 2-D spectral reduction suite PAMELA, provided by Tom Marsh, via custom scripts, using C-shell and Python.

Wavelength calibration

To convert the pixel scale of the extracted spectrum into a wavelength scale, arc frames are needed. These frames have the same set-up as all the other frames but are illuminated by lamps containing numerous known emission line features, such as neon, thorium and argon. A 1-D arc spectrum is extracted using the extraction files of the surrounding science frames (track and profile fit) to provide the most accurate calibration. Using their known excitation wavelengths, a polynomial fit provides a relation between pixel and wavelength, generally accurate to 1/10 of the spectral dispersion measure. To account for any drift of the scaling of the set-up during the night caused by flexure of the spectrograph, arc frames are taken throughout the observations to allow for a linear interpolation in time between nearest wavelength calibrations on either side of any target exposures.

Flux calibration

To calibrate the flux levels, spectra with the same set-up are acquired of spectrophotometric flux standards using a wide slit to collect all flux from the source. Fitting the known flux of the standard to the counts obtained in the set-up gives the conversion factor for each pixel[2]. For variable sources and variable sky conditions, it becomes necessary to take a simultaneous spectrum of a nearby constant source for accurate flux calibrations. Small deviations from the flux of the constant source are then only dependent on sky transparency and seeing and hence can be used to adjust the flux of the variable source as well. However, this requires a constant stellar source to lie within the length of the slit and prohibits the use of the parallactic angle to minimise the effects of atmospheric diffraction, hence this is not always practical or desirable.

Both the wavelength and the flux calibration are done within MOLLY, a spectral analysis program for 1-D astronomical spectra, provided by Tom Marsh and is also used for most of the data analysis.

2.3 Data analysis

The calibrated spectra are now ready for analysis. All analysis methods used in this thesis are described in the next section.

2.3.1 Line measurements

The line measurements probe the basic properties of the emission and absorption line features visible in the spectrum, and include equivalent width (EW), full width at half maximum (FWHM) and the full width at zero intensity (FWZI). As these measurements test the relative strengths and widths of the various lines irrespective of the quality of the absolute flux calibration, they are performed on continuum normalised spectra.

Equivalent width

The strength of a spectral line can be expressed as the width in ångströms (Å) needed for a box with the height fixed from zero to unity, to have the same area as the observed profile set by the spectral line (respectively black and blue shaded areas in Figure 2-4).

[2]See e.g. `http://catserver.ing.iac.es/landscape/tn065-100/workflux.php` for a list of spectrophotometric flux standards

EW is defined as:

$$\mathrm{EW}\,(\text{Å}) = \int \frac{F_c - F_\lambda}{F_c} d\lambda, \tag{2-1}$$

and calculates the area between the continuum flux (F_c) and the line flux (F_λ), resulting in a positive EW for absorption lines and a negative EW for emission lines.

FWHM

Spectral lines are widened by a range of influences: e.g. natural broadening due to the Heisenberg's uncertainty principle, the Doppler broadening due to bulk (thermal) motion of the atoms and pressure broadening due to collisions between neighbouring atoms. The broadening of a line can be expressed as the full width of the profile at half the maximum height (in km/s), independently of the shape of the profile. If the profile is Gaussian shaped, the FWHM is a measure of σ via:

$$\mathrm{FWHM}\,(\mathrm{km/s}) = 2\sqrt{2\ln 2}\sigma \approx 2.35482\sigma \tag{2-2}$$

with σ the standard deviation of the Gaussian shape (Figure 2-4). The profiles from the disc and the donor are dominated by Doppler broadening, whereas the WD lines are dominated by pressure broadening, which depends on the number density of the atoms in the atmosphere.

Stellar rotation adds another factor for line broadening as emission arising from the projected surface of the star is Doppler shifted according to the projection of the rotation velocity ($V_{\mathrm{rot}} = 2\pi R_*/P_{\mathrm{rot}}$) towards the line of sight. The approaching side of the stellar disc is blue shifted and the retreating side is red shifted. The FWHM of a spectral line dominated by this effect is equal to $V_{\mathrm{rot}} \sin i$. For a line broadened by the rotation of the tidally locked secondary, this measure is directly linked to the mass ratio via

$$\frac{V_{\mathrm{rot}} \sin i}{K_2} = (1+q)\frac{R_{\mathrm{L}}(2)}{a} \tag{2-3}$$

(Horne et al., 1986). Measuring the two observables (K_2 and $V_{\mathrm{rot}} \sin i$) provides us with a direct way to measure q, independent of the system inclination i, as the Roche lobe radius over of the secondary star over a is only a function of q (Equation 1-11 and Eggleton 1983).

FWZI

A quick measure to determine the origin of a spectral line is the full width at zero intensity (FWZI; indicated in Figure 2-4) and is a helpful tool to distinguish between two

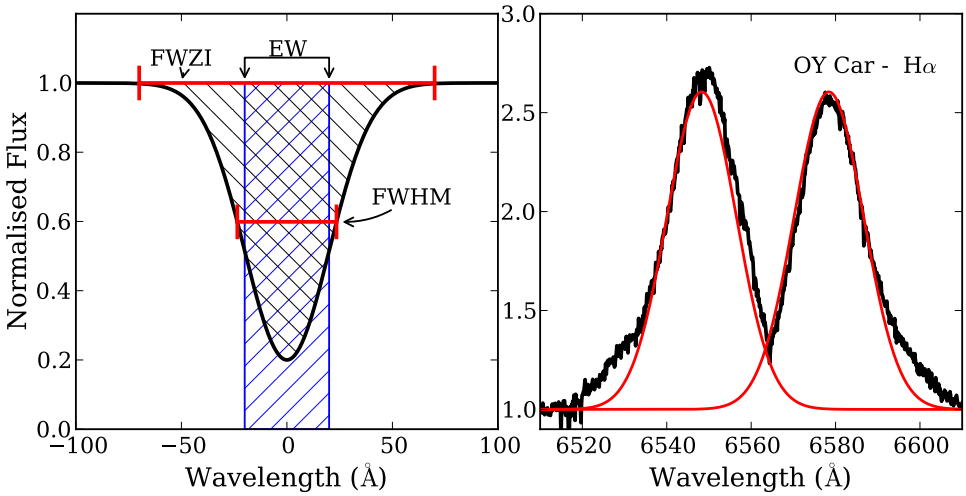

Figure 2-4: **Left:** Absorption profile indicating the FWHM, FWZI and EW. For the EW, the black shaded region denotes the area under under the absorption line. The blue shaded box has a width such that the area in the box with a height of unity is the same. **Right:** Gaussian fit to the Hα emission profile with the FWHM and peak values set to be identical for both Gaussians.

sources sharing the same profile shape. Both the WD and the optically thick accretion disc during outburst have Gaussian absorption profiles but the first will be a few tens of thousand km s^{-1} wide due to pressure broadening, while the latter is only up to a few thousands km s^{-1} wide.

2.3.2 Gaussian methods

As the majority of spectral shapes are well described by one or more Gaussian profiles, fitting Gaussians to these features returns key parameters such as shape and position, relative to the rest wavelength.

Fitting profiles

The Gaussian fitting tool within MOLLY, *mgfit*, is based on the algorithm for least-squares estimation of non-linear parameters as presented by Marquardt (1963) and fits the peak height (mJy), the FWHM (Å) and offset (km s^{-1}) of each Gaussian component from the rest wavelength of the given spectral line. The right panel of Figure 2-4 shows the result of a 2 Gaussian fit to the Hα disc emission line in OY Car. The fit command allows for a simultaneous fit of multiple lines across the spectral range while fixing and sharing fit parameters (e.g. common offset) as well as allowing for a fit against time:

e.g. orbital phase or absolute time of the spectrum.

Radial Velocity curves

As the components of the binary rotate around their common centre of mass, the projected radial velocities of the spectral features will follow a sinusoidal relation:

$$V(t) = \gamma + K \sin\left(\frac{2\pi(t - T_0)}{P}\right) = \gamma + K \sin\left(2\pi(\phi - \phi_0)\right) \tag{2-4}$$

where P is the period of the system, γ the relative velocity of the system in our line of sight (systemic velocity) and K the radial velocity amplitude of the emission component projected along the line of sight. The phase zero point (ϕ_0) is defined as the superior conjunction of the white dwarf. This equation is referred to as the radial velocity (RV) curve. Measuring the offset of spectral components as a function of binary phase provides measures the radial velocity of the component (e.g. disc and donor) and is a much used tool in many binary studies. See bottom panel of Figure 2-5 for an example RV curve of Hα in OY Car. In this work, we fix the orbital period to the literature value, and fit only γ, K and ϕ_0.

The quality of the Gaussian fit to the individual profiles depends strongly on the S/N of the individual spectra and the amount of freedom given and is measured in the form of a reduced χ^2 statistic. As the systematic errors, and visual inspection of the quality of fit are of great importance, we do not strive to reduce $\chi^2 \sim 1$ for the individual Gaussian fits to the profiles. Instead, we scale the errors on the individual Gaussian fits (given by *mgfit*) such that for the radial velocity fit the reduced χ^2 is close to 1. After such scaling, this provides us with 1σ errors on K, γ and ϕ_0 for all RV fits performed in this thesis.

Diagnostic Diagram

The diagnostic diagram returns a measure of the radial velocity of the WD primary (K_1) via the radial velocity of the disc ($K_{\rm disc}$). Single or multiple Gaussian fits are strongly biased towards the position of the peak of the profile. Unfortunately, in CVs the disc emission can be outshone by strong hot spot emission which dominates the inner regions of the double peaked disc emission profile. In addition, the outer disc regions which are easily deformed, also contribute to the inner profile due to their low Keplerian velocities. Both these effects could result in a larger radial velocity amplitude than the true radial velocity of the disc. In contrast, the inner disc governs the wings of the disc

profile. By fitting the observed profiles with 2 Gaussian profiles, set apart by a fixed separation, Δv, the inner regions of the profiles (originating in the outer regions of the disc) are avoided as the focus lies on the high velocity wings, from the high Keplerian velocities in the inner disc. The resulting fit to the RV curve as a function of increasing separation is strongly dependent on Δv, as described by Shafter (1983). This method serves to suppress the systematic distortion to the disc radial velocity produced by outer disc asymmetries. Plotting the fit parameters of the RV curve as a function of Δv in a 'diagnostic diagram' (DD) shows that the fractional error in K (σ_K/K) decreases as the separation increases, until Δv becomes too large and the fit to the profile is dominated by the noise in the continuum rather than by the extreme high velocity wings of the line profile.

An example diagnostic diagram is given for the Hα emission profile in the short period system OY Car (Figure 2-5). At small separations, the Gaussian fit is still dominated by the non-uniform emission at low velocities. This results in too high a value for K and large errors on all the parameters. At intermediate separations, the fit settles on K with small individual errors (minimum values for σ_K/K, displayed by the 'plateau' in the parameter panels). Finally, at large separations, the radial velocity curve fit becomes dominated by the continuum noise. The average value of the fit parameters on the plateau region gives the best solution and their scatter is used as a measure of uncertainty. If this error is smaller than the error on the individual solution, the latter is adopted.

Cross correlating spectra

If absorption features of the late type secondary star are visible and the spectral type is known, template spectra of similar type stars can be cross correlated with the CV spectra (Stover et al. 1980, Horne et al. 1986) using *xcor* in MOLLY. The template spectra can either be observed with the same set-up or we can use high-resolution catalogue spectra. The latter are provided by 'The UVES Paranal Observatory Project: A Library of High- Resolution Spectra of Stars across the Hertzsprung-Russell Diagram' (UVES POP; Bagnulo et al. 2003), and need to be processed so they have the same velocity resolution and rotational broadening as the science spectrum. During cross correlation, regions containing non secondary star related spectral features are masked out. The *xcor* tool carries out a standard computation of cross-correlation, interpolating over masked regions. Maximum cross-correlation is located by a parabsolic approximation

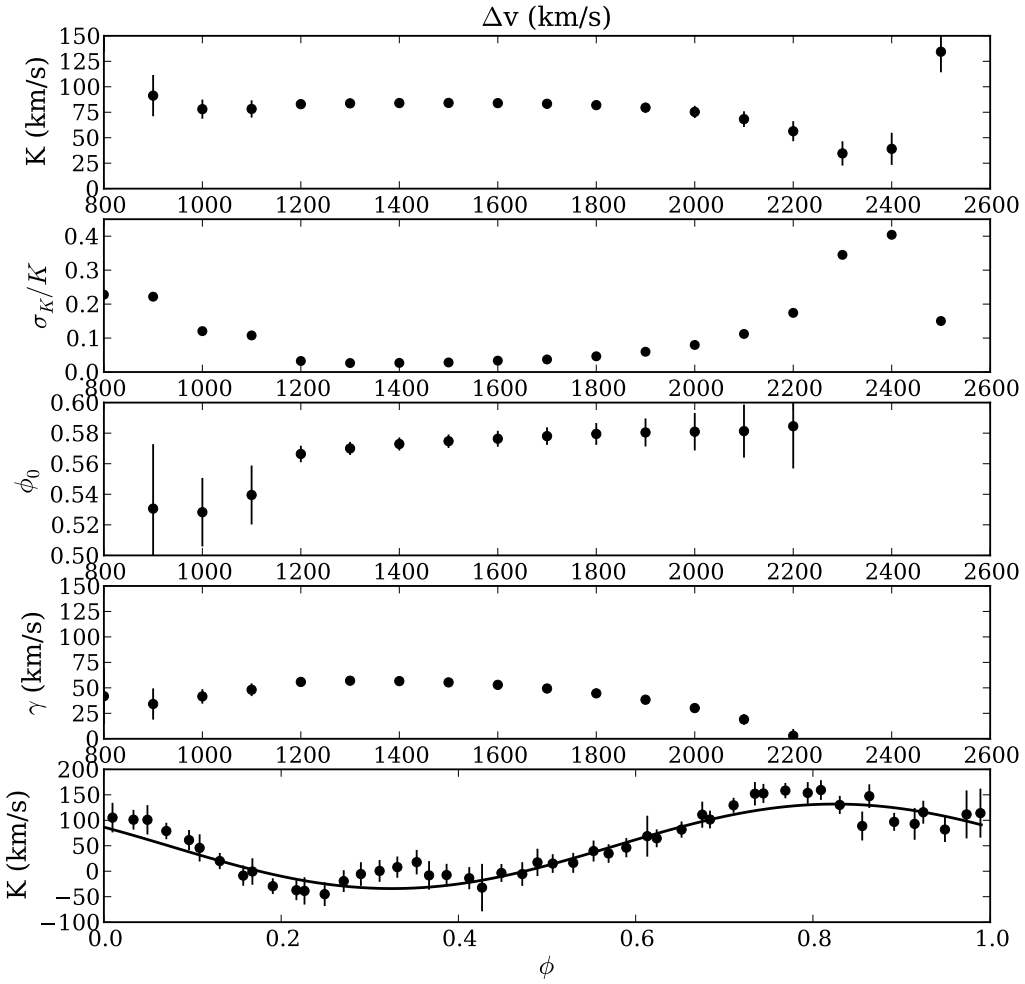

Figure 2-5: From top to bottom: Radial velocity amplitude, K, as a function of the Gaussian separation, fractional error on K (σ_K/K), phase zero point, systemic velocity and the best fit to the radial velocity curve when the individual phases are fitted with a two Gaussian profile with FWHM = 20 Å and Δv = 1500 km s^{-1}. The best fit parameters are determined by averaging over the fit parameters in the plateau range $\Delta v = 1200 - 2000$ km s^{-1}: $\gamma = 48.9 \pm 8.9$ km s^{-1}, $K = 83.0 \pm 3.3$ km s^{-1}and $\phi_0 = 0.575 \pm 0.004$.

and returns the offset velocity with a purely statistical uncertainty hence the best results are obtained using re-binned and normalised spectra.

Cross correlating spectra a time series of spectra is naturally followed by a RV fit to the returned velocity offsets. As before, the 1σ errors on the individual offsets are scaled such that for the sine-curve fit the reduced $\chi^2 \sim 1$. The method returns a measure for the radial velocity of the donor (K_2) via the radial velocity of the absorption lines located at the cold back side of the donor surface ($K_{\rm abs}$).

2.3.3 Doppler tomography

The spectral lines in CVs are projected at different radial velocities as the orientation of the binary changes. The spectral lines also show distortions as a function of orbital phase as different parts of the CV are obscured at the different phases. By tracing the spectral lines as a function of the orbital phase, we can follow this time dependency and try to pinpoint its origin in the binary configuration.

Position coordinates

The right panel in Figure 2-6 depicts a CV containing a Roche lobe filling donor star, the mass transfer stream, the accretion disc and the WD. Also indicated are their velocity vectors, denoted respectively by K_2, black filled circles, $K_{\rm disc}$ (indicated as K_D in Figure 2-6) and K_1. We directly measure the projection of these velocities along our line of sight as a function of the binary phase, $I(v, \phi)$. To reconstruct the image plane in position coordinates, $I(x, y)$, more information than provided is needed. Due to the overlap and blending between the various features in the spectra caused by the orbital motion of the binary, the identification of the origin of the features can problematic.

Velocity coordinates

Because of the rotation of the binary, a spot of emission will trace a sinusoidal radial velocity curve, or S-wave, in stacked spectra plotted against the binary phase (trailed spectra, $I(v, \phi)$; Figure 2-7). The velocity curve is set by the function $V(\phi) = \gamma - V_x \sin 2\pi\phi + V_y \cos 2\pi\phi$. Thus tracing an emission feature as a function of the binary phase provides a unique location in the velocity-velocity plane defined by V_x and V_y ($I(V_x, V_y)$, Doppler map or Doppler tomogram; left panel in Figure 2-6, Marsh & Horne 1988).

The donor star velocity is projected in a Doppler map to $V_x, V_y = 0, +K_2$. As the

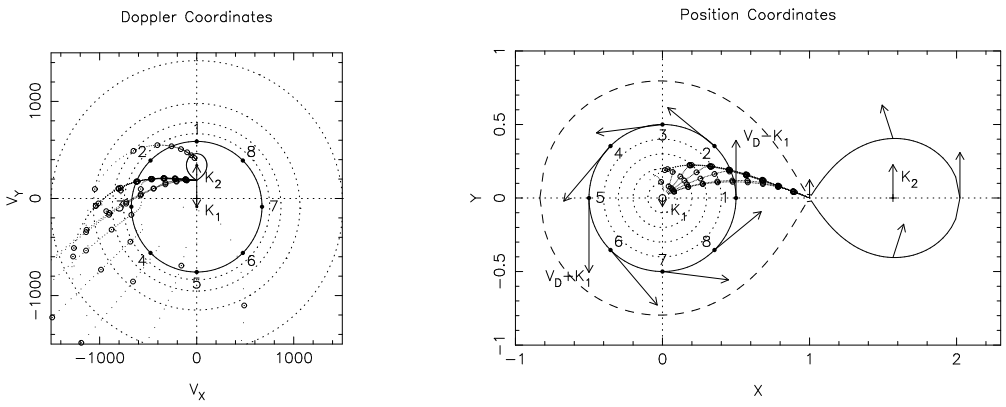

Figure 2-6: The conversion between spatial (right) and Doppler coordinates (left). In position coordinates, indicated are the Roche lobe filling donor star (with velocity K_2), the Keplerian accretion disc ($K_{\rm disc}$), the WD (K_1) and the mass transfer stream (black filled circles) and their velocity vectors are shown. Key locations are the location of the donor star at $V_x, V_y = 0, +K_2$ and the WD at $V_x, V_y = 0, -K_1$. The disc is projected inside out as the Keplerian velocities are largest at the inner edge of the disc and smallest at the outer rim. From Keith Hornes lecture notes: `http://star-www.st-and.ac.uk/ kdh1/pub0/doptom/doptom.html`.

donor star's position is fixed in the rotating frame of the binary, with every point having a fixed radial velocity ($\mathbf{\Omega}\times\mathbf{r}$) which is linear in the direction perpendicular to the rotation axis, its shape is preserved. The WD radial velocity is projected to $V_x, V_y = 0, -K_1$, but as the WD is rarely visible in emission, no emission spot is expected at this location. An ideal, symmetric and optically thin disc with a Keplerian velocity field ($V \propto R^{-0.5}$) has a symmetric velocity profile at all phases, e.g. shows the same set of V_x, V_y components at every phase angle. In this case, the disc is projected as a circular shape, but inside out. This feature is centred at the WD radial velocity as the disc traces the WD movement. Deviations from the circular shape and uniformity are caused by non-circular discs and asymmetries like the hot spot and spiral density waves (Steeghs et al., 1997). As $K_2 < K_{\rm disc}$, the emission spot of the donor always lies within the disc ring in velocity space.

Assumptions

Doppler imaging is the inversion from observed data ($I(v, \phi)$) to image data ($I(V_x, V_y)$), and the underlying assumptions for the creation of a valid Doppler map are:

- All elements of the binary are visible at all phases.
- The flux of each element of the binary is constant over an orbital cycle.

- All motion is parallel to the orbital plane.
- All velocity vectors rotate with the binary.
- The intrinsic width (e.g. the thermal width) of the profile from any point is negligible.

Not all assumptions are per definition matched: the donor can obscure the WD, accretion disc, hotspot and itself, violating the first assumption. Hence, care should be taken when interpreting a map. Both the effects of orbital smearing, when the velocity change of the emission component over the length of the exposure broadens the profile, and under sampling, when insufficient independent phases are obtained, require a minimum number of phases to construct a unique Doppler map.

The maximum exposure time that can be used, depends on the radial velocity amplitude of the component (K), as the projected velocity will change by an amount ΔV during an exposure of time t via:

$$\Delta\phi = \frac{t}{P_{\rm orb}} \sim \frac{1}{2\pi}\frac{\Delta V}{K} \tag{2-5}$$

(equation from Marsh 2001). The optimum situation is when the orbital smearing remains less than the spectral resolution of the set-up. For short orbital period binaries, this requires large telescopes. However, to improve the smoothness of the map due to sparse sampling of the orbit, we can enforce an interpolation between the phases when calculating the map to create a finer grid. This assumes that the profile varies gradually between the observed phases.

Maximum entropy inversion

The two main methods for the creation of Doppler maps are the Fourier filtered back projection of the spectra (e.g. appendix A of Marsh & Horne 1988) and maximum entropy inversion. With the increase of computing capabilities, the latter has become more widely used. Throughout this thesis, we have exploited the maximum entropy method using the package DOPPLER, provided by Tom Marsh, with the aid of personal C-shell scripts.

The maximum entropy method is based on finding the most uniform distribution consistent with the data by maximising the entropy (Marsh & Horne, 1988). Two main forms of uniformity can be chosen via a default map. The first one is defined as true uniformity and all pixels are treated equally. The second one, and used throughout this

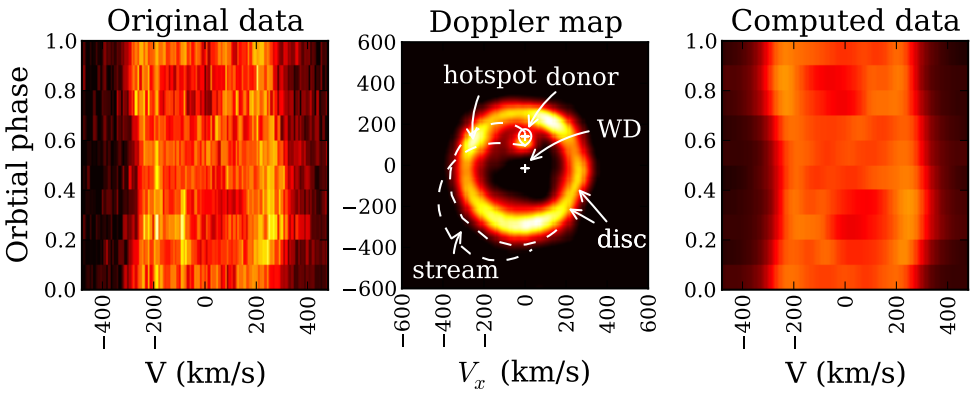

Figure 2-7: **Left:** Original trailed spectra of Ca II λ8662Å data of UV Per, binned into 10 phase bins. Visible are the double peaked emission lines from the disc and a weak S-wave emission in anti phase. **Middle:** The Doppler map from this data, rotated such that the donor emission is located at $V_x, V_y = 0, +K_2$. Also indicated are the disc, the location of the WD, the hotspot and the stream trajectories. **Right:** Reconstructed data from the Doppler map.

thesis, uses a Gaussian blur factor that ensures that the entropy becomes insensitive to large scale variations while smoothing the map on small scales.

Maximum entropy maps (MEMs) are created by comparing predicted data to the actual data in the search for a user defined minimum in the goodness of fit measure χ^2. This minimum is approached in two steps. The first step of initial optimisation produces a uniform map with the lowest goodness of fit to the data. The second step searches for the best non-uniform solution. The resultant map is defined by the smoothest and simplest map (i.e. maximum entropy) that can be reconstructed for the given data, at the specified level provided by the user. This minimum is set to a value based on visual inspection of the resultant map and normally defined by the transition between a smooth map and an over-fitted map when smoothness is lost as changing individual pixel values decreases the goodness of fit but simultaneously introduces spurious features. An example Doppler map for the Ca II λ8662Å emission line in UV Per can be can be seen in the middle panel of Figure 2-7. The reduced χ^2 achieved in this case was 1.6.

Centre of symmetry

For an ideal Keplerian disc the centre of the projected disc should be coincident with the WD at $V_x, V_y = 0, -K_1$. However, due to asymmetrical emission (e.g. the hotspot), it is not always possible to obtain a reliable estimate of K_1 from a Doppler map. To determine

the centre of the assumed symmetric disc, we subtract a symmetrical component of the map, centred on a chosen centre at V_x, V_y, followed by an inspection of residuals in a known symmetrical part of the disc. The symmetric component can be calculated with the command *imsymm* within the DOPPLER package, which calculates an axis-symmetric image constructed of a set of rings centred at a given V_x, V_y for a given map (Figure 2-8). When subtracted, this will reveal any remaining emission spots (like the donor and hot spot), which should be avoided when calculating the minimisation of the residuals. The centre of symmetry method is related to the two-Gaussian method and Diagnostic diagram and returns $K_{\rm disc}$. By focussing on high velocity, symmetric parts of the disc, contamination by any asymmetries in emission is avoided. The advantage of this technique is that such symmetric and undistorted regions can easily be identified using the Doppler map, and has been successfully used for Hercules X-1 Still et al. (1997) and Scorpius X-1 Steeghs & Casares (2002).

As the maximum entropy map uses non-linear algorithms, it is hard to propagate statistical uncertainties from the obtained spectra to the constructed map. As the error in the Doppler maps is dominated by the structure in the map itself and the demanded entropy, a reliable and physical meaningful error budget on the pixels is difficult to obtain. For MEM's the most used method to calculate errors is with the 'bootstrap' method (based on Monte Carlo simulations, Efron & Tibshirani 1994). This method uses the original data is to generate artificial data. The artificial dataset is the same as the original, apart from a set of points that has been replaced. Measuring the presence of an emission feature in multiple artificial maps gives an a measure of the significance of the feature (Marsh, 2001). However, this method requires large amounts of computing time, as around 1000 Doppler maps need to be calculated per data set, which, combined with the large number of maps contained within the thesis, is beyond the scope of this work.

A workable solution for our maps is to assume that the error on the centre of symmetry is set by the choice of grid resolution for the map ($\sigma_{V_y} = \sigma_{V_y}$). The grid is normally sampled on around half the spectral resolution of the data. The centre of symmetry is optimised on this grid resolution, first in V_y with $V_x = 0$, followed by optimising in V_x with V_y fixed on the previous value. Finally, we optimise again in V_y, with V_x fixed. We adopt an error set by the chosen grid resolution ($\sqrt{\sigma^2_{V_y} + \sigma^2_{V_y}} = \sqrt{2}\times$ grid resolution), and acknowledge this that is an optimistic lower limit and dominated by systematic errors.

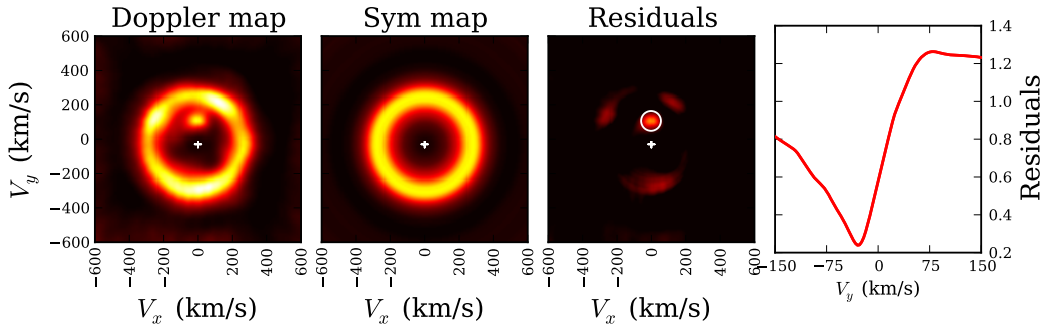

Figure 2-8: Example of a centre of symmetry search. **Left:** the original Ca II Doppler map of UV Per. **Second from left:** after a centre of symmetry search (both in V_x and V_y) the best fit symmetrical map is calculated. **Third from left:** The residual map (Doppler map minus symmetrical map) shows deviations from symmetry including the irradiated donor and hot spot regions on the disc. Indicated in all maps is the centre of symmetry at $V_x, V_y = 0, -30$ km s^{-1}. In the residuals map, we also indicate the location of the donor emission spot. **Right:** Example of the residuals level calculated as a function of the centre of the subtracted ring (V_y).

To find the influence on the centre of symmetry of using the correct systemic velocity, we have created a range of maps for UV Per, with γ in the range of $-50, 50$ km s^{-1} with steps of 10 km s^{-1}. For all these maps, the centre of symmetry was determined using the same area of the map. We find the best final value for $\chi^2 = 1.8$ for $\gamma = 20$ km s^{-1}. Interestingly, this systemic velocity also gives provides the best initial quality of fit $\chi^2 = 5.7$ after only optimising a completely uniform map to the data. These results can be found in Figure 2-9. As expected, we find a direct correlation between the assumed systemic velocity and the measured centre of symmetry. This implies that we can only determine the centre of symmetry when the Doppler map is created using the correct value for γ. In conclusion, the best way to determine the correct centre of symmetry (and hence $K_{\rm disc}$) for a dataset is to first optimise the Doppler map for the systemic velocity, and then search for the centre of symmetry. We apply this method to all centre of symmetry searches in this thesis.

A related method to both the diagnostic diagram and the centre of symmetry in Doppler maps, is the 'light centre' method as proposed by Marsh 1988. This method is based on the same principles and fits the returned RV with $-K_x \cos\phi + K_y \sin\phi$, where K_x, K_y indicates the centre of the emission in velocity space. Increasing the separation between the two Gaussian profiles moves the centre of the emission from the hotspot emission to the centre of the disc, i.e. the WD.

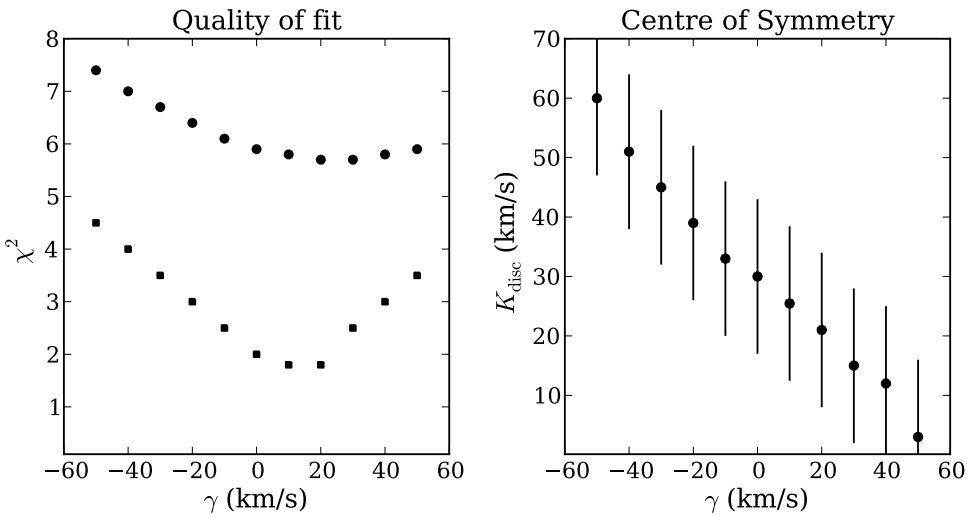

Figure 2-9: **Left:** The lowest χ^2 of the Ca II λ8662Å Doppler map for UV Per, as a function of γ (*black squares*). The quality of fit for the initial optimisation of a uniform map of the data is indicated in *black dots*. **Right:** The centre of symmetry as a function of the systemic velocity.

2-D Gaussian fit to emission

Doppler maps can also be exploited to locate the emission originating from the donor star. By fitting a 2-dimensional Gaussian profile to the emission spot either in the original or the residuals map, the location, $K_{\rm em}$, can be determined in V_x, V_y, see Figure 2-8. The width of the profile can be used as crude measure of the error on this location via FWHM$\approx 2.35\sigma$. This is an overestimate of the error as the profile has an intrinsic width due to the rotation of the donor star. Proper errors can be determined using Monte Carlo simulations in by measuring the location of the feature for a large number of artificial maps calculated by bootstrapping the original data. However, due to the large number of Doppler maps presented in this thesis, and hence the large amount of computing time required, we have decided not to pursue this method for this work.

2.3.4 Gravitational redshift

Low accretion rate WDs can show narrow photospheric absorption features of metal lines due to freshly accreted gas. These lines open a window to probe the WD atmosphere directly and give independent measurements for stellar parameters. For lines formed near the WD, a gravitational redshift is expected, introduced in the deep gravitational potential of the WD (Eddington 1924; Greenstein & Trimble 1967; Sion et al. 1994). A

measurement of this redshift in the rest frame of the binary could provide the WD mass directly when combined with mass-radius models for fully degenerate mass donors, such as Eggleton's relation as quoted in Verbunt & Rappaport (1988):

$$\begin{aligned}\frac{R}{R_\odot} &= 0.0114\left[\left(\frac{M}{M_{\rm Ch}}\right)^{-2/3}-\left(\frac{M}{M_{\rm Ch}}\right)^{2/3}\right]^{1/2} \\ &\times \left[1+3.5\left(\frac{M}{M_{\rm p}}\right)^{-2/3}+\left(\frac{M}{M_{\rm p}}\right)^{-1}\right]^{-2/3},\end{aligned} \tag{2-6}$$

where $M_{\rm Ch}$ is the Chandrasekhar mass ($1.44M_\odot$) and $M_{\rm p} = 0.00057M_\odot$, a numerical constant. Non-zero temperature mass-radius tables for different WD core and envelope combinations are given by e.g. Fontaine et al. (2001).

In the case of binaries, the directly measured redshift ($v_{\rm grav}$(line)) needs to be rectified for several contributions in order to get the true gravitational redshift induced by the WD only ($v_{\rm grav}$(WD)). These corrections include the systemic velocity of the binary (γ) and the effects of the gravitational potential of the donor star ($v_{\rm grav}$(donor)). This latter correction is justified as the line is also positioned in gravitational potential of the donor. Hence the gravitational redshift due to the WD is given by:

$$v_{\rm grav}({\rm WD}) = v_{\rm grav}({\rm line}) - v_{\rm grav}({\rm donor}) - \gamma. \tag{2-7}$$

A theoretical value for the gravitational redshift induced by an object of mass M at a distance d is given by:

$$z_{\rm g} = \frac{1}{\sqrt{1-\frac{2GM}{dc^2}}} - 1 \simeq \frac{GM}{c^2 d}. \tag{2-8}$$

When measuring gravitational redshifts via disc emission line features, Equation 2-8 can be rewritten as:

$$z_{\rm g} \equiv \frac{v_{\rm disc}^2}{c^2}, \tag{2-9}$$

as for Keplerian orbits $v_{\rm disc} = \sqrt{GM/d}$. As the material in the disc rotates at high velocities, we also need to account for time dilation or transverse Doppler redshift (e.g. Margon 1984). This effect occurs when light is emitted at the point of closest approach between emitter and receiver. For the observer the received light at this point was emitted slightly earlier and hence is shifted by the amount of:

$$z_{\rm T} = \gamma - 1 = \frac{1}{\sqrt{1-\frac{v_{\rm disc}^2}{c^2}}} - 1 \simeq \frac{v_{\rm disc}^2}{2c^2}. \tag{2-10}$$

This brings the total gravitational redshift for disc features to $z_{\rm total} = \frac{3v_{\rm disc}^2}{2c^2}$.

To determine the mass and radius of the WD directly, independently of q and the inclination i, we can now find the intercept between the theoretical value of the gravitational redshift induced by a WD of mass M and radius R (via Equations 2-6 and 2-8) and the measured gravitational redshift as given by Equation 2-7.

2.4 Irradiation modelling

As the surface of the donor star co-rotates with the system, emission arising from different locations will have projected radial velocities corresponding to their distance to the centre of mass of the binary. Emission arising from near the tip of the L_1 point will have a smaller projected radial velocity than the true velocity of the donor (K_2), whereas any features originating from the back of the lobe will have larger radial velocities, see Figure 2-10. Irradiation models can be constructed to determine the correction for an emission component, i.e $\Delta K = K_2 - K_{\rm em}$.

2.4.1 K-correction

Using the code *irradprof* within the package LCURVE provided by Tom Marsh, synthetic irradiation profiles for an irradiated donor star can be constructed to measure the so called K-correction factor for emission arising from L_1. The parameters controlling the total can be split into two categories: system parameters and instrumental parameters.

The first set govern the binary geometry: mass ratio, inclination, radius of the secondary star, and if Roche lobe filling, the radius of the primary star, the total vertical depth of the emitting layer on the donor surface (both optically thin and optically thick cases are possible), the ratio of the height of the disc over the extent of the disc and the projected velocity scale of the system ($K_1 + K_2$). In addition, the code can also account for Roche distortion, limb darkening and a secondary eclipse.

The parameters representing the instrumental set up are the orbital phase range, the number of phases to calculate, the length of the exposure time in terms of the phase, the number of subdivisions to account for finite exposure times, the accuracy limit in phases for eclipse calculations and the number of lattice strips across the surface of the donor star. The wavelength resolution and spectral range of the returned spectrum is set by a user defined minimum and maximum velocity to be calculated, the number of velocity bins, the FWHM and a blurring factor for these bins.

Extensive tests show that the K-correction is only weakly affected by the vertical depth of the emitting layer, disc height and radius of the primary star. We thus fix these

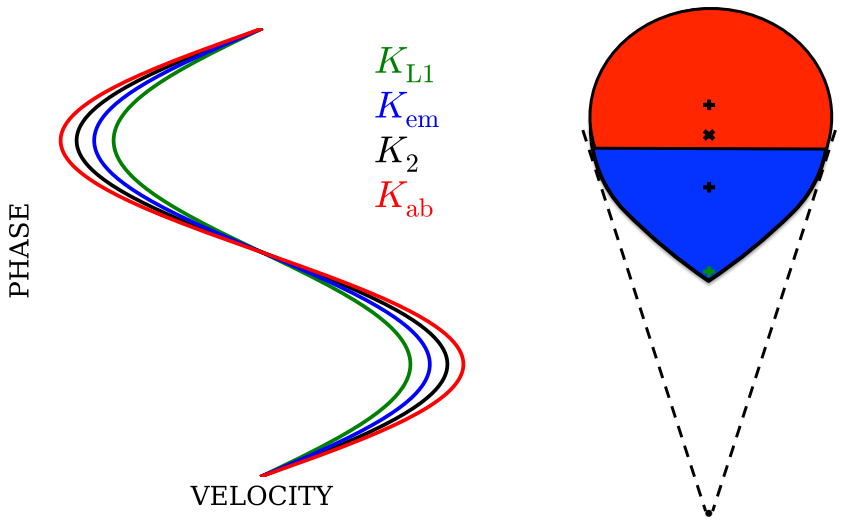

Figure 2-10: Dependence of the measured radial velocity amplitude of the emission/absorption components on the location on the donor surface. **Left:** Radial velocity curves from the different components. **Right:** Location on the donor star surface. Colour coding as indicated. The measured radial velocity amplitudes come from, ordered from smallest amplitude to largest amplitude: the location near the inner Lagrangian point ($K_{\rm L1}$, green), irradiation induced emission ($K_{\rm em}$, blue), true radial velocity of the donor which will not be measurable (K_2, black) and absorption arising from the cool backside of the donor ($K_{\rm abs}$, red).

parameters to standard values for all models. The binary parameters q and i should ideally be chosen close to their true value. To find ΔK, we optimise the model for the velocity scale ($K_1 + K_2$) such that the model trailed spectra follow an RV curve with an amplitude similar to $K_{\rm em}$. This way, we can use the observed $K_{\rm em}$ to constrain K_2.

2.4.2 Radial velocity of the emission component

To test the outcome of the irradiation model against the various instrumental and binary properties, we constructed a model dataset using our irradiation code *irradprof* for a typical system parameters of $q = 0.25$, $K = K_1 + K_2 = 600$ km s^{-1}. To simulate real data, we add noise to the data (via a signal to noise level: S/N) and fit a 1 Gaussian profile the returned emission component, followed by a RV fit, as described in Section 2.3.2.

First, we checked the model dependency on the intrinsic binary properties. Even though the inclination results in a simple $\sin i$ scaling of the projected radial velocity, we measured its consistency over the entire plausible range. By fixing the projected radial velocities while ranging the inclination, we find that the measured radial velocity component changes by ~ 10 km s^{-1} over the entire range, see Figure 2-11 for an example. Hence, the induced error by creating a model with the wrong inclination only matters in low inclination systems, when the projected radial velocities are very small. For the models created to measure ΔK for the systems in our survey that display donor emission, we fix the inclination to 45°, unless we know the binary inclination via independent methods.

To test the consistency of the observed radial velocity component K_2 under several experimental set-ups, we varied the spectral resolution, the number of phase bins per orbital period and the S/N and measured the resulting radial velocity of the emission line profile as a function of orbital phase for an example model. We find a strong correlation between the three properties, plotted in Figure 2-11. For example, for a spectral resolution of $\lesssim 4$ km s^{-1}, and $\gtrsim 20$ phase bins per orbit the error on $K_{\rm em}$ is dominated by the statistical error returned by the RV fit, independently of the S/N. For the more commonly used value of ~ 10 phase bins, the error on $K_{\rm em}$ is dominated by systematics for a S/N $\gtrsim 15$ and a spectral resolution of $\lesssim 8$ km s^{-1}. Figure 2-11 shows that for a large number of phase bins and a good spectral resolution, the measured $K_{\rm em}$ is consistent to within the 1σ (statistical) error. When we deviate away from these experimental configurations, we no longer find the correct $K_{\rm em}$ within the statistical 1σ error.

For a typical data set obtained at the William Herschel Telescope for this thesis, we achieve a S/N of ~ 10 with 10 phase bins and a spectral resolution of ~ 20 km s^{-1}. We see that for these properties, the error on the modelled of $K_{\rm em}$ (and hence ΔK) is small compared to the spectral data resolution and the error on the measured radial velocity amplitude ($K_{\rm em} = 340.6 \pm 1.9$ km s^{-1}) and hence the dominant error is provided by systemic errors. Figure 2-11 emphasises that even for low S/N, combined with a moderate resolution, the number of phase bins only needs to be in of order ~ 20 to accurately measure the radial velocity component of the donor.

Note the perceived independence on the S/N of the data show in Figure 2-11. In real data, the emission component is not isolated, but surrounded by often stronger, disc and hot spot features. To try and fit the profile of the emission without the contamination

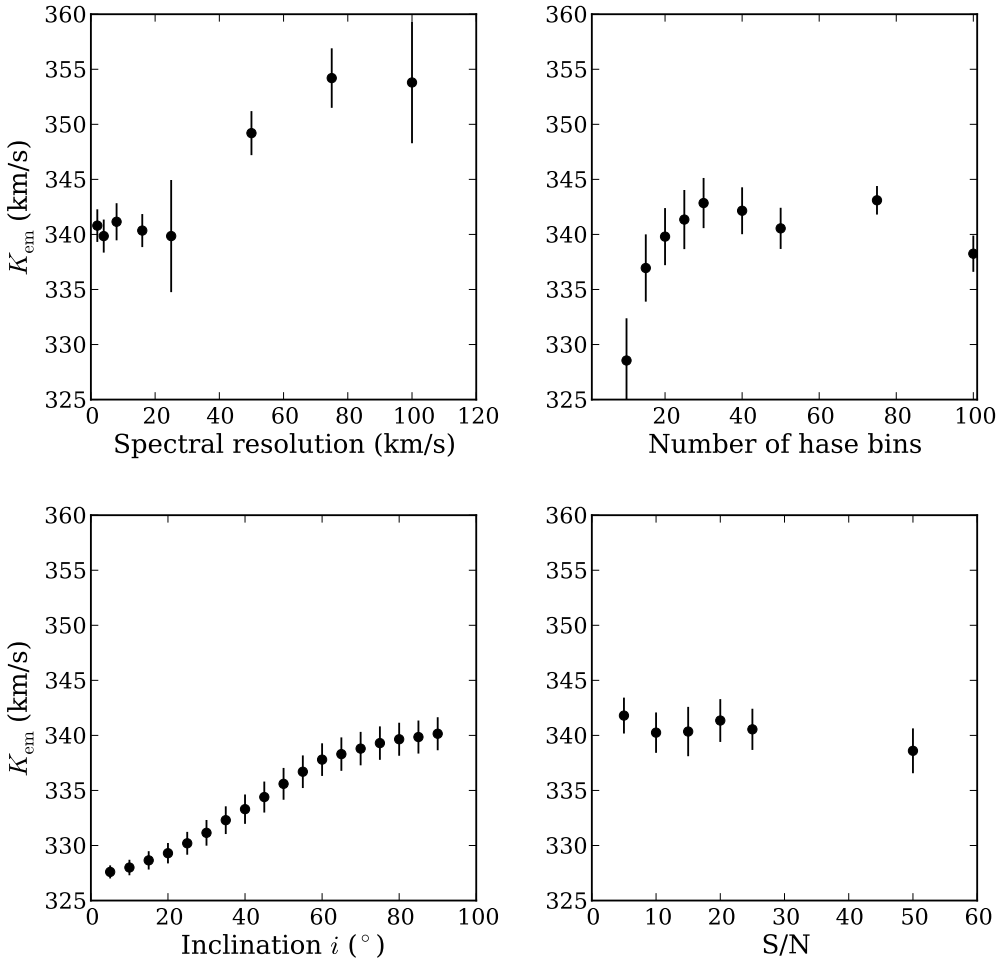

Figure 2-11: **Top left:** Measured $K_{\rm em}$ from the irradiation model profiles as a function of the spectral resolution. **Top right:** $K_{\rm em}$ as a function of the number of phase bins. **Bottom left:** $K_{\rm em}$ as a function of the inclination of the system. **Bottom right:** $K_{\rm em}$ as a function of the S/N of the data. For all models, the initial set of parameters is set to: $q = 0.25$, $K = K_1 + K_2 = 600$ km s^{-1}, spectral resolution $= 4$ km s^{-1} , 50 phase bins, $i = 85^\circ$ and S/N $= 25$, unless otherwise stated. For the influence of the inclination on $K_{\rm em}$, we fix $K_1 + K_2 = 600$ km s^{-1}. The correct $K_{\rm em} = 340.6 \pm 1.9$ km s^{-1}.

of the disc profile in low S/N data, we subtract the orbital average disc profile from each spectrum. However, low S/N data results in very low S/N residuals. These residual lines are much harder to fit than the ideal, isolated, model emission line. This results in larger errors on the individual Gaussian fit parameters than the model predicts.

2.4.3 Line strength variation

The visibility of the emission lines originating on the donor surface or, more precisely, the strength of these lines as a function of orbital phase is dependent on the inclination of the system as self obscuration of donor emission depends on the inclination angle. In principle, tracing the change in line strength as a function of phase, should give an indication of the inclination by modelling light curves using *irradprof*.

In order to fit the residual emission lines from the donor after subtraction of the average disc profile with a Gaussian with as variables the peak height and width as a function of the binary period, we require much higher S/N and spectral resolution than for finding the radial velocity. An example of the line strength variations for two models with different inclinations can be found in Figure 2-12.

The bottom 2 panels in Figure 2-12 show the strength of the lines in the high inclination varies by a factor of 8 whereas for the low inclination system it is only a factor of 2. Hence measuring the fraction as a function of the phase compared to model light curves potentially puts a handle of those systems that have an unknown inclination angle.

2.5 Exploring new emission line diagnostics for CVs near the minimum period

2.5.1 Motivation

As described in Chapter 1, a key expectation based on our current understanding of binary evolution is that angular momentum loss drives CVs to short orbital periods as their donor stars shed mass. Around 70-80 minutes, the now brown dwarf type donor star will become degenerate and further mass loss will increase the orbital period. We expect to find most CVs near their period minimum, and around 70% of all CVs should have reached this 'period bounce' stage (Kolb, 1993). Recent CV searches, such as the significant harvest of CVs from SDSS (e.g. Gänsicke et al. 2009; Southworth et al. 2007) are finally unearthing short-period systems in larger numbers. Although the orbital

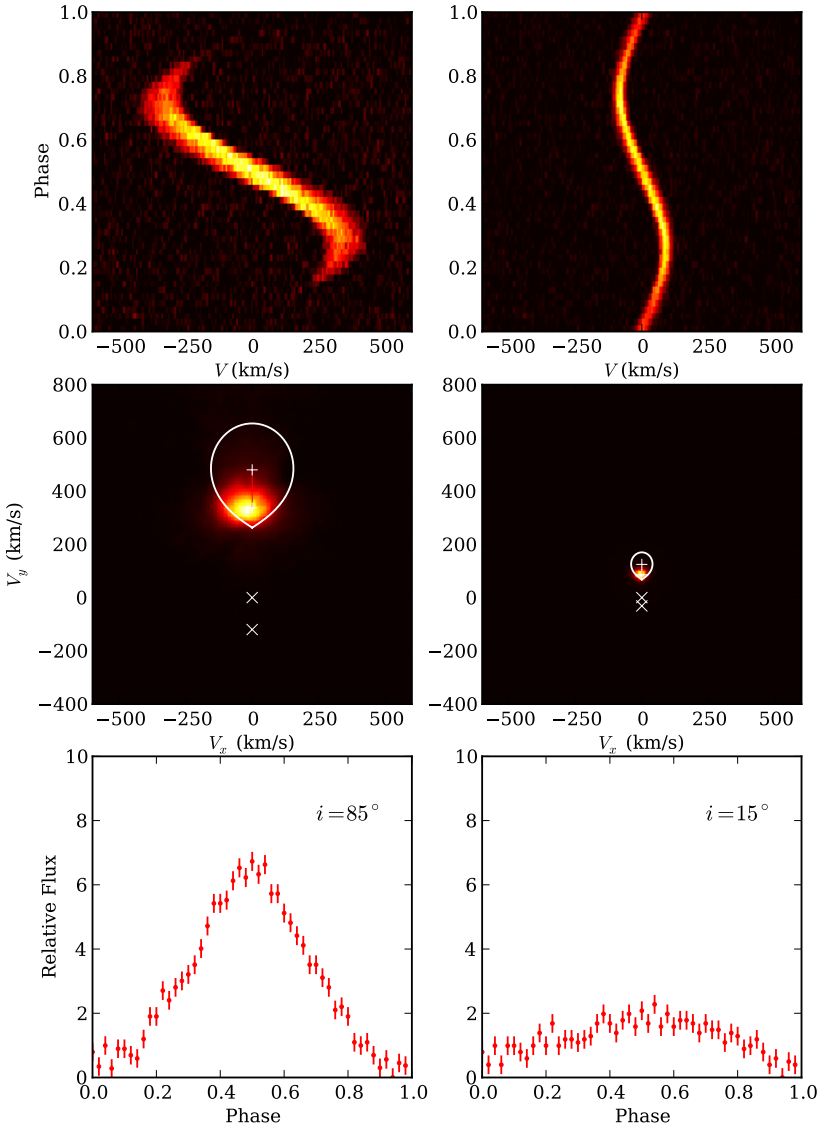

Figure 2-12: Synthetic light curve example for $q = 0.25$ and $V_2 = 482$ km s^{-1}and $V_1 = 121$ km s^{-1}. These velocities are projected onto K_1, K_2 for two example inclinations: $i = 85°$ (left) and $i = 15°$ (right). The top row shows model trailed spectra as a function of phase. The middle row shows the resulting Doppler maps, with the Roche lobe of the secondary (solid line), K_2 and $K_{\rm em}$ (+) and the centre of mass $(V_x, V_y = 0, 0)$ and K_1 (x). The bottom row shows the relative line strength variation of the profiles as a function of phase.

period is an important diagnostic, reliable mass estimates are needed for the donor stars to place a CV on its evolutionary track. The faintness of the low mass donor stars in comparison to the white dwarf and its accretion flow means that we actually have very few solid mass constraints in this short period regime. Only in 2006, the first secure CV with a brown dwarf donor was identified thanks to the tight mass constraints made possible because the system is eclipsing (Littlefair et al., 2006). In comparison, the more proto-typical candidates such as WZ Sge remain difficult to constrain conclusively (Patterson 2001; Steeghs et al. 2001; Steeghs et al. 2007).

At this moment in time, we do not know whether the period bouncers are truly deficient in number, or whether they are hiding amongst the known short period systems. There are very few systems in the 75-100 minute orbital period range with detected photospheric absorption features from their mass donors. Patterson (2001, 2011) has identified several potential candidates with low mass donors, but his method, which is based upon tidal instabilities of the discs, is indirect and poorly calibrated exactly at the small mass ratios which are of most relevance. We thus need to determine more mass ratios for the shortest period CVs. However, the use of traditional methods is limited by the faintness of the donor star in the commonly used absorption lines and hence we need to explore new spectral features in our search for the donor.

2.5.2 Emission line broadening

After strength, the most important feature of an emission line is the amount of broadening that creates the shape. Most strong disc emission lines are optically thick and saturated. In this case, the local line emissivity of a saturated line at rest wavelength λ_0 for a grid cell x, y in the disc can be expressed as:

$$J(x,y) = S_{\rm L} \frac{\Delta v}{\lambda_0} \cos i \sqrt{8 \ln \tau_0}, \tag{2-11}$$

where Δv is the total velocity dispersion along the line of sight (broadening), τ_0 the optical depth of the centre of the emission line and $S_{\rm L}$, the local line source function, can be a simple Planck function. Δv consists of two components:

$$\Delta v^2 = V_{\rm thermal}^2 + V_{\rm shear}^2, \tag{2-12}$$

where the thermal component is given by

$$V_{\rm thermal} = \sqrt{\frac{kT}{m_{\rm H} A}}, \tag{2-13}$$

where A the relative atomic mass of the line in question. The shear component is given by:

$$V_{\rm shear} = \frac{\Delta Z}{\cos i}\mathbf{e}\cdot\nabla\mathbf{V}\cdot\mathbf{e}, \tag{2-14}$$

where ΔZ is the vertical extent of the emission line layer (assumed to be in the range $0 \leq \Delta Z \leq H$), $\mathbf{e}$ denotes the vector from the grid cell towards the observer and $\nabla\mathbf{V}$ the tensor of the local velocity gradient. A more detailed description of these equations and their use can be found in Steeghs & Stehle (1999).

The outcome most relevant for this work is that for heavier atoms, shear broadening becomes more important as the thermal component decreases, which gives rise to more structure being visible in the disc as the thermal component no longer dominates the profile shape, see Figure 2-13.

A second broadening term dependent on the atomic mass, is the pressure broadening (equation 9.59 in Carroll & Ostlie 1996) which states that more massive atoms and lower number densities (n) result in sharper emission line peak:

$$v \propto n\sqrt{\frac{2kT}{m_{\rm H}A}}. \tag{2-15}$$

2.5.3 Emission line broadening as function of the inclination

Horne & Marsh (1986) calculate the influence of the three broadening terms (orbital, shear and thermal broadening) on the disc profile shape as function of the inclination for both the optically thin and thick cases. They show that for very low inclinations, the thermal broadening dominates and the disc profile is single peaked. For moderately small inclinations, the orbital broadening produces the double peaked profile. As shear broadening is still small compared to thermal broadening, little azimuthal variation is expected and the optically thin and thick cases look nearly identical, with the central dip in the profile resembling a U-shape. For moderately large inclinations, the orbital broadening produces again a double peaked profile. However, the shear broadening dominates over the thermal broadening and in the optically thick case, as the local emissivity becomes anisotropic, the profiles become V-shaped with broader emission peaks as absorption dominates the central regions of the profiles. The optically thin line profiles remains sharply double peaked with a shallow U-shaped central region.

2.5.4 Emission line models

Horne (1995) has calculated the emission line spectrum of a uniform slab of solar abundance gas, seen face on with a temperature of 10^4 K and a column density of 10^{22} cm^{-2}.

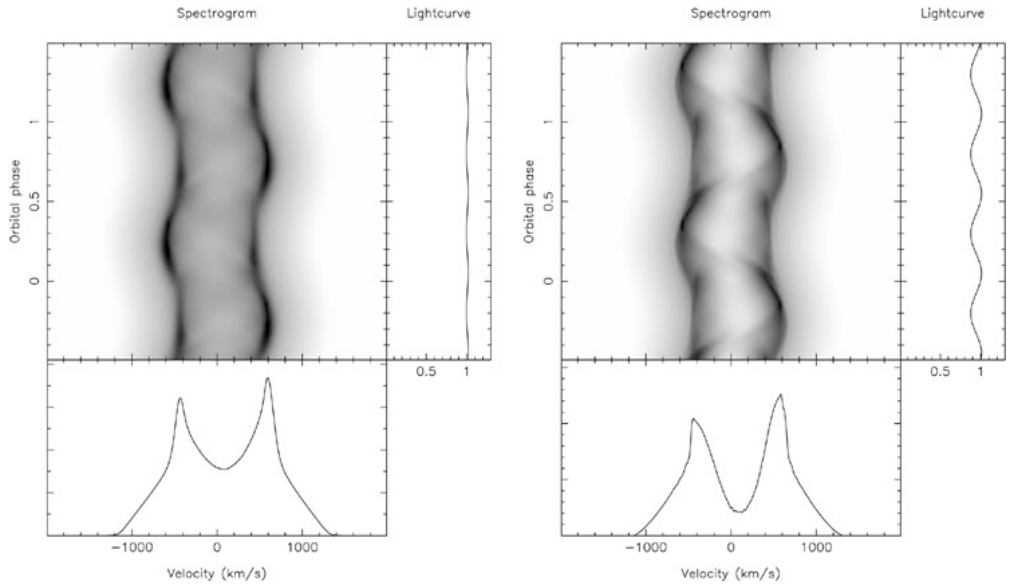

Figure 2-13: Figure 3 from Steeghs & Stehle (1999). **Left:** Line profiles as a function of orbital phase for a hydrogen line ($A = 1$). Here, the thermal broadening is dominant over the the shear broadening, suppressing the spiral wave structures. **Right:** The same profiles but now for a calcium line with $A = 40$, showing the stronger signatures of the spiral waves due to the higher importance of shear broadening compared to thermal broadening.

The velocity dispersion is varied with Mach numbers of 0, 1, 2, 4 and 8, with the Keplerian Mach number is defined as

$$M = \frac{v_{\text{disc}}}{C_s^2}, \tag{2-16}$$

where C_s the local sound speed. It is seen in Figure 2-14, that an increase in velocity dispersion increases the strength of the emission lines, as expected from Equation 2-11, while the continuum remains constant. When increasing the Mach number from 0 to 1, the growth of the metal lines is more pronounced than the growth in the Balmer lines, as the metal lines have thermal velocities much less than the sound speed whereas the Balmer lines have thermal velocities close to the sound speed. The difference in growth between the unblended Ca K line and the blended Ca H line is due to the latter line being blended with Hϵ and when the local broadening exceeds their separation, the saturation merges which suppresses the Ca H emission (Marsh & Dhillon, 1997). Weaker metal lines, like silicon II λ4130Å, initially grow but cease to do so when becoming optically thin.

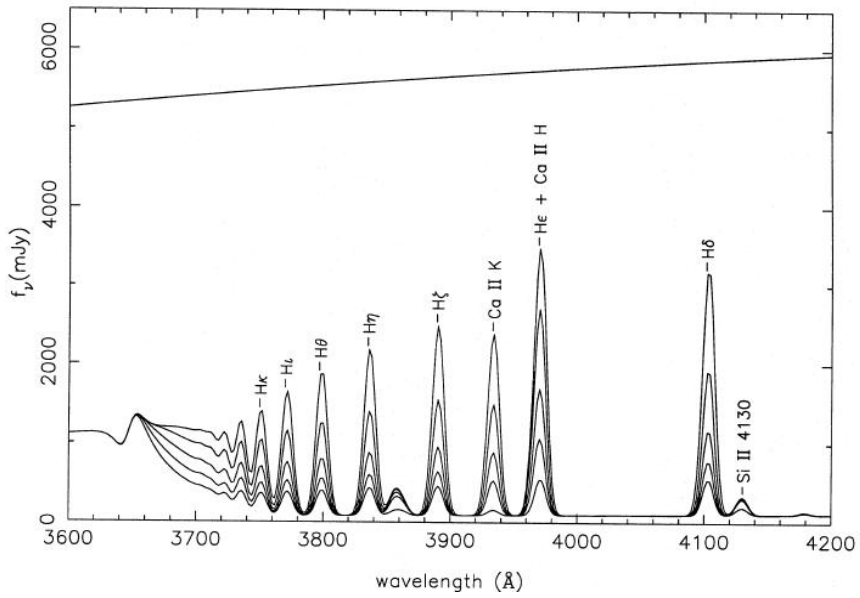

Figure 2-14: Calculated emission-line spectrum for different Mach numbers, figure 6 from Horne (1995). The top line is the Planck function for $T = 10\,000$K.

2.5.5 Diagnostic power of Ca II

As seen in the previous sections, the influence of the thermal broadening depends on the atomic mass of the line in question. Low mass atoms (like hydrogen) have $V_{\rm thermal} \geq V_{\rm shear}$, hence the thermal broadening dominates the line profile shape. Heavier atoms, on the other hand, e.g. calcium, have $V_{\rm thermal} \approx V_{\rm shear}$ and the shear broadening induced in, for example, spiral density shock waves in discs, are no longer obscured by the strong thermal broadening (Figure 2-13).

Another advantage of calcium over hydrogen for the search for disc structure and donor emission, is that due to the lower ionisation energy of calcium (6.1132 eV, compared to hydrogen at 13.5984eV and helium at 24.5874 eV), calcium can also be excited by relatively cool sources of radiation ($\sim 10\,000$K).

Previous studies have shown that calcium, even though relatively weak, can offer advantages over the commonly used Balmer lines for the search disc structures, as they can be excited by cooler sources, and have sharper and easily detectable peaks. However, the Ca II triplet lines in the *I*-band have been little used in the past, primarily because of their location from the major emission lines and the difficulties of using CCDs in the *I*-band, i.e. low quantum efficiency (QE) and fringing. However, the recent development of a new range of CCD's with a high QE and low fringing patters at these longer wavelengths, has these regions. for exploration. For example, Marsh & Dhillon (1997)

present a number of CV spectra, covering the Ca II lines, and indicate their potential power to detect strong spectral features from the components in CVs.

2.6 The plan for constraining q

If we want to dynamically constrain the mass ratio in short period CVs, we will need measurements for both K_1 and K_2. In this Chapter, we have described several ways to measure these quantities using time-resolved spectroscopy which will be used throughout this thesis. A summary of the methods to be used for the two values is given below, including their restrictions.

2.6.1 Measuring K_2

- 1-Gaussian profile fits, followed by a RV curve fit, to specific features in the spectrum, e.g. emission ($K_{\rm em,rv}$) or absorption ($K_{\rm ab,rv}$) arising from the surface of the donor.
- Cross correlation between template spectra and the absorption lines present in late type stars, followed by a RV curve fit ($K_{\rm ab,cc}$).
- Location of an emission spot in the Doppler map ($K_{\rm em,mem}$).

However, all these measurements need to be corrected for the origin of the emission/absorption on the surface of the donor star as $K_{\rm em} < K_2 < K_{\rm ab}$ and few systems display these features in the commonly observed Balmer dominated regions, which requires the search for these features in other emission lines, like Ca II.

2.6.2 Measuring K_1

- 2-Gaussian fits to the disc profiles, followed by an RV fit ($K_{\rm disc}$). This is, in principle, equivalent to K_1 as the disc traces the movement of the WD. However, due to asymmetric brightness distributions, these measurements tend to give too large a value for K_1 ($K_1 < K_{\rm disc}$).
- In addition, we construct a complete Diagnostic diagram of the double peaked disc emission profiles ($K_{\rm disc}$). This should provide better results for K_1, as the profiles are forced to fit the high velocity, inner regions of the disc. These regions are less affected by the hot spot and other asymmetrical regions residing in the outer disc,

and hence should provide better (e.g. lower) values for $K_{\rm disc}$ than the traditional 2-Gaussian method.

- 1-Gaussian profile fits, followed by a RV curve fit, to metal absorption lines arising from near the WD surface. These features are generally only visible in low accretion rate systems with a low inclination but provide a direct measure of not only the WD motion (K_1) but also of its mass via the gravitational redshift of the line.

- Centre of symmetry searches for the disc features in Doppler maps. By removing the asymmetrical parts of the disc from the analysis and concentrating on the high velocity regions (Keplerian orbits close to the WD) the bias towards larger velocities is minimised ($K_1 \lessapprox K_{\rm disc}$).

2.6.3 New lines

We initiated a spectroscopic survey to observe several short period CVs, simultaneously covering the Balmer lines in the blue and the Ca II triplet lines in the I-band. The main aim of this study has been to find signatures of both the disc and the, potentially, irradiated donor in the calcium lines and use these to determinee the mass ratio of the system. By exploiting the simultaneous coverage of several Balmer lines, Ca II in the I-band and the Ca H/K lines, we also aim to:

- Compare radial velocities derived from Balmer lines to those from Ca II to study the bias induced from the use of a specific line for the dynamical constraint of system parameters.

- Compare the strength of Ca II disc line profiles to Balmer disc line profiles and the influence of saturation and broadening on the discovery of disc features in Doppler maps.

- Determine the K-correction by optimising $K_1 + K_2$ to reproduce the measured $K_{\rm em}$ for the donor.

- Positively identify a low mass ratio system to anchor Patterson's superhump-mass ratio relation at the extreme end.

We will present a detailed study of the WZ Sge type DN GW Lib in Chapters 3 and 4. This system serves as the prototype system for the proposed method. Based on its success, we initiated a spectroscopic survey to exploit our method on a sample of CVs. These results are presented in Chapters 5, 6 and 7.

Chapter 3

GW Lib I: Time-resolved spectroscopy pre- and post superoutburst

Based on:

van Spaandonk, L., Steeghs, D., Marsh, T. R., Torres, M. A. P.

Time-resolved spectroscopy of the pulsating CV GW Lib

2010, Monthly Notices of the Royal Astronomical Society, **401**, 1857

3.1 Introduction

GW Lib is a dwarf nova which was discovered by González (1983) as it went into its first recorded outburst and rapidly increased in brightness by 8 magnitudes. It remained in its quiescent state after that period of activity until 2007. Van Zyl et al. (2000) found three periodicities in the quiescent photometric light curve at 236, 376 and 650 s, making the primary in GW Lib the first multi-period non-radial pulsating WD in an accreting binary. Thorstensen et al. (2002) measured the radial velocity curve using Hα and determined a rather short orbital period of 76.79 ± 0.02 min. In the latest Ritter & Kolb catalogue, only 8 systems with a smaller period are known when excluding the AM CVn systems which have H-deficient donors (Ritter & Kolb, 2003), implying an evolved binary close to the period minimum. From model fits to the WD absorption troughs and mean spectra, various temperatures have been found. UV spectra suggest $T_{\rm WD} = 14\,700$ K with a WD mass of $0.6 M_{\odot}$ (Szkody et al., 2002) or a dual temperature WD with $T_{\rm low} = 13\,300$ K and $T_{\rm high} = 17\,000$ K. The latter model can only explain the observed UV/optical pulse amplitude ratio in GW Lib (see table 2 in Szkody et al. 2002) as compared with single pulsating ZZ-Ceti stars, if the WD mass of GW Lib is larger than $0.8 M_{\odot}$. Thorstensen et al. (2002) fit the optical Balmer line profiles to find $T = 13\,220$ K and $\log g = 7.4$. However, all temperature estimates place the WD outside

the ZZ Ceti instability strip for single WD pulsators. A mass determination based on the detected pulsation periods combined with distance and UV flux constraints suggests a WD mass of $1.02 M_{\odot}$ (Townsley et al., 2004).

On 2007 April 12, amateur astronomers reported the sudden and rapid brightening of GW Lib (Templeton, 2007) indicating renewed outburst activity, 24 years after the discovery outburst. The outburst had an amplitude of ~ 9 magnitudes and lasted for several weeks, see Figure 3-1, identifying the burst as a superoutburst.

We present the first time-resolved optical spectroscopy of GW Lib in (super)outburst (Section 3.3) alongside time-resolved optical spectroscopy during quiescence before and after the outburst (Section 3.4). We present the possible system parameters in Section 3.4.4 and the discussion (Section 3.5).

3.2 Observations and reduction

We briefly describe the facilities used below. Full details of the observations can be found in Table 3-1.

3.2.1 Telescopes and instruments

The telescopes used were the Magellan Telescopes operated by the Carnegie Institution of Washington at the Las Campanas Observatory in Chile, the Smithsonian Astrophysical Observatory's Tillinghast Telescope at the Fred Lawrence Whipple Observatory, located on Mount Hopkins near Amado, Arizona and the William Herschel Telescope operated by the Isaac Newton Group on the island of La Palma.

Magellan Telescope

Time-resolved optical spectroscopy was acquired during quiescence with the Baade 6.5-m telescope equipped with the Boller and Chivens Spectrograph (B&C) on 2004 June 6 and 7. The B&C was used with a Marconi 2048×515 CCD with a 13.5 microns pixel size and a 1200 lines mm^{-1} grating covering the spectral interval $3500 - 5100$Å. A slit width of 0.8 arcsec gave a dispersion of 0.79Å pixel^{-1} and a resolution of 2.0Å.

On 2007 June 19 the telescope was equipped with the Inamori-Magellan Areal Camera and Spectrograph (IMACS: Bigelow & Dressler 2003) to acquire time-resolved spectroscopy of GW Lib. IMACS was used with the f/4 camera and the long-slit-mask with a 0.7 arcsec slit width and a 600 lines mm^{-1} grating centred at 5550Å. The spectra were dispersed along the short-axis of four SITe CCDs in the IMACS mosaic detector. The

CCD detectors were binned two by two during the observations. This instrumental setup provided a dispersion of 0.76Å pixel^{-1} and a spectral resolution of 1.29Å FWHM in the spectral interval $3950 - 7100$Å.

Tillinghast Telescope

The 1.5-m reflector Tillinghast Telescope (TT) equipped with the FAST instrument (Fabricant et al., 1998) acquired 7 epochs of time-resolved spectroscopy and 16 epochs of single spectroscopic frames in service mode. For the time-resolved observations, the FAST instrument was equipped with a 2688 × 512 UA STA520A CCD chip with a 15 microns pixel size. A grating of 1200 lines mm^{-1} covering $4150 - 5200$Å and a 1.5 arcsec slit width was used to deliver a dispersion of 0.38Å pixel^{-1} and spectral resolution of 0.86Å FWHM.

For the single frames the telescope was used in service mode with a grating of 300 lines mm^{-1} and an aperture of 3.0 arcsec to cover the spectral interval $3300 - 7600$Å. The pixels were binned two by two to give a dispersion of 1.47Å pixel^{-1} and a resolution of 5.9Å.

William Herschel Telescope

On two successive nights, three months after the 2007 super outburst, we acquired time-resolved spectroscopic data using the 4.2-m William Herschel Telescope (WHT) in combination with the two-armed Intermediate dispersion Spectrograph and Imaging System (ISIS). The blue arm of the spectrograph was equipped with a 4096 × 2048 EEV12 CCD. The slit width used was 1.0 arcsec and used with the R1200B grating with 1200 lines mm^{-1} providing a wavelength coverage of $4200 - 5000$Å. This setup delivers a dispersion of 0.224Å pixel^{-1}. The red arm was equipped with a 4096 × 2048 Red+ CCD with 15 microns pixels. Using the R1200R grating with 1200 lines mm^{-1} the unvignetted wavelength coverage was $8050 - 8800$Å with a dispersion of 0.243Å pixel^{-1}. The spectral resolution for both arms was 0.62Å.

3.2.2 Reduction

The different sets of spectroscopic data were reduced using several reduction packages.

Table 3-1: Observations of GW Lib,

Telescope	Inst	Date	HJD +2450000 (start)	Exp time (s)	n	Orbital coverage ($\frac{T_{\rm obs}}{P_{\rm orb}}$)	λ - range (Å)	Seeing ($''$)
Magellan	B&C	06/07/04	3193.491	60	62	1.00	3500 - 5100	0.5-1.0[a]
		07/07/04	3194.471	60	66	1.02		0.7-1.2
TT	FAST	14/04/07	4204.859	60	1	–	3300 - 7600	1-2
		14/04/07	4204.861	30	2	–		1-2
		20/04/07	4210.859	15	2	–		–
		09/05/07	4229.833	120	1	–		2
		09/05/07	4229.836	300	1	–		2
		11/05/07	4231.817	120	2	–		2
		15/05/07	4235.813	480	1	–		–
		18/05/07	4238.894	600	1	–		–
		20/05/07	4240.811	480	1	–		–
		23/05/07	4243.787	720	1	–		–
		09/06/07	4260.739	720	1	–		–
		16/06/07	4267.774	1200	1	–		–
		24/06/07	4275.691	1200	1	–		–
TT	FAST	14/04/07	4204.886	200	34	1.86	4150 - 5200	1-2
		15/04/07	4205.861	60	110	1.75		1-2
		20/04/07	4210.882	60	70	1.46		1-2
		23/04/07	4213.858	120	37	1.68		1-2
		10/05/07	4230.833	300	18	1.75		2
		12/05/07	4232.833	600	2	0.16		2
		17/05/07	4237.784	300	22	1.94		1-2
Magellan	IMACS	18/06/07	4270.531	30	73	1.09	3950 - 7100	0.6
WHT	ISIS	24/07/07	4306.365	240	19	1.08	4200 - 5000 8050 - 8800	1
		25/07/07	4307.350	240	25	1.35		1-2

[a]From Magellan Guide Camera Seeing at `www.lco.cl`

FAST service mode

The single frame spectra obtained with the FAST spectrograph in service mode were extracted for us, using the spectral extraction pipeline provided by the Telescope Data Center at the Harvard-Smithsonian Center for Astrophysics. This tailored pipeline is based on the IRAF PROCD package, see Tokarz & Roll (1997).

Magellan IMACS

The IMACS data were bias and flat-field corrected in the standard way using IRAF. The spectra were extracted from each CCD frame with the IRAF KPNOSLIT package by M.A.P. Torres. The pixel-to-wavelength calibration was derived from cubic spline fits to HeNeAr arcs acquired during the observations. Fitting 10 - 20 lines per frame gave a RMS < 0.017Å per chip (data reduction contributed by M.A.P. Torres).

All others

All other data sets were reduced in the following way. The average bias and flat-field correction was carried out using the FIGARO package from STARLINK and nightly average bias and tungsten frames. PAMELA was used for the optimal extraction of the spectra (Marsh, 1989). Regular CuAr arc lamp exposures allowed us to establish an accurate wavelength scale for each spectrum through interpolation between the nearest arcs in time. Each arc frame has been fitted with a 5th order polynomial to 10-40 lines to give a typical RMS of 0.1 pixel. The individual spectra were normalised to the continuum level using a spline fit to selected continuum regions.

3.3 GW Lib in outburst

The April 2007 super outburst of GW Lib triggered our target of opportunity program at the TT. Both time-resolved spectroscopy and single frame observations of GW Lib were obtained during this period of activity. See Table 3-1 for specific details.

3.3.1 Spectral evolution

In Figure 3-2 average representative normalised spectra during different stages of the super outburst of GW Lib are presented. The bottom spectrum is during quiescence 3 years before the 2007 outburst, the second spectrum is a day after outburst peak, the third during slow decline, the fourth during rapid decline and the fifth during the final decline towards quiescence. For reference, the top frame in Figure 3-1 shows the super outburst light curve in the V-band, as provided by AAVSO and its network of observers. The dates corresponding to the spectra plotted in Figure 3-2 are marked. The pre-outburst quiescent spectrum is given an arbitrary negative HJD for plotting purposes.

The single frame spectra at different nights throughout the super outburst make it possible to trace the evolution of various spectral features. We have measured the equivalent widths (EW) of the lines as a function of the outburst. For the Balmer lines, the overall continuum is normalised but any underlying broad absorption wings within the line was not removed. This results in positive EW values during absorption-dominated epochs and negative values otherwise. For consistency, the window for these lines is ± 2500 km s^{-1} for all epochs, which is limited by the proximity of the helium lines. For the helium lines, a slightly narrower window of ± 1500 km s^{-1} gives a consistent

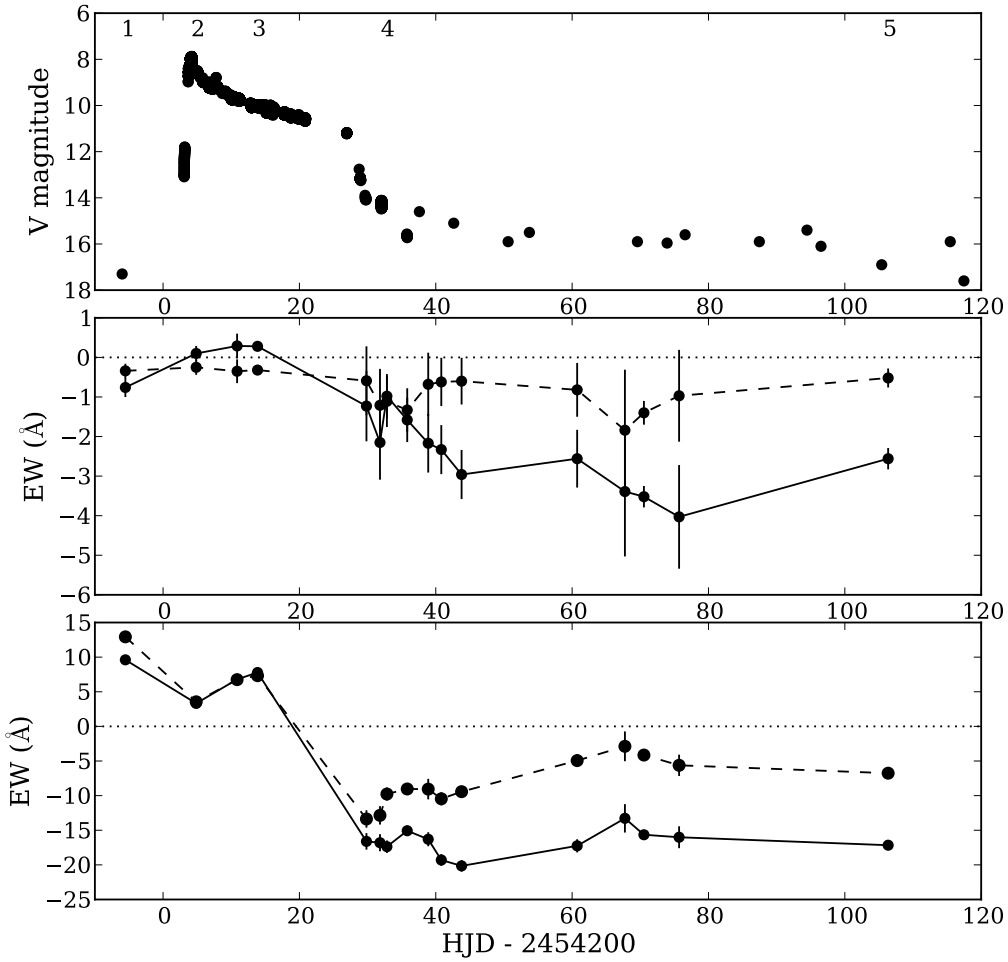

Figure 3-1: Time evolution of the equivalent widths of the principal spectral lines. The July 2004 quiescent epoch is plotted at an arbitrary negative HJD for comparison. In the bottom frame: *black solid* line for Hβ and *black dashed* line for Hγ. In the middle panel: *black solid* line for He I 4921Å, represents the general evolution of the He I lines and *black dashed* line for He II 4685Å. The top panel shows the V magnitude of the outburst, as provided by the AASVO, where the numbers indicate when the spectra shown in Figure 3-2 were obtained.

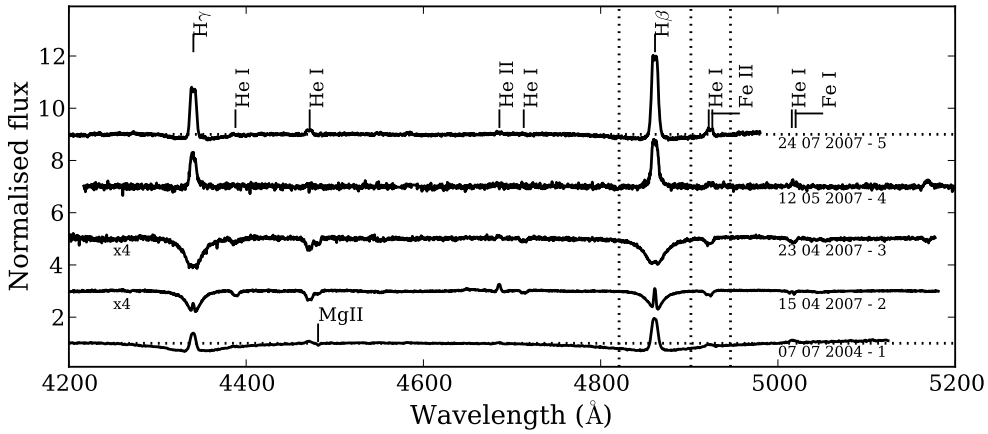

Figure 3-2: Comparison of average representative normalised spectra of GW Lib sampling the spectral evolution before and during the 2007 super-outburst. The April 2007 spectra have been multiplied by a factor of 4 to magnify the spectral features and allow for a better comparison. The vertical *dotted* lines annotate the $\pm$2500 km s^{-1} window for the Balmer lines and the $\pm$1500 km s^{-1} band for helium lines while the horizontal *dotted* lines the normalised continuum flux.

and comparable EW measurement, avoiding neighbouring lines. The spectra are locally normalised to avoid any contamination from underlying absorption due to nearby Balmer lines. Both regions are marked in Figure 3-2 together with the continuum level. The bottom panel in Figure 3-1 shows the EW evolution for the Balmer lines and the middle panel the same for the helium lines. The actual values for all lines and at all observed epochs are given in Table 3-2. We note that the spectral lines display rather complex changes as different components come and go. A single EW value clearly does not fully capture these details. Therefore, to complement the measured EW, a more detailed analysis of the separate components within the line profiles is provided below.

2004 July 7 - 1 During deep quiescence, 3 years before outburst, the average spectrum of GW Lib was typical for a CV spectrum with a low accretion rate. The accretion disc has very narrow Balmer emission lines which show a dip in their centres reflecting an underlying double-peaked profile (not visible on the scale of Figure 3-2). This profile shape is expected for optically thin accretion discs viewed at a low inclination angle i. The Hβ profile is fitted with two Gaussians simultaneously to the absorption trough and the narrow emission line component. The latter gives a FWHM of 7.82 $\pm$ 0.56Å corresponding to $\sim$ 482 km s^{-1} (all errors quoted in this Chapter are 3σ errors). Absorption troughs flank the emission features with a FWZI of $\sim$ 20 000 km s^{-1}, and can only originate from the WD as these velocities are too high for Keplerian velocities in

the accretion disc. This indicates a small accretion luminosity and a very low mass transfer rate such that the primary WD is visible. The measured EW of the Balmer lines are dominated by the WD absorption. The He I lines are all in emission. A small, but significant, amount of He II is present in emission with an EW of -0.34 ± 0.18Å in the average spectrum. Since the disc and companion star are expected to be too cool during quiescence to produce much He II emission, this line emission may be due to the relatively hot WD ionising gas near it. The feature is unfortunately too weak to permit any time-resolved analysis. We also note that an absorption line at Mg II 4481.15Å is present with an EW of 0.24 ± 0.09Å measured in a ± 300 km s^{-1} window and a FWHM of 3.18 ± 0.35Å. This is likely formed in the photosphere of the WD and such metal lines may be expected in accreting systems were metal-rich gas is deposited onto the WD surface. The determination of the gravitational redshift of such lines could in principle provide a direct measurement of the mass of the WD. However, our resolution prohibits a reliable measurement of the velocity of this weak feature at this point, as it is blended with the nearby He I line.

2007 April 15 - 2 Two days after the rise into super outburst started, the average spectrum of GW Lib shows broad absorption troughs in the Balmer lines. Given the 9 magnitude increase due to accretion these absorption features can no longer be associated with the WD but suggest an origin in the now optically thick accretion disc, supported by a FWHM of 23.05 ± 0.36Å. The lines also show strong emission peaks, see spectrum 2 in Figure 3-2. This is also seen in the Hα emission profile obtained by Hiroi et al. (2009) around this time. With a FWHM of only 3.14 ± 0.66Å, corresponding to ~ 194 km s^{-1}, the peak in Hβ has less than half the width of the emission during quiescence. The He I lines are all in absorption, with a hint of a very narrow emission peak at the centre, while the He II line at 4685Å is in emission at EW $= -0.25 \pm 0.19$Å. Finally Fe is marginally detected in absorption. We will revisit the discussion on the origin of these lines in section 3.3.2.

2007 April 23 - 3 Ten days after the beginning of the outburst, GW Lib slowly started to fade and the spectrum evolved. The strong and narrow emission in the Hβ and Hγ lines decreased in strength, increasing the overall EW slightly. The EW of the He I lines increases similarly suggesting the same narrow emission was indeed present. The accretion disc is still visible as an optically thick disc in absorption in the Balmer lines with a FWHM of 30.46 ± 0.26Å. The He II emission decreases slightly to an EW of

-0.32 ± 0.06Å.

2007 May 12 - 4 A month after outburst, as the system dropped from the outburst plateau (Figure 3-1) and the luminosity decreased rapidly, the spectrum had changed drastically, see spectrum 4 in Figure 3-2. The accretion disc contribution to the lines changed from an optically thick flow back into a chiefly optically thin disc, producing shallow double-peaked emission profiles in the Balmer line without the high velocity absorption, leading to a negative EW. The emission component in Hβ is visible again and now has a FWHM of 8.59 ± 0.03Å, close to the value of the pre-outburst emission line. As can be seen in Figure 3-1, the EWs of all lines make a small jump. WZ Sge type DNe often show brief brightenings shortly after their main outburst, referred to as echo-outbursts (Patterson et al., 2002). It remains unclear due to the sparse light curve sampling whether the observed behaviour in the lines is related to similar events.

2007 June 19 The Magellan spectra from June 2007 resemble the WHT July spectra in shape, see top spectrum in Figure 3-2 for the average spectrum. In addition, these spectra also cover the Hα and the He I 5876.62Å line. An interesting feature next to the strong He I line is the sodium doublet (Na D 5889.95Å-5895.92Å) seen in emission, see Figure 3-3. Due to the close proximity of GW Lib, interstellar absorption is expected to be weak, and indeed no evidence for diffuse interstellar band (DIB) absorption features can be found in the spectrum. Instead, the sodium doublet is dominated by broad emission components. To strengthen this case, the sodium doublet is also present in emission at 6154.23Å-6160.76Å. In the orbital average spectrum, the sodium doublet at 5889.95Å-5895.92Å, can be fitted with two double Gaussians (plotted in Figure 3-3) with the seperation between the two Gaussians set to 250 km s^{-1}. The Hα line has the same separation where for the nearby He I the line separation is 350 km s^{-1}. The offset of the centre of the double-peaked profiles from the rest wavelength for all lines is, within errors, -10 ± 5 km s^{-1}. These similar fitting values suggest a shared origin in the accretion flow for all lines. Time-resolved analyses of the He I and the Balmer lines give similar values compared to those in the July 2007 epoch (see section 3.4.2 and Table 3-4).

2007 July 24 - 5 Three months after the super outburst, during the slow decline towards quiescence, the system was still 1-2 mags brighter than the pre-outburst magnitude, and the double-peaked profile from the disc proved stronger against the dropping

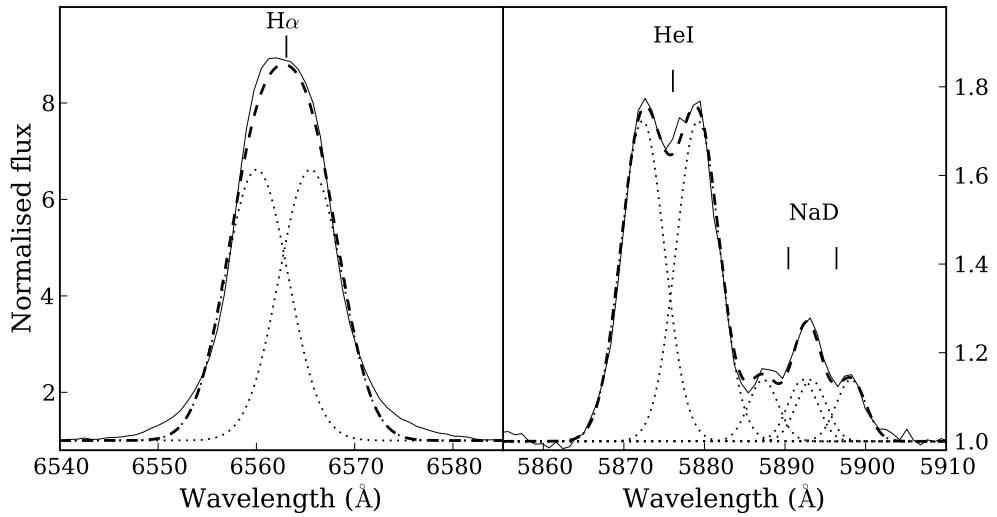

Figure 3-3: Normalised emission line profiles of Hα (left) and the He I - Sodium doublet (right). The *solid* line represents in both cases the average profile over 1 orbital period. The *black dotted* lines are the various Gaussian profiles fits and the *black dashed* line is the sum of all single Gaussians. As is clear from these fits, the Sodium doublet has, most likely, a very similar origin to the Hα and the He I lines.

continuum compared to the previous phase (compare spectrum 4 to spectrum 5 in Figure 3-2). The system has cooled sufficiently such that the WD absorption again flanks the emission lines in the Balmer lines, decreasing the EW of Hγ. Since both the disc and the WD are expected to be slightly hotter and brighter compared to the pre-outburst quiescent state it does not yet resemble spectrum 1 in Figure 3-2. For comparison, the WD in WZ Sge was still cooling after 17 months of post-outburst observations, (Long et al., 2004). The He I lines are all in emission and the He II emission line has an EW of -0.52 ± 0.24Å. The FWHM of the emission component in Hβ is 7.65 ± 0.03Å and has thus reached the value observed in the pre-outburst epoch even though the emission line flux itself is still much larger.

3.3.2 Time-resolved spectra

Several epochs (see Table 3-1) of time-resolved spectroscopy allow us to characterise the line behaviour in more detail. During outburst, these time-resolved spectra showed considerable orbital variability in the Balmer, He I and He II line profiles. We binned the spectra in bins of 1/20th of the orbital period using $P_{\rm orb} = 0.05332 \pm 0.00002$ days (Thorstensen et al., 2002). The Balmer profiles were fitted with a double Gaussian with the peak, FWHM and the offset from the rest wavelength as free parameters. The He I and He II profiles were fitted with a single Gaussian. All fits show that the peak and

Table 3-2: Equivalent widths in Å (with 3σ errors), of various emission lines as a function of the outburst. The Balmer lines are measured in a ± 2500 km s^{-1} window, whereas the helium lines are measured in a ± 1500 km s^{-1} window.

Epoch[a]	HJD +2450000 (start)	Hβ EW (Å)	Hγ EW (Å)	HeI 4387 EW (Å)	HeI 4471 EW (Å)	HeII 4685 EW (Å)	HeI 4921 EW (Å)
1	3194.471	9.61 ± 0.18	12.93 ± 0.15	-0.29 ± 0.18	-0.74 ± 0.12	-0.34 ± 0.18	-0.76 ± 0.24
2	4204.859	3.32 ± 0.16	3.55 ± 0.17	0.04 ± 0.18	0.47 ± 0.18	-0.25 ± 0.19	0.10 ± 0.19
	4210.859	6.79 ± 0.37	6.75 ± 0.37	0.04 ± 0.30	1.19 ± 0.30	-0.35 ± 0.30	0.29 ± 0.31
3	4213.858	7.78 ± 0.07	7.32 ± 0.09	0.50 ± 0.06	1.03 ± 0.07	-0.32 ± 0.06	0.28 ± 0.03
	4229.833	-16.61 ± 1.19	-13.37 ± 1.26	0.29 ± 0.91	-2.84 ± 0.97	-0.59 ± 0.87	-1.23 ± 0.89
	4231.817	-16.80 ± 1.23	-12.85 ± 1.33	-0.00 ± 0.98	-1.30 ± 0.98	-1.21 ± 0.92	-2.15 ± 0.94
4	4232.833	-17.37 ± 0.90	-9.77 ± 0.95	-0.96 ± 0.62	-0.01 ± 0.62	-1.11 ± 0.65	-0.98 ± 0.56
	4235.813	-15.07 ± 0.74	-9.04 ± 0.78	-0.36 ± 0.58	-0.84 ± 0.57	-1.33 ± 0.55	-1.58 ± 0.56
	4238.894	-16.30 ± 1.01	-9.06 ± 1.48	-0.83 ± 1.07	-1.06 ± 0.95	-0.68 ± 0.80	-2.17 ± 0.74
	4240.811	-19.30 ± 0.84	-10.46 ± 0.94	-1.15 ± 0.71	-1.43 ± 0.66	-0.62 ± 0.61	-2.33 ± 0.62
	4243.787	-20.15 ± 0.82	-9.43 ± 0.82	-1.51 ± 0.64	-1.32 ± 0.62	-0.60 ± 0.59	-2.96 ± 0.62
	4260.739	-17.25 ± 0.95	-4.94 ± 0.93	-1.09 ± 0.74	-0.29 ± 0.68	-0.82 ± 0.68	-2.56 ± 0.73
	4267.743	-13.28 ± 2.05	-2.88 ± 2.15	-0.57 ± 1.67	-0.74 ± 1.54	-1.84 ± 1.53	-3.39 ± 1.64
	4270.531	-15.65 ± 0.41	-4.14 ± 0.57	-0.65 ± 0.46	-2.04 ± 0.42	-1.40 ± 0.30	-3.52 ± 0.27
	4275.691	-16.01 ± 1.58	-5.62 ± 1.54	-1.32 ± 1.28	-3.62 ± 1.26	-0.97 ± 1.16	-4.03 ± 1.31
5	4306.355	-17.16 ± 0.35	-6.76 ± 0.27	-0.75 ± 0.24	-1.47 ± 0.21	-0.52 ± 0.24	-2.56 ± 0.27

[a]See Figure 3-2

FWHM of the line components are constant within 10 per cent of their average values and as these particular parameters show no sign of significant orbital dependence, they were thus fixed to their mean values for further analysis, keeping their velocity offsets as free parameters. In addition to our profile fits, all results were checked against a traditional double Gaussian analysis (Schneider & Young 1980) in combination with a diagnostic diagram (Section 2.3.2, Shafter 1983).

The radial velocity values of our line components were fitted with the function $V(\phi) = \gamma + K \sin(2\pi(\phi - \phi_0))$ and individual velocity data points were weighted according to their errors as derived from the profile fits. These errors were scaled such that the radial velocity curve fit has a goodness of fit close to 1. Here γ is the systemic velocity, K the radial velocity semi-amplitude of the absorption and/or emission line and ϕ_0 the phase offset relative to the ephemeris. The ephemeris zero point will be derived later in this Chapter (section 3.4) and is used throughout this Chapter when calculating orbital phases. Due to the lack of precision in the binary orbital period, the ephemeris cannot be extrapolated very far in time and thus the binary phase is arbitrary except for the July 2007 epoch where the zero-point is measured.

We discuss the results of the fits for the Hβ and He II profiles using the 2007 April 15 data as this set has the highest signal to noise, the best time resolution and the most features present for analysis. The behaviour of the lines during the other nearby epochs was the same, albeit determined with lower precision. The results can be found in Figure 3-4 and Table 3-3. Both Hβ and Hγ have similar amplitudes and phase offsets. The deep and broad absorption troughs can be identified with the accretion disc. However, they do not trace the WD movement as the velocity semi-amplitude is too large at 51.3 ± 6.5 km s^{-1}. The radial velocity of the primary WD is likely much smaller. Interestingly, this amplitude is consistent with that of the double-peaked emission profile during quiescence. On 2004 July 6, the velocity curve fit to Hβ emission gives a semi-amplitude of 45.1 ± 7.3 km s^{-1}. This similarity suggests that the distortions in the disc leading to the observed radial velocity curve of both the disc emission during quiescence and the broad disc absorption during super outburst are rather similar. Unfortunately, due to the uncertainty in the binary ephemeris, we cannot compare their relative phasing. Similar amplitudes, systemic velocities and phase zeros were found for the He I lines, suggesting that their profiles trace the same components. In contrast, the He II line moves in anti-phase and has half the amplitude. This highlights the difficulty with associating either of these radial velocity amplitudes with that of the primary WD.

Table 3-3: Radial velocity curve parameters on 2007 April 15. Note, ϕ_0 is anchored to the ephemeris, but due to lack of precision, arbitrary at this point.

Line	γ km s^{-1} $\pm 3\sigma$	K km s^{-1} $\pm 3\sigma$	ϕ_0 $\pm 3\sigma$	Identification
Hβ emission	-16.6 ± 0.8	3.0 ± 1.6	0.28 ± 0.06	Slingshot/WD?
Hβ absorption	22.5 ± 4.4	51.3 ± 6.5	0.19 ± 0.02	Accretion disc
Hγ emission	–	–	–	–
Hγ absorption	17.0 ± 4.8	43.6 ± 6.8	0.18 ± 0.02	Accretion disc
He II emission	-19.4 ± 4.7	26.6 ± 6.8	0.77 ± 0.04	–

In both the Hβ and Hγ profile, a second Gaussian is fitted to the narrow emission component in their cores. This component shows a remarkably small velocity amplitude of 3.0 ± 1.6 km s^{-1} (see Table 3-3). At this epoch, the arc fit is good to 0.003Å at the position of Hβ which is smaller than 1/100th of the 0.38Å/pixel scale. The 1σ errors on individual velocity measurements are much larger ($\sim$0.085 pixels) than this and are thus dominated by the statistical error. These errors are then propagated to provide the formal errors on the fit parameters as listed in Table 3-3, thus suggesting that this small amplitude is measured to a significant degree.

This strong central emission component in the cores of the Hβ and Hγ profiles is present in those epochs close to the start of the super outburst in all Balmer lines and a hint is present in the He I lines. On 2007 April 20 the dynamics of this component is similar to the behaviour on April 15. By 2007 April 23 the emission component had faded into the absorption lines, which maintained their radial velocity semi-amplitude throughout. The systemic velocity of this narrow emission component is consistent with that of the He II emission, while the broad absorption components in the Balmer lines have a rather different γ which is perhaps due to a slowly precessing disc.

GW Lib is one of the few CVs that have been followed through a super outburst spectroscopically. For comparison, the spectral evolution of SS Cyg (figure 5 in Hessman et al. 1984) showed broad, double-peaked emission lines that were gradually overtaken by the rising continuum, followed by the formation of line wings in absorption. This qualitative behaviour is expected as the accretion disc makes a rapid change from a low $\dot{M}$ optically thin configuration to a high $\dot{M}$ optically thick flow at the onset of the outburst. Near maximum light, SS Cyg shows narrow emission cores on top of the absorption lines from the accretion disc, which decay again after outburst. These are very similar to the spectral changes presented here for GW Lib, though no dynamical properties are available to compare the components quantitatively. Unfortunately, the very low binary inclination of GW Lib makes it difficult to study the accretion disc dynamics

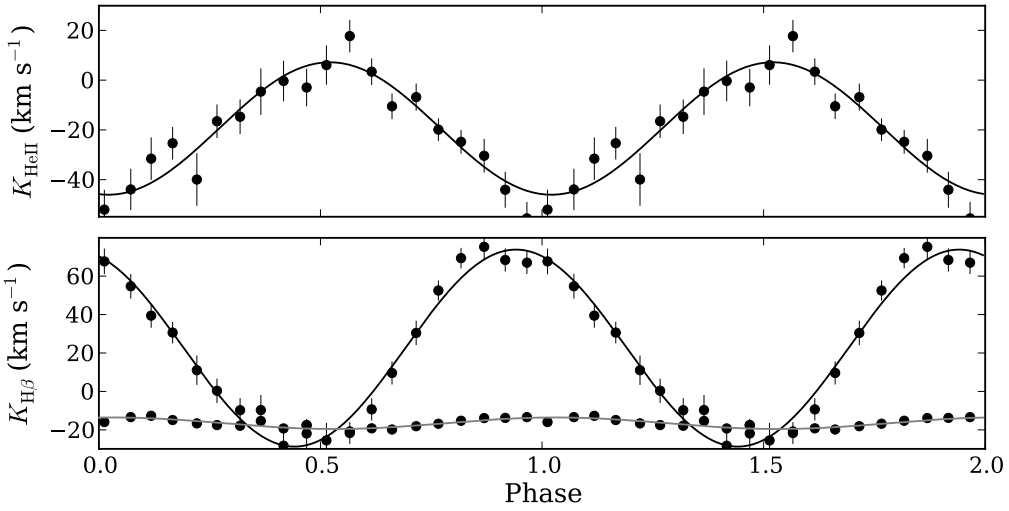

Figure 3-4: **Top:** the radial velocity curve of the He II emission. **Bottom:** the radial velocity curves of the Hβ profile are fitted with a low amplitude emission component (*grey solid*) and a high amplitude absorption component (*black solid*). Both are from the phase-binned 2007 April 15 data, showing two orbital cycles.

during the super outburst period. The absorption dominated disc lines are unsuitable for Doppler tomography and we therefore cannot search for disc asymmetries such as the tidal spirals seen in other DNe (e.g. IP Peg: Steeghs et al. 1997; U Gem: Groot 2001). When disc emission returns, little structure can be detected in its marginally double-peaked lines.

The stationary emission component in the spectra, visible only during the first couple of days of the outburst, does not obviously fit in with the typical components expected to dominate the line emission in a mass transferring binary system. The low velocity suggests a location near the centre of mass in the orbital plane or along the axis through the centre of mass, perpendicular to the orbital plane. GW Lib is not the first DN to show these features. Several DN systems have been reported to show low amplitude strong emission components in the Balmer lines. For example, Steeghs et al. (1996) report low velocity emission components in the Hα and He II 4686Å lines of the DNe IP Peg and SS Cyg and proposed slingshot prominences from the donor star as a possible origin for these features since their known system parameters rule out an origin near either the WD or the surface of the donor star. The rapidly co-rotating donor star may form prominences and such magnetic loops would be pulled towards the WD and could potentially find an equilibrium in between the inner Lagrangian point (L_1) and the WD. As the prominence material is illuminated by the disc during outburst, it

becomes visible as an emission source which is co-rotating with the binary orbit but located in the region near the centre of mass and thus displays very little radial velocity. If we follow the recipe pursued by Steeghs et al. (1996), the observed Hβ/He II ratio of the low velocity emission components is consistent with a gas temperature in the $10\,000 - 15\,000$K range.

In GW Lib, an alternative origin of the low-velocity emission may be near the surface of the WD, if its orbital velocity (K_1) is very small. Low state AM CVn systems often show such narrow emission components (Morales-Rueda et al. 2003, Roelofs et al. 2006). The low mass ratio derived from the late superhump by Kato et al. (2008) together with the low orbital inclination would indeed imply a very low value for K_1 in GW Lib. We will revisit these interpretations and the implications for the system parameters in section 3.4.4.

3.4 GW Lib post outburst

Binary evolution tells us that the majority of the current CV population should have evolved towards short orbital periods with the mass donor star depleted to a low mass degenerate brown dwarf (e.g. Knigge 2006, Kolb & Ritter 1992, Rappaport et al. 1983). Not only has this graveyard of CVs been elusive for many years (see Gänsicke et al. 2009), our sample of short period CVs with reliable binary parameters, other than the orbital period, is very small. This is mainly due to the fact that despite the low mass transfer rates, the donor stars are extremely faint and it is very difficult to perform traditional radial velocity studies using photospheric absorption lines from the donor. Most studies are confined to using the strong Balmer emission lines to try and constrain system parameters (e.g. table 2 in Marsh 2001, Southworth et al. 2007, Neilsen et al. 2008, Mennickent et al. 2006, Szkody et al. 2000), as only few systems show eclipses which allow for light curve fits. The Ca II triplet at 8498.03Å, 8542.09Å and 8662.14Å[1] offers advantages that more than make up for its relative weakness compared to the Balmer lines. It has a lower ionisation energy than either hydrogen and helium and is thus capable of being excited even by cool sources of radiation, and its thermal width and pressure broadening are much smaller than for hydrogen leading to sharper, more easily detected spikes of emission (Marsh & Dhillon, 1997). Studies have shown that Ca II is also more accessible than the Balmer lines for the study of velocity gradients and turbulence. This is because the thermal velocity broadening is smaller in general and

[1]From The Atomic Line List Version 2.04: `http:/www.pa.uky.edu/~peter/atomic/`

the Keplerian shear broadening starts to dominate at higher inclinations compared to the hydrogen lines (Horne, 1995). These studies show a promising, but so far neglected avenue for emission line studies of CVs. The average normalised spectrum of GW Lib in the *I*-band obtained on 2007 July 24 is plotted in Figure 3-5 and shows a strong Ca II triplet in emission.

3.4.1 Emission from the secondary

In Figure 3-6 (middle panels), we compare trailed spectrograms of Hβ (left) and Ca II 8662Å (right) obtained 3 months after outburst. Whereas the Balmer line shows a shallow double-peaked profile and a rather blurry trail, the Ca II trail is much sharper even at a lower S/N. It shows a clear double-peaked profile from the accretion disc and an S-wave moving in between. No such S-wave appears to be present in the Balmer lines.

To highlight this component, we averaged the profiles in a frame co-moving with the S-wave and show these in the top panels of Figure 3-6. The double-peaked profile from the accretion disc in this frame is averaged out, but the narrow S-wave is clearly visible on top on the broad profile in the Ca II case whereas its absence is noted in the Balmer profile. The S-wave is sharp and its amplitude is smaller than the velocity offset of the accretion disc peaks, suggesting it may originate from the secondary star rather than from the interaction point between the infalling stream and the accretion disc, the hotspot, since the latter would have a velocity equal to or larger than the outer disc edge.

Assuming the emission does indeed arise from the surface of the donor star, the ephemeris can be determined as the crossing from blue-to-red of its radial velocity curve, which corresponds to inferior conjunction of the secondary star. This gives:

$$\mathrm{HJD} = 2454307.36867 + 0.05332E,$$

where E is the cycle number. This ephemeris is used throughout the Chapter to define the orbital phase although the accuracy of the orbital period is not enough to give the super outburst data discussed in Section 3.3 a definite orbital phase since the accumulated uncertainty is too large (Figure 3-7).

The radial velocity semi-amplitude of the S-wave emission is determined using two different methods. The first method is the fitting of a Gaussian to the S-wave line component followed by a radial velocity curve fit. The second method is the localisation of the emission peak in the velocity-velocity plane using Doppler tomography.

Table 3-4: Radial velocity curve parameters on 2007 June 25.

Line	γ $\mathrm{km\,s^{-1}} \pm 3\sigma$	K $\mathrm{km\,s^{-1}} \pm 3\sigma$	ϕ_0 $\pm 3\sigma$	Identification
Balmer emission	-7.6 ± 5.6	19.2 ± 5.3	0.68 ± 0.04	Accretion disc
Ca II emission	20.6 ± 3.3	19.8 ± 4.2	0.73 ± 0.04	Accretion disc
Ca II emission	-13.1 ± 3.7	82.2 ± 4.9	0.00 ± 0.01	Donor star

For the first method, the spectra were phase-binned into 20 bins and a triple Gaussian profile with as variables the offsets, the peak heights and the FWHMs of the profiles is fitted. Here, two Gaussians trace the disc features and the third is for the donor S-wave. Both the peak height and the FWHM show a stochastic variability with a maximum amplitude of 8 per cent from the average value and were therefore fixed to their mean values, leaving just the velocity offset as a fit parameter. The offset velocity for the S-wave emission is plotted in Figure 3-7 together with a weighted radial velocity curve fit. For improved accuracy in the Ca II triplet, we performed a joint fit to the 3 triplet lines with a common velocity offset. We then find a semi-amplitude of $K_{\mathrm{em}} = 82.2 \pm 4.9\,\mathrm{km\,s^{-1}}$ for the S-wave in the Ca II profiles, see also Table 3-4.

To complement our radial velocity fits, Doppler maps are created with a Maximum Entropy Method Marsh (2001) for both the Balmer and the Ca II 8662Å lines, see bottom panels in Figure 3-6 for the MEM of the time-resolved spectra on 2007 June 24. Given the fact that the lines from the Paschen series overlap with the Ca II triplet lines, we always ensured that the Doppler reconstructions fitted to both lines simultaneously. The underlying Paschen line distribution is rather featureless, and the sharp S-wave component is only present in the Ca II reconstructions. Even if such a Paschen contribution is not included, the Ca II tomograms show very similar features.

The Balmer map (bottom left panel in Figure 3-6) shows a diffuse ring of emission from the accretion disc. Due to the sharper line profile, the Ca II map (bottom right panel) shows a much better defined accretion disc ring with a significant asymmetry at phases ~ 0.10, ~ 0.35 and ~ 0.70. Furthermore, the S-wave component manifests itself as a sharp emission spot peaking at a velocity of $\sim 85 \pm 5$ km s^{-1}. Its location relative to the disc ring is as expected for donor emission and thus the Ca II S-wave is revealing the secondary in GW Lib for the first time.

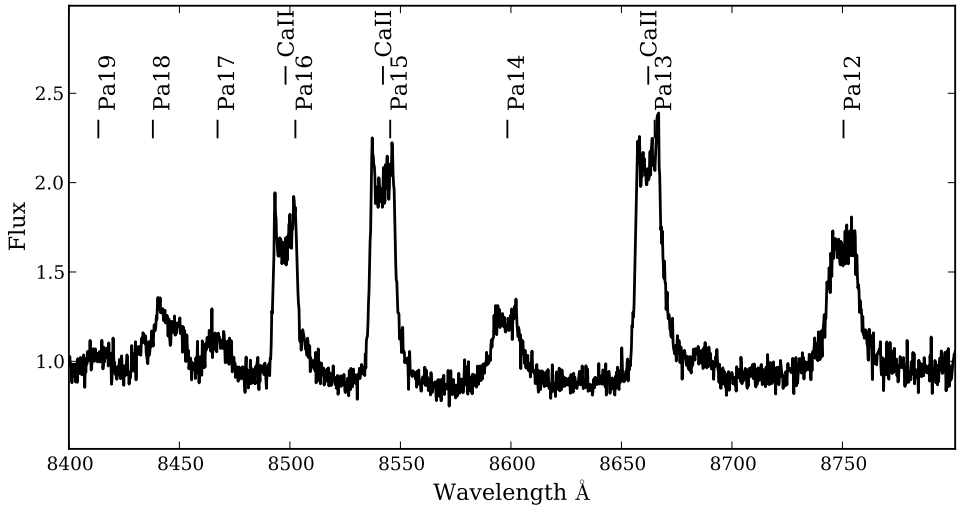

Figure 3-5: The average normalised *I*-band spectrum of GW Lib on July 24, 2007 showing the Paschen series and the double-peaked Ca II lines.

3.4.2 Emission from the accretion disc

With the super outburst activity decaying away, the disc contribution to the overall luminosity decreases and significant regions that are optically thin start to re-appear. These give rise to the characteristic double-peaked profile visible in both the Balmer lines and the Ca II lines. A single broad Gaussian profile fit to this feature in the phase-binned spectra together with a weighted radial velocity curve fit to both the Ca II and Balmer profiles on multiple nights gives an average value for the velocity amplitude of the disc of $K_{\rm disc} = 19.2 \pm 5.3$ km s^{-1}, see Table 3-4. Similar results are obtained using multiple Gaussian line fits and diagnostic diagrams with double Gaussians. This amplitude is significantly different from the amplitude of disc related features in the April 2007 and July 2004 data. The phase shift of both the Ca II and the Balmer disc lines coincide, but they are not in anti-phase with the donor star with respectively $\phi = 0.68 \pm 0.04$ and $\phi = 0.73 \pm 0.04$. They cannot directly track the WD and thus the radial velocity amplitude is disturbed by some residual disc asymmetry and cannot be straightforwardly connected to K_1.

The accretion disc in the Doppler map of Hβ appears rather featureless with little azimuthal structure, while the Ca II trail and MEM map show lower intensity in the disc around phases ~ 0.10, ~ 0.35 and ~ 0.70. The centre of emission of the disc in each map was determined by looking at their centre of symmetry (see Section 2.3.3). To determine the optimal centre of symmetry of the disc, we subtracted a symmetrical

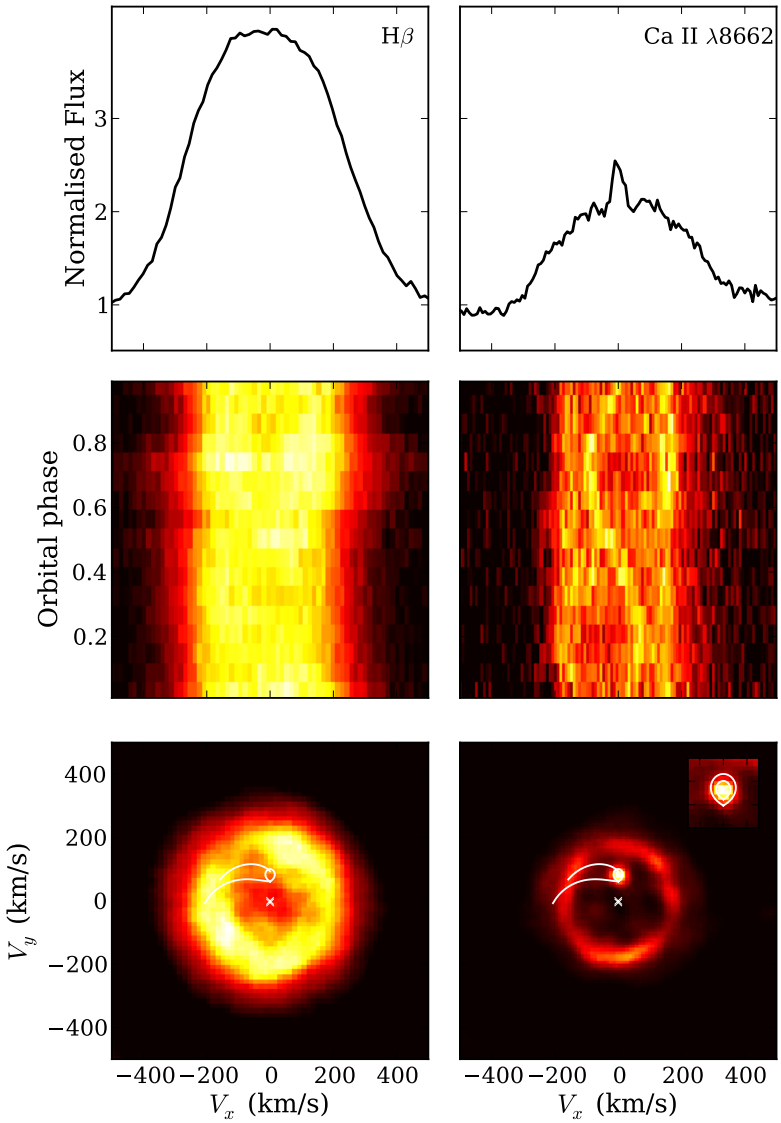

Figure 3-6: Comparison of the dynamics of the Balmer lines (Hβ, left column) versus Ca II (8662Å, right column). The top row show average profiles in the reference frame of the donor star S-wave. The sharp donor component stands out in Ca II but the Hβ profile is smooth. The middle row shows the phase-binned trailed spectrograms. The S-wave can be traced between the disc peaks in Ca II only. The bottom row plots the Doppler tomograms showing the superior sensitivity and sharpness in the Ca II lines. The S-wave is mapped to a sharp spot consistent with donor star emission. Overlaying the Doppler tomograms are the positions of the WD, the Roche Lobe of the donor star and two streams (the velocity of the gas and the velocity of the disc along the gas stream) for a model with the superhump derived mass ratio of $q = 0.062$. The inset in the Ca II Doppler map shows the Roche Lobe on the donor star in more detail for the superhump solution at $q = 0.062$ and the maximum solution determined by the dynamical upper limit for the mass ratio at $q = 0.23$.

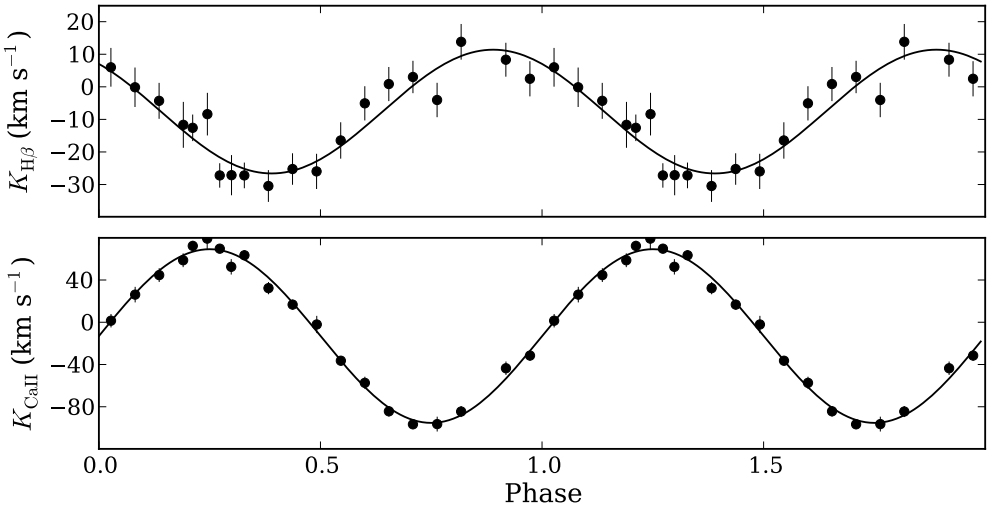

Figure 3-7: Both panels show phase-binnend data 2007 June 24 data. **Top:** the radial velocity curve of the Hβ emission. **Bottom:** the radial velocity curve of the Ca II 8662Å S-wave emission component.

component from both the Ca II and the Hβ Doppler map centred at V_x, V_y values in the ranges of -100 to +50 km s^{-1}, in grid steps of 2 km s^{-1}, and then inspecting the residuals in the lower half of the map (see also Steeghs & Casares 2002, Section 2.3.3). The best fits are found for $V_x = 0.0 \pm 5.0$ km s^{-1} and $V_y = -6.0 \pm 5.0$ km s^{-1} for the Ca II map. The fits for the Hβ map give identical values but with a larger error. The low V_x is encouraging from the point of view of linking the disc centre with the WD at $(0, -K_1)$. The implied $K_{\rm disc} = -V_y = 6$ km s^{-1} is smaller than the semi-amplitude derived using the Gaussian fits. On the other hand they are formally consistent when considering our error estimates, and both point to a small K_1.

3.4.3 Systemic velocity

The binary systemic velocity (γ) is a quantity that should obviously be the same in all spectral lines, reflecting the fixed radial velocity of the binary centre of mass with respect to us. For different lines at different epochs, the systemic velocity was determined using two methods.

The first method determined the systemic velocity as derived from the radial velocity curve discussed previously, see Figures 3-3 and 3-4. For the Balmer lines associated with the accretion disc $\gamma = -26 \pm 6.7$ km s^{-1} before outburst, during super outburst $\gamma = 22.5 \pm 4.4$ km s^{-1} and after super outburst $\gamma = -7.3 \pm 3.6$ km s^{-1}. The narrow Hβ emission during super outburst has $\gamma = -16.6 \pm 0.8$ km s^{-1}. For the Ca II profiles, we

found $\gamma = 20.6 \pm 3.3$ km s^{-1} for the disc emission and $\gamma = -13.1 \pm 3.7$ km s^{-1} for the donor star emission. The latter is the most reliable value for γ as the donor star has to move with the systemic velocity and is less contaminated than the disc lines.

The alternative method uses the dependence of MEM maps on the assumed systemic velocity. Reconstructed emission spots in the map have optimal sharpness at the correct value for γ, while reconstructions at significantly different values will broaden the features and introduce possible artefacts. Ranging γ between -50 to +20 km s^{-1} in steps of 5 km s^{-1} gives the best reconstruction for $\gamma = -15 \pm 5$ km s^{-1}.

Our various estimates of γ point towards a value of -15 ± 5 km s^{-1}, in agreement with the measurements by Szkody et al. (2000). The only outliers are the Balmer absorption line during super outburst with a systemic velocity of 22.5 ± 4.4 km s^{-1} and the Ca II emission associated with the accretion disc with $\gamma = 20.6 \pm 3.3$km s^{-1}. However, the latter two fits are distorted as the resolution is not sufficient to properly resolve the donor star S-wave and the disc emission peaks near phases 0.25 and 0.75. Subtraction of the S-wave and fitting the disc emission with a two-Gaussian profile with a fixed offset between the Gaussians gives a lower value of $\gamma = 7 \pm 2$ km s^{-1}. However, this is still inconsistent with -15 ± 5 km s^{-1}.

3.4.4 System parameters

In the previous section we have seen the superior sensitivity of the Ca II emission lines over the commonly observed Balmer lines. Not only do they provide a much sharper view of the accretion disc emission, the key result was the presence of an emission spot from the donor star. This has provided the first ever proxy for its orbital velocity.

Post-outburst radial velocity curves together with Doppler maps have given us estimates of the semi-amplitudes for the different components in the binary system. From both the Balmer and Ca II double-peaks, the radial velocity of the accretion disc was found to be $K_{\rm disc} = 19.2 \pm 5.3$ km s^{-1}. However, this value may be biased by disc asymmetries and the donor star S-wave. The observed phase-shift between the disc peaks and the donor does indeed suggest such a bias to be present, while the centre of symmetry searches returned lower K_1 estimates. We therefore consider $K_{\rm disc}$ from the disc peaks as an upper limit on the radial velocity of the WD: $K_1 < K_{\rm disc}$.

The donor star is detected in Ca II as a third peak on top of the accretion disc emission and gives $K_{\rm em} = 82.2 \pm 4.9$ km s^{-1}. Considering the faintness of the low mass donor star, this is unlikely to be powered by chromospheric emission. In any case, the

Ca II triplet in chromospherically active stars is generally seen in absorption (e.g. Kafka & Honeycutt 2006) and thus cannot explain the emission seen in GW Lib. A more likely origin is photo-ionisation in the irradiated hemisphere of the donor star facing the WD. The measured radial velocity semi-amplitude is then an underestimate of the true orbital velocity of the donor star ($K_2 > K_{\rm em}$). We calculated the magnitude of this bias, referred to as the K-correction, by simulating the expected emission profiles from an irradiated Roche lobe filling star. Synthetic profiles were calculated for relevant binary parameters including possible shielding of the equatorial regions of the donor by a vertically extended accretion disc.

The peak intensity of the donor star S-wave does not vary significantly as a function of the orbital phase, and instead scatters around a mean value with an RMS of 8 per cent, which is consistent with photon noise. The model profiles discussed above were also used to generate expected orbital light curves of the donor star emission as a function of binary parameters. Model light curves, assuming that the emission is optically thick and thus should be weighted with the projected area, produce larger orbital modulations than those observed. However, if we consider more isotropic emission, the modulation disappears at low orbital inclinations. This optically thin model is more appropriate for emission stimulated by photo-ionisation and thus the observed lack of variability is consistent with an irradiated secondary observed at low inclinations.

We can now derive conservative limits on the radial velocities of the stellar components in the system using the various methods and spectral lines discussed above. They can be summarised as $K_2 > 82.2 \pm 4.9$ km s^{-1} and $K_1 < 19.2 \pm 5.3$ km s^{-1}. These limits translate into a hard upper limit on the mass ratio of $q < 0.23$ regardless of the magnitude of the K-correction or the K_1 overestimate.

After the April 2007 outburst, two detections of superhumps have been reported. Copperwheat et al. (2009) detect a periodicity with a period excess of 4.12 min which implies a mass ratio of $q \simeq 0.211$ if interpreted as a superhump and the empirical superhump-excess mass ratio relation from Patterson et al. (2005) is applied. This is close to our hard upper limit for the mass ratio. However, the authors themselves question the nature of the humps and the implied donor star mass in combination with the WD mass from seismology due to the heating of the WD during the recent superoutburst. This places the WD far outside the instability strip for ZZ-Ceti stars. On the other hand, Kato et al. (2008) report a superhump period of 0.053925(4) days and a late superhump period of 0.054156(1) days which imply an extreme mass-ratio of $q = 0.062$.

Table 3-5: Derived system parameters for GW Lib using M_1 from Townsley et al. (2004). The left hand column lists the binary parameters derived from the formal solution based on the measured limits on K_1 and K_2. The right hand column lists the parameters when combining the mass ratio inferred from superhumps with the calculated K_2 from the Ca II $K_{\rm em}$.

	$q \lesssim 0.23$	$q = 0.062$
$M_1\,(M_\odot)$	1.02	1.02
$K_2\,(\mathrm{km\,s^{-1}})$	> 82.2	100.8 ± 7.1
$K_1\,(\mathrm{km\,s^{-1}})$	< 19.2	6.2 ± 0.4
$M_2\,(M_\odot)$	< 0.23	0.063
$v_1\,(\mathrm{km\,s^{-1}})$	< 122	34
$v_2\,(\mathrm{km\,s^{-1}})$	> 488	548
$i\,(^\circ)$	> 9.4	10.6 ± 0.8
SpT	M3.9-M5	M8-T

We looked at a model for the relation between M_2, K_1 and K_2 as a function of q for a range of M_1. Combining this with the above upper and lower limits on the radial velocities of the WD and donor star rules out systems with $M_1 < 0.75M_\odot$. We can obtain another limit on q and M by measuring the rotation velocity of the donor, $v \sin i$ (see Section 2.3.1). The observed FWHM of the Ca II donor emission in each phase bin ranges between 1.0 and 2.2Å due to contamination with the double-peaked profile. The FWHM is very close to the resolution of the data, 0.617Å, which equates to a $v \sin i$ of 21 km s^{-1}. The profile is thus at best marginally resolved. From the upper limits for the mass ratio ($q < 0.23$) and the constraint in $v \sin i$, we get a rough estimate of the WD mass at $1.0M_\odot \pm 0.25$, in agreement with the mass determined using asteroseismology models ($M_1 = 1.02M_\odot$; Townsley et al. 2004. Note that their window of solutions is constrained by the UV-flux of the WD in combination with the measured distance to GW Lib. For a parallax distance of 104^{+30}_{-20}pc (from Thorstensen 2003) they calculate $M_1 = 1.03 - 1.36M_\odot$, superseding the previous estimates by Szkody et al. (2002) and Thorstensen et al. (2002) that were based on a larger distance. For further analysis we will use the asteroseismologicaly suggested mass of $M_1 = 1.02M_\odot$ (Townsley et al., 2004).

When considering the empirical CV donor sequence of Knigge (2006) at the orbital period of GW Lib, we find a typical pre/post period bounce secondary star mass of $M_2 = 0.064 \pm 0.001M_\odot$ or $M_2 = 0.060 \pm 0.001M_\odot$, respectively. The small difference is due to the orbital period being very close to the bounce period. Knigge also calculates the expected absolute magnitudes for GW Lib in the infrared bands using its parallax distance, which implies a low mass secondary star of $0.080 \pm 0.005M_\odot$.

Formal solution

The so-called formal scenario assumes that the corrections that need to be applied to our K_1 and K_2 constraints are modest. Thus implying that the mass ratio is near its limit: $q = K_1/K_2 \lesssim 0.23$. The right hand column in Table 3-5 list the derived system parameters for this mass ratio. Thorstensen et al. (2002) calculated the inclination based on the FWHM of the shallow peaked Balmer emission lines in quiescence compared to the FWHM of WZ Sge and found $i \sim 11°$. This is in agreement with our calculations in combination with the solution Townsley et al. (2004) value of $M_1 = 1.02\,M_\odot$, and confirms that GW Lib is indeed observed at very low inclination.

For $q < 0.23$, the correction for K_2, as derived from our models, is at most $\Delta K_{\rm max} = 35$ km s^{-1}, giving a maximum value for K_2 of 118 ± 5 km s^{-1}.

The main problem with a high value for q near our limit is that the secondary would then need to be a $M_2 \sim 0.23\,M_\odot$ star with a spectral type around M4-M5 (Cox 2000). In that case, spectral features should be visible in a high resolution, high signal to noise red spectrum. We cannot identify any of such features in our post-outburst *I*-band spectra, nor in the pre-outburst Magellan data. Additional issues are the observed IR magnitudes of GW Lib which imply a faint donor and a main-sequence object near $0.23\,M_\odot$ would not fit within the Roche-lobe. All adding to the conclusion that the mass-ratio in GW Lib is likely not near the maximum value of $q \lesssim 0.23$.

Superhump solution

Measuring the late superhumps in GW Lib, Kato et al. (2008) found an extreme mass ratio for the system of $q = 0.062$. Which, when combined with the WD mass from seismology and the empirical donor star mass from the Knigge (2006) sequence and with a mass ratio smaller than the maximum value of $q < 0.23$, proves an attractive solution, within the boundaries of the formal solution. We calculated the magnitude of the K-correction at this mass ratio using our irradiated secondary model. In order to produce the observed $K_{\rm em} = 82.2 \pm 4.9$ km s^{-1}, we find a true $K_2 = 100.8 \pm 7.1$ km s^{-1} where the error is calculated by propagating the error on $K_{\rm em}$. The error on the observed $K_{\rm em}$ dominates over effects such as the assumed level of equatorial shielding or the optical thickness of the emission. The implied system parameters based on the superhump value of q and our corrected K_2 can be found in the left hand column of Table 3-5.

The small mass ratio scenario would correspond to a low mass donor with an M8 (Cox, 2000) or T spectral type (Knigge, 2006) if the donor is close to its main-sequence

configuration. This would agree with the infrared magnitude constraints mentioned previously and fits perfectly with GW Lib being close to the period minimum.

Interestingly, the derived K_1 (at 6.25 ± 0.4 km s^{-1}) in this scenario is close to the measured radial velocity of the narrow Balmer emission component in super outburst ($K = 3.0 \pm 1.6$ km s^{-1}) suggesting that this component may indeed trace the WD. Similar sharp emission components from the WD are seen in AM CVn systems (Morales-Rueda et al. 2003, Roelofs et al. 2006). However, a component arising at the surface of a WD is expected to be gravitationally red-shifted but the systemic velocity for this lines component was -16.6 ± 0.8 km s^{-1} which is similar to the systemic velocity of the system and cannot be biased by the Stark effect as is the case in AM CVn systems. Unfortunately the emission is only a transient feature and its K will be difficult to improve upon. The origin of the component and its possible connection with the WD thus remains unclear.

3.5 Discussion

We presented time-resolved optical spectroscopy of GW lib during a large number of epochs spanning before, throughout and after the 2007 outburst. We studied the long-term evolution of the spectral features, tracking large changes in the accretion geometry and intensity.

Pre-outburst spectroscopy obtained in 2004 data show clear features of the accreting WD including a detection of Mg II absorption. Here, the low inclination of GW Lib has an advantage over high inclination systems as it gives narrow disc emission lines instead of wide profiles, potentially resolving the Mg II line from the nearby He I line. In Chapter 4 we present high resolution, time-resolved spectroscopy of this line.

During the outburst, we initially see the optically thick accretion disc dominate through absorption features. Their radial velocities do not trace the WD and show semi-amplitudes of order 50 km/s. A peculiar, sharp emission line component was found in the Balmer lines that is effectively stationary. This could be some low velocity outflow in the z-direction or a component near the WD, but its mean velocity is similar to γ whereas a layer near the high gravity WD should be gravitationally red-shifted. As the system fades back towards quiescence, accretion powered double-peaked emission profiles appear. The absorption associated with the accretion disc continues to weaken until the system returns to a semi-quiescent state with strong double-peaked emission lines.

The Ca II triplet in GW Lib shows that these much neglected lines of CV spectra could be an interesting window to search for signs of both donor stars and accretion disc structures even in cases where the Balmer lines show no signs of the donor star whatsoever and the disc itself is barely resolved. GW Lib is a particularly challenging object in that sense due to its very low inclination and thus small projected velocities. The Ca II triplet in emission could be resolved into several components and the secondary star was discovered in emission moving in between the sharp double-peaked emission from the accretion disc. Doppler tomography and radial velocity fits of the Ca II lines provide a semi-amplitude of $K_{\rm em} = 82.2 \pm 4.9$ km s^{-1} for this donor star feature and indicates a disc centre of symmetry at $K_{\rm disc} = 6 \pm 5$ km s^{-1}. The disc is also visible in the Hβ maps but with less detail and sharpness and no donor star contribution is seen. Contrasting these lines highlights the diagnostic advantages provided by the Ca II triplet.

Based on previous studies together with the limits on K_1 and K_2 provided in this work, the allowed range of binary parameters were explored. While our dynamical limits place a hard upper limit on the binary mass ratio of $q < 0.23$, we favour a significantly lower value. A mass ratio near $q \sim 0.06$ is in accordance with estimates based on the detected super-hump modulations, the constraints on the faintness, and thus mass, of the donor star and the indications that K_1 is very small. Given such a mass ratio, our measured $K_{\rm em}$ implies $K_2 = 100.8 \pm 7.1$ km s^{-1} for the donor star component when applying the relevant K-correction. The implied $K_1 = 6.2 \pm 0.4$ km s^{-1} is then also close to our measured disc centre of symmetry. The combination of a WD mass near the value suggested by the pulsations and a low mass donor near the empirical sequence of an evolved CV near the period bounce appears to be consistent with the observational constraints to date.

Whether the spectral features of the donor seen in the Ca II lines, observed several months after the tail end of the 2007 super outburst are persistent remains to be established. As the WD continues to cool, donor star irradiation may be less effective in exciting the strong Ca II lines we observed. Nonetheless, high resolution spectroscopy resolving these lines at good S/N levels appears to be a viable tool to expand our knowledge of the binary parameters of short period cataclysmic variables and their faint donor stars.

Chapter 4

GW Lib II: WD mass determination

Based on:

van Spaandonk, L., Steeghs, D., Marsh, T. R., Parsons, S.G.

The Mass of the White Dwarf in GW Libra

2010, Astrophysical Journal Letters, **715**, L109

4.1 Introduction

Various methods to determine the system parameters of GW Lib have been exploited, including model fits to the WD absorption profiles, prominent in both the optical (Thorstensen et al., 2002) and the UV (Szkody et al., 2002) providing estimates for the WD $T_{\rm eff}$ and $\log g$. Asteroseismological models, combined with a UV-flux limit, suggest a WD mass of $M_1 = 1.02 M_\odot$ (Townsley et al. 2004). After its second recorded super-outburst in April 2007 (Templeton, 2007), the superhump period suggest a mass ratio of $q = M_2/M_1 = 0.06$ (Kato et al., 2008), when combined with Patterson's empirical relation (Equation 1-32; Patterson et al. 2005).

In this Chapter we explore the possibilities of using the gravitational redshift of the Mg II absorption line reported in Chapter 3 in combination with WD mass-radius relations to give an independent measurement of the mass and spin of the WD in GW Lib.

4.2 Observations and reduction

GW Lib was observed within the 69.D-0591 program at the 8.2-m Very Large Telescope (VLT), located at the Paranal Observatory in Chile as part of the European Southern Observatory, equipped with only the blue arm of the Ultraviolet and Visual Echelle Spectrograph (UVES: Dekker et al. 2000). We retrieved a total of 45 science frames obtained during 2002 May 16-17 covering 2.4 and 2.8 binary orbits on the respective nights.

Table 4-1: Details of observations.

Date	n spectra	Exp time (s)	Start/Finish UTC	Orbital Coverage ($T_{\rm obs}/P_{\rm orb}$)
16 May 2002	20	500	05:28:26 - 08:34:02	2.4
17 May 2002	25	500	04:49:03 - 08:24:08	2.8

The reduction of the raw frames was conducted by S.G Parsons, using the most recent standard recipe pipeline release of the UVES Common Pipeline Library (CPL) recipes. The resulting optimally-extracted spectra covered a wavelength range of λ4020-5240Å at a dispersion of 0.031Å pixel^{-1} and a spectral resolution of 0.10Å (5.77 km s^{-1}) as measured from the sky lines. The spectra were wavelength calibrated with one Thorium Argon arc per night. This calibration was tested against the two sky lines visible at λ5197.92Å and λ5200.28Å. The corresponding science frames were corrected for any remaining shifts. The residual shifts were scattered around zero with a maximum amplitude of 0.01 km s^{-1}. Next, heliocentric velocity corrections were applied to the individual frames to deliver spectra in a common heliocentric rest frame.

No flux standard was observed with the correct settings on the nights and, as no master response curve exists for the non-standard set-up used, the frames were not flux calibrated. The exposure time was 500 seconds, giving a signal to noise of ∼6.5 per spectrum. Details of the observations can be found in Table 4-1, while Figure 4-1 shows the average spectrum of GW Lib on the 16th of May. Prominent features are the Balmer disc emission lines on top of broad absorption troughs from the WD, visible due to the low mass accretion rate in the system. He I is also seen in emission as is He II at 4685.75Å.

Our pre-outburst, intermediate resolution spectra of GW Lib showed Mg II at 4481.21Å in absorption (Bottom spectrum in Figure 3-2). The archival VLT/UVES data presented in this Chapter confirm the presence of this line and, thanks to the superior spectral resolution combined with the low inclination of the system, shows it to be unblended from the nearby He I emission line at 4471Å. We measure an EW of Mg II of 0.25 ± 0.01Å (similar to the value of 0.24 ± 0.03Å in 2004) and a FWHM of 1.35 ± 0.04Å.

4.3 Gravitational redshift for Mg II

In low accretion rate dwarf novae, the luminosity of the accretion disc is low enough to show the broad absorption features of the WD and can even show the narrow absorption

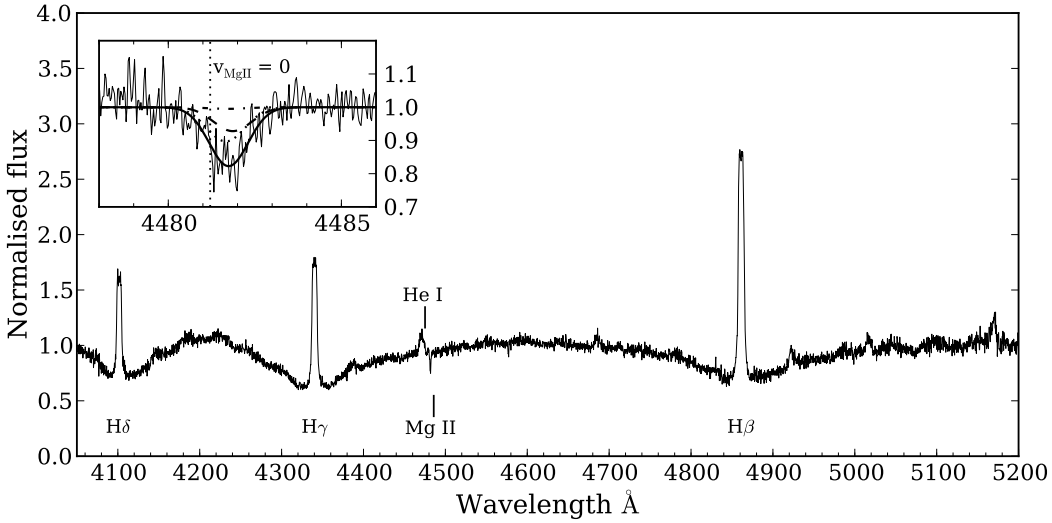

Figure 4-1: Average spectrum of GW Lib on the 16th of May 2002. The inset shows the Mg II absorption line averaged over 1 orbital period with the final Gaussian fit. The total fit (*thick solid line*) is the sum of three separate fits to the triplet lines, all according to their own transition probability, λ4481.126 (*dotted*), λ4481.150 (*dotted-dashed*), λ4481.325 (*dashed*).

features of metal lines due to freshly accreted gas. These lines open a window to probe the WD atmosphere directly and give independent measurements of stellar parameters. For lines formed near the primary, a gravitational red-shift is expected, introduced in the deep gravitational potential of the WD (Eddington 1924; Greenstein & Trimble 1967; Sion et al. 1994). A measurement of the gravitational redshift in the rest frame of the binary could provide the WD mass directly when combined with mass-radius models (e.g. Eggleton's relation as quoted in Verbunt & Rappaport 1988). This method has previously been used in CVs in the cases of U Gem (Long & Gilliland, 1999), VW Hyi (Smith et al., 2006) and WZ Sge (Steeghs et al., 2007).

In the case of GW Lib, the directly measured redshift of the magnesium line ($v_{\rm MgII}$) needs to be rectified for several contributions in order to get the true gravitational redshift induced by the WD only ($v_{\rm grav}$(WD)). These corrections consist of the systemic velocity (γ) of the binary system and the effects of the gravitational potential from the donor star ($v_{\rm grav}$(donor)). Hence the gravitational redshift due to the WD is given by:

$$v_{\rm grav}({\rm WD}) = v_{\rm MgII} - v_{\rm grav}({\rm donor}) - \gamma$$

We will discuss the various contributions and measurements independently. Firstly, all 45 spectra of the two nights were individually continuum normalised and then binned

into 20 equally spaced orbital phase bins to increase S/N.

4.3.1 $v_{\rm MgII}$

To measure the redshift of the magnesium line to the best precision and minimise any orbital effect we compared several methods.

Firstly, we made a orbital average, by weighing each phase bin according to their S/N, and fitted the Mg II absorption line with a weighted triple Gaussian, as the Mg II is a triplet line. The different components have rest wavelengths of λ4481.126Å with a transition probability of $\log(gf) = 0.7367$, λ4481.150Å with $\log(gf) = -0.5643$ and λ4481.325Å with $\log(gf) = 0.5818$[1]. The variables for the fit are the common offset (for all 3 lines) and the common FWHM to provide a good fit to the blue wing of the absorption feature. The peak height is also a common variable but scaled according to the various transition probabilities. This gives a best fit with a mean offset of 35.2 ± 1.1 km s^{-1}, a FWHM of 1.32 ± 0.08Å and a common absorption line depth of $2 \pm 0.1\%$.

Secondly, we fixed the FWHM and peak of the Gaussians to these values and checked the individual spectra for orbital variability. Unfortunately, the S/N is too low to give good individual fits (individual 1σ errors on the offset are $\sim$ 8 km s^{-1}) nor can we phase-lock this motion to the ephemeris of the system as determined in van Spaandonk et al. (2010b) due to the uncertainty in the period. The resultant radial velocity curve suggested motion, and a formal sine fit derived from Monte-Carlo simulations, delivered a semi-amplitude of $K = 13 \pm 2$ km s^{-1} (see Figure 4-2). To rectify for any orbital motion, we removed any measured shift compared to the mean from individual spectra.

A uniform orbital average was constructed, by assigning the same weight to each phase bin, to minimise any effects caused by varying S/N over the orbital period and finally we refit this last average with our triple Gaussian fit with as variables the common offset, the common FWHM and the weighted peaks as described above (see inset Figure 4-1).

This gives a final measurement of $v_{\rm MgII} = 35.8 \pm 1.5$ km s^{-1}. The line has a FWHM $= 1.30 \pm 0.05$Å. We have tested the accuracy of our measurement by following different recipes for combining and averaging the spectra but we find that the uncertainty on the gravitational redshift is dominated by the S/N and resolution of the data and not the specific recipe used.

[1]Data from The Atomic Line List Version 2.04: `http://www.pa.uky.edu/~peter/atomic/`

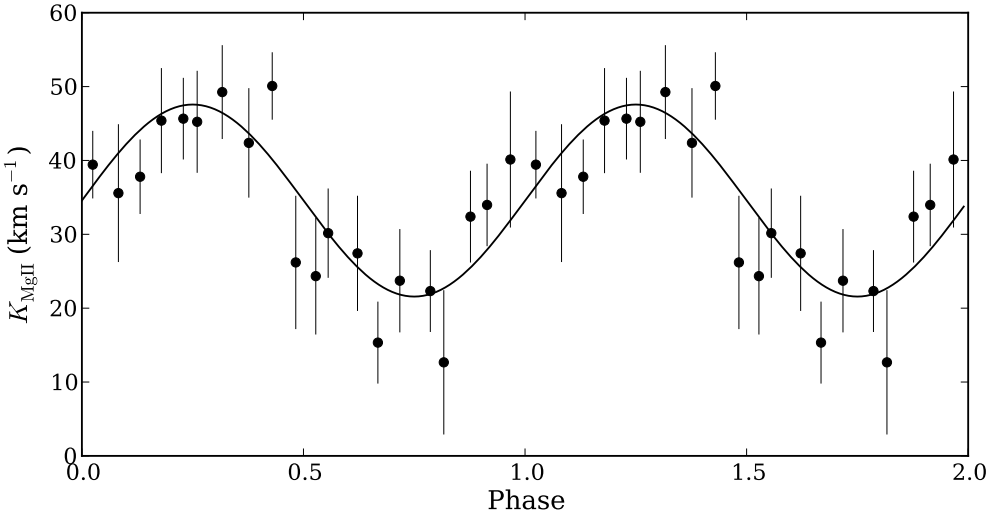

Figure 4-2: Radial velocity curve of the Mg II absorption line (the orbital coverage is plotted twice) with the best fit derived from Monte-Carlo simulations ($K = 13 \pm 2$ km s^{-1}).

4.3.2 v_{grav}(donor)

The first correction is due to the influence of the gravitational potential of the donor on the magnesium line. However, the expected low mass of the donor star ($\sim 0.05\ M_{\odot}$, Knigge 2006) gives only a small correction of 0.06 ± 0.02 km s^{-1} near the WD surface, effectively negligible given the measurement uncertainty in $_{\mathrm{MgII}}$.

4.3.3 The systemic velocity γ

From simultaneous double Gaussian fits to the double peaked Hβ and Hγ disc lines, combined with radial velocity curve fits provide a systemic velocity of -12.3 ± 1.2 km s^{-1} and a semi-amplitude of $K_{\mathrm{disc}} = 36.4 \pm 1.8$ km s^{-1}. These values are consistent with previously measured, pre-super outburst values ($K_{\mathrm{disc,H}_{\alpha}} = 38 \pm 3$ km s^{-1}, $\gamma = -17 \pm -2$ km s^{-1}; Thorstensen et al. 2002. $K_{\mathrm{disc,H}_{\beta}} = 45.1 \pm 1.7$ km s^{-1}; van Spaandonk et al. 2010b).

As we measure γ from disc lines, we need to take into account that this emission is red-shifted both by the WD and the donor star. As v_{grav} is reciprocal to the distance, the amount we have to account for is minimal at the edge of the disc, $R_{\mathrm{outer\,disc}} \approx 2.2 \times 10^{8}$ m (Equation 2.61 of Warner 1995) giving a minimal correction to v_{grav} of 1.7 km s^{-1}. A more realistic value for γ comes from the projected Keplerian velocity at the edge of the disc, $K_{\mathrm{disc}} \sim 200$ km s^{-1} (from the location of the disc ring in Doppler maps and

the estimate for i, see van Spaandonk et al. 2010b) which gives a Keplerian speed of $v_{\rm disc} = K_{\rm disc}/\sin i \sim 1070$ km s^{-1} and corresponds to a $v_{\rm grav} = v^2/c \sim 3.8$ km s^{-1} (via Equation 2-9). Including the transverse Doppler redshift (at half the strength of the gravitational redshift, see Section 2.3.4) this amounts to a total gravitational redshift at the location of the disc lines of 5.7 ± 1.6 km s^{-1}. The gravitational potential of the donor star has an effect of only 0.08 ± 0.02 km s^{-1} at a distance of $\sim 3 \times 10^8$ m. Hence the total $v_{\rm grav}({\rm disc}) = 5.8 \pm 1.6$ km s^{-1}.

The γ from the disc lines combined with the above correction should be consistent with the γ suggested by the radial velocity curve from the donor star (corrected for the effects of the gravitational potential at its surface). From the Ca II emission line in the i-band, we previously found $\gamma = -13.1 \pm 1.2$ (van Spaandonk et al., 2010b), and the correction at the surface of the donor star is 0.34 ± 0.15 km s^{-1} from the donor star and 1.4 ± 0.2 km s^{-1} from the WD (again including the transverse Doppler shift). Thus we have $\gamma_{\rm disc} = (-12.3 \pm 1.2) - (5.8 \pm 1.6) = -18.1 \pm 2.0$ and $\gamma_{\rm donor} = (-13.1 \pm 1.2) - (1.7 \pm 0.3) = -14.8 \pm 1.2$. Both estimates for γ are indeed consistent and with similar precision. Hence we have used $\gamma_{\rm disc}$ as derived from the same data set as used to determine $v_{\rm MgII}$.

4.3.4 The implied WD mass

Combining all values we find for the final gravitational redshift:

$$\begin{aligned} v_{\rm grav}({\rm WD}) &= (35.8 \pm 1.5) - (0.06 \pm 0.02) - (-18.1 \pm 2.0)\,{\rm km\,s^{-1}} \\ &= 53.8 \pm 2.5\,{\rm km\,s^{-1}} \end{aligned}$$

When combined with theoretical and empirical models for the mass-radius relationship for WDs this gives a direct measurement of the WD mass. The models we used are Eggleton's zero-temperature mass-radius relation as quoted by Verbunt & Rappaport (1988) and several appropriate non-zero temperature models for GW Lib from Fontaine et al. (2001). We plot these models in Figure 4-3 together with the $M_1(R)$ line demanded by our measured $v_{\rm grav}$ via Equation 2-8, where we substitute the distance d by the radius R. Accommodating the intersections between non-zero temperature models we find that $M_1 = 0.84 \pm 0.02\ M_\odot$.

4.3.5 System parameters and WD spin

Kato et al. (2008) reported the detection of superhump modulations in GW Lib. Combining the superhump period with the period from Thorstensen et al. (2002) and the

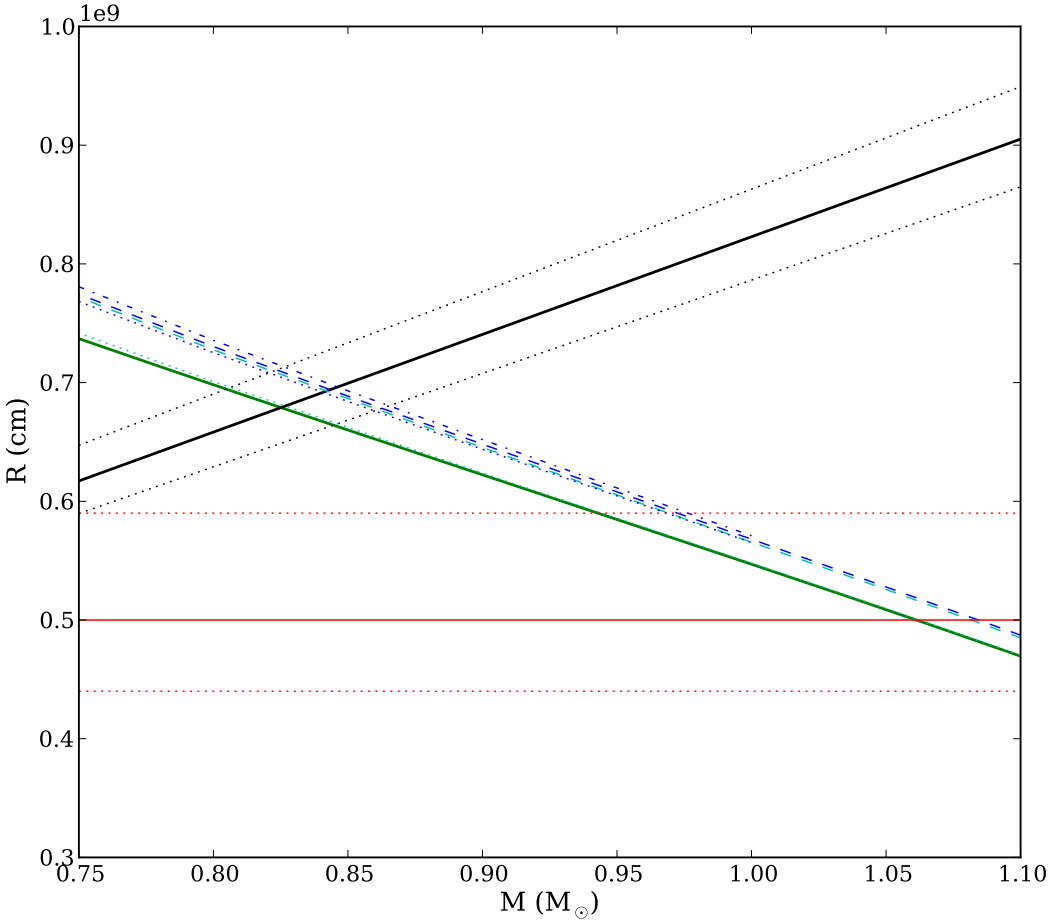

Figure 4-3: Mass-radius relationship for the measured $v_{\rm grav} = 53.8$ km s^{-1} (*black solid line from lower left to upper right*) with 1σ error lines (*black dotted lines*). The mass-radius models are Eggleton's zero-T relation (*green solid line from upper left to lower right*), a $T = 15\,500$ K, a hydrogen mass fraction of $q{\rm H} = 10^{-4}$ and $q{\rm He} = 10^{-2}$ C-core model (*blue dashed line*) and models with the same core but different temperatures at $T = 18\,000$ K and $T = 13\,000$ K (*blue dashed dotted* and *blue dotted*, respectively). For a WD with a CO-core, $T = 15\,500$ K, $q{\rm H} = 10^{-10}$ and $q{\rm He} = 10^{-2}$, the model is almost identical to the zero-T relation (*cyan dotted*), whereas the model with the same core but $q{\rm H} = 10^{-4}$ is lies closer to the C-core models (*cyan dashed*). The horizontal lines indicates the radius derived from the UV flux estimate from (Szkody et al., 2002), corrected for the latest distance measurement (Thorstensen, private communication - an improvement on the distance value quoted in Thorstensen et al. 2002) for GW Lib (*red solid line*) and 1σ errors (*dotted red lines*) and intercepts the mass-radius relations at $\sim 1.07\ M_\odot$.

Table 4-2: System parameters for GW Lib.

P (min)	76.78± 0.03	Thorstensen et al. 2002
M_1 ($M_\odot$)	0.84 ± 0.02	This Chapter
q	0.060 ± 0.008	Kato et al. 2008; Knigge 2006
K_2 (km s^{-1})	100.8 ± 7.1	Chapter 3
K_1 (km s^{-1})	6.25 ± 0.4	From q and K_2
M_2 ($M_\odot$)	0.050 ± 0.007	From q and M_1
v_1 (km s^{-1})	30.8 ± 0.5	Kepler 3rd Law
v_2 (km s^{-1})	513.4 ± 4.8	Kepler 3rd Law
i (°)	11.2 ± 0.4	From K_2 and v_2
$P_{\rm spin}$(s)	97 ± 12	From $v \sin i$

improved superhump excess - mass ratio relation given by Knigge (2006), the implied mass ratio of the system is $q = 0.060 \pm 0.008$. We previously determined the projected radial velocity of the donor star, K_2 in van Spaandonk et al. (2010b). Thus with an independent determination of M_1 from this paper, we can solve the system parameters for GW Lib using these constraints and list them in Table 4-2.

If one assumes that the width of the Mg II absorption line is dominated by rotational broadening, its FWHM can constrain the spin period of the WD. The FWHM of the absorption line fit is measured to be 1.30 ± 0.05Å which corresponds to a $v \sin i$ of 87.0 ± 3.4 km s^{-1} at this wavelength. Assuming i is equal to the value given in Table 4-2, this translates into a rotation speed of 448 ± 24 km s^{-1} at the surface of the WD. For a WD of mass 0.84 ± 0.02 $M_\odot$ and a radius of $6.95 \pm 0.15 \times 10^8$ cm, this results in a spin period of the WD of 97 ± 12 seconds.

4.4 Discussion

We have measured the gravitational redshift of the Mg II absorption line in high-resolution echelle spectra of GW Lib during quiescence. Assuming an origin in the photosphere of the accreting WD, we combined this redshift with non-zero temperature mass-radius relations for WDs to derive a WD mass of $0.84 \pm 0.02 M_\odot$. Combining this independent measurement with other constraints, confirms that GW Lib is a low mass ratio system observed at very low inclination (Table 4-2). Because the Mg II line was well-resolved in our data, we could also estimate the spin period of the WD to be 97 ± 12 seconds if we assume the width of the line to be dominated by rotational broadening.

Our mass value is significantly below the 1.03 $M_\odot$ lower limit derived by Townsley et al. (2004). They calculate the possible mass range to lie between $1.03 M_\odot$ and $1.35 M_\odot$

by combining the UV flux limit provided by Szkody et al. (2002), with the latest parallax distance at the time of their publication, $d = 104^{+30}_{-20}$pc (Thorstensen, 2003). Szkody et al. (2002) fitted WD models to UV spectra of GW Lib. Two different single temperature solutions were explored; $d = 171$ pc ($M_1 = 0.6M_\odot$, this would result in a $v_{\rm grav}$ of ~ 29 km s^{-1}) and $d = 148$ pc ($M_1 = 0.8M_\odot$, equivalent to $v_{\rm grav} \sim 49$ km s^{-1}) respectively. These solutions can be corrected to the latest parallax distance of 100^{+17}_{-13} pc (Thorstensen, private communication - an improvement on the distance value quoted in Thorstensen et al. 2002). At this distance, the observed UV flux implies a radius of roughly 5×10^8 cm (for a WD temperature of 14 700 K). However, such a small radius intercepts the mass-radius relations at 1.07 $M_\odot$, Figure 4-3 (*horizontal red solid line*, the 1σ errors are dominated by the error on the distance), and is consistent with the limit set by Townsley et al. (2004). A WD with a mass of $1.07M_\odot$ would result in $v_{\rm grav} \sim 95$ km s^{-1}, much larger than our measured redshift would suggest.

The high mass implied by the UV flux constraint is inconsistent with the mass and radius suggested by the gravitational redshift on a 2σ level. This suggests that either these two methods differ on a systematic level, or that the distance to GW Lib is underestimated. That is, a distance $d \sim 139$pc is needed to accommodate a WD with a radius of 6.95×10^8 cm at the same UV flux level. Hence, using the gravitational redshift to determine the WD mass the favoured method in this case, as this method is distance independent.

We note that Szkody et al. (2002) fail to find a good single temperature fit and claim the best fit arises by fitting a dual temperature model to the spectrum, allowing for a cooler zone that would place GW Lib within the ZZ Ceti instability strip for pulsating single WDs. However, the UV-flux versus implied WD radius then becomes a less clear-cut argument given the freedom of two temperatures and the surface coverage split between the two.

We note that the reverse has been seen in U Gem where the UV-flux places the WD at a lower mass than the gravitational redshift, which is measured from several absorption lines in the wavelength range 1162-1448Å, including C II, Si II and Si III Long & Gilliland (1999); Long et al. (2006).

As Townsley et al. (2004) warn, no WD rotation was included in their asteroseismology models and therefore their derived parameters ($M_1, M_{\rm acc}, \dot{M}$) may need to be revisited given our estimate of the spin period of the WD in GW Lib. A $P_{\rm spin} = 97 \pm 12$ seconds should give rise to rotationally split modes. Van Zyl et al. (2004) conducted a

thorough campaign with a baseline of over 4 years to find these modes in the power spectrum of GW Lib. The extensive search revealed a possible doublet around the 230s mode with a frequency difference between the components of 0.79 μHz. If this doublet originates from the rotation splitting of an $l = 1$ mode, the WD would have a spin period of $\sim$ 7.3 days which is much longer than expected for the WD in a CV. Approached from the other side, if a similar mode is split as a result of a rotation period of $\sim$ 100 s, the frequency difference would be $\sim$ 0.5 mHz and should be visible in the power spectrum. Note that for the proposed spin period, the first order approximation for frequency splitting is no longer valid and the splitting would become asymmetric. These asymmetric modes are much more difficult to locate and to identify. Hence, at this moment it is impossible to confirm the validity of the proposed spin period, based on the absence of frequency split pulsation modes.

From both GW Lib's and U Gem's comparison between WD mass found by gravitational redshift and the constraints from the UV-flux we can conclude that the measurement of the gravitational redshift through WD absorption lines gives an independent measurement of the WD mass in CVs, but is not always fully consistent with other constraints. Nonetheless, it suggests photospheric absorption lines in the atmospheres of accreting WDs can be a viable tool for mass measurements, in particular for low mass accretion rate CVs where the light from the WD dominates and especially for low i systems, as the broadening of disc emission lines remains small, and assures that narrow features like Mg II remains unblended from nearby strong disc features.

For GW Lib itself, we are still dependent on a number of assumptions in order to solve its system parameters. To properly align all methods, we need to revisit the mass from asteroseismology taking into account the effects of rotation and see if a WD model with a mass of $0.84 M_{\odot}$ at the latest distance can be fitted to the UV data with reasonable temperatures. To be able to calculate a direct mass ratio, a determination of K_1 from the Mg II line should be possible through high S/N phase-resolved spectroscopy. If furthermore matched with a reliable ephemeris using the emission from the donor star (giving K_2 and γ), a fully consistent and accurate WD mass for this prototypical accreting WD pulsator is entirely feasible.

Chapter 5

Ca II survey I: Observations and Analysis

Based on the success of GW Lib, where a sharp emission component from the donor star is visible in the Ca II triplet lines (Chapter 3), we have initiated a survey to search for similar features in a number of short period CVs. We aim to dynamically constrain the mass ratio in those systems where the donor star is undetected in absorption, prohibiting the use of traditional methods.

To maintain a clear overview of the large quantity of data acquired within the project, we first present the data acquisition and the basic data analysis of the systems observed within the survey. We leave the discussion of the results for later Chapters (6 and 7).

5.1 Observations and reduction

Within our survey, we dedicated five observing runs (in 2000, 2001, 2007, 2008 and 2009) to observe CVs near the period minimum, simultaneously covering the principal lines in the Balmer series and the Ca II triplet lines at medium to high resolution. The 2000 and 2001 runs had been designed to compare the disc emission features in the Balmer series to those in more massive metal lines, like the Ca II triplet lines, testing the predictions from Horne (1995), Marsh & Dhillon (1997) and Steeghs & Stehle (1999), see also Section 2.5. The later runs were primarily driven by the detection of emission from the donor in the Ca II triplet lines.

5.1.1 Target Selection

Using the lists of CVs from Ritter & Kolb (2003), Patterson (2011) and the initial survey presented by Marsh & Dhillon (1997), we selected objects for the programme with an orbital period near the bounce period and/or with detectable Ca II lines in archival or published spectra (i.e. in SDSS). Since we wish to test and calibrate the $\epsilon(q)$ relation, priority was given to DNe with a recent detected superoutburst followed by a

detection of superhumps or a previously recorded superhump period. We also included CVs with an independently determined q (e.g. via eclipses), alongside several systems with a longer period, to be able to validate and calibrate the proposed method.

The brightness constraint for the targets is set to give a $S/N > 5$ per resolution element with a 4-m class telescope when combined with a maximum exposure time set by $P_{\rm orb}/10$. We mainly used the WHT in combination with ISIS, restricting our survey to the Northern skies. OY Car is the only Southern object, observed with the VLT in combination with the Echelle spectrograph UVES, where its extremely high resolution justifies the use of the 8-m telescope.

The final list of observed systems ranges in orbital period between 77 minutes (GW Lib) and 396 minutes (SS Cyg). From the superhump periods, the mass ratio can be estimated using Patterson's relationship (as given in Equation 1-32) and ranges from $q = 0.05$ (IX Dra) to $q = 0.17$ (YZ Cnc). See Table 5-1 for more details. Official variable star names are used, as resolved via SIMBAD[1], unless otherwise stated.

5.1.2 WHT/ISIS

Four observing runs were conducted using the 4.2-m WHT in combination with the two-armed Intermediate dispersion Spectrograph and Imaging System (ISIS). During these epochs, time-resolved spectroscopic data were acquired for all objects but OY Car. In August 2000, the blue arm of the spectrograph was equipped with the EEV12 CCD and the H2400B grating. The red arm was equipped with the TEK2 CCD. For the later runs (July 2007, December 2008, August 2009) the blue arm was equipped with the EEV12 CCD and the R1200B grating and the red arm with the RED+ CCD, which has an improved efficiency in the I-band, and the R1200R grating. The only exception is 7 December 2008, when we used both the blue and the red arm with the R600B and the R600R grating, respectively. Depending on the different sky conditions and brightnesses of the objects, the CCDs were binned and the spectral resolution adjusted accordingly. The exposure time is set such that the orbital smearing is minimised but the S/N per exposure remains above 5. If poor weather conditions prohibited time-resolved spectroscopy with enough S/N, the exposure times were increased to check if Ca II is present and hence if the target is suitable for follow-up observations. Observing details for all targets can be found in Tables 5-2, 5-4, 5-5 and 5-6.

All WHT/ISIS spectra were reduced in the same way. The average bias and flat

[1] http://simbad.u-strasbg.fr/simbad/

Table 5-1: Period information of the observed systems. Listed are the orbital period ($P_{\rm orb}$) in minutes and in days, the superhump period when detected in days ($P_{\rm sh}$), the inferred mass ratio ($q_{\rm sh}$) from this superhump period, and independently derived mass ratios ($q_{\rm other}$; where an asterisk indicates which mass ratios are determined using eclipse mapping). All data is from Ritter & Kolb (2003) and references therein unless otherwise stated. The final column lists the last observed superoutburst pre-data acquisition, as catalogued in the AASVO International Database.

Object	$P_{\rm orb}$ (min)	$P_{\rm orb}$ (days)	$P_{\rm sh}$ (days)	$q_{\rm sh}$	$q_{\rm other}$	S Outburst
GW Lib	76.8	0.05332	0.0541	0.062	$< 0.23^{a}$	April 2007
V844 Her	78.7	0.054643	0.0559	0.106		April 2008
V455 And	81.1	0.056309	0.0572	0.078		September 2007
ASAS 0025	81.4	0.05654	0.0568	0.035		September 2004
WZ Sge	81.6	0.056688	0.0572	0.051	$0.045\text{-}0.092^{b}$	July 2001
V1108 Her	82.1	0.057	0.0575	0.050		June 2004
HS 2219	86.3	0.0599	0.0618	0.146	$0.14 - 0.19^{c}$	April 2007
OY Car	90.9	0.063121	0.0646	0.110	$0.102^{*\,d}$	February 2000
V632 Cyg	91.8	0.06377	0.0658	0.141		November 2008
UV Per	93.5	0.0649	0.0660	0.084		October 2007
IX Dra	95.7	0.06646	0.067	0.047		–
TY Psc	98.4	0.06826	0.0702	0.124		October 2008
GD 552	102.7	0.07134	–	–		–
IY UMa	106.4	0.073909	0.0758	0.118	$0.125^{*\,e}$	February 2007
HT Cas	106.1	0.073647	0.0759	0.138	$0.15^{*\,f}$	January 2008
SU UMa	109.9	0.07635	0.0788	0.141		August 2008
YZ Cnc	125.0	0.0868	0.0903	0.175	0.22^{g}	November 2008
IP Peg	227.8	0.158206	–	–	$0.48^{*\,h}$	October 1999
SS Cyg	396.2	0.27513	–	–	0.685^{i}	July 2000

[a] van Spaandonk et al. 2010a
[b] Patterson 2001; Steeghs et al. 2007
[c] Rodríguez-Gil et al. 2005
[d] Littlefair et al. 2008
[e] Steeghs et al. 2003
[f] Horne et al. 1991
[g] Shafter & Hessman 1988
[h] Copperwheat et al. 2010
[i] Bitner et al. 2007

Table 5-2: WHT - ISIS 2000 observations - P33

Object	Date	Phase Coverage ($T_{\rm obs}/P_{\rm orb}$)	Number of Spectra	Wavelength Coverage (Å)	Spectral Resolution (Å)	Exp time (s)
SS Cyg	08/08/2000	1.23	144	3800-4170	0.30	145
			175	8400-8850	0.56	120
IP Peg	09/08/2000	1.79	97	3800-4170	0.32	200
				8400-8850	0.82	200
	10/08/2000	1.80	100	3800-4170	0.30	200
				8400-8850	0.59	200

Table 5-3: VLT - UVES 2001 observations - 66.D-0505(A)

Object	Date	Orbital Coverage ($T_{\rm obs}/P_{\rm orb}$)	Number of Spectra	Wavelength Coverage (Å)	Resolution (Å)	Exp time (s)
OY Car	14/02/2001	5.2	158	3830 - 5060	0.12	120
			158	6400 - 8220	0.12	120
			158	8400 - 9500	0.12	125

Table 5-4: WHT - ISIS 2007 observations - P19

Object	Date	Phase Coverage (T_{obs}/P_{orb})	Number of Spectra	Wavelength Coverage (Å)	Spectral Resolution (Å)	Exp time (s)
WZ Sge	22/07/2007	1.52	55	4200-5000	0.66	120
				8050-8800	0.54	120
	24/07/2007	3.33	98	4200-5000	0.66	150
				8050-8800	0.54	150
	25/07/2007	0.44	35	4200-5000	0.66	150
				8050-8800	0.54	150
V455 And	22/07/2007	1.87	35	4200-5000	0.66	200/300
				8050-8800	0.54	200/300
	25/07/2007	2.64	39	4200-5000	0.66	300
				8050-8800	0.54	300
HS 2219	23/07/2007	4.09	34	4200-5000	0.66	600
				8050-8800	0.54	600

Table 5-5: WHT - ISIS 2008 observations - P35

Object	Date	Phase Coverage (T_{obs}/P_{orb})	Number of Spectra	Wavelength Coverage (Å)	Spectral Resolution (Å)	Exp time (s)
V455 And	07/12/2008	1.40	34	3800-5400	1.83	180
				7900-9400	1.55	180
	09/12/2008	2.26	25	3750-4550	1.09	300/360
				8350-9000	0.83	300/360
UV Per	07/12/2008	0.48	8	3800-5400	1.83	360
				7900-9400	1.55	360
ASAS 0025	10/12/2008	2.13	22	3750-4550	1.09	480
			18	8350-9000	0.83	480
YZ Cnc	09/12/2008	1.50	81	3750-4550	1.09	120
				8350-9000	0.83	120
SU UMa	10/12/2008	1.49	41	3750-4550	1.09	200
				8350-9000	0.83	200
	11/12/2008	1.66	45	3750-4550	1.09	200
				8350-9000	0.83	200
IY UMa	10/12/2008	0.37	7	3750-4550	1.09	360
				8350-9000	0.83	360
	11/12/2008	1.88	29	3750-4550	1.09	360
				8350-9000	0.83	360
TY Psc	11/12/2008	2.35	17	3750-4550	1.09	300/600
				8350-9000	0.83	300/600

Table 5-6: WHT - ISIS 2009 observations - P26

Object	Date	Phase Coverage (T_{obs}/P_{orb})	Number of Spectra	Wavelength Coverage (Å)	Spectral Resolution (Å)	Exp time (s)
UV Per	10/08/2009	2.90	26	3700-4600	0.83	480
				8100-8800	0.62	480
TY Psc	09/08/2009	2.42	27	3700-4600	0.83	480
				8100-8800	0.62	480
V632 Cyg	09/08/2009	0.50	5	3700-4600	0.83	600
				8100-8800	0.62	600
V844 Her	10/08/2009	2.64	31	3700-4600	0.83	300/480
			24	8100-8800	0.62	480
IX Dra	11/08/2009	0.99	16	3700-4600	0.83	300
				8100-8800	0.62	300
HT Cas	11/08/2009	2.04	47	3700-4600	0.83	240
				8100-8800	0.62	240
GD 552	11/08/2009	1.13	21	3700-4600	0.83	300
				8100-8800	0.62	300
V1108 Her	09/08/2009	0.62	11	3700-4600	0.83	240
				8100-8800	0.62	240

field correction was carried out using the FIGARO package from STARLINK and nightly average bias and tungsten frames. PAMELA was used for the optimal extraction of the spectra. Regular copper argon arc lamp exposures allowed us to establish an accurate wavelength scale for each spectrum by interpolation between the nearest arcs in time. Each arc frame was fitted with a fifth order polynomial to 10-40 lines to give a typical RMS of 0.1 pixel. The spectral resolution (presented in Tables 5-2, 5-4, 5-5 and 5-6) was measured by the FWHM of the arc lines, using an average of at least 10 lines. The individual spectra were flux calibrated using a spectro-photometric standard star observed on the same night, and normalised to the continuum level using a spline fit to selected continuum regions.

5.1.3 VLT/UVES

OY Car was observed within the 66.D-0505(A) program in 2001 with the VLT, using both arms and the 3 CCDs (BLUE and REDL/REDU) of the Echelle spectrograph UVES (see Table 5-3). The reduction of the raw frames was conducted using the most recent standard recipe release of the UVES Common Pipeline Library (CPL). The spectra were wavelength calibrated with one thorium argon arc per night. This calibration was tested against the telluric lines visible in the spectra and proves stable to < 3 pixels. The spectral resolution, given by the FWHM of the arc and telluric lines, is quoted in Table 5-2. One flux standard was observed with the correct settings on the night but as the flux coverage of the standard table does not cover the entire observed wavelength range,

the science frames were only continuum normalised.

5.2 EW measures

For each system, the EW is measured for all prominent lines covered in the set-up, using the continuum normalised spectrum averaged on the binary period. Each profile is velocity binned around the wavelength of the given line at the resolution dictated by the set-up. The continuum in this range is normalised separately, by fitting a second order polynomial to it, to correct for any deviations from unity which could otherwise affect the EW measurement. The EW is measured in a window optimised for each line individually, such that the entire profile is covered, yet contamination from nearby lines avoided. Deviations from this window were kept to a minimum per system, however, this proves not always possible.

EW measures for both the Balmer (a subset of Hα, Hβ, Hγ and Hδ) and Paschen lines (Pa 14 and Pa 12) are given in Table 5-7, and the EWs for the Ca II lines (Ca II triplet and Ca H/K) are presented in Table 5-8. To measure the strength of the emission arising from the disc alone, in those Balmer lines showing WD absorption troughs, any absorption troughs around these lines are first removed by fitting a higher order polynomial fit to the continuum and trough during the re-normalisation. Correlations between these EWs as a function of the system parameters will be discussed in section 6.1.

5.3 The survey

Our survey covers a total of 19 objects. With the large amount of data and the numerous analysis steps performed per object, this results in a rather exuberant amount of data that needs to be described. To improve readability, we have decided to split the data analysis from the data discussion. This section lists only the direct measures of the disc and donor features for all of the objects. In Chapter 7 we discuss the implications of these measures for the constraints of the mass ratio. In Chapter 6, we discuss the general properties of the Ca II versus the Balmer emission line profiles in the surveyed objects.

The systems are discussed below, in order of orbital period, from short to long (Table 5-1). All objects are accompanied by a set of figures which include average spectra, trailed spectra and Doppler maps of appropriate emission lines, for a full overview of

Table 5-7: EW measurements for the prominent hydrogen features, measured from the orbitally averaged spectrum. For each object the width of the window is set such that no blending occurs and most lines can be measured with the same width. Legend: '×' - not covered in wavelength range, '–' - covered, but line not detected above noise level, '+' - detected but blended with nearby Ca II lines so no independent EW measure possible. Those systems that have WD absorption removed are indicated with a *. Features with strong central absorption that made normalisation unfeasible have been eliminated from the analysis.

Object	Hα 6562.76 Å	Hβ 4861.327 Å	Hγ 4340.465 Å	Hδ 4101.735 Å	Pa 14 8598.392 Å	Pa 12 8750.473Å
GW Lib*	×	-34.5(1)	-18.6(1)	×	-7.1(2)	-13.1(2)
V844 Her	×	×	-25.7(2)	-18.4(2)	–	-18.4(10)
V455 And	×	-114.4(1)	-79.6(1)	-65.2(1)	+	-21.1(2)
ASAS 0025*	×	×	-24.4(6)	-13.8(5)	–	-2.7(9)
WZ Sge*	×	-42.6(1)	-20.9(1)	×	+	×
V1108 Her*	×	×	-26.7(4)	-20.1(4)	–	–
HS 2219*	×	-22.0(1)	-8.9(1)	×	–	–
OY Car	-73.0(1)	-33.8(1)	Strong central absorption		–	0.8(1)
V632 Cyg	×	×	-65.2(4)	-51.2(4)	-6.8(4)	-17.1(6)
UV Per*	×	×	-31.0(2)	-22.9(2)	-5.4(2)	-9.6(2)
TY Psc*	×	×	-26.1(3)	-17.4(3)	–	-9.7(3)
GD 552*	×	×	-41.4(1)	-25.9(1)	-2.8(2)	-12.9(2)
IY UMa	×	×	Strong central absorption		–	–
HT Cas	×	×	-39.7(1)	-27.9(1)	+	-8.4(2)
SU UMa	×	×	-43.9(1)	-37.0(1)	-1.3(1)	-5.0(1)
YZ Cnc	×	×	-21.3(1)	-18.4(1)	-1.1(1)	-4.3(1)
IP Peg	×	×	×	-103.7(2)	+	-5.0(1)
SS Syg	×	×	×	-48.8(1)	-1.6(1)	-5.5(1)

the objects and their associated figures and tables, see Table 5-9 and the references therein. The set of analysis steps is described first. All of the measurements of all of the objects are summarised in Tables 5-10, 5-11 and 5-12.

5.3.1 Time-resolved data analysis

The analysis steps for all systems are the same and are separated into measuring disc features and, when present, donor features using the methods described in Section 2.3. The order in which we present them per object is listed below.

General features

For each object we give two orbitally averaged spectra. The first one covers the Balmer series and the second one covers the Ca II triplet lines in the I-band. We present the key emission and/or absorption features, along with a short literature review of the scientific interest of the object.

Table 5-8: EW measurements for the calcium features, measured from the orbitally averaged spectrum. Legend as in Table 5-7. For each object the width of the window is set to avoid blending with nearby lines. For some objects, the blending of the Ca II lines at λ8498.02Å and λ8542.09Å was impossible to avoid, hence the EW over the entire feature was measured. Features with strong central absorption that made normalisation unfeasible have been eliminated from the analysis.

Object	Ca K 3933.67 Å	Ca H - Hϵ 3968.47 Å 3970.074 Å	Ca II - Pa 16 8498.02 Å 8502.483Å	Ca II - Pa 15 8542.09 Å 8545.383Å	Ca II - Pa 13 8662.14 Å 8665.019Å
GW Lib	×	×	-10.4(1)	-17.2(1)	-17.4(1)
V844 Her	-4.7(1)	-16.8(2)	–	–	-6.9(8)
V455 And	-14.5(1)	-49.7(1)	-29.2(2)		-25.0(6)
ASAS 0025	-4.9(4)	-14.7(4)	-5.0(9)	-13.4(9)	-12.6(7)
WZ Sge	×	×	+	+	+
V1108 Her	-7.0(3)	-13.3(3)	–	–	–
HS 2219	×	×	–	–	-8.7(8)
OY Car	Strong central absorption		-34.3(1)		-20.9(1)
V632 Cyg	-14.3(4)	-44.2(4)	-6.8(4)	-15.3(4)	-24.9(5)
UV Per	-13.3(2)	-24.2(2)	-16.4(2)	-27.2(2)	-25.0(2)
TY Psc	-8.4(2)	-18.2(2)	-8.2(2)	-11.6(2)	-15.9(2)
GD 552	–	-18.7(1)	-1.2(2)	-1.8(2)	-5.8(2)
IY UMa	Strong central absorption		-21.6(3)		-11.56(2)
HT Cas	Strong central absorption		-16.3(2)		-11.5(2)
SU UMa	-2.4(1)	-20.5(1)	0.7(1)	-2.7(1)	-5.6(1)
YZ Cnc	-4.7(1)	-15.0(1)	-4.3(1)	-6.4(1)	-8.2(1)
IP Peg	-29.2(2)	-60.3(2)	-13.6(1)		-6.8(1)
SS Cyg	-7.8(1)	-41.5(1)	-2.8(1)	-3.6(1)	-5.0(1)

Table 5-9: Location of section, details of observations, spectra and Doppler maps of the survey objects.

Object	Section		Details of Observations		Spectrum		Doppler Map		RV
		Page	Table	Page	Figure	Page	Figure	Page	Table
GW Lib	5.3.2	102	3-1	59	5-1	103	5-6	110	5-10
V844 Her	5.3.3	104	5-6	96	5-2	104	5-6	110	5-10
V455 And	5.3.4	105	5-4/5-5	95	5-3	106	5-6	110	5-10
ASAS 0025	5.3.5	107	5-5	95	5-4	107	5-6	110	5-10
WZ Sge	5.3.6	109	5-4	95	5-1	103	5-14	125	5-10
V1108 Her	5.3.7	114	5-6	96	5-2	104	N.A.	N.A.	5-10
HS 2219	5.3.8	115	5-4	95	5-1	103	5-14	125	5-10
OY Car	5.3.9	116	5-3	94	5-9	117	5-10	120	5-10
V632 Cyg	5.3.10	119	5-6	96	5-13	124	N.A.	N.A.	N.A.
UV Per	5.3.11	121	5-5/5-6	95/96	5-13	124	5-14	125	5-11
TY Psc	5.3.13	123	5-5/5-6	95/96	5-13	124	5-14	125	5-11
GD 552	5.3.14	126	5-6	96	5-2	104	5-15	131	5-11
IY UMa	5.3.15	127	5-5	95	5-4	107	5-15	131	5-11
HT Cas	5.3.16	128	5-6	96	5-13	124	5-15	131	5-11
SU UMa	5.3.17	129	5-5	95	5-3	106	5-15	131	5-11
YZ Cnc	5.3.18	130	5-5	95	5-4	107	5-18	138	5-12
IP Peg	5.3.19	132	5-2	94	5-16	133	5-18	138	5-12
SS Cyg	5.3.20	136	5-2	94	5-16	133	5-18	138	5-12

Disc features

We analyse the disc features in both a Balmer emission profile (either Hα, Hβ, Hγ or Hδ, depending on wavelength coverage) and the Ca II λ8662Å emission profile as this latter emission line is always unblended from nearby Ca II lines (for high inclination systems, the Ca II λ8498Å and Ca II λ8542Å often blend together). For those systems with a complete orbital coverage and with double peaked disc emission profiles, the analysis steps are:

- 2-Gaussian fits to the mean profile followed by phase resolved 2-Gaussian fits with the width and the separation set to the values derived from the mean profile. A radial velocity curve fit gives $K_{\rm disc,RV}$.
- Double Gaussian fits to the phase resolved profiles in combination with a diagnostic diagram give $K_{\rm disc,DD}$.
- A centre of symmetry search in the Doppler map gives $K_{\rm disc,MEM}$, after optimising the map for the systemic velocity γ.

For the few systems that either do not have full orbital coverage, or are dominated by absorption disc features, we only perform the appropriate subset of the above steps. These will be highlighted in the section on the systems in question.

Donor features

If donor features are present, in either emission or absorption lines, the analysis steps are:

- For the donor in emission, a 1-Gaussian is fitted to the phase resolved, emission line profiles. If the signal is too weak to be fitted on top of the double peaked disc features, the mean disc profile is subtracted and the remaining emission component is fitted with a 1-Gaussian as a function of phase. If the emission is still too weak or the S/N too low, the width and peak height of the Gaussian shape are fixed for all phases to the values derived from the mean profile. A radial velocity curve fit solves for $K_{\rm em,RV}$.
- If the donor is present in absorption, 1-Gaussian fits are fitted to (several) individual absorption lines. If the spectral type of the donor is known, a cross correlation is performed between the observed spectrum and a suitable template

spectrum. Both methods are followed by radial velocity curve fits providing $K_{\rm ab,RV}$ and $K_{\rm ab,CC}$, respectively.

- In a Doppler map, the emission spot associated with the donor is fitted with a 2-dimensional Gaussian, using the pick-tool in GAIA[2], to give $K_{\rm em,MEM}$. Note, the error accompanying these values is not the statistical 1σ error but the FWHM/2.35 value provided by GAIA. This value is a measure of the width of the features which is a combination of the intrinsic width, $v \sin i$, the resolution and any centroiding error.

Phase

The phase zero point is defined by the superior conjunction of the white dwarf. We find this phase zero point using several techniques.

- Firstly, we anchor the phase zero point to the ephemeris, if available.
- If the donor is present in either emission or absorption, the phase zero point can be found from the same radial velocity curve fit that provides $K_{\rm em,RV}/K_{\rm ab,RV}/K_{\rm ab,cc}$, as the RV fit simultaneously solves for $\phi_{0,\rm RV}$.
- Donor emission should map to $V_x, V_y = 0, +K_{\rm em}$ in the Doppler map. The angle of rotation needed to place the emission at this location is $\phi_{0,\rm MEM}$.

The latter two values should coincide but as the last measurement is the least influenced by errors introduced by the fitting at of, sometimes noisy, data, we used it to anchor the phase of all data within that epoch (e.g. setting $\phi_0 = \phi_{0,\rm MEM}$). For those few systems with a well determined ephemeris, the phase is initially set using this ephemeris and then checked for deviations. If this does not coincide within 3σ, the phase zero point from the survey data is used instead. If the donor is not detected nor a well defined ephemeris is known from previous studies, the phase is anchored to the first exposure of the data set.

WD

In a small number of cases when both the inclination and the mass accretion rate is low, Mg II is visible at λ4481Å, unblended with the nearby He I line at λ4471Å. As we discussed in Chapters 2 and 4, such features are believed to originate in the WD

[2]Graphical Astronomy and Image Analysis tool: `http://astro.dur.ac.uk/ pdraper/gaia/gaia.html`

atmosphere, and measuring the gravitational redshift provides an independent measure of the WD mass.

Previous studies

If any previous radial velocity studies exist for either the disc or donor features, these are compared at a basic level with the results from the survey.

Systemic velocity

All systems will return several measurement of the systemic velocity (γ), through the various RV and DD fits. In addition, the Doppler maps can be optimised for γ using *optgam* within DOPPLER (see Section 2.3.3). All these measures are listed in Tables 5-10, 5-11 and 5-12 and we will briefly discuss them in Section 5.4.

Let us start by again apologising for the denseness and dryness of the material presented next.

5.3.2 GW Lib

GW Libra has been extensively discussed in Chapters 3 and 4. For comparison purposes only, we replot the average spectra in Figure 5-1, and the RV measurements can be found in Table 5-10[3]. As indicated before, GW Lib does not only show very strong and double peaked disc emission in the Ca II triplet lines, it also reveals the donor star in emission in these lines. In contrast, the Balmer lines are blurred due to the higher intrinsic broadening (see Section 2.5.2). The difference is emphasised in the Doppler maps of the respective lines, see Figure 5-6.

Disc

Due to the low inclination of the system, initially a 1-Gaussian is fitted to the disc profiles in Hβ rather than a 2-Gaussian. The fit is followed by a 2-Gaussian fit with a small separation and by a Diagnostic Diagram ranging the separation from 25 km s^{-1} to 500 km s^{-1} with the FWHM fixed at 4.5Å. The best fit is found for $\Delta v = 300$ km s^{-1}, but we averaged over the stable region $\Delta v = 200 - 400$ km s^{-1} to find $K_{\rm disc,DD} = 15.9 \pm 1.2$, $\gamma = -7.7 \pm 1.4$ km s^{-1} and $\phi_0 = 0.61 \pm 0.01$, relative to the location of the emission in

[3]Figures and numbers presented for GW Lib in this Chapter are given for comparison purposes only and present no new data nor new fits beyond those presented in Chapters 3 and 4.

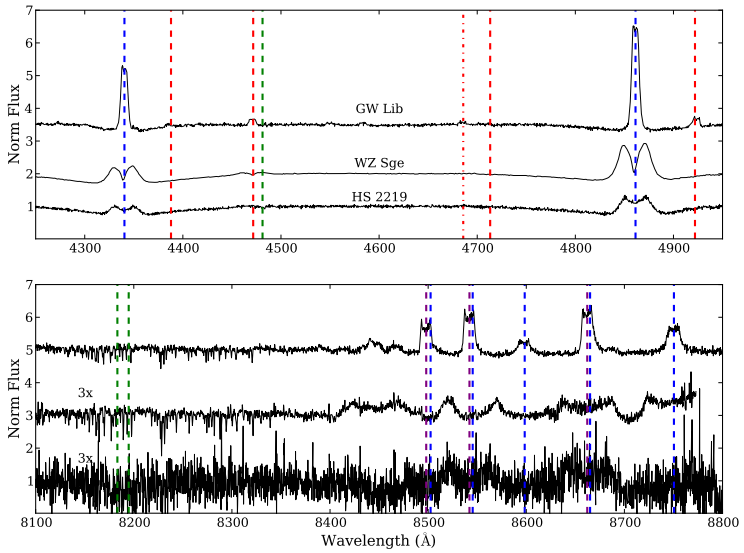

Figure 5-1: The average spectra (top panel blue arm, bottom panel red arm) of GW Lib (top spectrum), WZ Sge (middle spectrum) and HS 2219 (bottom spectrum) during the 2007 WHT campaign. The red spectra of WZ Sge and HS 2219 have been multiplied by a factor of 3 for clarity. The emission/absorption lines are indicated as follows: Blue: Balmer/Paschen. Red: helium I (*dashed*) and helium II (*dashed-dotted*). Purple: calcium II. Green: magnesium II and sodium I.

the Doppler map. Centre of symmetry searches give $K_{\rm disc,MEM} = 11 \pm 7$ km s^{-1} (see also Section 3.4.2).

For the disc lines in the Ca II profile, the DD fit is stable for $\Delta v = 100{-}300$ km s^{-1} and results in $K_{\rm disc,DD} = 15.7 \pm 3.1$ km s^{-1}, $\gamma = 19.0 \pm 2.7$ km s^{-1} and $\phi_0 = 0.65 \pm 0.01$. In the Doppler map, the centre of symmetry is found at $K_{\rm disc,MEM} = 6 \pm 7$ km s^{-1} (Section 3.4.2).

Donor and phase

The emission component associated with the donor can be fitted simultaneously in all three Ca II lines and gives $K_{\rm em} = 82.2 \pm 1.6$ km s^{-1}, $\gamma = -13.1 \pm 1.2$ km s^{-1} and $\phi_0 = 0.00 \pm 0.003$. We locate the emission spot in the Doppler map using a 2-D Gaussian fit to the feature at $K_{\rm em,MEM} = 83 \pm 14$ km s^{-1}, Figure 5-6.

The phase offset is set to the rotation angle required to align the Doppler map ($\phi_0 = 0.00 \pm 0.01$), and is consistent with the phase given by the RV fit to the donor emission.

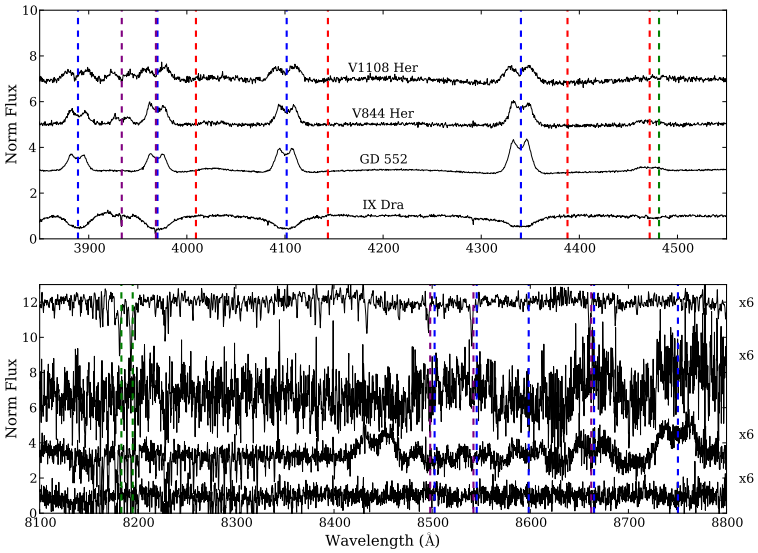

Figure 5-2: The average spectra of V1108 Her, V844 Her, GD 552 and IX Dra (top to bottom). Coloured lines as in Figure 5-1. The red spectra have been multiplied by 6 for clarity and extended bluewards to include the Na I doublet lines, visible in V1108 Her.

WD

1-Gaussian fits to the Mg II absorption line at 4481.21Å in the 2002 archival UVES data gives $K_{\rm wd} = 13 \pm 2$ km s^{-1}, however this is close to the detection limit as the errors on the individual fits are ~ 8 km s^{-1}, see Chapter 4 for an extensive review. Unfortunately, the uncertainty on both the period and ephemeris of GW Lib is substantial and the accumulated error for extrapolation over 5 years is too large to provide an accurate phase zero point for the UVES data set. This prohibits the direct comparison of the phase offset of the Mg II absorption line to the donor phase.

5.3.3 V844 Her

V844 Hercules has a short orbital period of 78.7 minutes, derived from an extensive spectral study (including EW and RV measurements, Thorstensen et al. 2002) after the system returned to quiescence following the 1997 outburst. We observed this system during our August 2009 run (Table 5-6, Figure 5-2).

Disc

The DD method on the Hγ profile returns $K_{\rm disc,DD} = 77.8 \pm 25.4$ km s^{-1}, $\gamma = 4.4 \pm 20.0$ km s^{-1} and $\phi_0 = 0.50 \pm 0.07$. The large error bars are introduced by the scatter in

the individual fits at the different separations. From the Doppler map (Figure 5-6), we find the centre of symmetry at $K_{\rm disc,MEM} = 77 \pm 21$ km s^{-1}, which is in good agreement with $K_{\rm disc,DD}$.

The Ca II lines are too faint to be fitted individually, nor does the DD method give a satisfactory fit. When the data is mapped into velocity space it shows the disc and some emission at the centre of the disc (Figure 5-6). However, this is not visible in the trailed spectra and is most likely an artefact of the low S/N. Inspection of the individual spectral reveals a pixel with a high flux ($\approx 3\sigma$) near the central wavelength in several spectra. A centre of symmetry search returns a physically implausible solution and hence is discarded.

Donor and phase

No donor star emission or absorption is visible in either the Balmer lines or the Ca II triplet lines. Combined with the absence of emission associated with the donor in the Doppler map, the phase zero point is anchored to the start of the observations.

Previous studies

Thorstensen et al. (2002) fit Hα with a double Gaussian with $\Delta v = 800$ km s^{-1} and FWHM = 40Å. Their RV fit gives $\gamma = -38 \pm 8$ km s^{-1} (2σ from our value for γ) and $K_{\rm disc} = 97 \pm 11$ (consistent with our value).

5.3.4 V455 And

V455 Andromeda is also known as HS 2331+3905. At a period of 81 minutes, it is close to the bounce period and exhibits permanent superhumps. Periodic light curve variations suggest a WD spin period at 1.12 minutes (Araujo-Betancor et al., 2005) and the presence of quasi periodic oscillations (QPOs) near 5-6 minutes. However, these features, initially identified as non-radial pulsations (similar to ZZ-Ceti systems) vary in position, number and strength on day-to-day basis (Gänsicke, 2007). The non-detection of molecular bands and the low J, H, and K fluxes imply that this object is a likely candidate for a brown-dwarf donor past the period bounce (Araujo-Betancor et al., 2005).

Hence, it is not unexpected that this object has been the subject of numerous campaigns, both photometric and spectroscopic covering a broad range of wavelengths. We observed V455 And in July 2007 (Table 5-4) pre-outburst, and December 2008 (Table

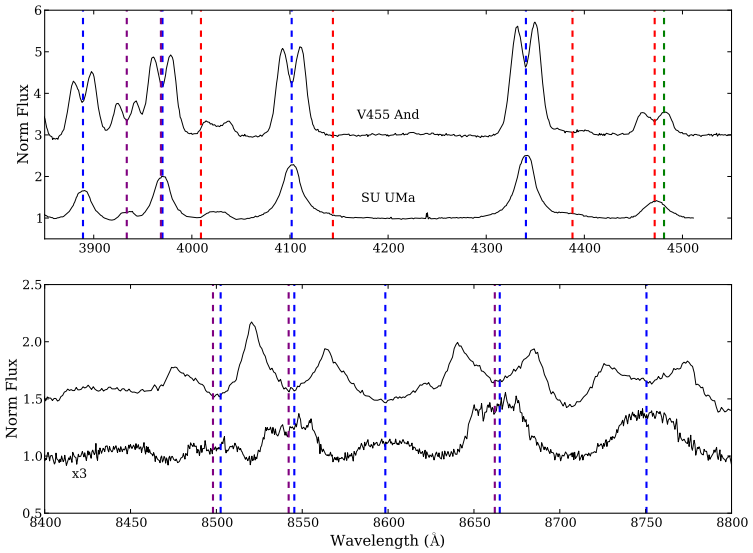

Figure 5-3: The average spectra of V455 And (top spectrum in each panel) and SU UMa (bottom spectrum). The red spectrum of the latter has been multiplied by a factor of 3 for clarity. Coloured lines as in Figure 5-1.

5-5) post-outburst. This offers us a unique insight into the influence of the outburst on the line strengths. We will discuss this in more detail in Chapter 6. For the average post outburst spectra, see Figure 5-3, and the Doppler maps can be found in Figure 5-6.

Disc

The DD method on the Hγ emission profile, returns $K_{\rm disc,DD} = 56.4 \pm 6.3$ km s^{-1}, $\gamma = -17.5 \pm 7.5$ km s^{-1} and $\phi_0 = 0.52 \pm 0.05$. A centre of symmetry search in the post-outburst Doppler map, places the centre of the disc at $K_{\rm disc,MEM} = 48 \pm 13$ km s^{-1}.

Both the pre- and post- outburst red data show Ca II emission, contaminated by the nearby, stronger, Paschen lines. The pre-outburst data has only weak emission and a 2-Gaussian fit does not converge as the hotspot emission dominates the spectral features. The post-outburst data reveals slightly stronger emission lines and the DD method returns $K_{\rm disc,DD} = 44.5 \pm 15.4$ km s^{-1}, $\gamma = 36.8 \pm 6.9$ km s^{-1} and $\phi_0 = 0.57 \pm 0.11$, in agreement with $K_{\rm disc,MEM} = 46 \pm 13$ km s^{-1}.

Donor and phase

No donor emission or absorption is visible, either before or after the outburst, in trailed spectra nor in the Doppler maps. Hence, a phase zero point cannot be determined and

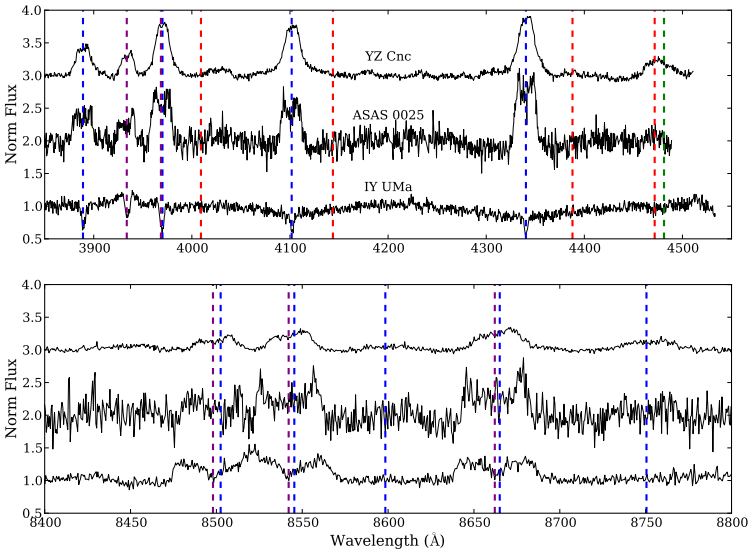

Figure 5-4: The average spectra of YZ Cnc, ASAS 0025 and IY UMa. Coloured lines as in Figure 5-1.

is set to coincide with the first exposure of the data set.

Previous studies

Araujo-Betancor et al. (2005) use the strongest Balmer and He I lines in their spectra and quote a systemic velocity of $\sim$ 1 km s^{-1}, and a radial velocity of $\sim$ 32 km s^{-1}, which is in agreement with our value of $K_{\rm disc}$.

5.3.5 ASAS 0025+1217

ASAS 0025+1217 (hereafter ASAS 0025) has only recently been classified as a DN (Price et al., 2004), but has been catalogued by several surveys, including the Hamburg-Quasar (HS) survey (Hagen et al., 1995) and the ROSAT all-sky survey (Voges et al., 1999). Infra-red spectroscopy is best fitted with a spectral energy distribution (SED) similar to an M9 donor star (Ishioka et al., 2007). This, combined with a short period of 81.4 minutes and a small superhump period excess suggests a small mass ratio ($q \sim 0.054$), hinting that this system is potentially past the minimum period. However, according to Knigge (2006), an M9 is too early a spectral type for a post-bounce system as his semi-empirical donor sequence suggest spectral types later than L for post-bounce systems.

We observed ASAS 0025 in December 2008 (Table 5-5, Figure 5-4), but unfortunately due to bad weather the S/N is rather low and exposure times had to be increased at the

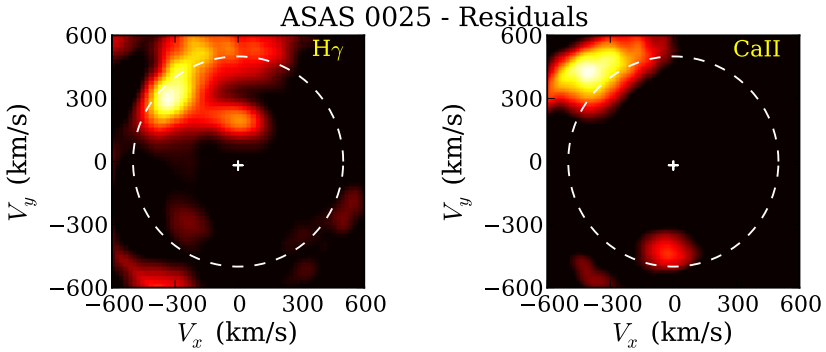

Figure 5-5: **Left:** The Hγ residual map of ASAS 0025 showing the hotspot and emission near the expected location of the donor with $K_{\rm em} \sim 193$ km s^{-1}. **Right:** Ca II residual map, showing the hotspot and remaining emission in anti-phase with the emission in the Hγ maps. The feature has $K_{\rm em} \sim 438$ km s^{-1}. Indicated in both maps is a disc ring, centred on the WD and with a radius of $V_x, V_y \sim 500$ km s^{-1}.

expense of phase resolution.

Disc

The Hγ line combined with the DD method provides $K_{\rm disc,DD} = 22.5 \pm 7.8$ km s^{-1}, $\gamma = -28.9 \pm 1.4$ km s^{-1}and $\phi_0 = 0.58 \pm 0.14$. The Doppler map (Figure 5-6) shows an accretion disc with a strong hotspot. The centre of symmetry is found to be at $K_{\rm disc,MEM} = 18 \pm 13$ km s^{-1}.

The Ca II profiles are too weak to be fitted individually, nor does the DD method provide a viable fit. The Ca II Doppler map shows a similar accretion disc to the Balmer map but with a better defined location for the hotspot. Centre of symmetry measurements, centre the disc at $K_{\rm disc,MEM} = 18 \pm 13$ km s^{-1}.

Donor and phase

Both the Hγ and the Ca II trailed spectra show faint features that could be associated with a donor emission feature. After subtraction of the symmetric disc component in both Doppler maps, residual emission remains in both maps. Each map contains two sources of asymmetrical emission, one most likely associated with the hotspot and one potentially with the donor. For Hγ this latter emission lies at $K_{\rm em,MEM} = 193 \pm 16$ km s^{-1}, and when rotating the map such that this emission locates to $V_x, V_y = 0, +K_{\rm em}$, we find for the potential donor emission in the Ca II map $K_{\rm em,MEM} = -438 \pm 49$ km s^{-1}, see Figure 5-5. As the two possible donor emission spots are at opposite

locations in the Doppler map and have very different values for the radial velocity, it is impossible to associate them both with the donor star.

Both residual maps show emission most likely from the hotspot, which map to the same location when using the same phase offset for both maps. When we rotate the Hγ donor emission to the expected location of the donor, the asymmetrical emission in this map is rotated onto the location of the hotspot, confirming its origin in the hotspot. If the rotate the Ca II by the same rotation angle, the emission associated with the hotspot lands on the same position as for the Hγ map, whereas the Ca II emission associated with the donor is placed at a phase difference of ~ 0.45, too large to be associated with the donor.

The second way to distinguish between the most likely source of donor emission is by comparing the radial velocity of the potential donor emission components to the velocity of the outer disc in the Doppler map. The radial velocity of this ring is ~ 500 km s^{-1}, and plotted in Figure 5-5 as the *dashed* circle. The location of the donor emission spot in Hγ is located at a smaller velocity and well separated from the disc emission. Whereas in the Ca II map, the emission potentially from the donor, is located at velocities similar to those of the disc and the hotspot emission.

Both the large radial velocity component of the emission component in the Ca II map, and the phase offset with the hotspot emission, result in a highly unlikely identification of this emission with donor emission, and it is far more likely to be associated with asymmetries in the disc. Hence, the phase zero point is anchored to the donor emission feature in the Hγ map.

Previous studies

Templeton et al. (2006) fit three Balmer lines (Hα, H*beta* and Hγ) for the radial velocity of the disc and, depending on the line used, find a radial velocity in the range $46 \rightarrow 78$ km s^{-1}, and a systemic velocity in the range of $-36 \rightarrow -110$ km s^{-1}, both these values are larger than the values presented here. Their spectral resolution is 0.6Å in the blue arm and 0.8Å in the red arm, equivalent to ~ 41 km s^{-1} at Hγ and 37 km s^{-1} at Hα, which is larger than our resolution.

5.3.6 WZ Sge

WZ Sagittae is the prototype for the subgroup of DNe that only show very rare super-outbursts on timescales of tens of years. WZ Sge has an orbital period of 81.6 minutes

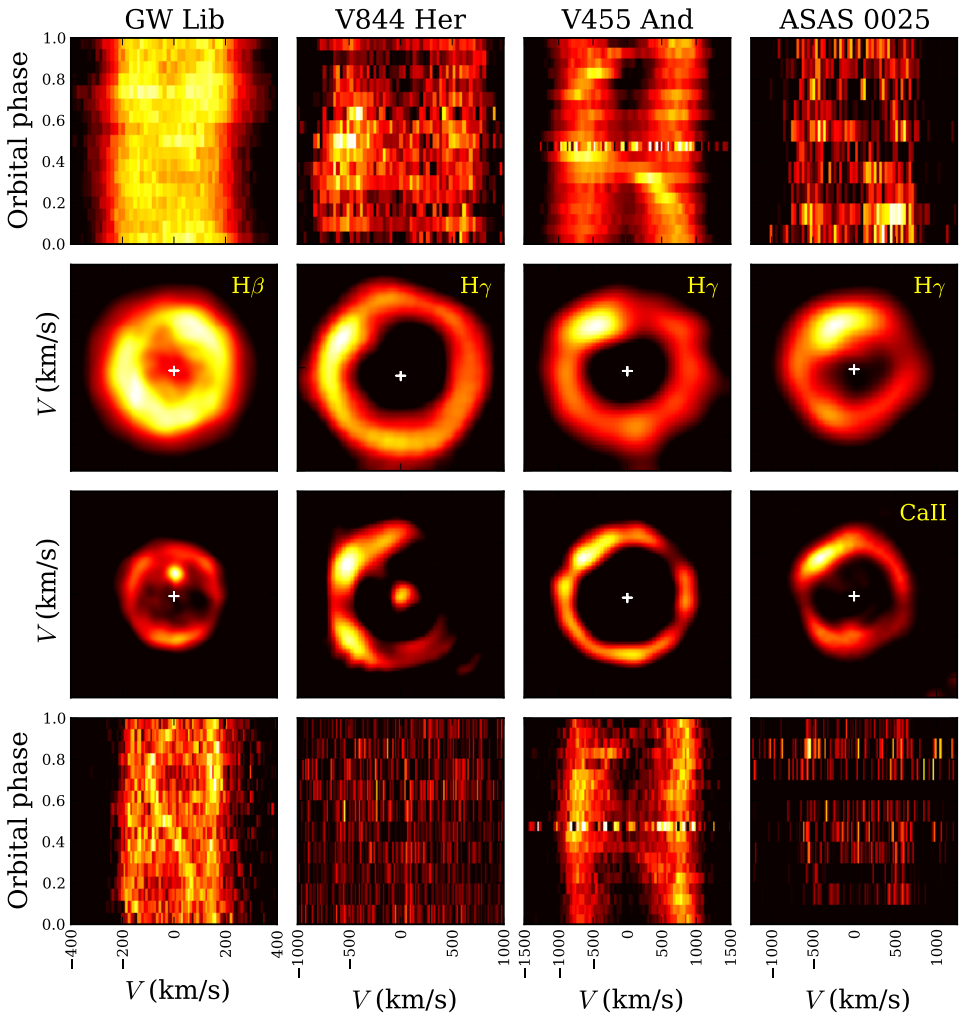

Figure 5-6: Trailed spectra and Doppler maps of the Balmer emission line (top two rows; line as indicated in the map) and the Ca II 8662Å emission line (bottom two rows) for GW Lib, V844 Her, V455 And and ASAS 0025 (left to right). The x-axis scale in each column is different, but kept the same for the entire column as indicated for the Ca II trailed spectra. Each Doppler map is square in V_x and V_y, and the axis are set by the V scale indicated in the bottom Ca II trail. GW Lib reveals a donor spot both in the Ca II trail and the map. V844 Her shows a bright artefact at the centre of the Ca II map due to strong pixels near the central wavelength of he line in the trailed spectra. V455 And shows only disc emission in both maps. ASAS 0025 . The centre of symmetry locations are indicated with a white + in those maps that allowed for a centre of symmetry measurement.

(Patterson et al., 1998), a recurrence time of $\sim$ 30 years, and an outburst amplitude of around 7 mags, reaching almost $V \sim 8.2$ during outburst, and $V \sim 15.5$ during quiescence (Patterson et al., 2002). The parallax distance of WZ Sge is 43.3 parsec (Thorstensen, 2003). WZ Sge is the first CV to provide us with a WD cooling curve after its most recent superoutburst in 2001 (Godon et al., 2004). For single WDs, this decline spans thousands of years, while for accreting WDs it takes only roughly 5 years as only the outer layers are heated during the outburst.

In many respects WZ Sge is the twin of GW Lib. It has a short orbital period, a long recurrence time scale, shows superhump behaviour after outburst and displays narrow absorption features that form in the upper atmosphere of the WD during quiescence (Steeghs et al., 2007). However, the WD in WZ Sge has not revealed any non-radial pulsations, unlike GW Lib. During quiescence, a strong oscillation signal near 28 seconds has been found in many studies (e.g. Patterson et al. 1998, Skidmore et al. 1999). This component is better explained by an oblique rotator model (Warner & Woudt, 2002) rather than by ZZ Ceti like pulsations in the WD. Primarily, as shortly after the 2001 super outburst, a similar feature was seen at 15 seconds (Knigge et al., 2002) when the WD is too hot ($T_{\rm eff} \sim 25\,000$ K, Long et al. 2004) to be near the instability strip ($13\,650 \geq T_{\rm eff} \geq 11\,960$ K, Bergeron et al. 1995).

Even though the system is well studied, it proves difficult to constrain the system parameters. Patterson (2001) argues for $q = 0.045 \pm 0.020$ after combining all previous studies and adding the requirement that $K_1 < 40$ km s^{-1}, however no direct origin for these values is argued by the authors. He continues to use WZ Sge as a calibrator for his $\epsilon(q)$ relation (Patterson et al., 2005). On the other hand, Steeghs et al. (2007) used UV spectroscopy to find $K_{\rm wd} = 47 \pm 3$ km s^{-1} and $v_{\rm grav,wd} = 56 \pm 5$ km s^{-1}, which imply $M_1 = 0.85 \pm 0.04 M_\odot$ and $q = 0.092 \pm 0.008$, when combined with their previously determined value for $495 < K_2 < 585$ km s^{-1} (Steeghs et al., 2001).

We have observed WZ Sge during the July 2007 campaign on three separate nights (see Table 5-4). The spectra show very strong and broad double peaked emission lines from the accretion disc on top of shallow absorption troughs from the WD in the blue arm. The red arm shows broad Paschen lines, blended with Ca II emission, due to the high inclination angle of the system at $i = 77 \pm 2°$ (Steeghs et al., 2007), see Figure 5-1. The three nights of data are phase folded into 50 bins using the ephemeris of Patterson et al. (1998)

$$\mathrm{HJD}_0 = 2437547.72840 + 0.0566878460(3)E. \qquad (5\text{-}1)$$

Disc

The DD method, using Hβ, finds $K_{\rm disc,DD} = 50.6 \pm 16.2$ km s^{-1}, $\gamma = -64.5 \pm 2.54$ km s^{-1} and $\phi_0 = 0.57 \pm 0.07$. Visual inspection of the RV fits suggest that both the 2-Gaussian fit and the DD fit are strongly contaminated by hotspot emission. The Doppler map for this line is given in Figure 5-14 and we find the centre of symmetry at an ever greater radial velocity with $K_{\rm disc,MEM} = 90 \pm 13$ km s^{-1}.

For the Ca II lines, the hotspot feature dominates at all phases, which contaminates the DD method and invalidates the use of a 2-Gaussian RV fit. For the blend of Paschen 13 and the Ca II λ8662Å lines, we constructed a simultaneous map disentangling the two lines, see Figure 5-7. The Ca II map is dominated by the hotspot but shows a feeble disc feature, centred at $K_{\rm disc,MEM} = 48 \pm 13$ km s^{-1}.

Donor

The trailed Ca II spectra reveal a possible signature of the donor star between phases 0.25 - 0.75. The absence of the feature at other phases is expected for a system at high inclination as the donor emission is most probably due to irradiation of the inner hemisphere rather than chromospheric emission and is obscured by the donor star itself around phase zero. The donor star feature is weak compared to the strong hotspot and disc features and proves impossible to fit independently with a 1-Gaussian RV fit. The proposed donor maps towards the position one would expect to occopy in the Doppler map at $K_{\rm em,MEM} = 438 \pm 49$ km s^{-1}.

We isolate the donor star feature by setting the entire map to zero, except for a square box around the feature (Figure 5-7). Next, the trailed spectrum corresponding to this feature can be computed using *comdat*, part of the DOPPLER package. A 1-Gaussian fit to the resulting S-wave gives $\gamma = -67.1 \pm 0.4$ km s^{-1} and $\phi_0 = 0.0400 \pm 0.0002$ and $K_{\rm em} = 402.9 \pm 0.5$ km s^{-1}. The quoted errors are a vast underestimation of the true errors, as contamination with disc and hotspot emission bas been neglegted, and the calculated data assumes an ideal source of emission, remaining constant with phase and at a high S/N.

In Figure 5-7, we show the maps for Ca II, He I, a zoom around the emission from the donor star in Ca II, the original trailed spectra and the computed spectra from the emission spot associated with the donor. The maps are all rotated by a phase angle of 0.04, similar to the phase offset calculated by Steeghs et al. (2001). Plotted on top of these maps are the gas stream and Roche Lobe surfaces for two mass ratio

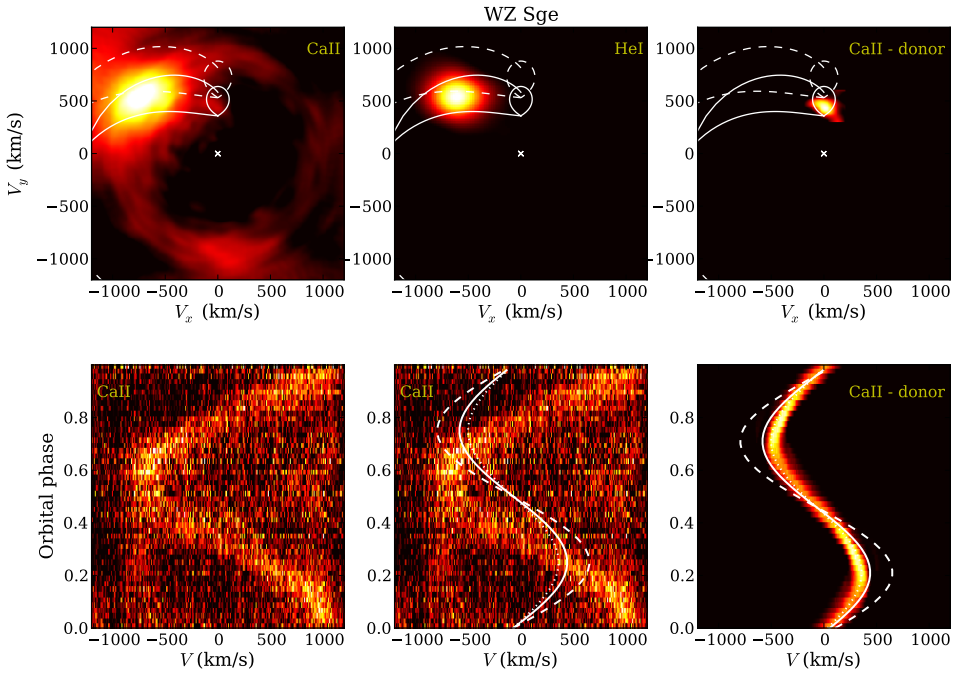

Figure 5-7: From left to right and top to bottom: Doppler map of the Ca II λ8662Å line in WZ Sge (disentangled from the Pa 13 line). Visible are the hotspot, a feeble disc and the donor star in emission. All Doppler maps show the Roche lobe and gas stream for two different values of the mass ratio, fixed to $K_1 = 47$ km s^{-1}: *solid white line* $q = 0.092$, *dashed white line* $q = 0.065$; the He I λ4471Å map shows only a strong hotspot and no disc features; isolated donor emission feature in Ca II; trailed Ca II-Paschen spectra with a clear S-wave from the hotspot and a faint S-wave (only seen at phases 0.3 - 0.6) from the donor star; the same trailed spectra, but with K_2 solutions derived from the mass ratios overplotted: *solid white line* $q = 0.092$, *dashed white line* $q = 0.045$ and the measured $K_{\rm em} = 430$ km s^{-1} (*dotted white line*); computed data from the isolated emission spot with the same RV curves overplotted as in the previous trail.

solutions proposed for the system, anchored on the measured radial velocity for the donor emission.

Phase

As the ephemeris of the system is known to high accuracy, it is used to anchor the phase zero point. Both the RV fit and the angle of rotation of the Doppler map are offset by $\phi = 0.04$, similar to the value seen by Steeghs et al. (2001).

Previous studies

The two most important studies for comparison with our survey are Steeghs et al. (2001) and Steeghs et al. (2007). The former provides a measure of the radial velocity of the donor star as the donor star is irradiated during the 2001 outburst and visible as a narrow emission component on top of the double peaked disc emission in Hα. The best value is determined using a 2D-Gaussian fit to the emission spot in the Doppler map and gives $K_{\rm em} = 495 \pm 2$ km s^{-1}, a higher value than that found in our data. Our values for the systemic velocity all agree to within the error bars, see Table 5-10, and with $\gamma = -72 \pm 2$ km s^{-1} from Steeghs et al. (2001) and references therein.

All measurements for $K_{\rm disc}$ are less than 100 km s^{-1} and congregate around $\sim$ 50 km s^{-1}, close to the measured value for $K_1 = K_{\rm wd} = 47 \pm 3$ km s^{-1} by Steeghs et al. (2007). In the ideal case, the disc traces the movement of the WD around the centre of mass and this seems to be the case with our observations. Further discussion of our measurements and their implications for WZ Sge's system parameters and the comparison between our solution for the mass ratio and the two previously published mass ratios, can be found in Section 7.3.3.

5.3.7 V1108 Her

V1108 Hercules was only discovered in 2004 (Green, 2004) when it went into outburst. The orbital period is 82.1 minutes and SED fitting suggests it has an L1-type companion (Ishioka et al., 2007). Due to time constraints, we observed this system in August 2009 for only 0.6 orbits (Table 5-6).

Disc

The blue spectra show the typical double peaked disc emission line features expected from an accretion disc (Figure 5-2). As no full period has been covered our 2-Gaussian fit

only provides indicative values at $K_{\rm disc,RV} = 111.0 \pm 7.0$ km s^{-1}, $\gamma = -120.4 \pm 6.7$ km s^{-1} and $\phi_0 = 0.88 \pm 0.02$. Unfortunately, as no full phase covering exist, these values are indicative only and no conclusions can be drawn from them, nor can a Doppler map be constructed.

The red spectra shows both the Na I doublet lines (λ8183.27 - 8194.81Å) and the Ca II triplet lines in sharp absorption (Figure 5-2). All of these lines are stationary and have an offset of $\gamma = -65 \pm 5$ km s^{-1} determined from a 1-Gaussian fit to both the individual and combined lines. The origin of these lines is hence more likely to be the interstellar medium rather than the disc or donor.

Donor and phase

As no donor emission is detected nor an ephemeris known, the phase zero point is anchored to the start of observations.

5.3.8 HS 2219+1824

HS 2219 +1824 (hereafter HS 2219) was discovered in the Hamburg-Quasar survey (Hagen et al., 1995). Its orbital period, 86.3 minutes, is derived from light curve variability (Rodríguez-Gil et al., 2005) and is consistent with the spectroscopic line variability. The data of Rodríguez-Gil et al. (2005) show the WD as broad absorption troughs surrounding the Hα disc features, which is a strong indication of a low mass accretion rate. More importantly, superimposed on the double peaked Hα disc emission, is a third emission peak, moving in anti-phase to the disc motion in the trailed spectra. This emission is associated with chromospheric emission from the donor. We observed HS 2219 during the 2007 campaign (see Table 5-4, Figure 5-1) for 4 orbital periods.

Disc

We performed the DD method on the Hγ line and find $K_{\rm disc,DD} = 67.6 \pm 16.7$ km s^{-1}, $\gamma = 4.4 \pm 2.1$ km s^{-1} and $\phi_0 = 0.45 \pm 0.02$. The Doppler map is given in Figure 5-14, the centre of symmetry is at $K_{\rm disc,MEM} = 45 \pm 13$ km s^{-1}.

Unfortunately, the S/N is too low in the Ca II profiles to fit Gaussian profiles to individual spectra. The DD method converges towards a solution at $K_{\rm disc,DD} = 68.2 \pm 18.0$ km s^{-1}, $\gamma = -63.0 \pm 8.9$ km s^{-1} and $\phi_0 = 0.30 \pm 0.02$. The systemic velocity is rather different for Ca II than for Hγ. The Doppler map shows the characteristics of an accretion disc (Figure 5-14), centred on $K_{\rm disc,MEM} = 53 \pm 13$ km s^{-1}.

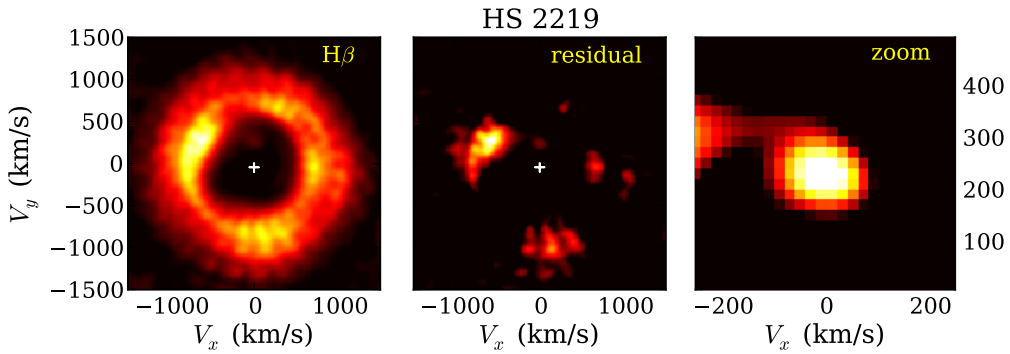

Figure 5-8: **Left:** Hβ Doppler map of HS 2219, some faint emission is visible at $K_{\rm em} \sim 250$ km s^{-1}. **Middle:** Residual map for Hβ, emphasising the presence of weak emission. **Right:** Close-up of the same residual map, showing the residual emission more clearly.

Donor, Phase and previous studies

In analogue with the Hα study performed by Rodríguez-Gil et al. (2005), we performed a thorough analysis of the Hβ emission profile in search of donor star emission. The trailed spectra show weak emission features, which are more clear after subtraction of the average disc profile. The resulting residual spectra are still dominated by hotspot emission and too weak to be fitted with a Gaussian profile. But the residual Doppler map, after subtraction of the symmetric disc emission ring clearly shows a faint emission spot with a radial velocity smaller than the outer edge of the disc (Figure 5-8).

The phase zero point of all data is anchored to the phase which places the emission spot at the expected location of the donor emission in the Doppler map. Both the radial velocity of the donor spot ($K_{\rm em} = 250 \pm 50$ km s^{-1}) and the phase offset $\Delta\phi = 0.44 \pm 0.04$ between the disc and donor features, are consistent with the values of 257 ± 10 km s^{-1} and $\Delta\phi \sim 0.4$ reported by Rodríguez-Gil et al. (2005). Unfortunately, no evidence of the donor is detected in Ca II.

5.3.9 OY Car

OY Carina has a period of 90.9 minutes. The high inclination of $83.3 \pm 0.2°$, allows eclipse mapping to provide robust values for the system parameters: $M_1 = 0.84 \pm 0.04 M_\odot$, $M_2 = 0.086 \pm 0.0004 M_\odot$ and $q = 0.102 \pm 0.003$. These imply $K_1 = 48 \pm 1$ km s^{-1} and $K_2 = 470 \pm 7$ km s^{-1} (Littlefair et al., 2008).

OY Car was observed with the Echelle spectrograph UVES at the VLT in 2001 for 5.2 periods, covering the majority of the optical spectrum at high resolution, see Table 5-3, under UVES Paranal Observatory Project ESO DDT Program ID 266.D-5655. The

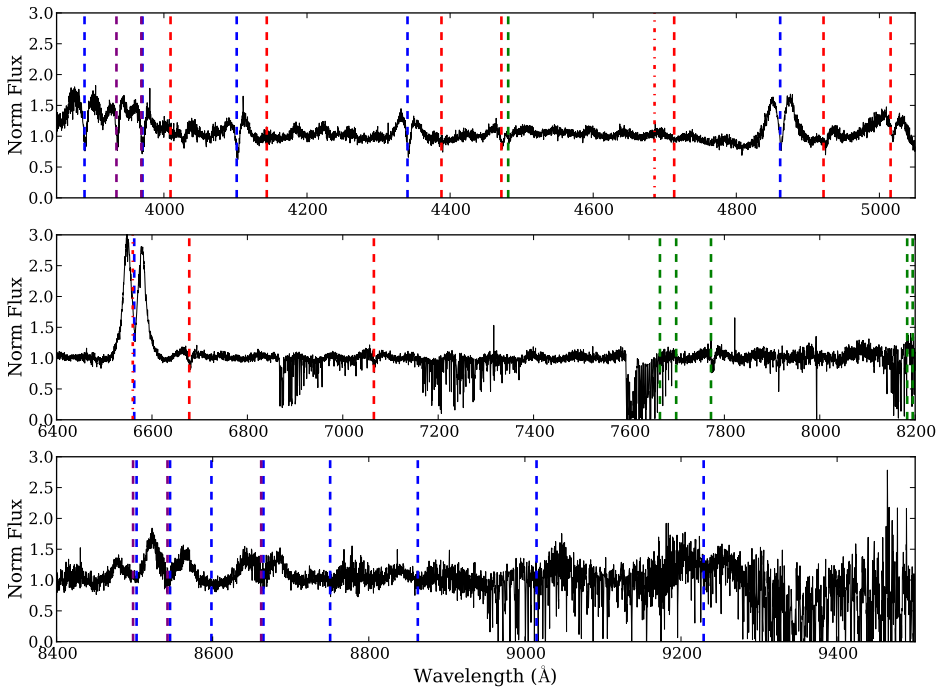

Figure 5-9: The average spectrum of OY Car in 2001 for all 3 arms. Blue: Balmer/Paschen lines. Red: He I (*dashed*) and He II (*dashed-dotted*). Purple: Ca II. Green: Mg II, K I, O I and Na I.

spectra were phase folded onto the ephemeris provided by Wood et al. (1989):

$$\mathrm{HJD}_0 = 2443993.553839(9) + 0.0631209239(12)E. \tag{5-2}$$

Disc

The average spectrum can be found in Figure 5-9. Prominent features are the Balmer double peaked disc emission with V-shaped, central absorption, typical of optically thick disc emission seen in high inclination systems. Similar features are visible in a range of He I lines, in oxygen I (O I) at λ7771.91Å and the Ca II triplet lines.

The trailed spectra (Figure 5-10) show two S-waves on top of the double peaked disc emission in Hα. The first one has a maximum amplitude similar to the strong peaks from the disc emission. The second S-wave has a smaller maximum amplitude, a slight delay in phase, and is only visible between phases 0.15 - 0.75. The first S-wave can be identified with the hotspot, though interestingly it appears to show an 'eclipse' at $\phi \sim 0.37$. We find that the radial velocity fit does not strongly depend on the (fixed)

FWHM of the Gaussian profiles, so these are set to the values given by a completely free fit to the average profile. This gives $K_{\rm disc,DD} = 85.0 \pm 2.6$ km s^{-1}, $\gamma = 57.2 \pm 1.7$ km s^{-1} and $\phi_0 = 0.57 \pm 0.01$. The Doppler map reveals the disc with some asymmetry and a strong hotspot (Figure 5-10). Centre of symmetry searches, including only symmetrical parts of the disc, place the disc centre at $K_{\rm disc,MEM} = 45 \pm 10$ km s^{-1}.

The Ca II emission lines show the double peaked profiles from the accretion disc and trailed spectra reveal the S-wave of both the hotspot and the donor star in emission in all 3 Ca II lines from $\phi \sim 0.16$ to $\phi \sim 0.77$. Fitting the disc profiles of Ca II λ8662Å using the diagnostic diagram method, we find $K_{\rm disc,DD} = 84.9 \pm 6.3$ km s^{-1}, $\gamma = 61.2 \pm 4.2$ km s^{-1} and $\phi_0 = 0.54 \pm 0.04$, in good agreement with the values for Hα (Table 5-10). Centre of symmetry searches, including only the symmetrical parts of the disc, centre the disc at $K_{\rm disc,MEM} = 60 \pm 22$ km s^{-1}.

Due to the high inclination of the system, we do not expect to see the Mg II λ4481Å absorption line from the WD atmosphere (as detected in GW Lib: Chapter 4), as the nearby He I emission line at λ4471Å is expected to be broadened, blending the two lines. However, trailed spectra reveal the central disc absorption at both wavelengths, as well as emission from the hotspot. The trailed spectra also show the central disc absorption in O I λ7771Å along with strong S-wave emission. The origin of these lines is supported by the fact they are in phase with the hotspot emission and central disc absorption seen in both the Ca II and the Balmer lines. The O I feature also shows a 'shadow' component right after the hotspot goes past its maximum redshift. A similar feature was first reported in WZ Sge by Spruit & Rutten (1998).

Donor and phase

Trailed spectra reveal the donor in emission on top of disc and hotspot emission for all three Ca II triplet lines (Figure 5-10). The donor is also visible in emission in Hα but not in any other Balmer lines as the hotspot emission is too strong. In Hα, after subtraction of a symmetric disc, the map reveals an emission feature at the location of the donor star (Figure 5-11) with $K_{\rm em,MEM} = 410 \pm 112$. In Ca II, masking the disc emission lines and removing the central absorption, we fit the donor star emission line with a single Gaussian to the strongest emission profile i.e. Ca II λ8498Å. The best fit to the radial velocity curve gives $K_{\rm em,rv} = 395.3 \pm 1.8$ km s^{-1}, $\gamma = 74.9 \pm 1.8$ km s^{-1} and $\phi_0 = -0.040 \pm 0.001$. Doppler maps reveal this emission feature on the expected location of the donor star (Figure 5-10) and a 2-D Gaussian fit to the donor emission spot locates

it at $K_{\rm em,MEM} = 407 \pm 46$ km s^{-1}.

We carried out telluric correction and constructed an average spectrum in the rest frame of the donor by shifting out its orbital motion. We searched in vain for any donor star absorption features. Littlefair et al. (2008) fitted the eclipse light curve and found $M_2 = 0.086 \pm 0.005 M_\odot$, which, according to Knigge (2006) equals a spectral type in the range M6-9. The absence of absorption features, in combination with a steep drop in S/N in the continuum after λ8800Å, support the idea of a late spectral type for the donor. Remarkably, the telluric correction reveals emission lines at the wavelengths of potassium I (K I), at λ7664.91 Å which has a transition probability of $\log(gf) = 0.135$ and λ7698.98Å which has $\log(gf) = -0.168$[4]. These lines follow the donor emission in Ca II, and Doppler tomography maps them to the same position: $K_{\rm em,MEM} = 410 \pm 45$ km s^{-1} (Figure 5-11).

The phase zero point is fixed to the ephemeris (Equation 5-2), this results in a $\Delta\phi \sim -0.02$ for all emission associated with the donor. We rotate the Doppler maps by this angle to place the emission at the expected location.

Previous studies

As K_1 and K_2 are known from eclipse mapping (Littlefair et al., 2008), OY Car is a benchmark system not only for the $\epsilon(q)$ relationship. But as we know both $K_{\rm em}$ and K_2, we can try to understand the K-correction, which is one of the most crucial steps in using Ca II for measuring q. An additional constraint is added by the presence of K in emission. This discussion goes beyond the scope of the present Chapter and OY Car's use as a calibrator is presented in Section 7.3.3.

5.3.10 V632 Cyg

V632 Cygnus was classified as a variable star by Hoffmeister (1949). Sheets et al. (2007) report an orbital period of 91.8 minutes, derived from radial velocity measurements to Hα. The superhump period was determined by Kato et al. (2009) following the 2008 outburst. We observed V632 Cyg in August 2009 for only ∼0.5 orbital periods due to timing constraints (Table 5-6, Figure 5-13).

[4]Data from The Atomic Line List Version 2.04: `http://www.pa.uky.edu/~peter/atomic/`

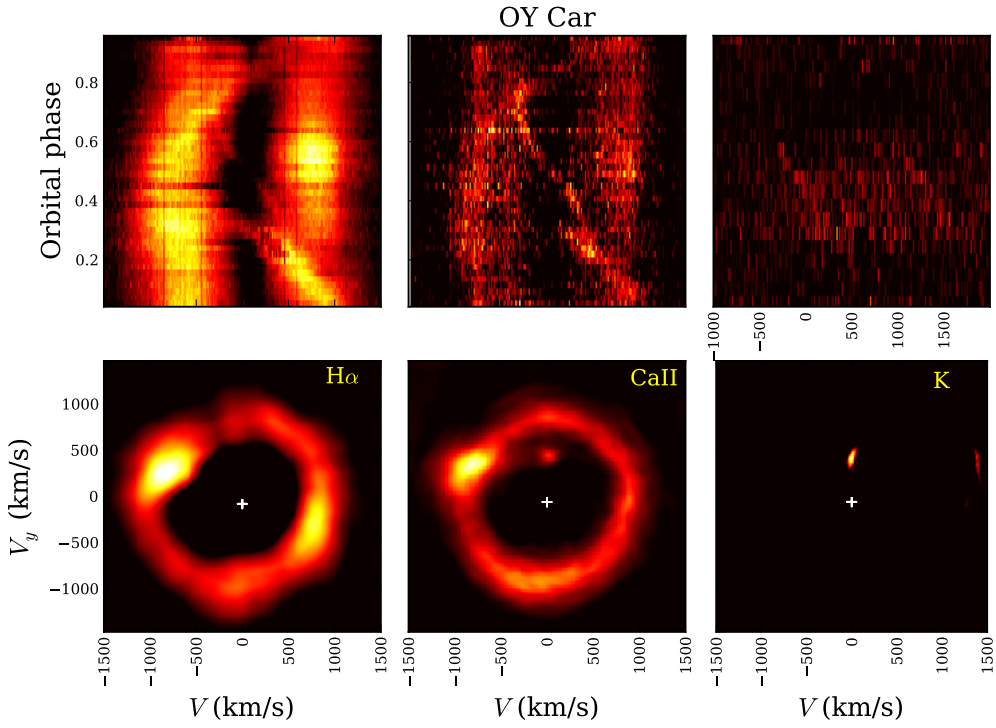

Figure 5-10: Left to right, top row: Hα trail showing the disc, hotspot and potentially some emission from the donor star; Ca II trail showing the disc, the hotspot and the donor; Potassium I (K) trail, after subtraction of the telluric lines, some emission is visible just above the noise level in both K lines and suggest a donor related origin as the S-wave is similar to the donor emission S-wave in Ca II. The bottom row shows the respective Doppler maps and shows that the K I donor emission feature does indeed map to the same location as the donor emission in Ca II. See also Figure 5-11.

Disc

Due to insufficient phase coverage and poor S/N, we cannot perform the radial velocity measurements as we have done for other objects. However, both the Balmer and Ca II profiles do show the double peaked disc profiles associated with a disc.

Donor

After subtraction of the average Ca II profile, some Ca II emission remains and resembles the signature of an irradiated donor star. Regrettably, this can not be confirmed due to the inadequate phase covering to construct a Doppler map, but it does suggest that V632 Cyg is a good target for follow-up observations.

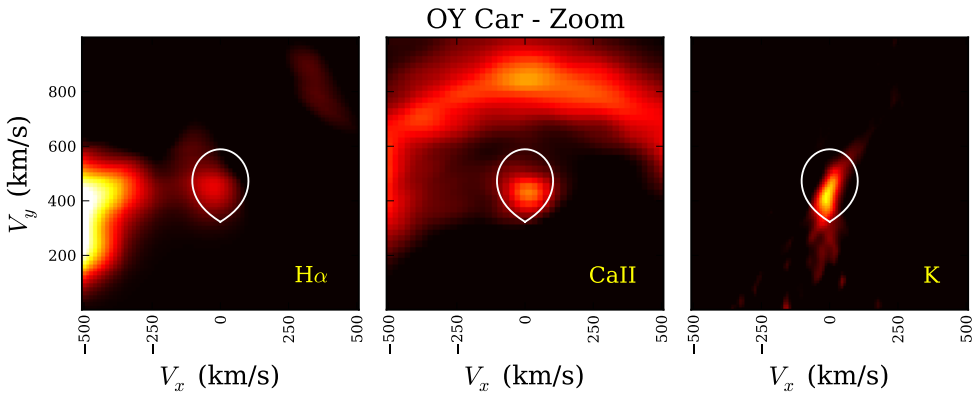

Figure 5-11: Zoom of the Doppler maps of Hα (left), Ca II (middle) and K I (right) in OY Car. The Ca II map is constructed from the original data, whereas the Hα map has had a symmetric disc subtracted. At the position of the donor star emission in the Ca II map, we see emission in the Hα map, as suggested by the Hα trailed spectra in Figure 5-10. The K I map also reveals an emission spot at the same position as the Ca II spot, after careful subtraction of the telluric lines. Over plotted is the Roche lobe from the eclipse solution (Littlefair et al., 2008).

5.3.11 UV Per

UV Perseus has been know as a variable object since 1911 (D'Esterre, 1913) but, despite its short orbital period (93.5 ±0.2 minutes; Thorstensen & Taylor 1997) and relative brightness (V∼ 17.9), it has received little observational attention. We observed UV Per on two occasions. December 2008 (Table 5-5) was unfortunately governed by bad weather but revealed promising strong Ca II triplet lines similar to the spectrum of GW Lib. Based on this succes, we re-observed UV Per in August 2009 (Table 5-6). We phase binned both data sets using variance weights, as no notable changes were discovered between the two data sets (Figure 5-13).

Disc

Using the standard recipe for fitting the disc lines in Hγ, we find $K_{\rm disc,DD} = 31.2 \pm 2.8$ km s^{-1}, $\gamma = 14.2 \pm 8.1$ km s^{-1} and $\phi_0 = 0.57 \pm 0.01$. Due to the low inclination, the individual disc profiles are very narrow. Figure 5-14 shows the Doppler map containing a doughnut shaped disc ring. From a centre of symmetry search, we find $K_{\rm disc,MEM} = 44 \pm 7$ km s^{-1}.

The Ca II map gives $K_{\rm disc,DD} = 21.5 \pm 3.2$ km s^{-1}, $\gamma = 37.1 \pm 6.0$ km s^{-1} and $\phi_0 = 0.54 \pm 0.01$. The data maps into a ring (Figure 5-14) with a centre of symmetry of $K_{\rm disc,MEM} = 30 \pm 4$ km s^{-1}.

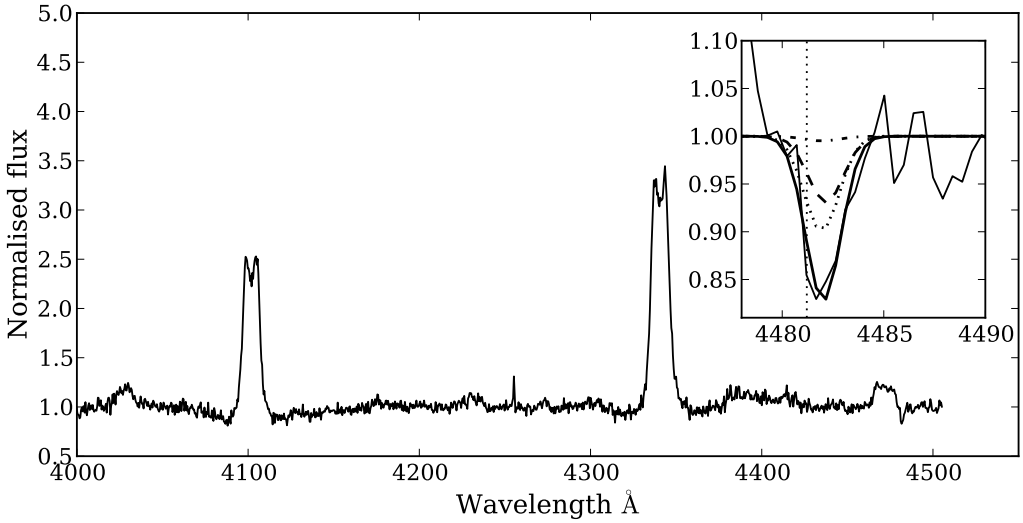

Figure 5-12: Average spectrum of UV Per. The inset shows the Mg II absorption line averaged over 1 orbital period with the final Gaussian fit. The total fit (*thick solid line*) is the sum of three separate fits to the triplet lines, each weighted by their own transition probabilities: λ4481.126Å (*dotted*), λ4481.150Å (*dotted-dashed*), λ4481.325Å (*dashed*). The dotted vertical line denotes the rest wavelength of Mg II at λ4481.21Å.

Donor and phase

After subtraction of the average disc profile from the Ca II profile, we fit the remaining emission component with a 1-Gaussian to find $K_{\rm em,RV} = 103.3 \pm 1.6$ km s^{-1}, $\gamma = -2.4 \pm 1.1$ km s^{-1} and $\phi_0 = -0.012 \pm 0.002$. This feature maps onto the expected location of the donor star in the Doppler map ($K_{\rm em,MEM} = 111 \pm 37$ km s^{-1}). The presence of the donor in emission allows us to anchor the phase zero point to the inferior conjunction of the white dwarf by the secondary star.

Previous studies

Thorstensen & Taylor (1997) find $K = 29 \pm 4$ km s^{-1} by fitting Hα, which is consistent with our findings.

WD

UV Per reveals Mg II in absorption at 4481.21Å, similar to GW Lib, see Figure 5-12. A measure on the phase averaged profile gives a redshift of 0.79 ± 0.13Å which is equivalent to 54.6 ± 7.6 km s^{-1}. However, the measured offset is below the resolution of the data at 0.88Å and higher resolution spectra are required to resolve this feature.

The feature also proves too weak to be fitted as a function of phase, prohibiting the

determination of its phase dependence and its phase offset with the donor feature. This latter is a crucial measurement as the $\Delta\phi$ between WD and donor has to be 0.5 in order to positively identify the WD atmosphere as the origin of the absorption feature. Hence, UV Per is a good candidate for follow up high-resolution, time-resolved spectroscopy simultaneously covering the Ca II triplet and the Mg II lines.

5.3.12 IX Dra

IX Draco is an active object, with an outburst recurrence time of only 3.1 days and a superoutburst every $\sim$ 54 days. It has an orbital period of 95.7 minutes (Olech et al., 2004). The period excess suggests a very low mass ratio of $q \sim 0.047$ which, even with a relatively massive WD, would imply a brown dwarf donor. IR spectroscopic SED fittings are inconclusive as no typical features of late type dwarfs are visible (Ishioka et al., 2007). On the other hand, it is highly unlikely that this CV harbours a brown dwarf donor as the very short outburst cycle indicates a high mass transfer rate, which is not expected for short period CVs just above or below the period bounce (Chapter 1).

We observed IX Dra in August 2009 for a full orbital period (Table 5-6). Our spectra are dominated by optically thick absorption lines in the Balmer series, and the red spectra are featureless, indicating we caught IX Dra in outburst (Figure 5-2). Therefore no further analysis is done.

5.3.13 TY Psc

Thorstensen et al. (1996) report a photometrically determined orbital period of 98.4 minutes, consistent with the spectroscopic modulation for TY Pisces. It has a recurrence time scale of 11–35 days and a superoutburst cycle of ∼370 days (Szkody, 1987). We observed TY Psc both in December 2008 and August 2009 (Tables 5-5, 5-6) and both datasets have been combined using variance weights as no notable changes were discovered between the two data sets (Figure 5-13).

Disc

We fit the disc profile in Hγ using the DD method, returning $K_{\rm disc,DD} = 76.5 \pm 4.1$ km s^{-1}, $\gamma = 0.5 \pm 17.0$ km s^{-1} and $\phi_0 = 0.53 \pm 0.02$. A centre of symmetry search gives $K_{\rm disc,MEM} = 100 \pm 18$ km s^{-1} (Figure 5-14).

For the Ca II lines, the DD method returns $K_{\rm disc,DD} = 93.0 \pm 1.9$ km s^{-1}, $\gamma =$

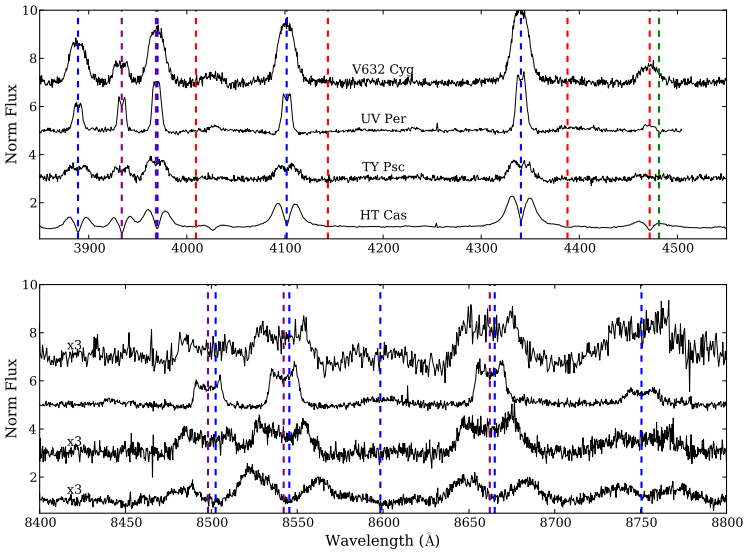

Figure 5-13: The average spectra of V632 Cyg, UV Per, TY Psc and HT Cas. Coloured lines as in Figure 5-1. The red spectra of all but UV Per have been multiplied by 3 for clarity.

5.9 ± 14.8 km s^{-1} and $\phi_0 = 0.51 \pm 0.01$. The location of the centre of symmetry is at $K_{\rm disc,MEM} = 42 \pm 7$ km s^{-1}.

Donor and phase

Trailed spectra reveal a third emission line superimposed on the Ca II disc profiles, similar to previously detected donor features. However, the feature is too weak to fit with a single Gaussian, even after subtraction of the average profile. When constructing a map from the Ca II data, we find that the emission is located at the expected position of the donor star, confirming the donor as the origin of the emission. A 2-D Gaussian fit to the emission feature in the map gives $K_{\rm em,MEM} = 230 \pm 48$ km s^{-1}. The phase zero point for this data is anchored to the phase zero point determined by the location of the donor emission in the Ca II Doppler map.

Previous studies

Thorstensen et al. (1996) find $K_{\rm disc} = 53 \pm 5$ km s^{-1} and $\gamma = -29 \pm 4$ km s^{-1}, using the DD method on Hα. These values do not comply with our RV measurements, but are close to our $K_{\rm disc,MEM}$ in Ca II.

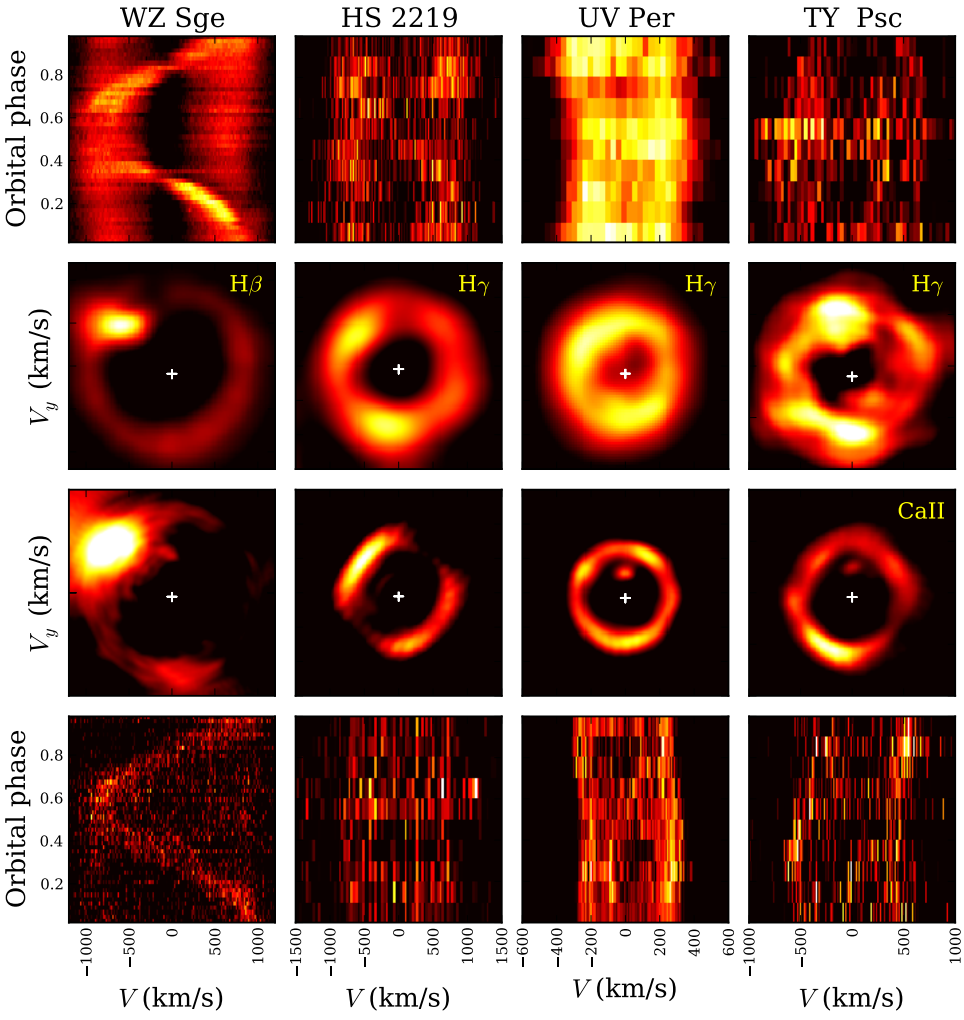

Figure 5-14: Trailed spectra and Doppler maps of the Balmer (top two rows) and Ca II (bottom two rows) emission lines in WZ Sge, HS 2219 (after outburst), UV Per and TY Psc (left to right). The centre of symmetry for each map is indicated with a white +. The x-axis scale in each column is different, but kept the same for the entire column as indicated for the Ca II trailed spectra. Each Doppler map is square in V_x and V_y, and the axis are set by the V scale indicated in the bottom Ca II trail. All but HS 2219 show the donor star in the Ca II trail and the maps.

5.3.14 GD 552

GD 552 is a high proper motion binary with double peaked emission characteristic of a disc and an orbital period of 102.7 minutes. No outburst has been detected during the past decade of monitoring. Previous spectroscopic searches for a near main sequence companion star in the I-band have been unsuccessful and Unda-Sanzana et al. (2008a) conclude that either the system has already passed through the period minimum and harbours a brown dwarf donor or that the system was formed with a brown dwarf donor in the first place. The latter would explain the absence of outbursts, the low orbital velocity of the white dwarf and the system's low luminosity. Archival spectra from Unda-Sanzana et al. (2008a) show strong features in the I-band, near the Ca II lines, but no time-resolved data is available. Based on the presence of these strong features, we observed GD 552 in August 2009 (Table 5-6, Figure 5-2).

Disc

The trailed spectra show a typical double peaked signature from the disc with a very strong S-wave in Hγ. As this wave extends its velocity as far as the disc lines, it is most likely the hotspot. We fit the profiles with a triple Gaussian to minimise the impact of the hotspot location on the disc profile fits. The first two Gaussians have a common offset, a fixed common FWHM and a common peak value free to vary, to fit the double peaked disc emission. The third Gaussian is to fit the remaining peak independently and has all three parameters variable. The 2-Gaussian fit returns $K_{\rm disc,RV} = 19.0 \pm 4.3$ km s^{-1}, $\gamma = -55.9 \pm 4.0$ km s^{-1} and $\phi_0 = 0.04 \pm 0.06$. The hotspot emission is strong and dominates even at large Gaussian separations, as even the DD method returns $K_{\rm disc,DD} = 56.9 \pm 14.6$ km s^{-1}. The Doppler map (Figure 5-15) confirms this and shows a disc with a very strong hotspot. The centre of symmetry, excluding the location of the hotspot, gives $K_{\rm disc,mem} = 45 \pm 13$ km s^{-1}.

The S/N in the Ca II profiles is too low to fit the profiles independently. However, the blue spectra show the absence of Ca K. This suggests that the Ca II triplet profiles are actually dominated by Paschen lines. Hence, we constructed a Doppler map centred on Paschen 13 rather than Ca II. This map reveals a feeble disc and a hotspot at the same location as the Balmer map (Figure 5-15).

Donor and phase

As no donor star is detected, we set the phase zero point to coincide with the start of observations. For visual consistency, we rotate the maps by $\Delta\phi \sim 0.4$, such that the hotspot emission is located in the upper left corner.

Previous studies

Hessman & Hopp (1990) find $K_{\rm disc} = 17 \pm 4$ km s^{-1} from Hα. Unda-Sanzana et al. (2008a) confirm this measurement and place an upper limit on $M_2 < 0.08$M$_\odot$ by failing to detect donor emission in deep I-band spectroscopy. Combining this with the average mass for a WD ($M_{\rm wd} \sim 0.75$M$_\odot$; Knigge 2006) results in a soft upper limit for the mass ratio of $q < 0.11$.

5.3.15 IY UMa

IY Ursa Majoris was not classified as a DN until 2000, when it went into superoutburst. With a period of 106.4 minutes it sits somewhat further away from the period bounce than other systems within this survey. Steeghs et al. (2003) report $M_1 = 0.79 \pm 0.04 M_\odot$ and $M_2 = 0.10 \pm 0.01 M_\odot$, corresponding to a mass ratio of $q = 0.125 \pm 0.008$, derived from eclipse mapping. The white dwarf eclipse width implies $i = 86.0 \pm 1°$. This mass ratio is used by Patterson as a calibrator for his $\epsilon(q)$ relation (Patterson et al. 2000, 2005, Patterson 2001). We observed IY UMa on two consecutive nights in December 2008 (Table 5-5, Figure 5-4) and the phase zero is set to the ephemeris defined by Steeghs et al. (2003):

$$\mathrm{HJD}_0 = 2451570.85376(2) + 0.07390897(5)E. \qquad (5\text{-}3)$$

Disc

The blue spectrum does not show the double peaked disc emission line profiles we expected from CVs in quiescence, but instead shows narrow Balmer absorption lines superimposed onto the broader WD absorption lines (Figure 5-4). This resembles the central absorption from a disc seen nearly edge on, which is supported by the high inclination angle i. We fit the narrow features with a single Gaussian as a function of the orbital phase and find $K_{\rm disc,RV} = 89.7 \pm 9.9$ km s^{-1}, $\gamma = 46.1 \pm 8.1$ km s^{-1} and $\phi_0 = 0.55 \pm 0.02$. In Figure 5-15, we plot the inverted trail (where absorption is light coloured and emission is dark) and as Doppler tomography can only be applied correctly to optically thin emission, we construct no map.

The Ca II triplet lines display a double peaked profile and the DD method returns $K_{\rm disc,DD} = 121.2 \pm 20.2$ km s^{-1}, $\gamma = 70.4 \pm 12.2$ km s^{-1} and $\phi_0 = 0.53 \pm 0.03$. A centre of symmetry analysis places the disc at $K_{\rm disc,MEM} = 63 \pm 10$ km s^{-1}.

Donor and phase

A donor S-wave appears to be present during phases $0.25 - 0.75$, after subtraction of the average disc profile, as the donor emission is self-obscured for the remaining phases due to the high inclination. A single Gaussian fit to the residuals gives $K_{\rm em} = 304.2 \pm 18.3$ km s^{-1}, $\gamma = -56.6 \pm 16.9$ km s^{-1} and $\phi_0 = -0.02 \pm 0.02$. A 2-D Gaussian fit to the emission spot in the Doppler map gives $K_{\rm em,MEM} = 383 \pm 120$ km s^{-1}. After we fix the phase to the ephemeris (Equation 5-3), we require a marginally significant phase offset of $\Delta\phi = -0.05 \pm 0.01$ to place the emission at the expected location of the donor in the Doppler map.

Previous studies

(Rolfe et al., 2002) find limits on the radial velocity of the donor star ($380 < K_2 < 540$ km s^{-1}) by cross correlating the Na I absorption doublet with an M4 star spectrum. Unfortunately, our red data does not stretch this far blue wards, hence we cannot confirm the presence of these lines. We will use IY UMa as a calibrator for our method to determine the mass ratio using the Ca II profiles, subject to a K-correction (Section 7.3.3).

5.3.16 HT Cas

HT Cassiopeia has a period of 106.1 minutes and a parallax/proper motion determined distance of $d = 131^{+22}_{-17}$parsec (Thorstensen et al., 2008). Due to its high inclination ($i = 81 \pm 1°$) the lightcurve shows eclipses which can be fitted to obtain $M_1 = 0.61 \pm 0.04 M_\odot$ and $M_2 = 0.09 \pm 0.02 M_\odot$ (Horne et al., 1991). The donor star is visible in absorption with a spectral type of M5.4 $\pm$ 0.3 and a radial velocity of $K_2 = 460 \pm 25$ km s^{-1} determined from Na I absorption lines (corrected from $K_{\rm abs}$; Marsh 1990). We observed HT Cas for 2 full periods in August 2009 (Table 5-6, Figure 5-13).

Disc

The double peaked Balmer emission lines show the characteristic disc profiles for an optically thick disc with V-shaped central absorption. The Hγ profiles give $K_{\rm disc,DD} =$

96.3 ± 6.7 km s^{-1}, $\gamma = 0.6 \pm 7.0$ km s^{-1} and $\phi_0 = 0.62 \pm 0.01$. The Doppler map shows an irregular shaped accretion disc and the centre of symmetry can be placed at $K_{\rm disc,MEM} = 42 \pm 13$ km s^{-1} (Figure 5-15).

The Ca II disc profiles yield $K_{\rm disc,DD} = 90.2 \pm 2.4$ km s^{-1}, $\gamma = 45.2 \pm 1.0$ km s^{-1} and $\phi_0 = 0.60 \pm 0.005$. The Doppler map provides us with a measure of the centre of symmetry at $K_{\rm disc,MEM} = 86 \pm 14$ km s^{-1}.

Donor and phase

The trailed spectra for the Ca II triplet lines show a third emission component, visible only during phases $0.2-0.8$. After subtraction of the average profile, we fit this emission line with a single Gaussian, and the RV fit returns $K_{\rm em,RV} = 344.4 \pm 4.7$ km s^{-1}, $\gamma = 25.1 \pm 5.2$ km s^{-1} and $\phi_0 = -0.021 \pm 0.004$. The location of the emission spot in the Doppler map is $K_{\rm em,MEM} = 351 \pm 58$ km s^{-1}. The phase zero point for the data set is anchored to the rotation angle needed to place the emission at the expected location in the Doppler map.

Previous studies

The previous radial velocity determined from the absorption lines from the donor is larger than the radial velocity found for the emission component, which is as expected (Figure 2-10). Due to the system parameters found via eclipse mapping, HT Cas is of importance fur use as a calibrator for the Ca II method, which will be discussed in greater depth in Section 7.3.3.

5.3.17 SU UMa

The prototype of the DNe with super-outbursts is SU Ursa Major is(Section 1.3). SU UMa is bright (V$\sim$ 14.2) and has a long period (109.9 minutes). Even though SU UMa is the prototype of its class, it has received little observational interest over the years. Archival spectra show strong Ca II features (Marsh & Dhillon, 1997), hence we obtained time-resolved spectra in December 2008 (Table 5-5, Figure 5-3).

Disc

The Hγ emission profile gives $K_{\rm disc,DD} = 39.9 \pm 2.6$ km s^{-1}, $\gamma = -8.4 \pm 1.9$ km s^{-1} and $\phi_0 = 0.60 \pm 0.01$. As the Doppler map of this feature does not resemble the standard

disc ring, it is not strange to find that the centre of symmetry search does not converge on a sensible solution (Figure 5-15).

The much cleaner Ca II disc profiles, return $K_{\rm disc,DD} = 43.7 \pm 12.5$ km s^{-1}, $\gamma = 115.7 \pm 13.4$ km s^{-1} and $\phi_0 = 0.44 \pm 0.06$, and the disc is centred in the Doppler map at $K_{\rm disc,MEM} = 31 \pm 15$ km s^{-1}.

Donor and phase

We subtracted the average Ca II disc profile to reveal an emission line moving in anti-phase to the disc profile. We fit the residuals with a 1-Gaussian and find $K_{\rm em,RV} = 206.8 \pm 4.8$ km s^{-1}, $\gamma = 10.9 \pm 3.8$ km s^{-1} and $\phi_0 = 0.003 \pm 0.005$. This feature maps to the location of the donor star at $K_{\rm em,MEM} = 211 \pm 75$ km s^{-1}, after setting the phase zero point such that the emission lands at the expected location.

The difference between the systemic velocity measured from the Ca II disc emission and from the donor emission is $\sim$ 100 km s^{-1}, and equals the offset expected when fitting Pa 13 as Ca II. This implies that the disc features are dominated by Paschen emission rather than calcium emission.

Previous studies

Thorstensen et al. (1986) find $K_{\rm disc} = 59 \pm 7$ and $\gamma = 27 \pm 5$ km s^{-1} via RV fits to Hα in emission, which is within 2σ of the value we find for $K_{\rm disc}$.

5.3.18 YZ Cnc

YZ Cancri is a bright CV with a quiescent magnitude of V$\sim$ 14.5 and was classified as a SU UMa type DNe after superhumps were detected in 1979 (Patterson, 1979). It has one of the shortest recurrence timescale sof $\sim$12 days for normal outbursts (Szkody & Mattei, 1984) and an orbital period of 125.0 minutes (Shafter & Hessman, 1988).

The only time-resolved spectroscopic study available is presented by Shafter & Hessman (1988), but due to the absence of the donor star in either emission or absorption, and the absence of eclipses, the mass ratio is inferred from the Half Width at Zero Intensity (HWZI) of Hα combined with the constraints on the inclination and results in $q \sim 0.22$. However, this value is strongly based upon the assumption that $M_2 = 0.17 M_\odot$ (not justified by Shafter & Hessman 1988), and results in a WD mass of $M_1 = 0.75 - 0.9 M_\odot$ and an inclination $i = 35 - 40°$. We observed YZ Cnc in December 2008 (Table 5-5, Figure 5-4).

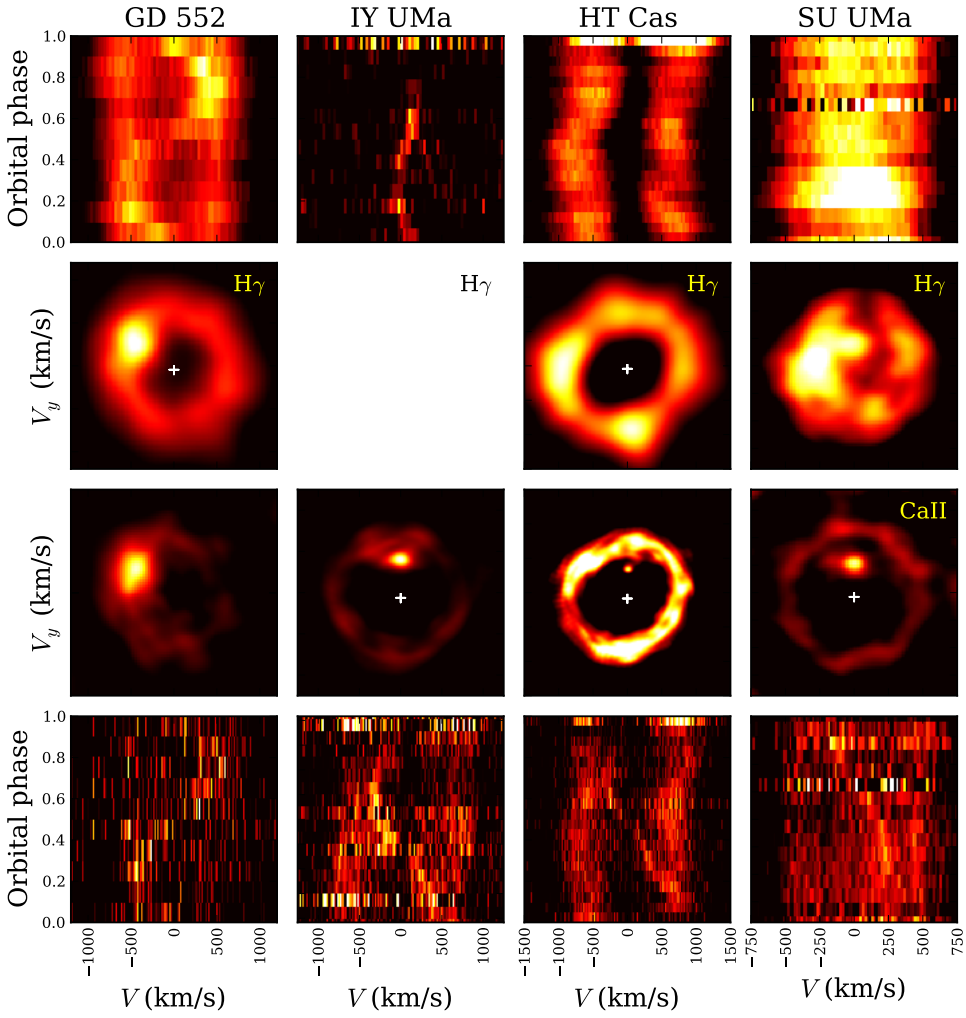

Figure 5-15: Trails and maps of Balmer (top two rows) and Ca II (bottom two rows) for GD 552, IY UMa, HT Cas and SU UMa (left to right columns). The centre of symmetry measures are indicated with a white +. The x-axis scale in each column is different, but kept the same for the entire column as indicated for the Ca II trailed spectra. Each Doppler map is square in V_x and V_y, and the axis are set by the V scale indicated in the bottom Ca II trail. All but GD 552 show the donor star in the trail and the maps. The red map for GD 552 is constructed on Paschen 13, rather than Ca II. The Balmer trail of IY UMa is inverted, i.e. the narrow central absorption is red and the continuum is black, no Doppler map is constructed for this line.

Disc

The DD method on the Hγ profiles give $K_{\rm disc,DD} = 31.8 \pm 1.9$ km s^{-1}, $\gamma = 50.8 \pm 4.2$ km s^{-1} and $\phi_0 = 0.52 \pm 0.01$. The small separation of the peaks results in a blurred disc in the Doppler map, which prohibits a centre of symmetry search, see Figure 5-18.

The Ca II disc profiles return $K_{\rm disc,DD} = 87.7 \pm 42.5$ km s^{-1}, $\gamma = 95.7 \pm 22.2$ km s^{-1} and $\phi_0 = 0.58 \pm 0.06$. The search for the centre of symmetry does not converge on a solution.

Donor and phase

After subtraction of the average profile from the Ca II line, a single Gaussian fit between phases $0.2 - 0.9$ gives $K_{\rm em,RV} = 145.5 \pm 1.9$ km s^{-1}, $\gamma = 45.4 \pm 2.0$ km s^{-1} and $\phi_0 = -0.004 \pm 0.002$. The donor emission in the Doppler map is only visible after mapping the residuals. This locates the emission at $K_{\rm em,MEM} = 160 \pm 70$ km s^{-1} and the phase zero point is locked to this position.

Previous studies

Shafter & Hessman (1988) measured $K_{\rm disc} = 50 \pm 20$ km s^{-1} and $\gamma \sim 20$ km s^{-1} by combining DD measures of Hα and He I λ5876Å.

5.3.19 IP Peg

IP Pegasus is a well studied system, and part of the U Gem group as it shows no stand stills (Z Cam systems) or superoutbursts (SU UMa systems, Section 1.3). The short outburst recurrence time scale ($\sim$ 95 days), makes IP Peg an ideal system to study the effects of the outburst on the accretion disc morphology. It was in this system that Steeghs et al. (1997) discovered the predicted spiral density waves for the first time. IP Peg has a long orbital period of 227.8 minutes and the donor star has a spectral type of M3-4/5. The high inclination (83.8°) causes eclipses, enabling the system parameters to be determined: $M_1 = 1.16 \pm 0.02 {\rm M}_\odot$, $M_2 = 0.55 \pm 0.02 {\rm M}_\odot$, $q = 0.48 \pm 0.01$, $K_1 = 151 \pm 3$ km s^{-1} and $K_2 = 317 \pm 2$ km s^{-1} (Copperwheat et al., 2010). The ephemeris for IP Peg is set to the value determined by Copperwheat et al. (2010):

$$\text{BMJD(TDB)} = 53594.206270(1) + 0.1582061029(3)E \tag{5-4}$$

For the accuracies required in this work, we convert the Modified Julian Date on the Barycentric Dynamical Timescale (BMJD(TDB)) into Helicentric Julian Date (HJD) by

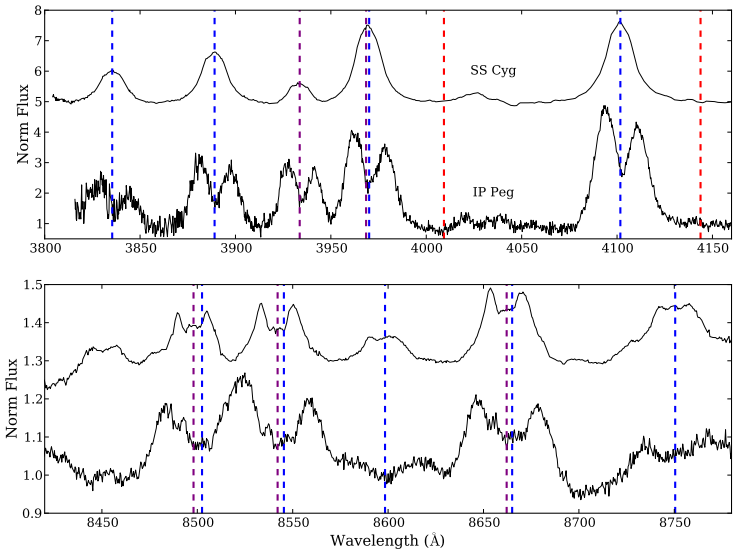

Figure 5-16: The average spectra of SS Cyg and IP Peg. The emission/absorption lines are indicated as follows: Blue: Balmer/Paschen. Red: He I (*dashed*) and He II (*dashed-dotted*). Purple: Ca II. Green: Mg II and Na I.

adding 240 000.5 days to the ephemeris. Here, we ignore the motion of the Sun around the solar system Barycentre, as this is only of the order of seconds in a Jupiter year. A third conversion is needed from TDB into UTC, and is caused by leap seconds: in 2000 this amounted to a difference of ~ 62 seconds which is negligible for this work.

We observed IP Peg for 2 nights in August 2000 as part of the program to compare disc features in the Balmer and Ca II lines, as proposed by Steeghs & Stehle (1999). See Table 5-2 for the observation details and Figure 5-16 for the average spectra. The trailed red spectra reveal detailed disc features, the donor in emission as well as in absorption (Figure 5-17), and all profiles are eclipsed.

Disc

The DD method on Hδ gives $K_{\rm disc,DD} = 141.1 \pm 4.1$ km s^{-1}, $\gamma = 25.2 \pm 6.0$ km s^{-1} and $\phi_0 = 0.51 \pm 0.01$.

The Ca II disc returns $K_{\rm disc,DD} = 186.0 \pm 11.1$ km s^{-1}, $\gamma = 51.3 \pm 5.4$ km s^{-1} and $\phi_0 = 0.470 \pm 0.003$. The centre of symmetry is found at $K_{\rm disc,MEM} = 126 \pm 13$ km s^{-1}.

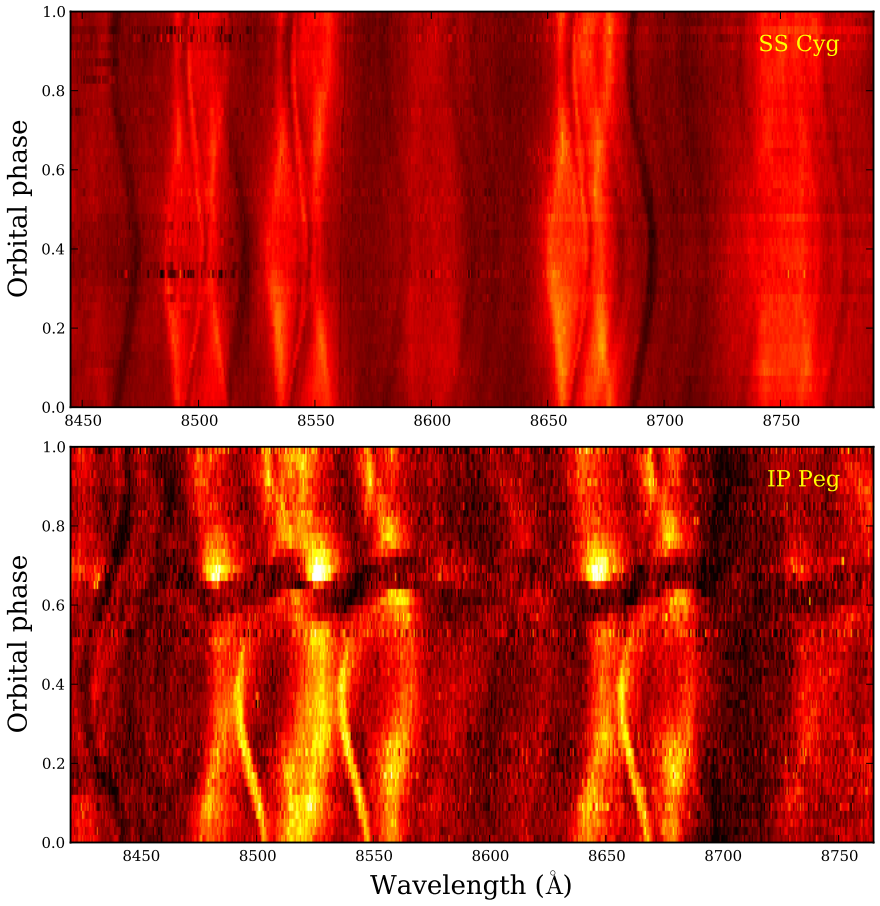

Figure 5-17: Trailed spectra of SS Cyg (top) and IP Peg (bottom). Note the slight change in wavelength range. Both systems show strong Ca II triplet lines with disc features and the donor star in emission and in absorption. Other absorption lines are visible in the background. Furthermore, IP Peg shows an eclipse, where the approaching side of the disc (blue) gets obscured before the receding (red) side of the disc.

Donor

The Hδ trailed spectra show weak signatures of the donor star in emission, but this feature is overshadowed by the strong disc features and the hotspot. In the Doppler map, some emission does indeed map onto the expected location of the donor (Figure 5-18), but even after subtraction of a symmetric disc centred at $K_{\rm disc,MEM} = 172 \pm 13$ km s^{-1}, the donor cannot be resolved with a high enough S/N to be fitted.

After subtraction of the average profile in Ca II, we can fit the remaining emission peak with a single Gaussian with a peak value fixed at 0.26 normalised flux units and a FWHM of 3.0Å during phases 0.25-0.75. A RV fit gives $\gamma = 10.1 \pm 2.4$ km s^{-1} and $\phi_0 = -0.065 \pm 0.004$ and $K_{\rm em} = 190.0 \pm 4.1$ km s^{-1}. This feature is associated with the irradiated side of the donor star as it is consistent with the location in the Doppler map, $K_{\rm em,MEM} = 218 \pm 75$ km s^{-1}.

Several features are in absorption in the red arm and follow the movement of the donor star features in emission. Cross correlation of the spectra with the spectrum of an M4III template star (Bagnulo et al., 2003) gives a radial velocity fit of $\gamma = 5.2 \pm 3.6$ km s^{-1} and $\phi_0 = -0.056 \pm 0.002$ and $K_{\rm ab,CC} = 360.8 \pm 4.8$ km s^{-1}, a much higher amplitude than measured in the emission feature. This absorption feature must be associated with the outer hemisphere of the donor.

Phase

The phase zero point is anchored to the ephemeris provided by Copperwheat et al. (2010), and results in a misalignment of the donor in the map of $\Delta\phi = -0.06 \pm 0.01$.

Previous studies

The eclipse mapping solution for IP Peg solves for $K_1 = 151 \pm 3$ km s^{-1} and $K_2 = 317 \pm 2$ km s^{-1} (Copperwheat et al., 2010). Beekman et al. (2000) report that $K_{\rm abs} \sim 330$ km s^{-1}, which is closer to K_2 than our measured $K_{\rm ab,CC}$. Harlaftis (1999) shows Doppler maps containing donor features in an incredible array of metal lines, visible just after outburst.

As IP Peg shows eclipses and has a well defined set of system parameters, combined with the presence of both emission and absorption of the donor in Ca II, we will exploit IP Peg as a calibrator for our method to constrain the mass ratio via the radial velocities for both the donor and the disc emission measurable in the Ca II triplet lines. Due to the presence of both emission and absorption features from the donor star, we can also

use IP Peg as an excellent example to test our K-correction technique. This will be discussed in Section 7.3.3.

5.3.20 SS Cyg

SS Cygnus is a long period CV at an orbital period of 396.2 minutes and belongs to the U Gem subclass. It is one of the few systems that has been followed spectroscopically during outburst and has a recurrence time scale of $\sim$ 50 days. The spectral type of the donor is K4-5 (Bitner et al., 2007). Unlike IP Peg, SS Cyg is not eclipsing and its parameters are more indirectly determined. We observed SS Cyg as part of the same programme as IP Peg, in August 2000 (Table 5-2, Figure 5-16).

Trailed spectra of reveal Balmer lines with little evidence for double peaks. The Ca H and K lines display marginally resolved double peaked disc profiles, but more importantly, superimposed is the signature of the donor star in emission. The Ca II triplet lines show emission and absorption features from the donor simultaneously, on top of double peaked disc features from the disc, which contain much more detail than the Balmer lines.

Disc

The Hδ line gives $K_{\rm disc,DD} = 78.2 \pm 4.2$ km s^{-1}, $\gamma = -32.3 \pm 7.3$ km s^{-1} and $\phi_0 = 0.51 \pm 0.02$. The profiles do not resolve into a disc, but remain blurred in the Doppler map. A centre of symmetry search finds $K_{\rm disc,MEM} = 77 \pm 13$ km s^{-1} (Figure 5-18).

The features in the Ca II triplet lines are difficult to fit as the width, strength, offset and number of lines visible all vary with the orbital period. Hence, we used the less affected Ca K line to measure the disc features: $K_{\rm disc,DD} = 77.9 \pm 27.9$ km s^{-1}, $\gamma = 14.7 \pm 0.9$ km s^{-1} and $\phi_0 = 0.52 \pm 0.01$ and $K_{\rm disc,MEM} = 100 \pm 13$ km s^{-1}, see Figure 5-18 for the trailed spectra.

Donor and phase

After removing the average profile, we fit 1-Gaussian to the remaining emission in Ca K and find $K_{\rm em,RV} = 111.6 \pm 4.8$ km s^{-1}, $\gamma = -2.1 \pm 2.9$ km s^{-1} and $\phi_0 = 0.004 \pm 0.005$. This feature maps onto the location of the donor in the Doppler map (Figure 5-18) with $K_{\rm em} = 150 \pm 50$ km s^{-1}. The Doppler map of the Ca II λ8662Å line (Figure 5-18) shows a squashed accretion ring with weak emission close to the L_1 point ($K_{\rm em,MEM} = 90 \pm 50$ km s^{-1} and absorption at the back of the Roche lobe.

As can be seen in Figure 5-17, the trailed spectrum shows absorption lines in phase with the donor emission. The absorption centred at λ8687.48Å can be fitted with a single Gaussian and gives $K_{\rm ab,RV} = 154.4 \pm 1.8$ km s^{-1}, $\gamma = 43.9 \pm 1.1$ km s^{-1} and $\phi_0 = 0.005 \pm 0.015$. When cross correlating the entire spectral range with the spectrum of a KIII star, we find $K_{\rm ab,CC} = 156.8 \pm 0.6$ km s^{-1}, $\gamma = 30.9 \pm 0.4$ km s^{-1} and $\phi_0 = 0.005 \pm 0.005$, in perfect agreement with the Gaussian fit to the individual line.

The phase zero point is anchored to the rotation angle needed to place the emission in the Ca II Doppler map at the expected location of the donor.

Previous studies

For comparison, Stover et al. (1980) find $K_{\rm em} = K_{\rm WD} = 90 \pm 2$ km s^{-1} using Hβ, Hγ and Hδ profiles and $K_{\rm abs} = K_{\rm donor} = 153 \pm 2$ km s^{-1} with $\gamma = -15 \pm 4$ km s^{-1} by cross correlating with K4-K5 template stars.

5.4 Summary

In this Chapter, we have presented the results of a survey to study the Ca II triplet lines in CVs. The main findings can be summarised as follows:

Disc

- We find disc features in the Ca II triplet lines in 16 out of the 18 quiescent systems ($\sim$ 90%). These lines are often clearer/sharper than the Balmer features, even though they are weaker.
- We measure the radial velocity of the disc features in both the Balmer and Ca II profiles, using three different methods: 2-Gaussian fits to the disc profile, a diagnostic diagram and via a search for the centre of symmetry in the Doppler maps. Generally, the first two methods agree within the error bars and the latter method proves highly inconsistent.
- The two Gaussian methods are both susceptible to disc asymmetries, such as the hotspot, and do not allow us to avoid these regions easily. In contrast, the Doppler map allows us to deal with these asymmetries in a superior way, by permitting an easy identification of these regions, which then can be avoided for centre of symmetry searches. Tables 5-10, 5-11 and 5-12 indicate that the Ca II profiles

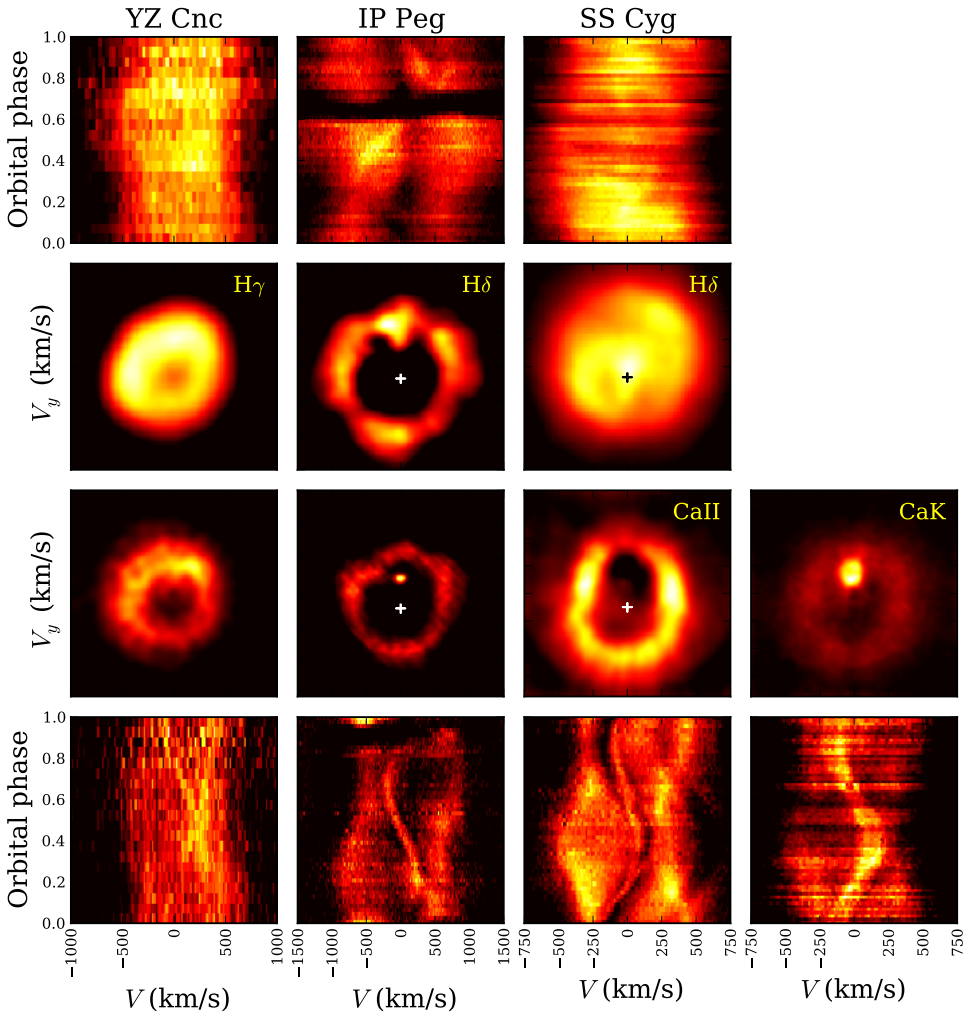

Figure 5-18: Trails and maps of Balmer (top two rows) and Ca II (bottom two rows) for YZ Cnc, IP Peg and SS Cyg (left to right columns). IP Peg and SS Cyg show a clear donor star emission spot in both the Ca II trails as the Ca II maps. YZ Cnc shows emission from the donor in the trail, but not very clearly in the Doppler map. The right most column, shows the trail and Doppler map for Ca K in SS Cyg. The donor is visible in all maps and trails, and the centre of symmetry is indicated by a +. The x-axis scale in each column is different, but kept the same for the entire column as indicated for the Ca II trailed spectra. Each Doppler map is square in V_x and V_y, and the axis are set by the V scale indicated in the bottom Ca II trail.

provide a more stable solution than the Balmer lines with all three techniques and thus appears to be a superior probe of K_1.

- Comparisons to previous studies show that the radial velocity derived using double Gaussian fits to the disc profiles is highly variable. It is generally accepted that disc emission can by asymmetrical, distorting both the phase and, more importantly, the radial velocity of the disc. In those cases, when the previous measurements did not agree with our values, especially when different lines were used, a strong hotspot was visible and/or there had been an outburst between measurements. As these effects can potentially change the morphology of the disc profile, we can only conclude that the disc profiles are inadequate tracers of K_1.

Donor

- We find donor emission in the calcium lines in 11 systems. This is 60% of our total sample and 70% of those CVs that show Ca II lines in emission. In two systems, we find emission from the donor in the hydrogen lines, but not in calcium. OY Car is the only system with donor emission in hydrogen, calcium and potassium lines. Overall, we find donor emission in 13 out of 18 systems ($\sim 75\%$).

- All donor features can be located in Doppler maps, allowing for measurements of its radial velocity semi-amplitude and the determination of a phase zero point.

- For 10 systems, we can fit 1-Gaussians to the (residual) emission components, followed by a radial velocity curve fit, to improve the value derived directly from the Doppler map.

- As expected, only the two longest period systems show donor absorption lines in the observed wavelength range (IP Peg and SS Cyg).

- When previous measures of donor emission have been published, these have were consistent with our values.

WD

- We were able to detect absorption associated with the WD in the Mg II λ4481Å line in only two systems. In GW Lib, we were able to track the movement of this line as function of the binary orbit. This resulted in a measure for K_1, even though the value is close to the resolution limit of the data. Unfortunately, for

UV Per, the presented data was not of sufficient resolution to positively associate the line with the WD, and the poor S/N prevented from tracking the WD motion as a function of the binary orbit.

Systemic velocity

- The different measures for the systemic velocity are: RV, DD fits to both Balmer and Ca II disc lines, RV fits to the donor emission and the search for the optimal systemic velocity using the Doppler map.
- The Doppler map does not always converge towards a satisfactory answer, especially when the map lacks the distinctive ring feature of the disc
- The difference between γ values derived from disc and donor features can be explained by the different gravitational redshift induced by the donor and WD potentials. However, this is of order of a few km s^{-1} and cannot explain the large differences we see.

Two final notes regarding the systemic velocity: First, care should be taken when optimising the Doppler map for γ, especially when both the disc and donor features are present. Visual optimisation, based on appearance of the donor emission, will solve for the systemic velocity of the donor emission, whereas the disc features are projected on a different value, due to a different gravitational redshift. Second, the misidentification of Paschen 13 as Ca II λ8662.14Å will give rise to an offset in the systemic velocity of ~ 100 km s^{-1}. But, as only SU UMa displays this behaviour, we are confident that in most cases we truly measure Ca II rather than Paschen 13.

The comparison of systemic velocity measurements with previous studies remains rudimentary at best, especially when comparing measures derived from disc features, and hints at an underlying problem with measuring γ using the above techniques. The most reliable systemic velocity is derived from the donor star, as this should trace γ, with only marginal corrections for the redshift, and unbiased by asymmetries in the disc. Care should be taken, if this value is derived from emission lines after removing the underlying disc profile, as the dependence of the value on this action has not been explored.

We have observed 18 quiescent CVs in search of donor emission features and crucially found these features in 13 systems. We intentionally included 4 eclipsing systems, with

solutions for K_1 and K_2, and 2 long period systems, where K_2 can be determined via absorption lines.

With measures for $K_{\rm disc}$ and $K_{\rm em}$ in hand, we can set firm upper limits on the dynamical mass ratio. We can derive a better estimate after applying a K-correction to $K_{\rm em}$, using irradiation models. With these estimates for q, we can test our method for constraining q, comparing the Ca II value against the published eclipse solutions.

Table 5-10: Radial velocity measurements (all errors are 1σ). The phase zero point is calibrated to the ephemeris (denoted by *), donor emission spot (denoted by $^+$) or the start of observations (denoted by $^\times$). The last column lists the fixed parameters for the fit. For DD methods, these are the plateau range in Δv, used to average the measures, and the fixed FWHM of the profiles. For single Gaussian fits we list the FWHM and peak in normalised flux units, when fixed. For 2-Gaussian fits, we add the fixed offset. 1G stands for 1-Gaussian fit.

Object	Line	Feature	Method	K (km s^{-1})	γ (km s^{-1})	ϕ_0	Fixed parameters Δv, FWHM, flux (km s^{-1}), (Å), flux
GW Lib	Hβ	Disc	RV	19.2±1.8	-7.6±1.9	0.68±0.01$^+$	
			DD	15.9±1.2	-7.7±1.4	0.61±0.01	200-400, 4.5
			MEM	11±7	0±5		
	Ca II	Disc	RV	19.8±1.4	20.6±1.1	0.73±0.01	
			DD	15.7±3.1	19.0±2.7	0.65±0.01	100-300, 6.0
			MEM	6±7	-10±5		
		Donor	RV	82.2±1.6	-13.1±1.2	0.00±0.003	–, 1.5, –
			MEM	83±14		0.00±0.01	
V844 Her	Hγ	Disc	RV	55.4±4.2	2.8±3.0	0.46±0.01	970, 11.4
			DD	77.8±25.4	4.4±20.0	0.50±0.07	500-1500, 12.0
			MEM	77±21	3±5		
V455 And	Hγ	Disc	RV	49.5±5.9	-18.7±4.4	0.51±0.03	1300, 14.4
			DD	56.4±6.3	-17.5±7.5	0.52±0.05	1200-1400, 14.5
			MEM	48±13	-23±5		
	Ca II	Disc	RV	50.9±3.5	41.0±2.3	0.65±0.01	1280, 21.0
			DD	44.5±15.4	36.8±6.9	0.57±0.11	1000-2000, 21.5
			MEM	46±13	-45±10		
ASAS 0025	Hγ	Disc	DD	22.5±7.8	-28.9±1.4	0.58±0.14$^{+?}$	800-1200, 10.3
			MEM	18±13	35±5		
		Donor?	MEM	193±16		0.00±0.03	
	Ca II	Disc	MEM	18±13	-5±5		
WZ Sge	Hβ	Disc	RV	64.6±2.7	-57.2±2.0	0.75±0.01*	1240, 15.0
			DD	50.6±16.2	-64.5±2.5	0.57±0.07	1000-2000, 15.0, 1.2
			MEM	90±13	×		
	Ca II	Disc	DD	269.9±30.9	52.1±1.2	0.68±0.01	950-1150, 16.5, 0.2
			MEM	48±13	-70±10		
		Donor	RV	402.9±0.5	-67.1±0.4	0.0400±0.0002	
			MEM	438±49		0.040±0.01	
V1108 Her	Hγ	Disc	RV	111.0±7.0	-120.4±6.7	0.88±0.02	1370, 15.6
	Ca II	Disc	RV	×	-65±5	×	
HS 2219	Hγ	Disc	RV	76.3±10.2	1.3±7.3	0.63±0.02	2500, 13.6
			DD	67.6±16.7	4.4±2.1	0.62±0.04	1000-2000, 13.6
			MEM	45±13	0±10s		
	Hβ	Disc	MEM	40±13	-10±10		
		Donor	MEM	250±50		0.18±0.01	
	Ca II	Disc	DD	68.2±18.0	-63.0±8.9	0.48±0.02	1000-1500, 25.8, 0.2
			MEM	53±13	×		
OY Car	Hα	Disc	RV	85.4±16.5	54.3±84.2	0.55±0.05*	1400, 20.0
			DD	85.0±2.6	57.2±1.7	0.57±0.01	1200-1700, 20.0
			MEM	80±15	45±10		
		Donor	MEM	410±112		-0.02±0.01	
	Ca II	Disc	RV	76.0±3.0	49.9±3.7	0.53±0.01	1300, 20.0
			DD	84.9±6.3	61.2±4.2	0.54±0.04	1200-1700, 20.0
			MEM	60±22	25±5		
		Donor	RV	395.3±1.8	74.9±1.9	-0.04±0.001	1G, 2.2, 0.4
			MEM	407±46		-0.02±0.02	
	K	Donor	MEM	410±45		-0.02±0.01	

Table 5-11: Radial velocity measurements (all errors are 1σ), as in Table 5-10.

Object	Line	Feature	Method	K (km s^{-1})	γ (km s^{-1})	ϕ_0	Fixed parameters Δv, FWHM, flux (km s^{-1}), (Å), flux
UV Per	Hγ	Disc	RV	26.9±1.6	9.5±1.1	0.57±0.01^{+}	430, 6.0
			DD	31.2±2.8	14.2±8.1	0.61±0.02	400-700, 6.0
			MEM	44±7	8±5		
	Ca II	Disc	RV	26.6±1.6	24.8±1.1	0.57±0.01	370, 8.8
			DD	21.5±3.2	37.1±6.0	0.54±0.01	200-600, 8.8
			MEM	30±4	20±5		
		Donor	RV	103.3±1.6	-2.4±1.1	-0.012±0.002	1G, 1.2, 0.6
			MEM	111±37		0.00±0.01	
TY Psc	Hγ	Disc	RV	75.7±7.6	-6.6±5.4	0.52±0.02^{+}	1000, 13.6
			DD	76.5±4.1	0.5±17.0	0.53±0.10	1000-1400, 13.5
			MEM	100±18	×		
	Ca II	Disc	RV	93.5±3.6	5.5±2.7	0.51±0.01	770, 17.5
			DD	93.0±1.9	5.9±14.8	0.50±0.02	600-1200, 17.5
			MEM	42±7	-10±10		
		Donor	MEM	230±48		0.00±0.01	
GD 552	Hγ	Disc	RV	19.0±4.3	-55.9±4.0	0.04±0.06$^{\times}$	930, 11.5
			DD	56.9±14.6	-66.5±0.9	0.03±0.004	1150-1550, 11.5
			MEM	45±13	-55±10		
IY UMa	Hγ	Disc	RV	89.7±9.9	46.2±8.1	0.55±0.02*	1G, 4.0, -0.27
	Ca II	Disc	RV	118.2±8.9	36.5±6.9	0.51±0.02	1000, 17.4
			DD	121.2±20.2	70.42±12.2	0.53±0.03	850-1500, 17.9
			MEM	63±10	60±10		
		Donor	RV	304.2±18.3	-56.6±16.9	-0.02±0.02	
			MEM	383±120		-0.05±0.01	
HT Cas	Hγ	Disc	RV	87.1±4.2	7.2±3.0	0.62±0.01^{+}	1420, 13.8
			DD	96.3±6.7	0.6±7.0	0.64±0.01	1200-1600, 15.7
			MEM	42±13	0±10		
	Ca II	Disc	RV	93.3±3.3	43.1±2.2	0.61±0.05	1200, 18.0
			DD	90.2±2.4	45.2±1.0	0.60±0.004	1000-1500, 18.7
			MEM	86±14	-20±10		
		Donor	RV	344.4±4.7	25.1±5.2	-0.021±0.004	1G, 2.5, 0.2
			MEM	351±58		0.00±0.01	
SU UMa	Hγ	Disc	RV	36.1±1.5	-2.4±1.1	0.60±0.01^{+}	750, 22.0
			DD	39.9±2.6	-8.4±1.9	0.58±0.001	850-1250, 17.1
			MEM	×	-5±10		
	Ca II	Disc	RV	89.6±2.9	68.6±2.3	0.69±0.01	650, 15.5
			DD	43.7±12.5	115.7±13.4	0.44±0.06	800-1200, 19.6
			MEM	31±15	5±10		
		Donor	RV	206.8±4.8	10.9±3.8	0.003±0.005	1G, 2.0, 0.1
			MEM	211±75		0.00±0.01	

Table 5-12: Radial velocity measurements (all errors are 1σ), as in Table 5-10.

Object	Line	Feature	Method	K (km s^{-1})	γ (km s^{-1})	ϕ_0	Fixed parameters Δv, FWHM, flux (km s^{-1}), (Å), flux
YZ Cnc	Hα	Disc	RV	37.0±1.9	77.3±1.5	0.54±0.01^{+}	300, 15.8
			DD	31.8±1.9	50.8±4.2	0.52±0.01	400-1000, 16.3
			MEM	×	75±25		
	Ca II	Disc	RV	89.6±2.6	68.6±2.3	0.57±0.01	535, 15.6
			DD	87.7±42.5	95.7±22.2	0.58±0.06	500-800, 16.3
			MEM	×	45±10		
		Donor	RV	145.5±1.9	45.5±2.0	-0.004 ±0.002	1G, 20.0, 0.1
			MEM	160±70		0.00±0.01	
IP Peg	Hδ	Disc	RV	172.7±2.9	29.3±2.5	0.51±0.03*	–, 16.2
			DD	141.±4.1	25.2±6.0	0.51±0.01	1000-1400, 16.2
			MEM	172±13	20±20		
	Ca II	Disc	RV	185.3±3.4	70.9±2.3	0.480±0.003	1160, 19.7
			DD	186.0±11.1	51.3±5.4	0.47±0.003	900-1300, 19.7
			MEM	126±13	60±10		
		Donor (em)	RV	190.0±4.1	10.1±2.4	-0.065±0.004	1G, 3.0, 0.26
			MEM	218±75		-0.06±0.01	
	–	Donor (abs)	RV	316.8±8.1	-52.0±6.0	-0.08±0.01	1G, 3.0, -0.1
			CC	360.8±4.8	5.2±3.6	-0.056±0.002	
SS Cyg	Hδ	Disc	RV	61.2±1.9	-26.6±1.4	0.534±0.004^{+}	
			DD	78.2±4.2	-32.3±7.3	0.51 ±0.02	600-1000, 10.2
			MEM	77±13	-30±10		
	Ca II	Disc	RV	21.2±1.4	-17.2±1.0	0.48±0.01	–, 12.6
			DD	77.9±27.9	14.7±0.9	0.51 ±0.01	400-800, 14.2
			MEM	100±13	-5±20		
		Donor (em)	MEM	90±50		0.00±0.01	
	Ca K	Donor (em)	RV	111.6±4.8	-2.1±2.9	0.004±0.005	1G, –, 0.3
			MEM	150±50		0.00±0.01	
	–	Donor (abs)	RV	154.4±1.8	43.9±1.1	0.005±0.015	1G, 4.0, -0.02
			CC	156.8±0.6	30.9±0.4	0.005±0.005	

Chapter 6

Ca II survey II: Emission line properties

In Chapter 5, we focused on measuring the radial velocities and EWs of the most prominent spectral lines of the systems covered in our survey. Here, we revisit the general properties of these profiles and search for correlations and trends within our survey sample, including the dependence of bulk emission line properties on various system parameters. We focus on the strongest Balmer and Paschen lines and the Ca II lines (triplet and Ca H/K when covered). We include all observed quiescent systems, which provides us with 18 CVs for this population study.

6.1 EW measures

All EWs for the strongest Balmer, Paschen and Ca II lines have been measured in Chapter 5, and are listed in Tables 5-7 and 5-8. Here, we will discuss the relative strengths of the lines of various elements using these EWs.

Balmer lines

To measure the strength of the emission arising from the disc alone in the Balmer lines, we remove any WD absorption troughs present around these lines, using a high order polynomial fit to the continuum during the renormalisation. The results are plotted in the top panel of Figure 6-1, the formal error bars on individual points are generally smaller than the marker size, and systems are ordered according to orbital period.

It is evident from both Table 5-7 and Figure 6-1, that all systems have strong Balmer features associated with disc emission. For all systems, it is unambiguous that the strength of the Balmer lines decreases with higher order Balmer lines and that the Balmer decrement is steeper in optically thin cases than in optically thick cases. For example, we compare GW Lib and V455 And. While GW Lib has a low inclination ($\sim 11°$) and displays a U-shaped central region of the disc emission profile (as described

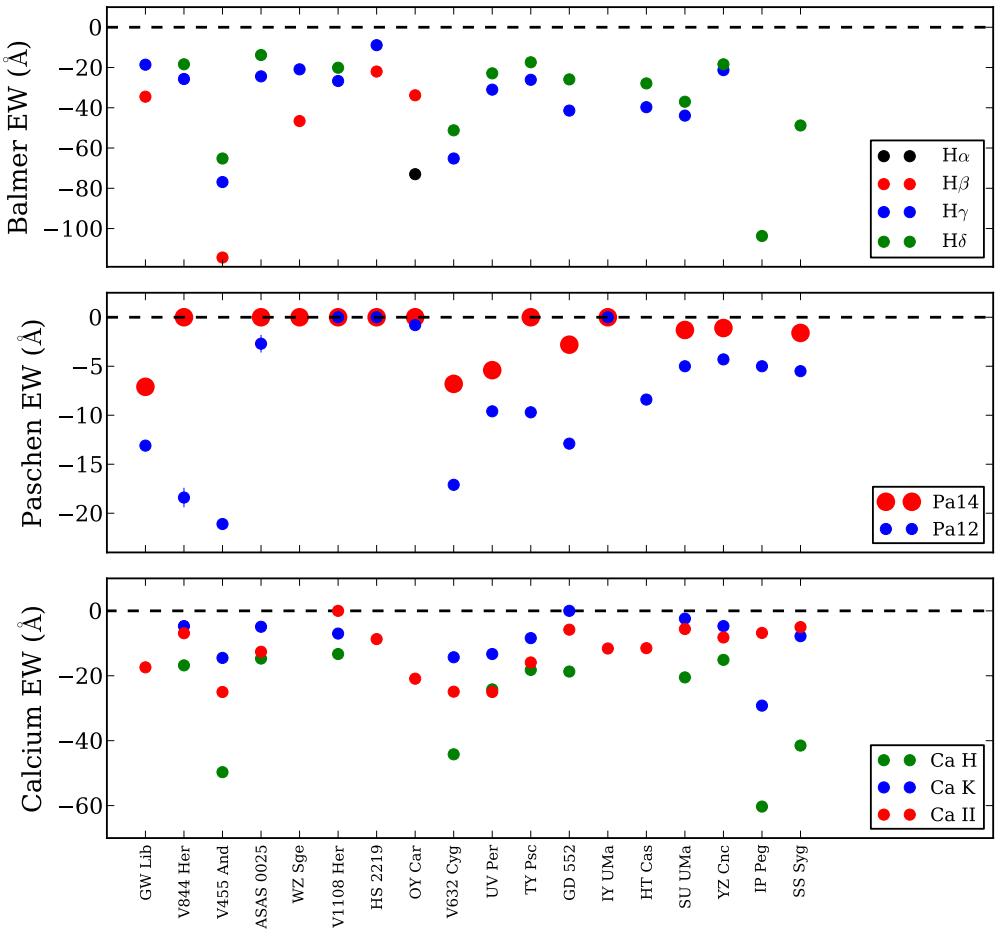

Figure 6-1: EW measurements for all systems (ordered according to orbital period). **Top panel:** EW of the Balmer lines visible in the spectra. **Middle panel:** EW of Paschen 14 and Paschen 12 lines. **Bottom panel:** EW of the Ca H/K and Ca II 8662Å disc profiles. Error bars are generally smaller than individual marker size. An EW equal to zero reflects the absence of the line, while the absence of a marker denotes a non-measure (i.e. outside wavelength coverage or blended with nearby lines; see Tables 5-7 and 5-8 for further details).

by Horne & Marsh 1986, Section 2.5.3, Figure 5-1). V455 And displays the typical V-shaped optically thick disc emission lines viewed at high inclination ($\sim 75°$; Figure 5-3). From Figure 6-1, we see that that even though the absolute decrement from Hβ to Hγ is larger for V455 And than for GW Lib (EW of 34.8Å versus 15.9Å), its fractional decrease is lower at $\sim 30\%$ compared to $\sim 50\%$ for GW Lib.

Paschen lines

The absolute EWs for the Paschen lines are presented in the middle panel of Figure 6-1 and in Table 5-7. The Paschen 12 line at λ8750Å is undetected in V1108 Her, HS 2219 and IY UMa. V1108 Her actually only displays narrow absorption lines in its red spectrum (Figure 5-2).

The main use of the Paschen lines is to evaluate the contribution of underlying hydrogen to the Ca II triplet lines. By estimating the progression of the strength from Paschen 12 to Paschen 14, the contribution of Paschen 13 to Ca II λ8662Å can be estimated. With this estimation, we can assess the presence of calcium, as all Ca II triplet lines are blended with, and hence potentially dominated by, nearby Paschen lines. We will give an example of this method in Section 6.5.2 and Figure 6-11.

The influence of blending is visible in WZ Sge, were all lines are broadened such that is it impossible to distinguish the individual profiles. This prohibits the measurement of reliable EWs for the Ca II and Paschen profiles (Figure 5-1).

Ca II triplet lines

Out of the 18 quiescent systems we observed, 16 display double peaked emission at the location of the λ8662Å line. The majority of the systems also show broad double peaked disc emission in the Ca λ8498Å and λ8542Å lines, but their close proximity in high inclination systems often results in overlapping profiles. See Table 5-8 and bottom panel in Figure 6-1 for the individual EW measures.

All systems but two display the Ca II λ8662Å line as the strongest of the triplet lines, and the exceptions have a minimal difference in line strength between this line and Ca II λ8542Å. The transition probability for the Ca II λ8498Å line is $\log(gf) = -1.259$, Ca II λ8542Å has $\log(gf) = -0.3073$ and Ca II λ8662Å has $\log(gf) = -0.5687$[1], hence it is unexpected to find λ8662Å as the strongest line. The relative strength of this line can be attributed to the underlying presence of the Paschen 13 line at λ8665Å blending with Ca II λ8662Å, whereas the Ca II λ8542Å line is blended with the higher order, and hence weaker, Paschen 15 line at λ8545Å. However, both HS 2219 and IY UMa have the strongest emission in Ca II λ8662Å while Paschen is undetected.

[1]Data from The Atomic Line List Version 2.04:`http://www.pa.uky.edu/~peter/atomic/`

Ca H/K lines

During most of our observing runs, we aimed to cover the calcium H and K lines together with the Balmer series in the blue arm of our experimental set-up. We observe that the absolute strength of the Ca II lines orders from Ca H, the strongest line, to Ca II and Ca K. This is most likely attributed to the blend of Ca H with Hϵ, followed by Ca II blended with Pa 13, while Ca K is isolated from nearby hydrogen lines. This order is visible in all systems (bottom panel Figure 6-1, Table 5-8), except for UV Per, which shows Ca II $\gtrsim$ Ca H.

The main advantage of the Ca K line over other Ca II lines lies in its isolation from nearby hydrogen lines, providing us with a true measure for the amount of calcium present, as all other lines are blended with nearby hydrogen lines within ~ 5Å (equivalent to $\sim$ 375 km s^{-1}). Including the Ca K line in the experimental set-up can be extremely valuable for the identification of the origin of lines. This is emphasised in GD 552, as we detect the Ca II/Pa triplet lines and the Ca H/Hϵ line, but nothing for Ca K. This strongly suggest the emission in the first two profiles originates from hydrogen alone rather than calcium.

Unfortunately, in high inclination systems, the Ca H/K lines are generally dominated by strong central absorption which is visible in both these lines and the neighbouring hydrogen lines. This, combined with the blending of these lines, prevents us from reliably normalising the continuum levels and hence prohibits us from obtaining a realiable measure of the EW. Thus, the use of Ca H/K for the detection of calcium is no more straightforward than the use of the triplet lines in the I-band.

6.2 Disc emission line features in CVs

The disc emission is generally visible as a double peaked profile, and the separation provides a rough indication of the inclination. The systems with a known low inclination ($i < 20°$; i.e. GW Lib, UV Per, TY Psc) display narrow double peaked disc emission lines. As all these systems happen to undergo mass transfer at low rates, the Balmer disc lines are flanked by WD absorption troughs. For the Balmer lines, the low inclination is expressed in narrow disc profiles with shallow central U-shaped absorption, which results in blurred disc features in Doppler maps. This is in stark contrast with the disc features in the Ca II triplet lines, which are more profoundly double peaked and provide a clearly resolved Doppler maps, even at low inclinations.

Table 6-1: Known system parameters and emission line features in the surveyed CVs. The system parameters listed are the mass and temperature of the WD, the spectral type of the donor and the inclination of the system, from Ritter & Kolb (2003) and references therein, unless otherwise stated. The emission line features include the shape of the disc profile being single or double peaked (S/D) in the Balmer and calcium lines, if the donor is visible in the Ca II or Balmer lines (the latter is denoted by E_H) in emission and/or absorption (E/A) and if the WD is visible (yes/no). Note, the temperatures taken from Urban & Sion (2006) are indicative only. For example: GW Lib has a double peaked disc profile in both hydrogen and calcium lines (DD), and the donor is present in calcium emission (E). Whereas SS Cyg has a single peaked disc profile in hydrogen, a double peaked disc profile in calcium (SD), and the donor is present in emission in calcium and in absorption (EA).

Object	M_{WD} $M_\odot$	T_{wd} K	SpT	i (°)	H/Ca disc S/D	donor –/E/A	WD Y/N
GW Lib	0.84(2)	13 300[a]	M9	11.2(4)	DD	E	Y
V844 Her					DD	–	N
V455 And		10 500[a]	>L2	∼ 75	DD	–	Y
ASAS 0025			M9		DD	E_H	Y
WZ Sge	0.85(4)	14 900[a]		77(2)	DD	E	Y
V1108 Her			L1		D–	–	Y
HS 2219		16 000[b]	> M5		DD	E_H	Y
OY Car	0.64(4)	15 000[a]		83.3(2)	DD	E	N
V632 Cyg					SD	–	N
UV Per	0.80(20)[d]	20 000[c]		18[d]	DD	E	Y
TY Psc	0.55(20)[d]	16 000[d]		18[d]	DD	E	Y
GD 552	0.6[e]	10 900[f]			D–	–	Y
IY UMa	0.79(4)	14 500[g]	M4	86.0(10)	–D	E	∼
HT Cas	0.61(4)	14 000[a]	M5.5	81(1)	DD	E	N
SU UMa	0.8(2)[d]	28 000[d]		41[d]	SD	E	N
YZ Cnc	0.82(8)	23 000[d]		38(3)	SD	E	N
IP Peg	1.16(2)	12 500[h]	M5	83.8(5)	DD	EA	N
SS Cyg	0.81(19)	50 000[i]	K4-5	51(5)	SD	EA	N

[a] Szkody et al. 2010
[b] Rodríguez-Gil et al. 2005
[c] Godon et al. 2009
[d] Urban & Sion 2006
[e] Unda-Sanzana et al. 2009
[f] Unda-Sanzana et al. 2008b
[g] Patterson et al. 2000
[h] Copperwheat et al. 2010
[i] Sion et al. 2010

For those systems with strong emission features and a moderate inclination ($20° < i < 55°$; SU UMa, YZ Cnc and SS Cyg) the Balmer disc lines can become single peaked as the optical depth along the line of sight increases. These particular systems also have a high accretion rate, which obscures the WD absorption troughs around hydrogen and saturate the hydrogen lines, resulting in strong, single peaked emission lines, unresolved in Doppler maps. In contrast, the Ca II triplet disc emission line profiles remain distinctly double peaked and resolved in Doppler maps.

In high inclination systems ($i > 75°$; OY Car, IY UMa, HT Cas, IP Peg, WZ Sge and V455 And), the double peaked profiles are dominated by strong V-shaped central absorption. This central absorption suppresses the disc emission in higher order hydrogen lines. In the case of IY UMa, all hydrogen lines covered in our set-up are dominated by the central absorption (Table 6-1). For the Ca II disc lines, thee higher inclination exhibits itself in a widening of the double peaked profile such that Ca II λ8498Å and λ8542Å blend together. Only Ca II λ8662Å remains unblended from nearby calcium features and contains any central absorption as the distance between this line and the nearest Ca II line (Ca II λ8542Å) is large enough. The calcium Doppler maps display clearer disc ring features, including better defined asymmetries for these systems.

Our results clearly show that over the entire inclination range and in all cases when Ca II triplet lines are present ($\sim 90\%$), these lines show more distinct disc profiles compared to the hydrogen lines and also resolve into clearer and sharper Doppler maps.

6.3 Donor features in CVs

The spectrum of a CV with an early type donor star is dominated by the spectrum of the cool donor redwards of Hα. The absorption line features, arising from the cool donor surface, form the basis for the traditional method of measuring the donor radial velocity. For later type stars, this domination retreats towards redder wavelengths and late M-type donors typically do not display signatures at wavelengths short of 10 000Å, prohibiting the detection of the radial velocity of the donor star with optical spectroscopy. However, it is these late type (and low mass) stars that are of interest to us as they accompany the WD in short orbital period CVs. To try and find an additional method for measuring donor features, we explored the easily ionised Ca II lines in search of donor features to provide the dynamical constraints, important for the mass ratio, for those systems where traditional methods fail.

We find emission associated with the donor in the Ca II triplet in 11 out of the 18 observed systems, while only 3 out of these 18 systems show the donor in emission in Balmer lines, and only OY Car shows donor emission in more than one line simultaneously. The two systems with the longest period (IP Peg and SS Cyg) also display donor absorption features.

Line strength variation of the donor emission profile

The S/N for the Ca II lines is generally too low to fit the donor emission with individual 1-Gaussian profiles with the offset, FWHM and peak height as free parameters. Those systems that do allow individual Gaussian fits to the residual spectra, only succeed when the peak height of the Gaussian is fixed to an amplitude in the range $0.1-0.4$ normalised flux units and the FWHM is fixed at $1-3$Å (Tables 5-10, 5-11, 5-12). This prohibits us from searching for inclination dependent variations in the line strength as a function of the orbital phase in most systems (Section 2.4.3).

Only GW Lib and SS Cyg have the S/N that allows us to fit the strength of the donor emission profiles as a function of the orbital phase. For GW Lib, we fix the FWHM of the profile to 1.5Å and allow the peak height to vary. The results are shown in the top panel in Figure 6-2, and show little variation (RMS scatter of $\sim 8\%$ around the average value), nor any periodic behaviour. The low inclination of GW Lib ($i \sim 11^{\circ}$) combined with optically thin disc emission models, indeed predict little variability, see also Section 3.4.4 for a discussion.

For SS Cyg, we can measure the strength of the emission line associated with the donor in Ca K as a function of the orbital period using a 1-Gaussian profile with all 3 fitting parameters set to vary, see middle panel Figure 6-2. If we assume the emission in SS Cyg to come from irradiation of the inner face of the donor, we expect the largest flux to be found around $\phi \sim 0.50$ as around this phase, the irradiated side of the donor is viewed face on, and we expect a minimum at $\phi \sim 0.00$, when the donor is self-obscured. However, the line strength in SS Cyg displays a variation with two maxima (at $\phi \sim 0.25$ and $\phi \sim 0.75$). This modulation is better fitted with a sinusoid on half the period.

The most common form of such an modulation is ellipsoidal modulation. Ellipsoidal modulation is observed as a variation on the flux throughout the orbital phase, as the viewing angle shows different aspects of the gravitationally distorted secondary star which gravitationally darkens the inner face of the donor star and hence this region emits less flux. This has been seen in several low-mass X-ray binaries (e.g. A0620-00

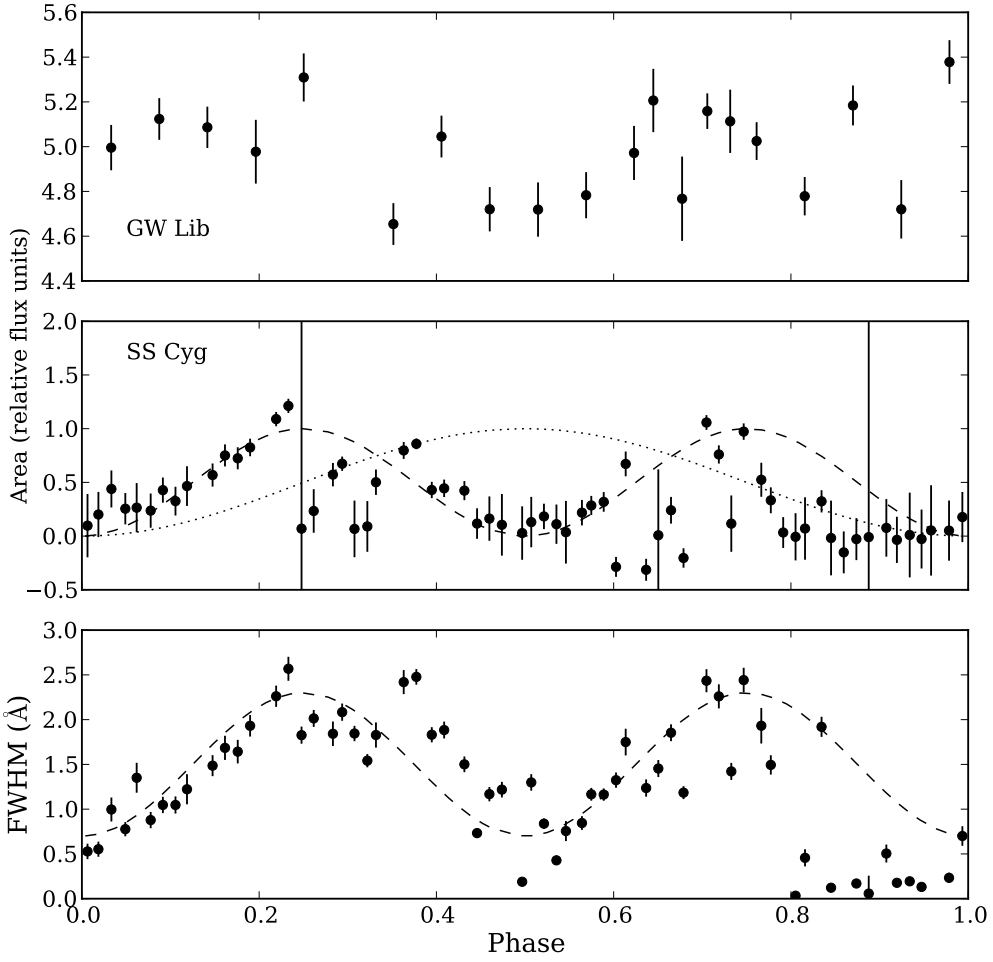

Figure 6-2: **Top:** The light curve of the donor emission in Ca II for GW Lib. **Middle:** The light curve of Ca K in SS Cyg. Over-plotted is a sinusoid, displaying the expected contribution of the donor (*dotted*) and a sinusoid with half the period with maxima at $\phi = 0.25$ and $\phi = 0.75$ (*dashed*). **Bottom:** FWHM measurements of SS Cyg as a function of the orbital phase. Over-plotted is again the sinusoidal with half the period.

(Shahbaz et al., 1994)) and is least contaminated by disc contributions in (mid) IR wavelengths (Marsh et al., 1994). Using the modulation, constraints can be placed on the mass ratio and inclination.

Another possibility comes from a bimodal spread of emission on the donor surface. This idea arrises from the fact that we do not measure the true flux in normalised spectra, but the normalised peak and the width of the emission profile. The value for the peak (in relative flux units) does not vary, but scatters around an average value, which suggests the FWHM is the main contributor to the variation, see bottom panel of Figure 6-2). We see the same modulation in both the FWHM as in the 'area', but with a different amplitude as the 'area' is scaled to the peak measurement in relative flux units. The bimodal spread results in two sources of emission to lie on the donor surface, and gives rise to two emission lines with the same phase but different radial velocity amplitudes. These two separate emission components would cross the line of sight at phases $\phi \sim 0.00$ and $\phi \sim 0.50$, minimising the spread of emission. At phases $\phi \sim 0.25$ and $\phi \sim 0.75$, the difference in radial velocity of the two componets would be largest, and hence the combined emission profile widest.

We will discuss this donor emission feature, and its most likely origin, in more depth in Section 7.3.3.

Both the example of GW Lib and SS Cyg highlight the difficulty with measuring the light curve variability as a function of orbital phase and emphasise the need for high time-resolution, high spectral resolution and high S/N to achieve the data quality needed to measure the predicted variability. Also needed is careful flux calibration to measure the absolute flux, rather than the relative flux. But such detailed studies are worth pursuing as the phase dependence of an irradiated donor can constrain the mass ratio and binary inclination.

6.4 Correlations and trends

To search for correlations and trends, we now point our attention towards the various known system parameters of the objects within our sample and compare these with the line strengths of the Ca II lines and the presence of donor star emission. Table 6-1 lists the relevant system parameters (WD mass, WD temperature, spectral type and inclination). The orbital periods are listed in Table 5-1. Unfortunately, not all systems have a complete set of parameters, reducing our sample size. Hence, all conclusions are

preliminary only, as they are based on small number statistics.

As the absolute strength of the emission lines varies from one object to another, impeding the search for direct correlations, we introduce the 'relative strength', which measures the strength of a line scaled to the strength of another, as expressed by their EW ratios.

Period

Figure 6-3 shows that at long periods, the calcium and Paschen lines are weak compared to the Balmer lines. For intermediate periods, these strengths seem to increase slightly, followed by a strong dip (around $\log(P_{\rm orb}) = -1.2$days). For short periods, the strength seems to peak again, followed by a weakening at the shortest orbital periods. This trend is visible in both the Balmer and Paschen EW ratio's and possibly in the Ca II ratio. An explanation could be that the period space in the observed dip is occupied by observed period-bounce systems only (i.e. GD 552), when both the disc and the donor features fade due to the extreme low mass transfer rates and the cool WD, and that our survey doesn't include pre-bounce systems at this period range.

All systems with a period longer than the period of GD 552 (102.7 minutes) show both the disc and the donor in emission in the Ca II triplet lines. For those systems with a shorter period, Ca II disc emission is generally present ($\sim 80\%$), but donor emission is only present in $\sim 50\%$ of these cases (Table 6-1).

Overall, we cannot discern any strong trends in the strength of the lines as a function of the orbital period. This is mainly due to our limited sample size and the large gaps in the coverage of the orbital period, especially at longer periods.

WD Mass

Ritter & Kolb (2003), and references therein, list WD masses for several of our tagets (Table 6-1). We accept an additional number of masses given by Urban & Sion (2006), with a generous error budget of 0.2 $M_{\odot}$ for plotting purposes only.

The middle panel of Figure 6-4 shows the relative strength of the Ca II lines to the various Balmer lines versu WD mass. We also plot the WD mass versus the orbital period in the middle panel of Figure 6-5. Indicated in both plots, by red and blue circles, is the presence of the donor in emission and absorption, respectively. Both Figures display large scatter, with no apparent correlations. Within our survey, GD 552 is the

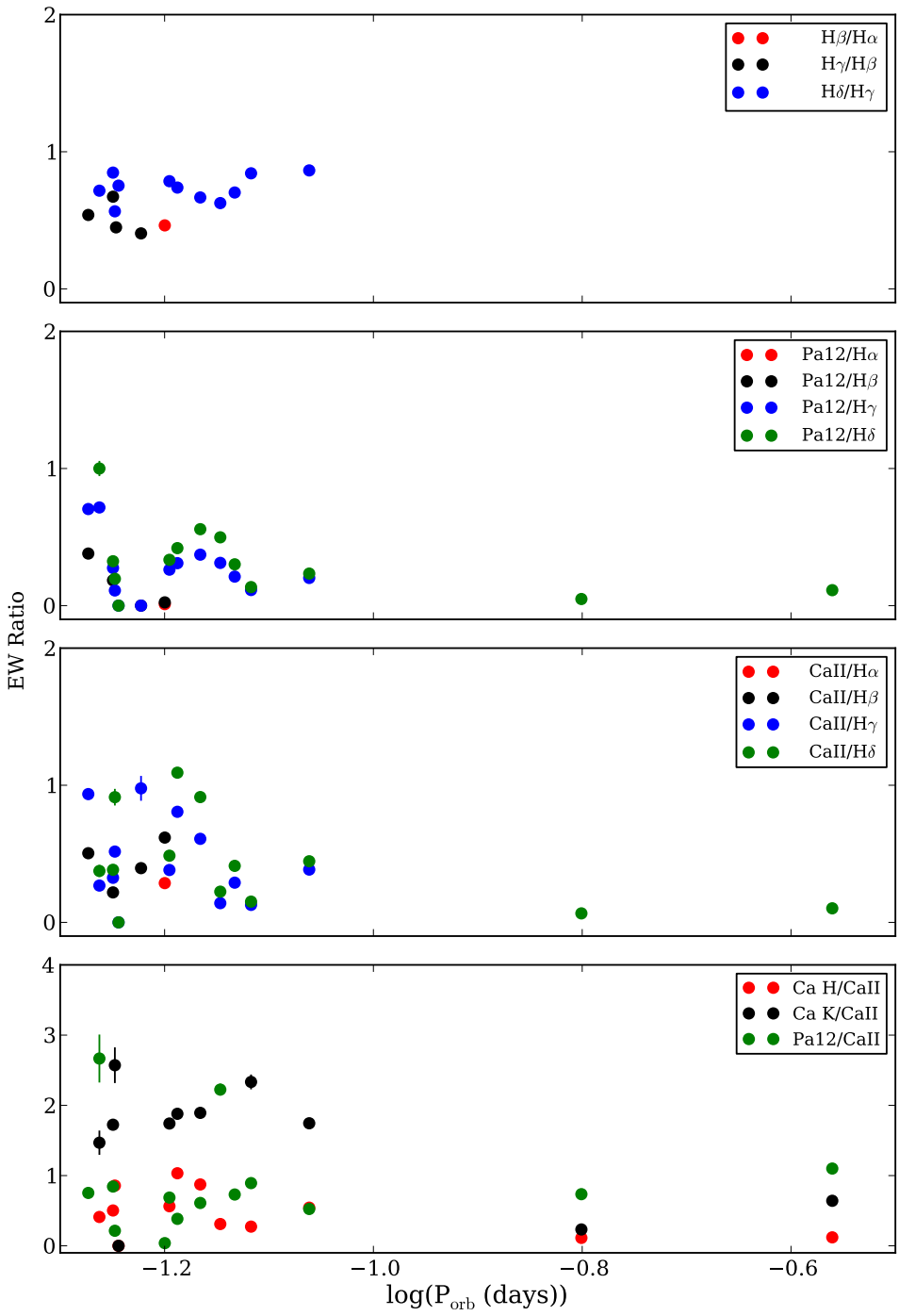

Figure 6-3: The relative strength (EW ratio) of the disc profiles visible in the spectra as a function of the period. **Top:** Balmer over Balmer. **Middle-Top:** Paschen over Balmer. **Middle-Bottom:** Ca II λ8662Å over Balmer. **Bottom:** Ca H, Ca K and Paschen 12 over Ca II λ8662Å. Error bars are generally smaller than the marker size.

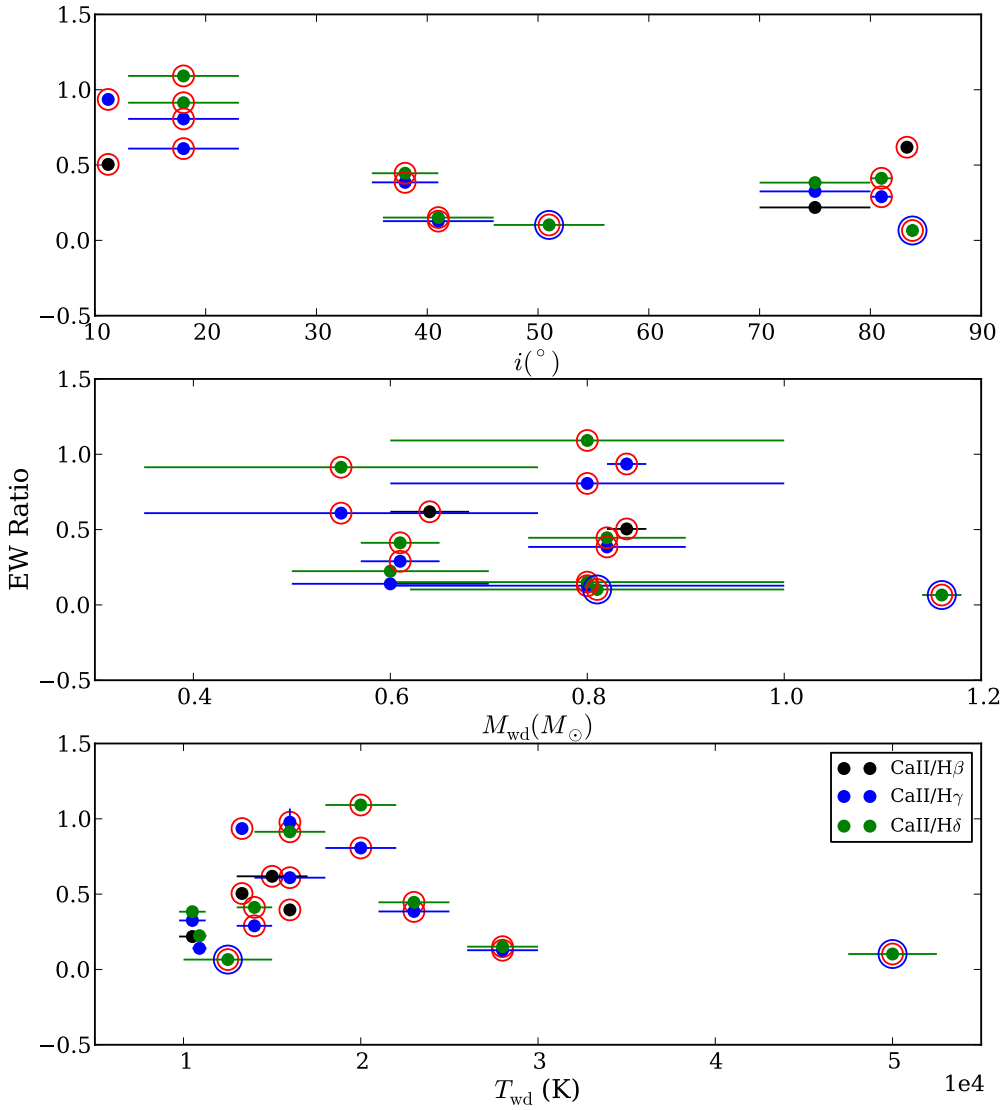

Figure 6-4: **Top:** The relative strength of the Ca II to the Balmer lines visible as a function of inclination i. All labels as indicated in the bottom panel. All data points with a red circle show the donor star in emission in the Ca II triplet lines, while blue circles denote the presence of donor absorption lines. **Middle:** Relative strength as a function of the mass of the WD. **Bottom:** Relative strength against temperature of the WD.

only observed system with a known WD mass ($\sim 0.6 M_\odot$) and no visible donor features.

For the short period systems, we lack system parameters exactly when the presence of donor emission is not guaranteed, reducing our limited sample size even further. This prohibits a search for the correlation between the WD mass and the presence of donor emission. Hence, we cannot draw any conclusions on the relation between the emission line ratios, the WD mass and the presence of donor emission.

WD Temperature

The bottom panel of Figure 6-4 shows the relative strength of Ca II compared to the Balmer lines as a function of the WD temperature (Table 6-1). As no errors are given for the WD temperature fits provided by Urban & Sion (2006), we adopt a conservative error of ±2500 K on their listed values for plotting purposes only.

We see that the trend between relative strength and WD temperature pivots at $T_{\rm WD} \sim 20\,000$ K, and displays a roughly linear decrease of relative strength towards lower temperatures and a roughly exponential decrease towards higher temperatures. The decrease in relative strength of the Ca II disc lines, combined with the absence of donor star emission at the lowest temperatures, suggests a tentative lower limit to the temperature needed to ionise Ca II at $\sim 11\,000$ K. This limit seems to be independent of the WD mass and orbital period (V455 And and GD 552 are the points without circles in Figure 6-5).

The trend shown in Figure 6-4 could be associated with the contribution of the WD towards the irradiation. At short periods, the disc is relatively cool due to low mass accretion rates and the donor is closer to the WD as the orbital separation is small. Hence the WD contribution towards the donor irradiation is relatively high compared to the disc contribution. With increasing period, the contribution of the WD decreases compared to the contribution of the disc as both the mass loss rate and the separation increase. We can cautiously say that the WD temperature does not affect the ratio of Ca II at long periods (only based on 2 data points), while it influences the ratios at short periods with a maximum contribution at a WD temperature and orbital period similar to that of UV Per (20 000 K and 93 minutes).

The WD temperature is potentially a more important parameter for the ionisation of the donor in low mass rate systems than the presence of outbursts. The cooling times of WDs is on scales of tens of thousands of year, while the increase in outburst temperature is only on timescales of 3–5 years as only the outer layers of the WD are heated. This temporary increase in temperature is much less important for systems that only exhibit an outburst on timescales of tens of years. If the WD is too cool to irradiate the donor, it will prohibit the use of the Ca II method for post-bounce systems as the WD is older, and hence cooler, in these systems.

Despite the existence of some tentative trends, we are limited by small number statistics, and more systems are needed to determine the correlation between the WD temperature

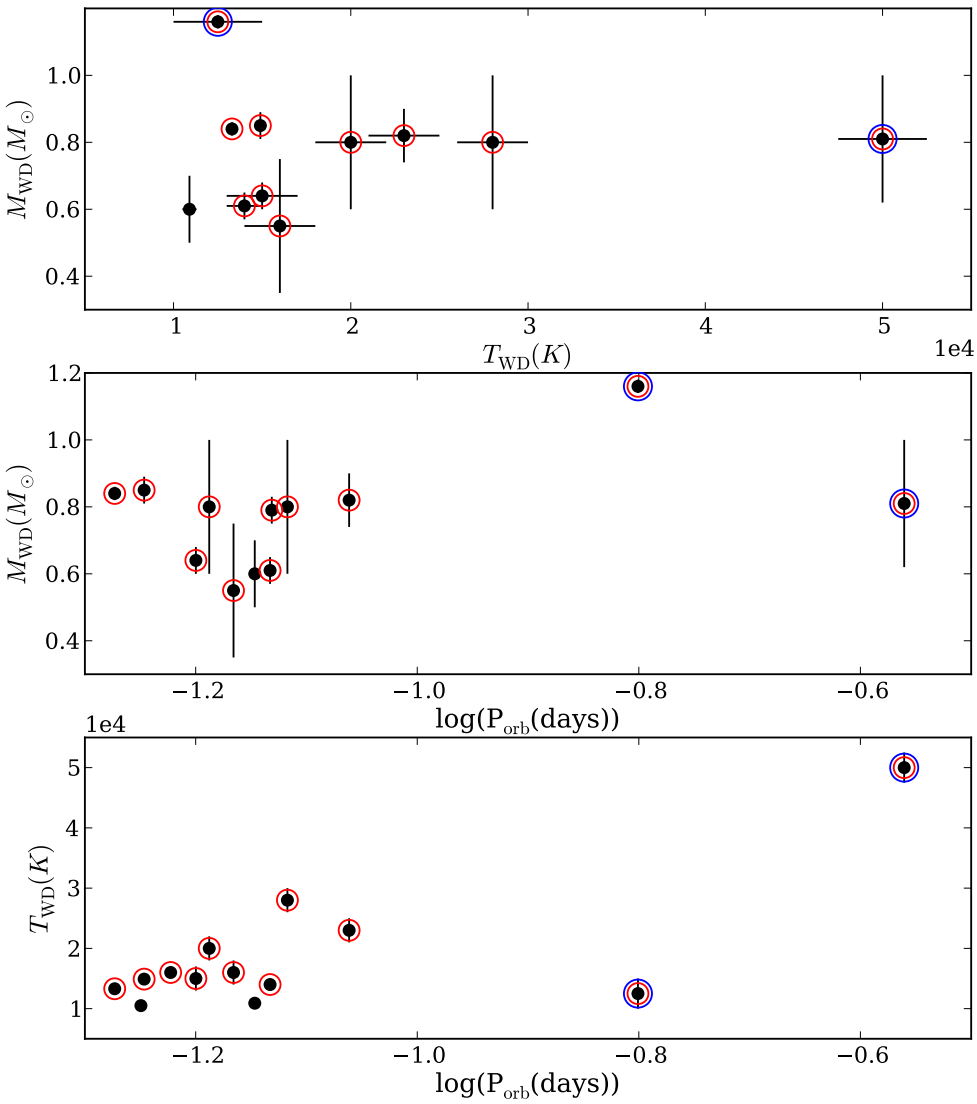

Figure 6-5: **Top:** $M_{\rm WD}$ as a function of $T_{\rm WD}$ for those systems that we have measurement of both. **Middle:** $M_{\rm WD}$ as a function of the orbital period. **Bottom:** $T_{\rm WD}$ as a function of the orbital period. The red circles denote the presence of the donor star in emission in the Ca II triplet lines and the blue circles denote the presence of donor absorption lines. The point without a donor is GD 552 in the top two panels, which is accompanied by V455 And in the bottom panel.

and the presence of donor emission (Figures 6-4 and 6-5).

Inclination

The top panel of Figure 6-4 shows the relative strength of Ca II lines to the Balmer lines as a function of binary inclination. For low inclination systems ($i < 20°$), the relative strength is high, decreasing towards moderate inclinations ($35 - 55°$) and returning towards slightly higher values at high inclinations ($i > 75°$). For intermediate inclinations,

the suppression in relative line strength can be explained by the fact that the Balmer lines all show strong, saturated single peaked disc profiles which are much broader and stronger than the Ca II profiles which remain double peaked.

The strength of disc emission lines is strongly dependent on the binary inclination i. Warner (1987) shows that the EW follows a $\cos i$ relation, that is, the total flux is smallest when we see the disc face on and largest when we see the disc edge on. This is counter intuitive, as it does not scale according to visible area (figure 8, Warner 1987), but can be explained if one assumes that the emission lines mostly form in an optically thin volume which is not totally obscured by the disc at high inclinations.

In accordance with Warner, we plot the EW for Balmer, Paschen and Ca II lines as a function of the inclination, see Figure 6-6. We also plot several $A\cos i$ relations for guiding purposes, with the amplitude A set to the maximum measured EW for each element, as no equation is given by Warner (1987). Independent of the proposed relation, we see in the top panel in Figure 6-6 that for all three lines (Balmer, Paschen and Ca II), the low inclination systems seem to have an equally strong or stronger EW than intermediate inclination systems.

The Balmer lines (top panel Figure 6-6) and Ca H (bottom panel, green points) are the only lines that broadly follow the proposed trend by Warner (1987), as the EW generally increases with increasing inclination, but the scatter is considerably. The Ca H line is most probably tracing the EW of the nearby Hϵ line rather than the EW of Ca H due to its proximity. All other lines show considerable scatter, and do not seem to follow the relation. For low inclination systems all EWs are stronger than the predicted value, but it is impossible to say whether the predicted value is incorrect due to an error in the assumption of a $A\cos i$ relation in general, or that the general trend should be of the form $A\cos i + B$, as the EW does not converge to zero at the inclination approaches zero. Whereas at large inclination, the relation is anchored to the largest measurement of EW for each line.

Thus, we cannot confirm the $\cos i$ dependence of the EW as proposed by Warner (1987).

6.5 Evolution of Ca II emission line features

In Chapter 5, we have seen that donor emission is present in the Ca II lines of 11 of our 18 observed CVs. To obtain a measure of the stability of these emission features, we have observed two objects on more than one occasion during our survey. By analysing

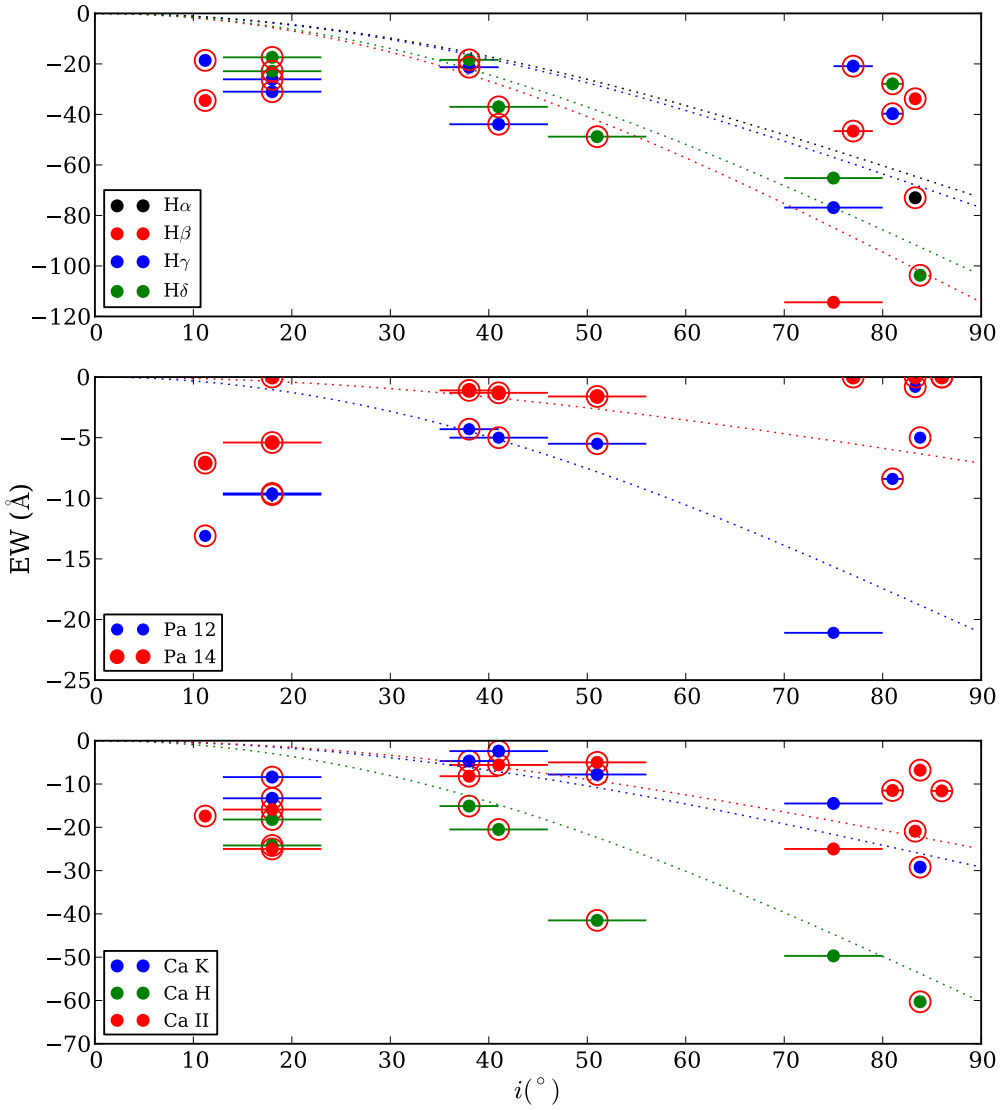

Figure 6-6: **Top:** The EW of the Balmer disc profiles as a function of inclination i for the CVs listed in Table 6-1. The *dotted* line is the expected $A\cos i$ dependency of the strength of the lines (Warner, 1987). All data points with a red circle show the donor star in emission in the Ca II triplet lines, points without are circle display no donor emission features. **Middle:** The EW of the Paschen lines as a function of the inclination. **Bottom:** The EW of the calcium lines as a function of the inclination.

Table 6-2: WHT - ISIS GW Lib and V455 And observations.

Date	Phase Coverage (T_{obs}/P_{orb})	Number of Spectra	Wavelength Coverage (Å)	Spectral Resolution (Å)	Exp time (s)	S/N
GW Lib						
24/07/2007	1.08	19	4200-5000	0.6	240	15
			8050-8800	0.62	240	10
25/07/2007	1.35	25	4200-5000	0.6	240	15
			8050-8800	0.62	240	9
26/05/2008	1.17	20	4600-5200	1.3	240	8
			8300-9050	1.14	240	7
06/04/2009	1.11	17	4450-5350	1.3	240/320	9
			8150-9150	1.14	240/320	6
V455 And						
22/07/2007	1.87	35	4200-5000	0.66	200/300	–
			8050-8800	0.54	200/300	–
25/07/2007	2.64	39	4200-5000	0.66	300	–
			8050-8800	0.54	300	–
07/12/2008	1.40	34	3800-5400	1.83	180	–
			7900-9400	1.55	180	–
09/12/2008	2.26	25	3750-4550	1.09	300/360	–
			8350-9000	0.83	300/360	–

the data as a function of time, this will provide an insight into the long term evolution of the strength of Ca II emission lines in DNe. For this particular purpose, we observed GW Lib on 4 nights at different intervals after its long anticipated outburst in April 2007, and V455 And was observed both before (July 2007) and after the September 2007 super outburst (December 2008).

6.5.1 GW Lib

Observations and reduction

GW Lib was been observed on two consecutive nights in July 2007, and on one night in both May 2008 and April 2009. All runs cover a minimum of one orbit. The first two nights were part of our 2007 WHT/ISIS run and the data acquisition and reduction is discussed in section 3.2. The latter two epochs were obtained via service mode observations with WHT/ISIS and have been reduced in the same manner as all spectra obtained with this instrument (Section 5.1.2). Table 6-2 lists the details for all observations of GW Lib. Figure 6-7 shows the orbitally averaged Hβ and Ca II triplet profiles for the 3 distinct epochs in 2007, 2008 and 2009.

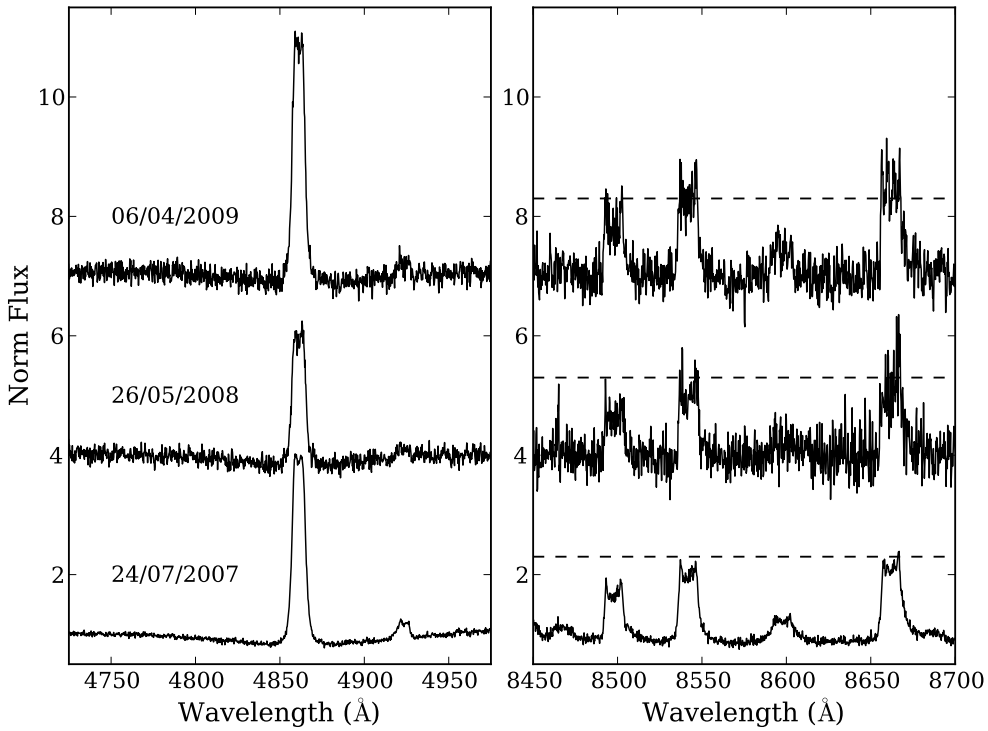

Figure 6-7: The average spectra of GW Lib at 3 different epochs. Left: Hβ on (from bottom to top) 24 July 2007, 26 May 2008 and 6 April 2009. Right: The Ca II triplet lines during these same epochs. The maximum relative flux in the July 2007 Ca II spectrum is indicated with the *dashed* line. This same level is also indicated in the May 2008 and April 2009 data.

EW measures

We measured the EW of the Hβ and the Ca II triplet lines for all epochs (Table 6-3). As window for Hβ we used $\pm$1000 km s^{-1}, while we employed $\pm$500 km s^{-1} for all Ca II lines. In the same manner as described in Section 5.2, we removed the absorption feature from the WD by re-normalising the window before measuring the EW of the disc. In 2008, the Hβ profiles and EW measures suggest a decrease in strength of $\sim$ 25% for all lines. However, this trend does not continue as the lines are back to original strength in 2009.

The maximum flux for the Ca II λ8662Å emission line in July 2007 is 1.306(3) in relative flux units. In Figure 6-7, we indicate this level with a *dashed* line. Despite the decrease in S/N, the relative flux for the lines does not change significantly at all epochs.

Table 6-3: EW measurements for GW Lib and V455 And as a function of time. For GW Lib, the window for Hβ is $\pm$1000 km s^{-1} and $\pm$500 km s^{-1} for all Ca II lines. For V455 And the window is set to $\pm$2000 km s^{-1} for Hγ and $+1600/-2100$ km s^{-1} for Ca II λ8662Å/Pa 13. The overlapping Ca II/Pa 16-15 lines are covered from λ8428 - 8598Å. The last 3 columns list the values for $K_{\rm disc}, K_{\rm em}$ and the superior conjunction of the WD (HJD$_0$), determined from the Doppler maps for the 4 epochs of GW Lib.

Date	Balmer EW (Å)	Ca II-Pa16 EW (Å) 8498.02 Å 8502.48Å	Ca II-Pa15 EW (Å) 8542.09 Å 8545.38Å	Ca II-Pa13 EW (Å) 8662.14 Å 8665.02Å	$K_{\rm disc}$ (km/s)	$K_{\rm em}$ (km/s)	HJD$_0$ + 2 454 000
GW Lib	Hβ						
24/07/2007	-34.5(1)	-10.4(1)	-17.2(1)	-17.4(1)	9±7	80±34	306.38053
25/07/2007	-36.7(1)	-12.2(1)	-19.1(1)	-19.8(1)	11±7	90±36	307.38228
26/05/2008	-25.2(3)	-10.2(4)	-13.9(3)	-14.7(4)	12±11	85±37	612.61999
06/04/2009	-37.4(2)	-14.6(3)	-19.1(3)	-21.1(3)	6±11	76±35	928.55358
V455 And	Hγ						
July 2007	-42.3(1)		-7.5(2)	-14.0(2)			
Dec 2008	-83.9(1)		-29.2(2)	-25.0(6)			

Signal to Noise

The decline of the entire system towards quiescence expresses itself as a decrease in S/N over time, as seeing conditions at all epochs are comparable and exposure times remain equal (with the exception of the 2009 epoch). This decrease in S/N can also be seen in the individual Ca II Doppler map of the λ8662Å line for all 4 epochs (Figure 6-8). The July maps show clear disc and donor features. The May 2008 map shows a lower S/N, and very asymmetric disc ring but still a strong donor emission spot. The April 2009 map displays an almost absent accretion disc and only weak emission at the location of the donor. However, these latter data suffered from worse weather conditions, requiring an increase in exposure time and hence a poorer phase resulution. Note that the donor star can nonetheless be seen in all 4 epochs.

Quality of maps

In Table 6-3 we list the values for $K_{\rm disc}, K_{\rm em}$ and the superior conjunction of the WD (HJD$_0$) as determined from the Doppler maps at the 4 individual epochs. As in Chapter 5, the rotation angle of the Doppler map is translated into the phase zero point which can be converted into HJD. The centre of symmetry searches for the disc emission returns $K_{\rm disc,MEM}$, and the emission spot associated with the irradiated donor gives $K_{\rm em,MEM}$. As these values are the minimum requirement to constrain the dynamical mass ratio, it is encouraging that the values derived over the 4 different epochs are consistent with

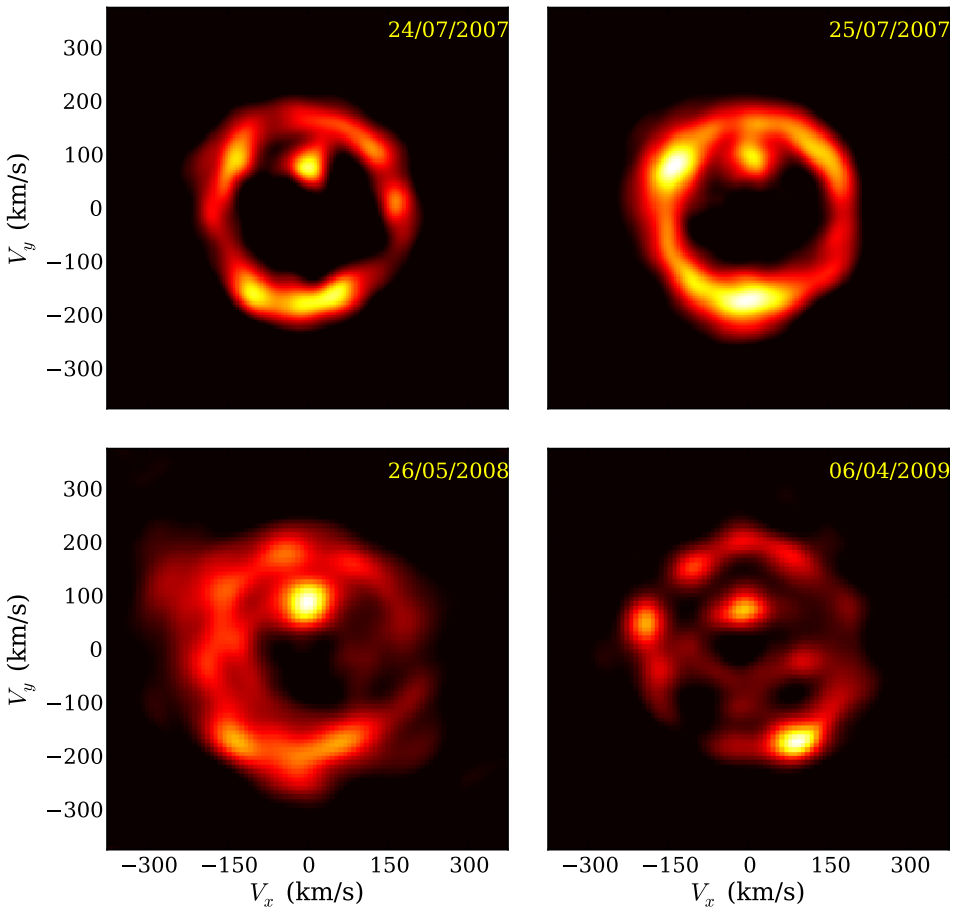

Figure 6-8: The Doppler maps of GW Lib at 4 different epochs. All maps are rotated such that the donor emission locates itself at $V_x \sim 0$. Using the rotation angle of the map as a measure of the ϕ_0 of the orbital period, it is possible to determine an absolute ephemeris, listed in Table 6-3.

each other. Even the latest map, which was obtained during poor observing conditions provides consistent values for all quantities.

Period constraints

Using the Doppler map, we can determine individual phase zero points, even when individual RV fits to the emission line are not possible. These zero points can be used as a first constraint on the period, when the traditional method of using RV fits to time-resolved spectra fail. This section explores the possibilities of this method using the 4 epochs of data of GW Lib. We do not aim to improve the already published orbital period ($P_{\rm orb} = 0.05332(2)$days; Thorstensen et al. 2002) or ephemeris (3.4.1) of GW Lib, but only wish to display the strength of Doppler maps in low S/N cases.

From the four epochs of data, we can determine the phase zero points, see Table 6-3. With the use of a simple periodogram based on a least squares analysis, an indication of the period can be found by testing the quality of a sinusoid function fit with as only constraint it has to pass through to all four zero points, see Figure 6-9. We also indicate the spectroscopically determined period. As expected, 4 data points are not enough to uniquely constrain the period. Note, additional care should be taken when interpreting the phase zero point of the Doppler maps as these maps have been created using the period listed above, and the location of the emission (and hence the angle), changes slightly when the spectra are folded onto a different period. Nonetheless, such a method would in principle permit a measurement of the orbital period when traditional methods fail due to low S/N.

6.5.2 V455 And

Observations and reduction

We observed V455 And on two separate occasions with WHT/ISIS. The first observations were carried out during the July 2007 campaign. The second set of observations was driven by the recorded superoutburst in early September 2007 (Maehara, 2007). Unfortunately, the earliest opportunity for Ca II observations after this outburst was not until December 2008. Details of the observing runs are listed in Table 6-2. The July 2007 orbital average Hγ profile and red spectrum (Figure 6-10) are constructed from a total of 74 spectra with exposure times of 300 seconds (Table 5-4) while the December 2008 average spectra (Figure 6-10) are constructed from a total of 59 spectra with exposure times in the range 180 - 360 seconds (Table 5-5). The change in exposure time

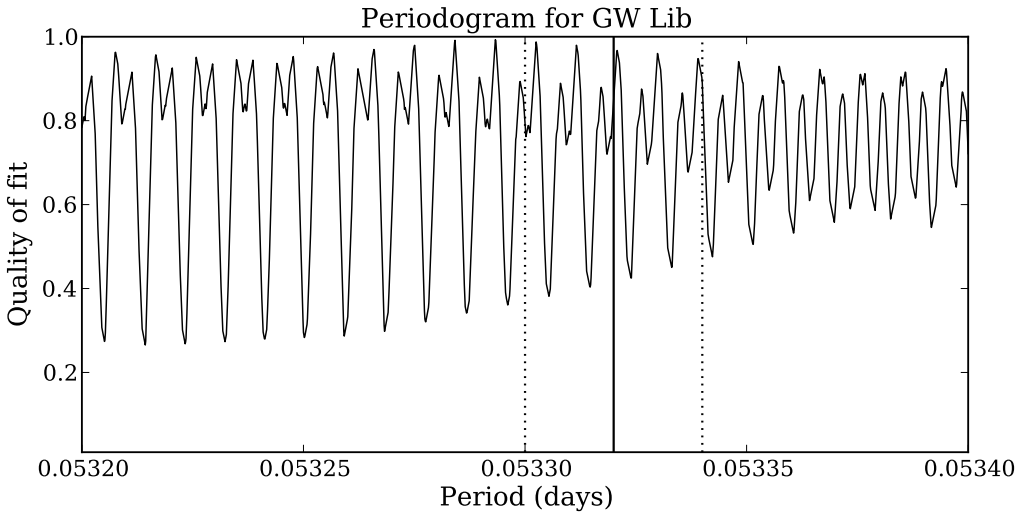

Figure 6-9: Periodogram for GW Lib using the 4 phase zero points listed in Table 6-3. For a range of periods, the quality of the fit for these solutions is calculated, minima indicate better solutions. The vertical *solid* line indicates the orbital period as determined by Thorstensen et al. (2002) (with *dashed* error bars).

is dictated by the use of a higher resolution diffraction grating and a brightening of the system, hence S/N values are not directly comparable and for this reason omitted from the table.

EW measures

The EWs of both epochs are given in Table 6-3 using a ± 2000 km s^{-1} window for Hγ after normalisation of the spectrum, and a $+1600/-2100$ km s^{-1} window for the Ca II λ8662Å – Pa 13 λ8665Å combination. The two other Ca II lines are measured together due to blending. Concentrating on the Hγ and Ca II λ8662Å – Pa 13 profiles, it is clear that the EW increases by a factor of 2.0 and 1.8, respectively, after the outburst. Unfortunately, no signatures of the donor are visible in either epoch.

Dominant blend contribution: Paschen?

Using the triple peaked profile centred on the Ca II λ8662Å-Pa 13 blend (Figure 6-10), we can try to determine which is line is the dominant contributor to the blend. For this, we fit the profile with 2 double Gaussians representing the Paschen 13 and Ca II lines while forcing one of the two to be the main contributor to the profile.

We first investigate whether the main profile is produced by Paschen, and Ca II is used to fit the left most peak. To recover the strength of this latter peak, we need to

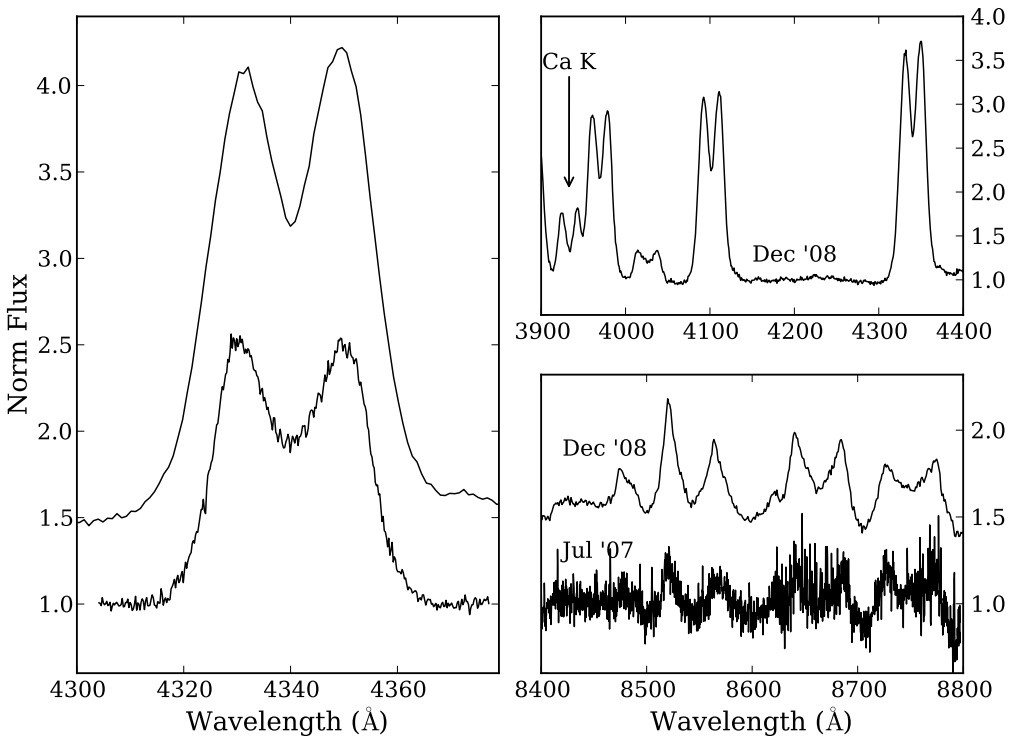

Figure 6-10: **Left:** The normalised orbital average profile for Hγ for V455 And in July 2007 (bottom) and December 2008 (top). **Bottom right:** The average red spectra covering the Ca II triplet lines. **Top left:** A broader wavelength coverage for the blue December 2008 spectrum, indicated is the Ca K line.

offset the 2-Gaussian representing Ca II by ~ -700 km s^{-1}. The resulting combined profile fits the high velocity wings of the profile well and the right side of the Ca II profile fills the centre of the combined profile (bottom left panel, Figure 6-11). The quality of the fit is $\chi^2 \sim 28$. The main weakness of this fit lies in the offset needed for the Ca II profile with respect to the Paschen line to fit the left most peak, and the fact that there appears to be strong Ca K emission at λ3933Å without this offset (see top right panel in Figure 6-10).

Dominant blend contribution: Or Calcium?

Next, we investigate the possibility of fitting the profile predominantly with Ca II. For this case, we identify the left most peak as part of the Pa 14 λ8598Å disc profile. This Paschen line blends with Ca II λ8662Å on the left hand side and with Ca II λ8592Å on the right hand side. The complexity of the combined profile discourages a complete free fit. The bottom right panel in Figure 6-11 displays our fit to the peak with mainly Ca II

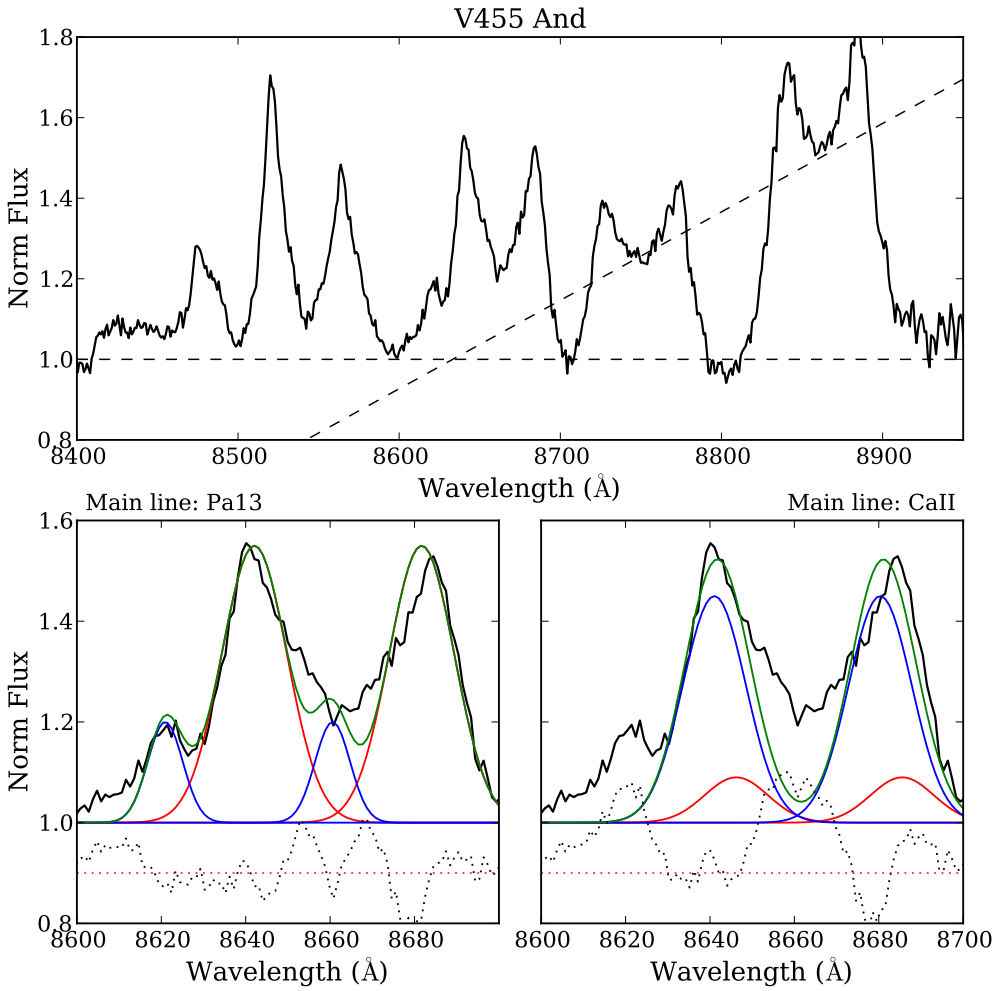

Figure 6-11: **Top:**The V455 And average, normalised red spectrum in December 2008. The normalisation level is shown by the *dashed* horizontal line. The strength of Pa 13 under the Ca II λ8662Å line can be interpolated from the strengths of the Pa 12 and Pa 11 profiles (*dashed* diagonal line). We estimate that the Pa 13 contribution (measured for the central dip in the profile) is $\sim 20\%$ of the total profile. **Bottom left:** Average Ca II λ8662Å- Pa 13 profile with the best double 2-Gaussian fit, and the main contribution being forced to be Paschen (red) while Ca II (blue) is shifted to fit the small left peak. The goodness of fit is $\chi^2 \sim 28$. The black *dotted* line shows the residuals of the combined fit (green) and are shifted upwards to 0.9 (*dotted* red line). **Bottom right:** The same profile, but now regarding the small left peak as Pa 14, which is ignored when fitting the profile with Ca II (blue) and Pa 13 (red) at 20% of the strength of Ca II. The residuals are plotted (around 0.9, *dotted* red line) and give $\chi^2 \sim 30$.

and a small Paschen contribution. In this fit, the left most peak is ignored, and the contribution of Paschen to the disc profile is estimated to be $\sim 20\%$ using the trend in the Paschen series (*dashed* diagonal line in the top panel of Figure 6-11). The separation, FWHM and offset for both profiles are free parameters while the height is constrained such that $\text{peak}_{\text{Pa13}} = 0.2\text{peak}_{\text{Ca II}}$. The residuals look rather poor but are of similar quality to the earlier fit when dominated by Paschen, with $\chi^2 \sim 30$. This poor χ^2 is mainly driven by the misfit to the centre of the profile, which is because the 2-Gaussian is not a perfect representation of the low velocity centre of the disc profile.

Even though we cannot distinguish the two fits based on the χ^2 value, the fact that Ca II λ8662Å would have to be Doppler shifted by ~ -700 km s^{-1}, whilst Ca K appears to be present with no shift, leads us to believe that Ca II λ8662Å-Pa 13 blend is mainly dominated by calcium rather than Paschen. Our conclusion is further supported by the downward trend from Paschen 11 to Paschen 12 (diagonal dashed line in Figure 6-11), which indicates only a small contribution of Paschen 13 to the profile.

Time since outburst

For all our CV observations we have determined the time since the most recently observed super outburst, using the AASVO data base (Table 5-1). Even though the time since outburst was not a selection criterion for our targets, we observed systems within less than a month to more than 5 years post outburst in our survey. We plot the EW ratios of Ca II over Balmer versus the time since outburst (in months) in the top panel of Figure 6-12, and indicate the presence of a donor emission component by circles (red: donor in emission, blue: donor in absorption). The last data point in Figure 6-12 is V1108 Her, which is not a reliable point as we lack phase coverage to claim the absence or presence of the donor. The same is true for V632 Cyg, at ~ 9 months. The absence of donor features seems to be independent of the time since outburst as both V455 And and V844 Her were observed within 15-16 months of their outburst and show no signs of donor emission, whilst ASAS 0025 displays emission more than 3 years after its outburst.

For GW Lib, we separately plot the EW ratio as a function of time since outburst (bottom panel, Figure 6-12) as we can measure this ratio at 4 separate epochs. Remarkably, this ratio is constant over timescales of 2 years, even though the individual EWs vary by $\sim 30\%$ (Table 6-3).

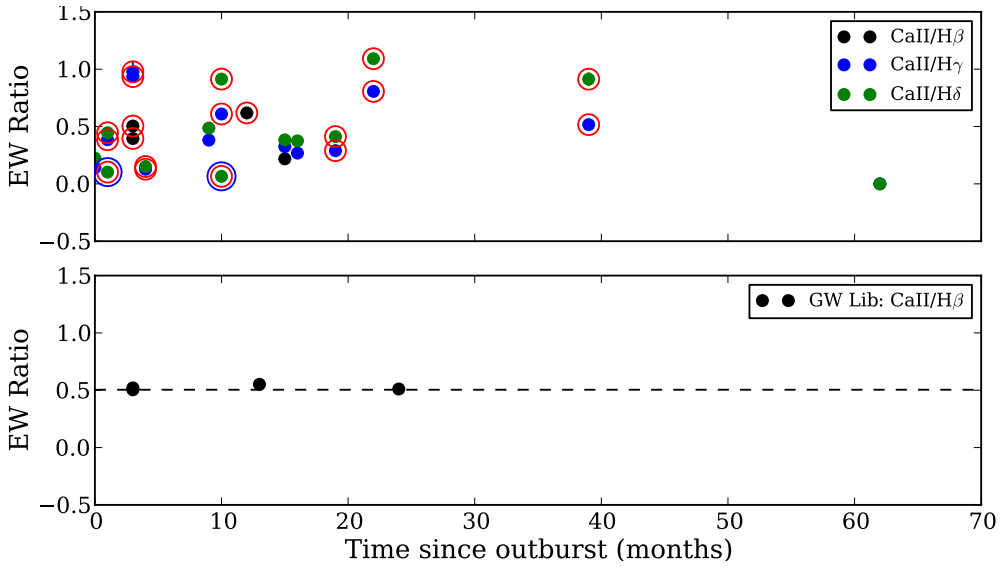

Figure 6-12: **Top:** Ca II/Balmer EW ratio versus time since outburst in months. The red circles surrounding the data points denote the presence of the donor in emission, and the blue circles denote the presence of the donor in absorption. **Bottom:** The EW ratio of Ca II to Hβ in GW Lib as a function of the time since outburst. The *dashed* horizontal line is the ratio of the first epoch.

6.6 Summary

In this Chapter we discussed the emission line profiles in relation to the various system parameters. We find:

- At long periods ($\gtrsim$100 min) both disc and donor star features are visible. At shorter periods, Ca II disc features are very common ($\sim$ 90% of the sample) but donor emission is present in only half of the sample.

- At low inclination ($\lesssim 20°$), the Ca II triplet disc lines display more detail as the double peaked profiles are intrinsically wider for calcium than for hydrogen at the same inclination. For modest inclination systems ($35 - 55°$), with strong, saturated hydrogen profiles and hence single peaked, the Ca II lines keep their distinct double peaked shape. The Balmer features in high inclination systems ($\gtrsim 75°$) are dominated by strong central absorption. In stark contrast, the Ca II triplet lines remain free from this effect. Thus in all cases, the Ca II lines offer a cleaner insight into the disc. This is highlighted in the cleaner and sharper Doppler maps for Ca II for all systems.

- The ratio of Ca II to Balmer EW is largest at low inclinations.

- We cannot confirm the proposed $\cos i$ relation by Warner (1987) between the inclination and the EW.
- Low WD temperatures ($\lesssim 11\,000$ K) seem unable to irradiate the donor and/or disc sufficiently to generate in Ca II emission.
- The WD temperature contributes to the EW ratio of the Ca II to Balmer lines in short period systems. This effect decreases with increasing orbital period, and hence increase in orbital separation, as the WD contribution becomes less important for larger and hotter discs.
- No dependence on WD mass is found for the detection of disc and donor emission lines in Ca II.
- The time since outburst does not seem to be of importance for the presence of donor emission in Ca II, as we find donor emission in a broad range of times since outburst, and an absence of donor emission even in systems that had a very recent outburst.
- The strength of the Ca II lines is stable over the course of 2 years for GW Lib. In V455 And, the outburst increases the strength of the disc lines, but the donor remains absent in this system.

Chapter 7

Ca II survey III: Ca II as tracer of q in DNe

In the previous Chapter we discussed the general properties of the emission line profiles present in the spectra of our sample. Now, we will return to the more detailed study of those systems that display donor features. In Chapter 5, we compiled radial velocity curve fits for the different binary components visible in the spectra (disc, donor and WD; Tables 5-10, 5-11 and 5-12). As the measured radial velocity depends on the both the method and the line used, the determining the true motion of the WD (K_1) or donor star (K_2) is complex and prone to systematics. In this Chapter, we will discuss how to translate the observed radial velocities into constraints on the true radial velocities of the stellar components.

With the best estimates for K_1 and K_2 in hand, the dynamical mass ratio can then be constrained in our sample of short period CVs. We will compare our derived mass ratios with independently derived values for several systems in order to validate our method and test the quality of our results.

7.1 Measuring K_1

The radial velocity of the WD is only directly measurable through photospheric absorption lines of metals originating in its atmosphere. However, these lines are only rarely visible and require both a low mass accretion rate and a low inclination to avoid blending with nearby rotationally broadened lines. The most commonly used method to trace the WD motion is via the radial velocity of the disc lines as the disc should trace the WD motion. To measure this motion, the commonly used methods are a 2-Gaussian fit to the profiles and the diagnostic diagram method. In addition to these methods, we exploited Doppler tomography, in which the influence of any disc asymmetries can be avoided or at least reduced, by using the centre of symmetry of the disc ring as a measure of $K_{\rm disc}$.

7.1.1 Methods

Below is a description of the merits of each of these methods. We list the average value of $K_{\rm disc}$ (excluding any outliers by more than 5σ) in Table 7-1, followed by the minimum value of $K_{\rm disc}$. Since higher values are most likely distorted by hotspot emission and other disc asymmetries, the method that returns the lowest value may be considered the least affected by such asymmetries.

Direct measure of $K_{\rm wd}$

In a few cases (GW Lib, WZ Sge and UV Per), a direct measure of the radial velocity of the WD is possible as absorption lines from the WD atmosphere are visible. However, in none of these cases do these absorption lines trace the WD motion directly. For WZ Sge, the emission is misaligned with the donor phase (Steeghs et al., 2007). UV Per lacks sufficient signal to noise to fit the absorption lines as a function of orbital period. For GW Lib, the error on the orbital period is too large to phase-lock the motion of the donor with the absorption.

Despite the lack of direct measures in this work, this is the most secure route to measure K_1 as it should trace the WD directly and the presence of photospheric absorption lines highlights the potential for the direct measure of the WD motion in several systems.

2-Gaussian fits to disc lines

For the 2-Gaussian fits, we fix the offset between the two Gaussians to the offset given by a completely free fit to the orbital average disc profile. During the phase-resolved fit, we allow the peak and FWHM to vary, but impose the constraint that they have to be the same for both profiles. The error bars on the individual fits are scaled such that the reduced χ^2 of the RV fit is ~ 1. A visual inspection of the fit to the initial profiles is vital to judge the quality of the fit as the hotspot dominates the fit in most cases.

DD-diagram of disc lines

Using a diagnostic diagram, we find radial velocity amplitudes of the disc as a function of the fixed offset between the two Gaussian profiles. In principle, this method allows one to probe the high velocity wings of the profile, avoiding the hotspot. However, in practice we find that this method returns very similar results for all RV fit parameters when compared to the 2-Gaussian method, within the individual errors. Also, the results

of the DD method depend on the S/N of the data, a problem not encountered with the centre of symmetry method.

To obtain errors, we average the results over the Gaussian separations that form the minimum plateau (Figure 2-5), and the final error is given by the standard deviation of the results.

Centre of symmetry

Searching for the centre of symmetry of the disc feature in a Doppler map generally returns the smallest value for $K_{\rm disc}$. Care should be taken with this method, however, as the centre of symmetry must be calculated for a multitude of regions and only after optimising the map for the systemic velocity. In some cases, the results are highly dependent on the choice of these parameters. This is typically the case if the map shows no clear disc ring, in which case the results are omitted from Tables 5-10, 5-11 and 5-12. As with the Gaussian fits, the errors on $K_{\rm disc}$ determined from the maps are typically dominated by systematic effects, see Section 2.3.3 for a discussion.

Table 7-1 lists the average $K_{\rm disc}$, calculated from the values in Tables 5-10, 5-11, 5-12. The minimum value for $K_{\rm disc,min}$ is listed alongside published radial velocities of the WD ($K_{1,\rm prev}$). These values are either direct measures or derived from eclipse solutions. Tulloch et al. (2009) show that for the eclipsing CV SDSS 1433+1011 the derived value for the WD, K_1, via time-resolved spectroscopy of the double peaked Hα profile, is consistent with the value derived from the eclipse light curve fit by Littlefair et al. (2008). This supports the validity of results obtained using the eclipse fitting technique.

7.1.2 Balmer versus Ca II

The choice of whether to use Balmer or Ca II lines to determine system parameters is governed by the interplay between their relative strength, the orbital inclination (including broadening and central absorption) and contamination with nearby lines.

Whereas the Balmer disc lines are easily accessible, generally strong and plentyfiful, they are more easily saturated. This results in the loss of the double peaked emission line signature of the disc and a blurred Doppler map. Both effects reduce the effectiveness of using Balmer lines for measuring $K_{\rm disc}$ via any of the above methods.

On the other hand, the Ca II lines show a wider and clearer double peaked disc profile, which results in better measures of $K_{\rm disc}$ for all methods. The advantage of

Ca II over Balmer lines is highlighted in the Doppler maps, as even for low inclination systems, the disc ring is clearly resolved in the Ca II maps, while in the Balmer maps, the disc remains featureless and does not resolve into a ring.

The main drawback with the Ca II lines is that they are not always present and due to the faintness of the red end of the spectrum, combined with the decreased effectiveness of CCDs at this wavelength, require longer observations to return the same S/N levels. A second issue comes from their close proximity to the neighbouring Paschen lines. The Ca II profiles are actually a blend between Ca II and Paschen. The only way to measure the contribution of Paschen 13 to the Ca II λ8662Å profiles is to estimate the trend from Paschen 11 to 12, their direct neighbours, as is done in Section 6.5.2. Finally, in high inclination systems, the two Ca II lines at λ8458Å and λ8542Å blend together, which leaves only Ca II λ8662Å free to use for analysis.

Finally, it is worth mentioning Ca K at λ3933Å; this line is easily covered simultaneously with several Balmer lines and remains unblended at moderate inclinations. The main disadvantage of this line is that it is situated on the edge of the Balmer line forest, which makes the underlying continuum difficult to normalise and it has a tendency to be dominated by central absorption for moderate to high inclinations.

We conclude that if the radial velocity of the WD is not directly measurable, the next best method is to measure $K_{\rm disc}$ using the Ca II triplet lines, via a centre of symmetry search.

7.2 Measuring K_2

In Chapter 5, we measured the emission and absorption components arising from the donor surface using various methods, see Table 7-1. Here we will discuss the quality of each of these methods. To find the true radial velocity of the donor star K_2, we will calculate emission line models to derive the K-correction, $\Delta K = K_2 - K_{\rm em}$.

7.2.1 Methods for measuring $K_{\rm em}$ or $K_{\rm abs}$

The various methods to measure these values are: 1-Gaussian fits to the profiles (emission and absorption), fitting the location of the donor emission in the Doppler map and cross correlating absorption spectra.

Table 7-1: Radial velocity measurements and K-correction. The average $K_{\rm disc}$ is calculated from the values in Tables 5-10, 5-11, 5-12. The minimum value for $K_{\rm disc,min}$ is listed alongside published radial velocities of the WD ($K_{1,\rm prev}$). These values are either direct measures or derived from eclipse solutions. The value for $K_{\rm em}$ is generally taken from RV fits, and for those values only measurable from MEM maps, the error on the value is given as a 10% error rather than the FWHM of the spot. The ΔK is derived from multiple irradiation models to reproduce the measured emission radial velocity, such that $K_2 = K_{\rm em} + \Delta K$. Finally, previously measured radial velocities of the donor ($K_{2,\rm prev}$) and absorption components ($K_{\rm ab}$) are listed. The absorption measures for IP Peg and SS Cyg are also given in Chapter 5.

Object	$K_{\rm disc}$ km s^{-1}	$K_{\rm disc,min}$ km s^{-1}	$K_{1,\rm prev}$ km s^{-1}	$K_{\rm em}$ km s^{-1}	ΔK km s^{-1}	K_2 km s^{-1}	$K_{2,\rm prev}$ km s^{-1}	$K_{\rm ab}$ km s^{-1}
GW Lib	14.6±1.8	11±7	13±2[1]	82.2±1.6	22±5	104.2±5.3	–	–
ASAS	19.5±6.7	18±13	–	193±16	41±6	234±17	–	–
WZ Sge	63.3±6.2	48±13	47±2[2]	402.9±0.5	94±37	497±27	493-585	–
HS 2219	58.8±6.4	40±13	–	250±25	70±8	320±26	–	–
OY Car	78.6±5.3	60±22	48±1	395.9±1.8	95±20	491±20	470±7	–
UV Per	28.7±1.3	21.5±3.2	–	103.3±1.6	32±6	153±6	–	–
TY Psc	84.7±2.4	47±7	–	230±23	83±23	313±33	–	–
IY UMa	109.7±8.1	63±10	55±2	383±38	100±11	483±40	443±10	380-540
HT Cas	90.6±3.3	42±13	58±11	344.4±4.7	89±9	433±10	389±4	450±25
SU UMa	37.7±4.9	31±15	–	206.8±4.8	47±13	254±14	–	–
YZ Cnc	64.0±10.6	31.8±1.9	–	145.5±1.9	46±9	192±9	–	–
IP Peg	172.4±6.7	141.0±4.1	151±3	190.0±4.1	132±43	322±43	317±2	360.8±4.8
SS Cyg	73.6±7.8	61.2±1.9	–	111.6±4.8	70±20	182±21		156.8±0.6

1-Gaussian fits to emission lines

Ideally, we would like to fit a 3-Gaussian profile to the entire emission profile, consisting of a 2-Gaussian with a fixed separation to trace the double peaked disc profile and a separate 1-Gaussian, independently tracing the donor emission component. Due to low S/N and limited phase coverage, this method is only possible in GW Lib. In many systems, an additional complication arises from the presence of a strong hotspot signature. This emission is typically stronger than the donor emission and prevents the use of a triple Gaussian fit.

For all other systems, we obtain the best results after the subtraction of the orbital average profile from the spectra, in order to remove the disc emission. This allows us to fit a 1-Gaussian profile to the remaining donor emission component. In most cases, we have to fix the peak height and FWHM of the profile to the orbital average value. All errors on the returned offset from the rest wavelength are scaled such that the reduced $\chi^2 \sim 1$ for the RV fit. For systems with a high inclination, the donor emission component is self-obscured and invisible around $\phi \sim 0$ and, depending on the inclination, we omit these parts of the curve from the fit. The errors on the radial velocities range from a

few km s^{-1} to a few tens of km s^{-1}, depending on the S/N of the data.

Location in Doppler map

We rotate the Doppler maps such that the emission associated with the donor is positioned at $V_x = 0, V_y = +K_{\rm em}$. Using the 2-dimensional locator tool in Gaia, a 2-D Gaussian is fitted to the emission spot. We can improve this fit for low S/N and or low phase resolution maps, by first subtracting a symmetric disc ring, centred on the centre of symmetry.

The FWHM of the fitted 2-D Gaussian profile can be interpreted as a rough estimate of the error on the donor's location via $\sigma \sim$FWHM/2.35. As the emission spot has an intrinsic width and is further broadened by the lack of sufficient phase and spectral resolution, the FWHM returns a significant overestimate of the error on the location and hence radial velocity of the donor. The donor radial velocity found in Doppler maps is in good agreement with the value derived from the RV fit to the single emission line. The main advantage of this method over the RV method is that even with low S/N data, the emission component is visible in the Doppler map. This is because the tomographic process reinforces real, weak features whilst suppressing noise in the spectra. For practical purposes, if only the Doppler map determined $K_{\rm em}$ is available, we set the error to 10% of the radial velocities for further calculations, see Table 7-1.

1-Gaussian fits to absorption lines

Similar to the 1-Gaussian fit to emission lines, we fit 1-Gaussians to the absorption lines visible in IP Peg and SS Cyg. The origin of the specific line is difficult to identify due to the presence of a forest of donor absorption lines in the immediate surroundings and hence, the rest wavelength of the fitted line is not reliably identified. This propagates into an unreliable measure of the systemic velocity, though it will not impact on the semi-amplitude determination, $K_{\rm abs}$.

Cross correlation of absorption lines

For the cross correlation, we used appropriate template spectra from the UVES POP (Bagnulo et al., 2003). After rebinning the template spectra onto the velocity resolution of the data, broadening the profiles to account for rotational broadening, and masking emission line regions, we find in both IP Peg and SS Cyg a similar value for the radial velocity as the 1-Gaussian fit value. The value for ϕ_0, derived from cross correlation is

in good agreement, albeit with smaller errors. The systemic velocity is reliable, as it is derived from a range of lines rather than just the assumed rest wavelength of a single line. Hence, we prefer the system parameter values from the cross correlation over the 1-Gaussian fit (Table 7-1).

Table 7-1 lists the value for $K_{\rm em}$ which is generally taken from RV fits. For those values only measurable from MEM maps, the error on the value is given as a 10% error rather than the FWHM of the spot. The ΔK is derived from multiple irradiation models to reproduce the measured emission radial velocity, such that $K_2 = K_{\rm em} + \Delta K$. Finally, previously measured radial velocities of the donor ($K_{2,\rm prev}$) and absorption components ($K_{\rm ab}$) are listed. The absorption measures for IP Peg and SS Cyg are also given in Chapter 5.s

Emission versus absorption

Both IP Peg and SS Cyg show the donor star in emission and in absorption. In both cases $K_{\rm em} < K_{\rm abs}$. This is visible in the trail of SS Cyg (Figure 5-17) as the absorption feature displays a larger radial velocity amplitude than the emission in the Ca II lines, and crosses the emission profile twice. The systems also display a difference in the profile width as the absorption is wider than the emission. This suggests a more localised origin for the latter.

The origin of the absorption is placed at a larger distance from the centre of mass, and with a larger area, most likely the back side of the donor. The most likely place of origin for the emission, on the other hand, is the front side of the lobe, near the L_1 point, see Figure 2-10. All this favours irradiation as the source of the emission rather than chromospheric emission, as the latter would arise from the entire Roche lobe and hence result in a larger radial velocity for the emission, combined with wider profiles.

7.2.2 Balmer versus Ca II

The only system in our survey that displays donor emission in more than one line simultaneously is OY Car, which displays emission in Hα, Ca II and K I. All lines return $K_{\rm em,MEM} \sim 410$ km s^{-1}, the first with an error of $\sim 25\%$, and the latter two with an error of $\sim 10\%$. This tentatively indicates that more massive elements provide a better localisation for the donor emission. ASAS 0025 and HS 2219A display the donor in Balmer lines only. However, the lack of sufficient S/N Ca II data means that it is

difficult to firmly rule out any Ca II donor emission.

Several studies find the presence of donor emission in Balmer lines in a small number of systems shortly after an outburst, and even in various metal lines (e.g. IP Peg; Harlaftis 1999). The outburst could supply the power to irradiate the donor up to higher latitudes, which results in a higher $K_{\rm em}$. This complicates the direct comparison between the donor emission in different lines and during different stages of the outburst cycle in DNe. However, all emission components present additional constraints for the final solutions as they must be smaller than K_2 due to irradiation.

Due to the short lived nature and unpredictable behaviour of outbursts in DNe, it is difficult to obtain time-resolved spectroscopy shortly after outburst, or revisit the system to confirm presence the of donor emission. Hence, we can conclude that Ca II is a fantastic alternative to the strong Balmer lines to find stable donor emission, in the long and easily accessible periods of quiescence in DNe.

7.2.3 K-correction

For those systems with donor emission, we construct light curve models to calculate the K-correction (ΔK) by optimising $K_1 + K_2$ to return $K_{\rm em}$ such that $\Delta K = K_2 - K_{\rm em}$ (Section 2.4). The models show a strong dependence on q, as in our irradiation code the emission is placed near the L_1 point, and the velocity of this point is a direct function of the mass ratio and the size of the system. Increasing the mass ratio moves L_1 towards the WD and we are required to stretch the system to keep the emission near the fixed, observed value. To identify the scale of the corrections imposed for different mass ratios, we use OY Car as an example and calculate the velocity scale (K_1+K_2) needed to return $K_{\rm em}$ for a range of mass ratios (Figure 7-1). As q increases, so does the required scale and hence K_2, prompting a higher value for the correction. The Figure includes a close-up of the Ca II Doppler map, showing the two extreme Roche lobe surfaces calculated for $q = 0.06$ and $q = 0.15$.

We calculate model light curves for all systems with donor emission and determine ΔK for a sensible range of mass ratios. To determine the final value of ΔK, we constructed models around $q_{\rm max}$, include the average value of ΔK to compute a new value for q and average the values into the final value of ΔK and $q_{\rm best}$. (Table 7-1). As the error is then governed by the spread in ΔK rather than the error on $K_{\rm em}$ as given by the choice of model parameters (Section 2.4.2), the models are constructed with a resolution

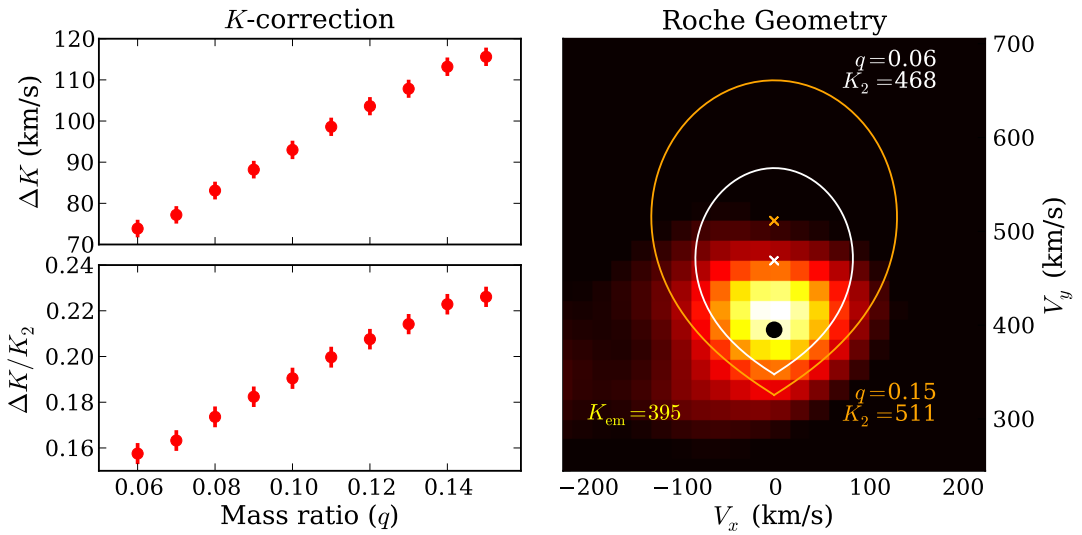

Figure 7-1: Calculated K-correction as a function of q for OY Car to give $K_{\rm em}$ = 395 km s^{-1}. **Top left:** Absolute K-correction with $\Delta K = K_2 - K_{\rm em}$. **Bottom left:** Fractional K-correction to K_2. **Right:** Close-up of the emission in the Ca II map overplotted by the Roche geometry for the minimum q model calculated (white) and the maximum q model (orange). Also plotted are the K_2 value ($\times$) and the Roche lobe for both models, and the location of the measurement of the donor emission ($\bullet$).

of 4Å, a phase resolution of 50 and a S/N ratio of 16 (i.e. much better than the data) to guarantee a good fit.

As seen in Section 2.4.2, the influence of the inclination on the measure of the radial velocity of the emission component is less than a few percent over the entire range. We endeavour to fix the inclination of the model to the system's value whenever possible, while for systems with an unknown inclination, we typically fix the model inclination to 45°.

7.3 Putting the puzzle together: constraining q

For those systems that display a donor star in emission, we can immediately derive an upper limit for the mass ratio ($q_{\rm max}$) using the measured radial velocity of the disc and the emission associated with the donor. As $K_1 < K_{\rm disc}$ and $K_2 > K_{\rm em}$, a firm upper limit on the mass ratio is set by:

$$q_{\rm max} = \frac{K_{\rm disc}}{K_{\rm em}}. \tag{7-1}$$

The best estimate for the mass ratio ($q_{\rm best}$) is derived from our best measure for $K_{\rm disc}$, which is typically the method that gives the lowest value since this should be least affected by disc asymmetries while still tracing the WD. We combine this $K_{\rm disc}$

Table 7-2: The limits on the mass ratio of the CVs in our sample. For reference purposes, previously determined mass ratios ($q_{\rm other}$) are also given (eclipse solutions, apart from WZ Sge and YZ Cnc, the superhump mass ratio ($q_{\rm sh}$; see references in Table 5-1) as well as the $v \sin i$ solution ($q_{v \sin i}$) and the links to the figures.

Object	$q_{\rm max}$ ($K_{\rm disc}/K_{\rm em}$)	$q_{\rm best}$ ($K_{\rm disc,min}/(K_{\rm em}+\Delta K)$)	$q_{\rm other}$	$q_{\rm sh}$	$q_{v \sin i}$	Figure
GW Lib	0.18±0.02	0.106±0.068	–	0.072	–	7-3
ASAS	0.10±0.03	0.077±0.056	–	0.035	–	7-4
WZ Sge	0.16±0.02	0.097±0.027	0.092±0.008	0.051	–	7-5
HS 2219	0.24±0.04	0.125±0.042	–	0.146	–	7-6
OY Car	0.20±0.01	0.121±0.040	0.102±0.003	0.110	–	7-7
UV Per	0.28±0.01	0.159±0.025	–	0.083	–	7-8
TY Psc	0.37±0.04	0.150±0.027	–	0.123	–	7-9
IY UMa	0.29±0.04	0.130±0.023	0.125±0.008	0.118	–	7-10
HT Cas	0.27±0.01	0.097±0.030	0.148±0.034	0.138	–	7-11
SU UMa	0.18±0.02	0.122±0.059	–	0.141	–	7-12
YZ Cnc	0.44±0.07	0.166±0.013	0.22±0.02	0.175	–	7-13
IP Peg	0.91±0.04	0.438±0.060	0.48±0.01	–	0.32±0.07	7-14
SS Cyg	0.66±0.07	0.337±0.040	–	–	0.685±0.015	7-15

with the best measure for the radial velocity for the emission from the donor ($K_{\rm em,RV}$, unless $K_{\rm em,RV} \ll K_{\rm em,MEM}$ as the emission spot measurement in the Doppler map created from the entire phase coverage is more reliable than RV fits to a part) and the K-correction towards K_2 (ΔK) via

$$q_{\rm best} = \frac{K_{\rm disc,min}}{K_{\rm em} + \Delta K}. \tag{7-2}$$

We calculate both $q_{\rm max}$ and $q_{\rm best}$ for all systems and list them in Table 7-2.

7.3.1 Constraining K_2

The measured $K_{\rm em}$ is constrained on two sides. As an upper limit, the emission cannot come from a location past the true radial velocity of the donor star. As a lower limit, the emission cannot come from a location inside the inner Lagrangian point as this would no longer constrain the emission to the donor surface.

Some long period CVs have reported slingshot prominences present shortly after or during outburst (e.g. IP Peg and SS Cyg: Steeghs et al. 1996, BV Cen: Watson et al. 2007). In these cases, the emission is associated with the donor, but enclosed within a magnetic loop extending into the primary Roche lobe. As these loops tend to find equilibrium near the centre of mass, they have a much smaller radial velocity component than K_2. More recently, similar emission features have been found in short period CVs in quiescence (e.g. SDSS J003941.06+005427.5: Southworth et al. 2010). As these features have very low radial velocities we can safely assume that the origin of

the emission seen in this work lies on the donor surface and is constrained between the inner Lagrangian point and the centre of the donor star such that $K_{L_1} < K_{\rm em} < K_2$ (see also Figure 2-10). We can estimate the radial velocity of the inner Lagrangian point using the approximation for R_{L_1}/a (Equation 1-10):

$$K_{L_1} = K_1 \left[(1 + \frac{1}{q}) \frac{R_{L_1}}{a} - 1 \right]. \tag{7-3}$$

Because R_{L_1}/a is only a function of q, the radial velocity of the inner Lagrangian point becomes a function of K_1 and q alone. We can plot the constraint on $K_{\rm em}$ in the K_1, q plane and do the same for the constraint of K_2 on $K_{\rm em}$. Additionally, we can constrain K_2 using the absorption lines, as $K_2 < K_{\rm abs}$. These constraints are all independent of any specific K-correction model.

7.3.2 Constraining q

Using the initial constraints on K_1 and K_2 as discussed above, we can constrain q in the K_1, q plane. For the example of OY Car, see Figure 7-2. The plane of possible solutions is given according to the next set of criteria:

- $K_1 < K_{\rm disc}$: horizontal black *solid* line (with *dotted* error bars). Here, we use the average value for $K_{\rm disc}$ as given in the first column of Table 7-1.
- $K_{\rm L_1} < K_{\rm em}$: top diagonal black *solid* line (with *dashed* error bars). $K_{\rm L_1}$ is plotted as a function of K_1, q as the shaded background.
- $K_{\rm em} < K_2$: bottom diagonal black *solid* line (with *dashed* error bars) with K_2 directly calculated from q and K_1.
- $q_{\rm max}$: vertical black *solid* line (with *dotted* error bars). Calculated from $K_{\rm disc}/K_{\rm em}$.
- When absorption measurements are present, the additional requirement is $K_2 < K_{\rm abs}$: red *solid* diagonal line (with *dashed* error bars). This line reduces the previously span plane (note: OY Car does not have a $K_{\rm abs}$ measure).

Also indicated in black points (•) are the solutions from *irradprof* indicating the K_1 needed to return $K_{\rm em}$ for that particular q. When an independent solution is available, these are indicated with orange points for eclipse and radial velocity solutions and cyan points for $v \sin i$ solutions. Finally, the best estimate for q as $K_{\rm disc,min}/(K_{\rm em} + \Delta K)$ is indicated with magenta points.

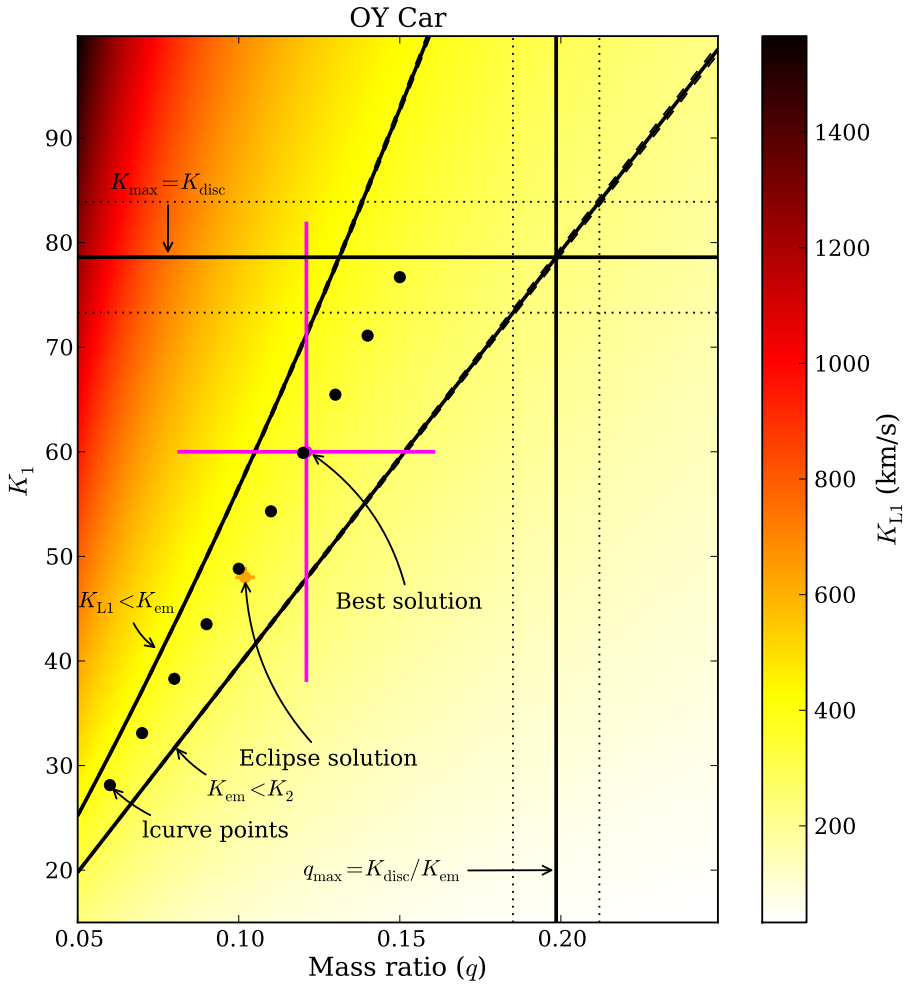

Figure 7-2: The K_1, q plane for OY Car. The plot is span as a function of q and K_1. The shaded background is the radial velocity of the inner Lagrangian point (K_{L_1}). The emission is located at $K_{em} = 395 \pm 1.8$ km s^{-1} which places two constraints in q, K_1 space as $K_{em} > K_{L_1}$ and $K_{em} < K_2$ (diagonal *solid* lines plus *dotted* errors). K_{disc} constrains the space as $K_1 < K_{disc}$ (horizontal *solid* line) while q is constrained by $q < K_{disc}/K_{em}$ (vertical *solid* line). The black points are the solutions from *irradprof*, see also Figure 7-1. Also plotted is the eclipse solution of OY Car (orange) and our best solution ($K_{disc,min}/(K_{em} + \Delta K)$, magenta)

We present the results on all systems in order of orbital period, as indicated in Table 7-2, in Figures 7-3 – 7-15. On the left hand side we show the K_1, q plane, overplotted with the measured curves/points that that constrain q. hand The right side shows a close-up of the Doppler map that contains the emission associated with the donor; in most cases this is the Ca II λ8662Å map. For ASAS 0025 (Figure 7-4) and HS 2219 (Figure 7-6) we plot the Balmer map instead.

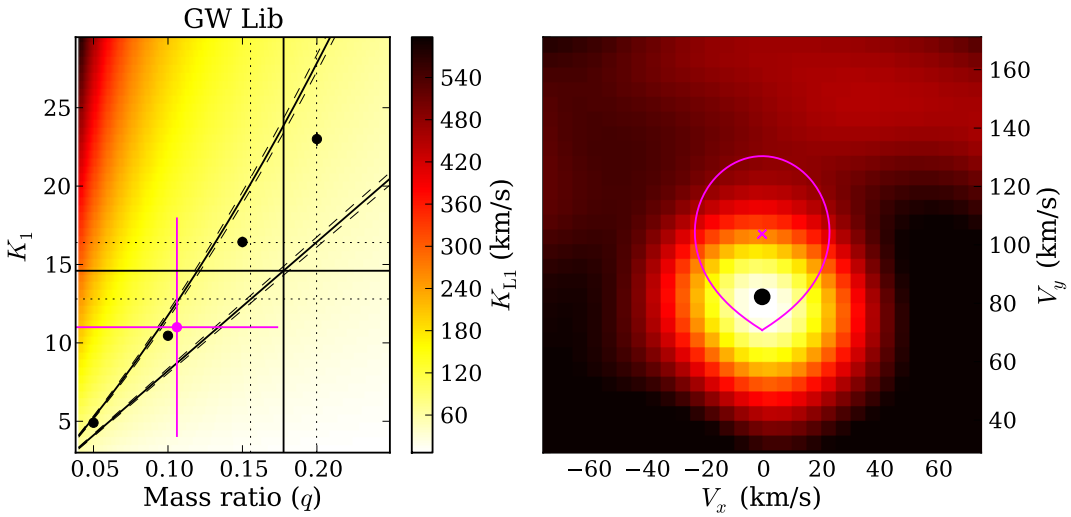

Figure 7-3: **Left:** K_1, q-plane for GW Lib. The best value for $q_{\rm best} = 0.106 \pm 0.068$, in magenta. All lines as indicated in Figure 7-2. **Right:** A close-up of he residual Ca II Doppler map (Doppler map minus the symmetric disc), with the Roche lobe model for the best solution in magenta. The $\times$ denotes the calculated K_2 for the model and the bullet point the location of the measured $K_{\rm em}$.

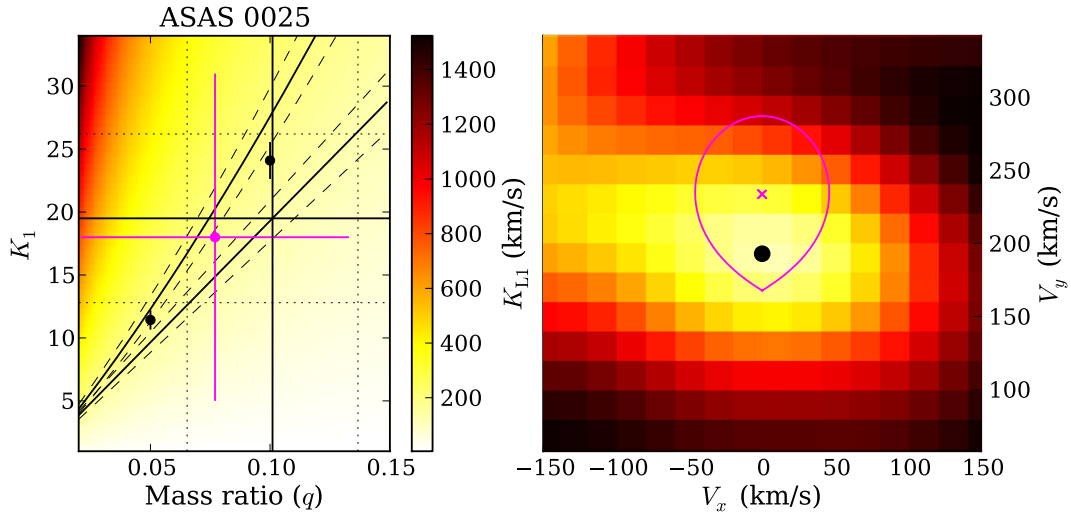

Figure 7-4: **Left:** K_1, q-plane for ASAS 0025. The best value for $q_{\rm best} = 0.077 \pm 0.056$ is indicated in magenta. All lines as indicated in Figure 7-2. **Right:** The residual Hγ Doppler map, indicated is the Roche lobe model calculated from the best solution, as in Figure 7-3.

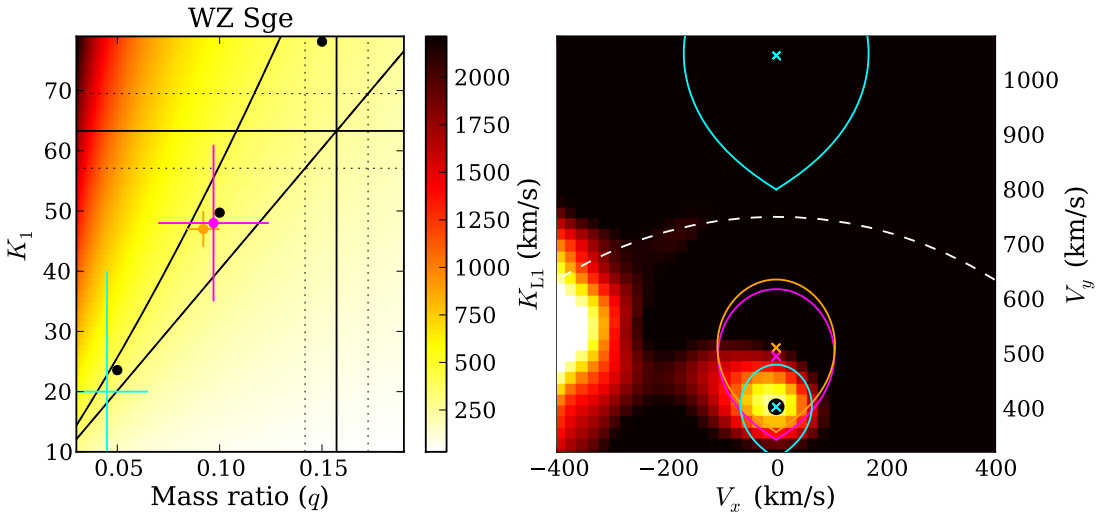

Figure 7-5: **Left:** K_1, q-plane for WZ Sge. The best value for $q_{\rm best} = 0.097 \pm 0.027$ is indicated in magenta. The solution from Steeghs et al. (2007) is indicated in orange, and the solution range proposed by Patterson (2001) is indicated in cyan. All lines as indicated in Figure 7-2. **Right:** The residual Ca II Doppler map, indicated is the Roche lobe model calculated from the best solution (magenta), the model for the solution proposed by Steeghs et al. (2007) (orange). The two cyan models denote the solution as proposed by Patterson (2001) with $q = 0.045$. This, combined with K_1 fixed to 47 km s^{-1} (Steeghs et al. 2007) gives the top lobe and with $K_2 = K_{\rm em} = 395$ km s^{-1} (this Thesis) the bottom lobe. The dotted white line denotes the location of the accretion disc.

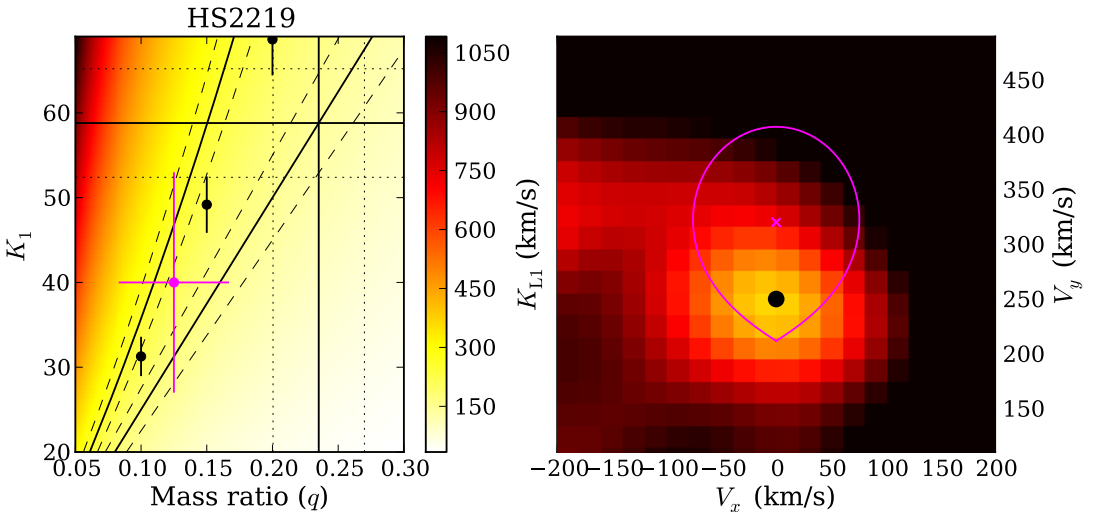

Figure 7-6: **Left:** K_1, q-plane for HS 2219. The best value for $q_{\rm best} = 0.125 \pm 0.042$ is indicated in magenta. All lines as indicated in Figure 7-2. **Right:** The residual Hβ Doppler map, indicated is the Roche lobe model calculated from the best solution, as in Figure 7-3.

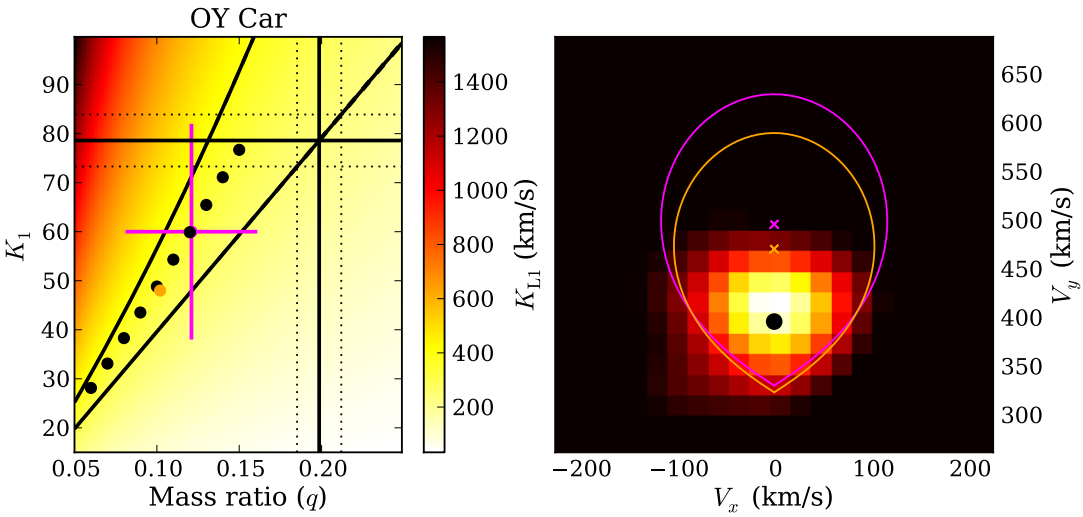

Figure 7-7: K_1, q-plane for OY Car. The best value for $q_{\rm best} = 0.121 \pm 0.040$ is indicated in magenta, the eclipse solution ($q_{\rm ecl} = 0.102 \pm 0.003$) is indicated in orange. All lines as indicated in Figure 7-2. **Right:** The residual Ca II Doppler map, indicated is the Roche lobe model calculated from the best solution (magenta), as well as the eclipse solution (orange).

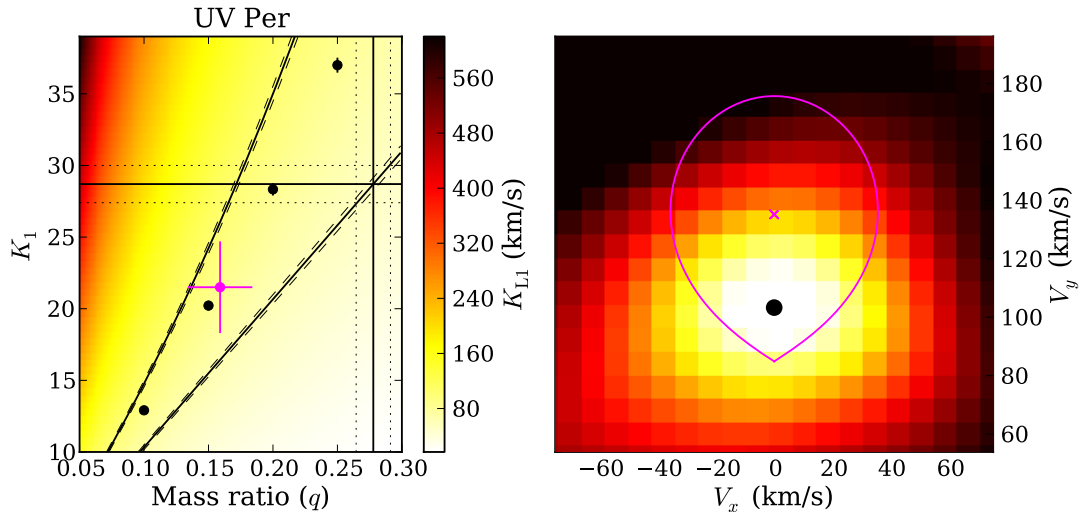

Figure 7-8: As in Figure 7-3, but for UV Per with $q_{\rm best} = 0.159 \pm 0.025$.

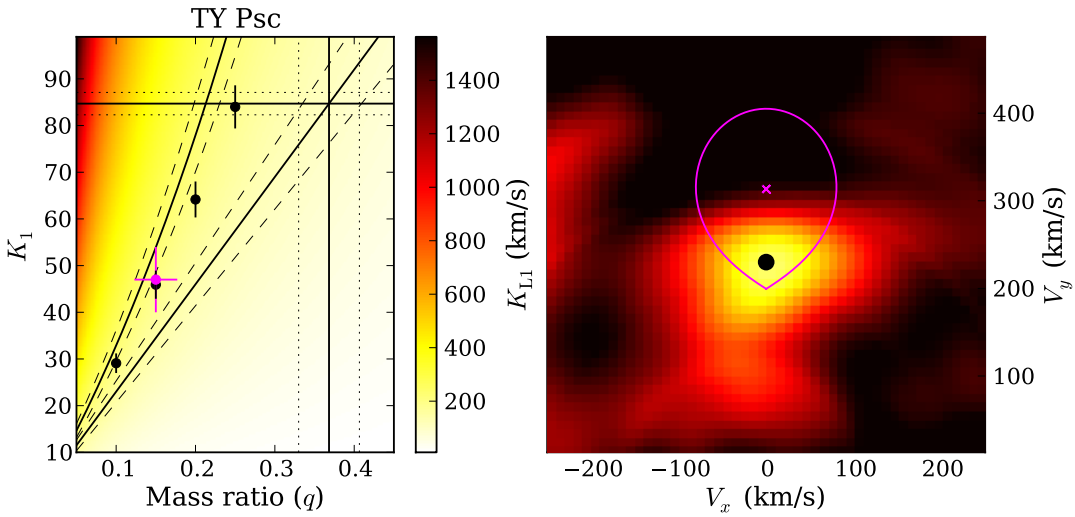

Figure 7-9: As Fin igure 7-3, but for TY Psc with $q_{\rm best} = 0.150 \pm 0.027$.

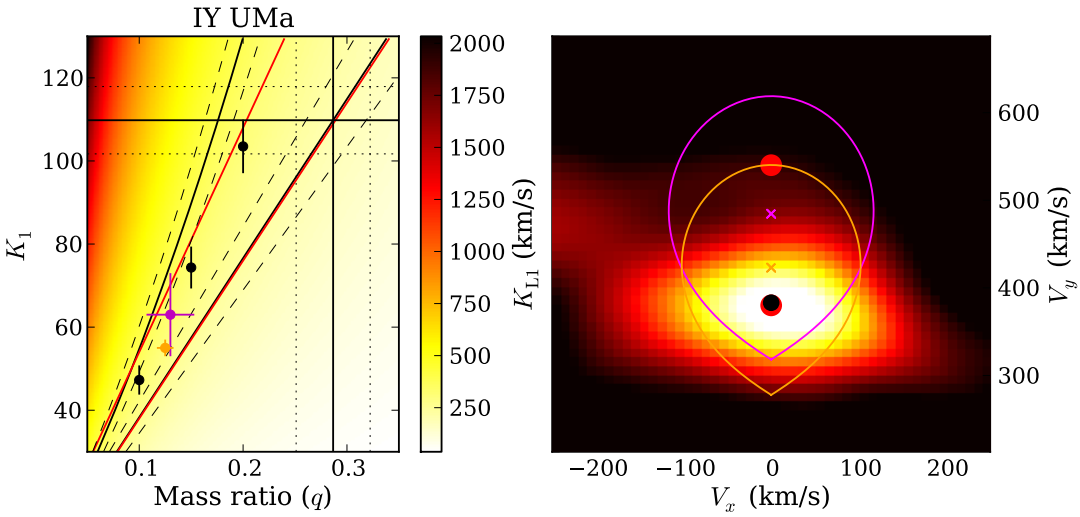

Figure 7-10: As in Figure 7-7, but for IY UMa with $q_{\rm best} = 0.130 \pm 0.023$ (magenta) and $q_{\rm ecl} = 0.125 \pm 0.008$ (orange). Additionally, IY UMa has detected absorption (which results in the range $K_2 = 380 - 540$ km s^{-1}). This range is indicated by the red lines (Bottom: $K_2 = 380$ km s^{-1}, top $K_2 = 540$ km s^{-1}). **Right:** As in Figure 7-7, with the addition of the two extreme values for K_2 (red bullets).

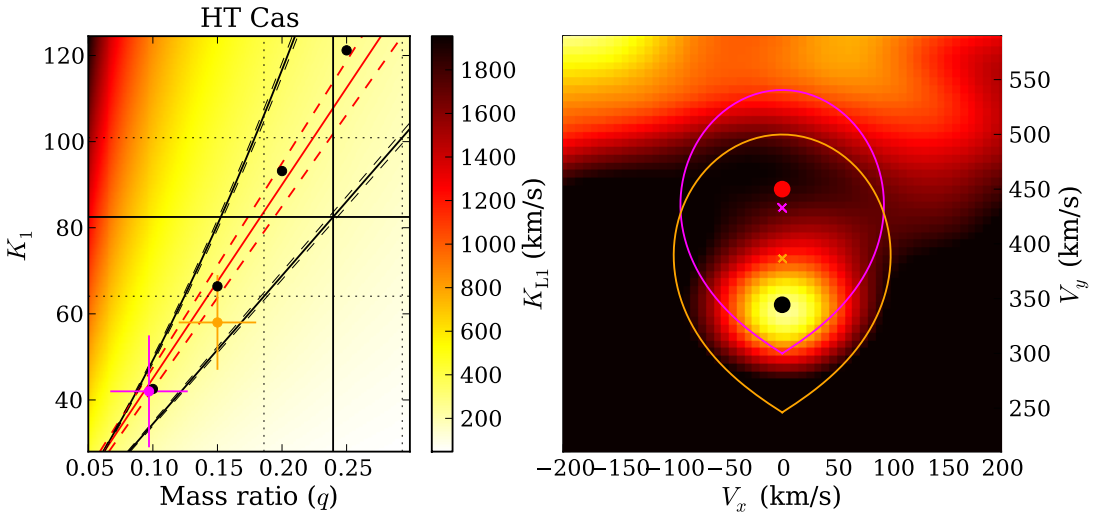

Figure 7-11: As in Figure 7-10 for HT Cas, but with $K_{\rm abs}$ now denoted by a red line/bullets and with $q_{\rm best} = 0.097 \pm 0.030$, $q_{\rm ecl} = 0.148 \pm 0.034$, and $K_{\rm abs} = 450 \pm 25$ km s^{-1}.

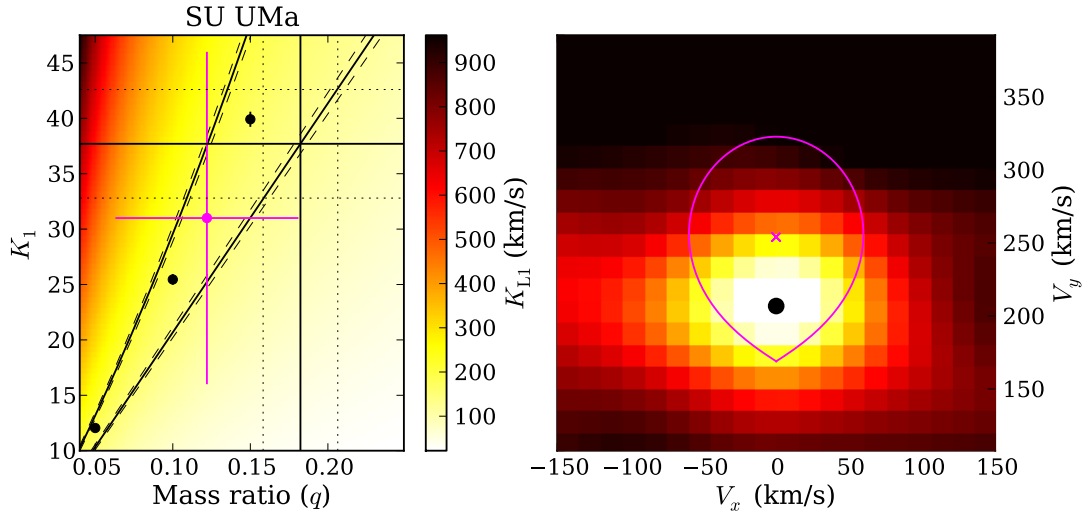

Figure 7-12: As in Figure 7-3, but for SU UMa with $q_{\rm best} = 0.122 \pm 0.059$.

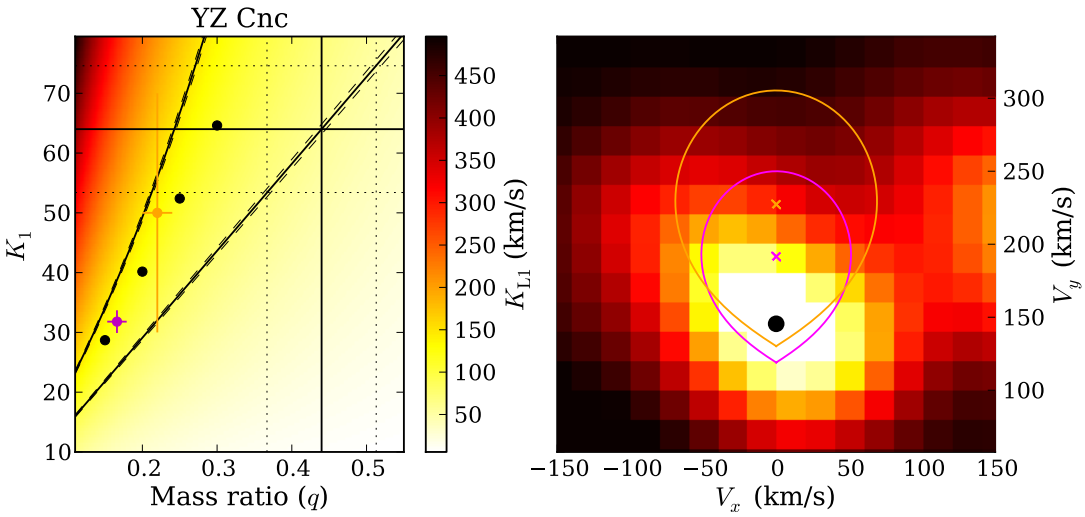

Figure 7-13: As in Figure 7-7, but for YZ Cnc with $q_{\rm best} = 0.166 \pm 0.013$ (magenta) and $q_{\rm other} = 0.22 \pm 0.02$ (orange).

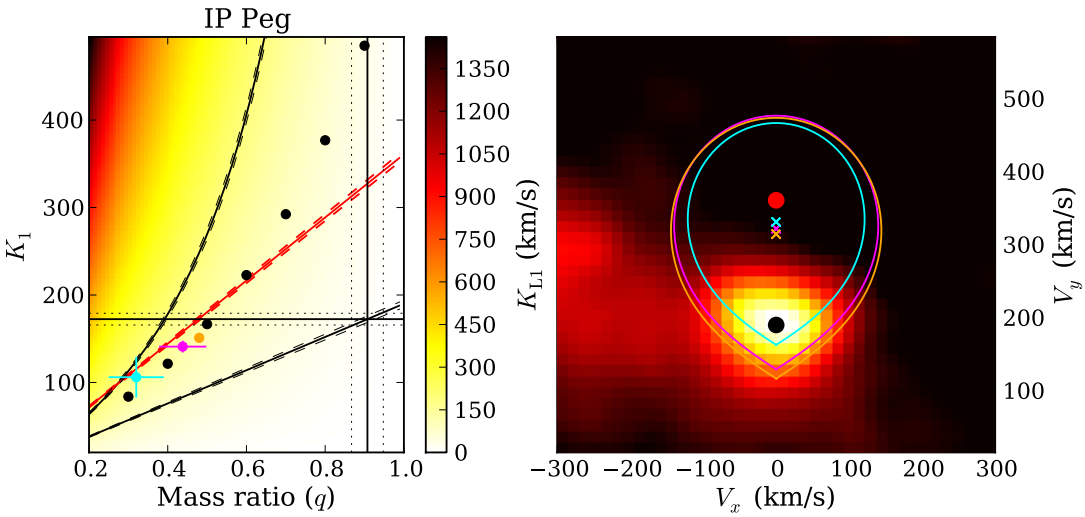

Figure 7-14: As in Figure 7-11, but for IP Peg with $q_{\rm best} = 0.438 \pm 0.060$ (magenta), $q_{\rm ecl} = 0.48 \pm 0.01$ (orange), $K_{\rm abs} = 360.8 \pm 4.8$ km s^{-1}, and the addition of $q_{v \sin i} = 0.32 \pm 0.02$ (cyan).

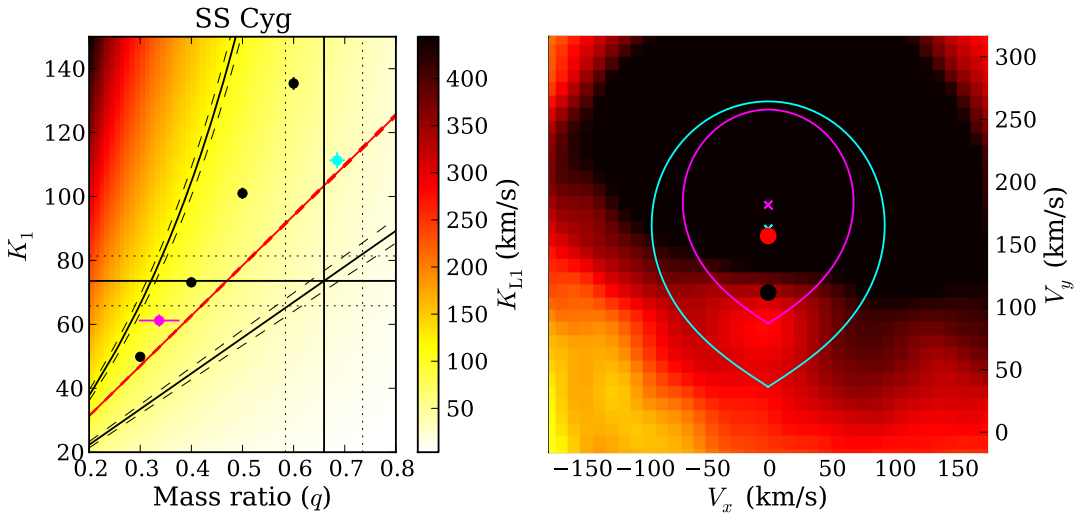

Figure 7-15: As in Figure 7-14, but for SS Cyg with $q_{\rm best} = 0.337 \pm 0.040$ (magenta), $q_{v \sin i} = 0.685 \pm 0.015$ (cyan) and $K_{\rm abs} = 156.8 \pm 0.6$ km s^{-1}.

7.3.3 Notes on specific systems

The systems with an independent measure for q require some extra attention. We will discuss the eclipsing systems (i.e. OY Car, IY UMa, HT Cas and IP Peg) as we can use their published eclipse solution to test the validity of our method . SS Cyg is also discussed because a published $q_{v \sin i}$ exists from donor absorption lines. We shall also give some special attention to GW Lib and WZ Sge as GW Lib has been extensively covered in Chapters 3 and 4, and WZ Sge remains a crucial calibrator for the $\epsilon(q)$ relation, despite its much debated mass ratio.

OY Car

The best mass ratio solution for OY Car, $q_{\rm best} = 0.121 \pm 0.040$ arises from using $K_{\rm disc,min} = 60 \pm 22$ km s^{-1}, $K_{\rm em} = 395.9 \pm 1.8$ km s^{-1} and $\Delta K = 95 \pm 20$ km s^{-1}. The eclipse solution presented by Littlefair et al. (2008) gives $q = 0.102 \pm 0.003$, $K_1 = 47 \pm 2$ km s^{-1} and $K_2 = 470 \pm 7$ km s^{-1}, and is consistent with our $q_{\rm best}$. Figure 7-7 shows the K_1, q plane with both these solutions located within the region determined by $K_{\rm disc}$, $K_{\rm em}$ and the theoretical value for $K_{\rm L_1}$. We also plot a close-up of the emission spot in the Ca II Doppler map, together with the Roche lobes for both solutions (best solution: magenta; eclipse solution: orange). These agree with the location of the emission arising from the front half of the Roche lobe.

We can conclude that our best value for the mass ratio of OY Car, as derived from the Ca II emission profiles, agrees with the eclipse solution within the formal errors and that both Roche lobe models are compatible with our data. This provides us with some confidence that our employed methods return reliable constraints on q.

IY UMa

For IY UMa (Figure 7-10), using $K_{\rm disc,min} = 63 \pm 10$ km s^{-1}, $K_{\rm em} = 383 \pm 38$ km s^{-1} and $\Delta K = 100 \pm 11$ km s^{-1}, we find $q_{\rm best} = 0.130 \pm 0.023$. This is in excellent agreement with the eclipse solution (Steeghs et al., 2003): $q_{\rm ecl} = 0.125 \pm 0.008$, $K_1 = 55 \pm 2$ km s^{-1} and $K_2 = 443 \pm 10$ km s^{-1}. Rolfe et al. (2002) report the presence of absorption in the Na I doublet, but not its measured radial velocity amplitude. They conclude that K_2 is constrained between $380 - 540$ km s^{-1}. Both the eclipse solution and our best solution lie within these limits limits, and are placed close to the central value. Note that, the emission from the donor star is just above the lower limit of 380 km s^{-1}, again indicating that K_2 is unlikely to be this low.

We can conclude that our method works for reproducing the mass ratio of IY UMa.

HT Cas

The best solution for HT Cas is $q_{\rm best} = 0.097 \pm 0.030$, derived from $K_{\rm disc,min} = 42 \pm 13$ km s^{-1}, $K_{\rm em} = 344.4 \pm 4.7$ km s^{-1} and $\Delta K = 89 \pm 9$ km s^{-1}. The eclipse solution presented by Horne et al. (1991) gives $q = 0.148 \pm 0.034$ and requires $K_1 = 58 \pm 11$ km s^{-1} and $K_2 = 389 \pm 4$ km s^{-1}. In addition, absorption has been found at $K_{\rm abs} = 450 \pm 25$ km s^{-1} (Marsh, 1990). Not only do our measurements underestimate the radial velocity of the WD, but they also overestimate that of the donor star, which results in a lower value for $q_{\rm best}$ than $q_{\rm ecl}$. On the other hand, these differences are within 2σ. Both solutions fall within the constraint region in the K_1, q-plane, including the extra constraint set by the absorption measure (Figure 7-11). The Roche lobes for both solutions physically fit the emission spot at the front face of the donor star and show that $K_{\rm abs}$ is larger that both values for K_2, implying both solutions are possible.

We can only conclude that both solutions agree within formal 2σ errors.

IP Peg

IP Peg has three mass ratio solutions that we can compare: $q_{\rm best}$, $q_{\rm ecl}$ and $q_{v\sin i}$. The eclipse solution finds $q_{\rm ecl} = 0.48 \pm 0.01$, $K_1 = 151 \pm 3$ km s^{-1} and $K_2 = 317 \pm 2$ km s^{-1} (Copperwheat et al., 2010). Our best estimate for the mass ratio is $q_{\rm best} = 0.438 \pm 0.060$ from $K_{\rm disc,min} = 141.0 \pm 4.1$ km s^{-1}, $K_{\rm em} = 190.0 \pm 4.2$ km s^{-1} and $\Delta K = 132 \pm 43$ km s^{-1}, which is in agreement with $q_{\rm ecl}$ (left panel of Figure 7-14) and the reported Hα emission at $K_{\rm em} \sim 240$ km s^{-1} (Steeghs et al., 1996). Figure 7-14 shows that the measured absorption at $K_{\rm abs} = 360.8 \pm 4.8$ km s^{-1}. In combination with our *irradprof* models, this places a hard upper limit on the mass ratio of $q < 0.6$, independent of the upper limit provided by $K_{\rm disc}$. The final solution comes from the reported $v \sin i = 125 \pm 15$ km s^{-1} by Beekman et al. (2000), which combined with their reported $K_{\rm abs} = 331.3 \pm 5.8$ km s^{-1} from TiO lines, results in a low value: $q_{v\sin i} = 0.322 \pm 0.075$. This q value, and the corresponding Roche lobe, are indicated in Figure 7-14 in cyan.

All three solutions locate into the area with plausible solutions for K_1, q, and their Roche lobes fit the emission residuals (right panel, Figure 7-14). It is promising that the best solution agrees, within formal errors, with the eclipse solution while the $v \sin i$ solution is out by more than 2σ.

In summary, the eclipsing systems have validated our methods as $q_{\rm ecl} \sim q_{\rm best}$ to within the errors.

SS Cyg

With an inclination of $i \sim 41°$ (Urban & Sion, 2006), no eclipse solution is available for SS Cyg. The best solution from our work is $q_{\rm best} = 0.337 \pm 0.040$, with $K_{\rm disc,min} = 61.2 \pm 1.9$ km s^{-1}, $K_{\rm em} = 111.6 \pm 4.8$ km s^{-1} and $\Delta K = 79 \pm 20$ km s^{-1}, which gives $K_2 = 182 \pm 21$ km s^{-1}. This is larger than our value of $K_{\rm abs} = 156.8 \pm 0.6$ km s^{-1} (Figure 7-15).

When comparing the Ca II Doppler map against the Ca K map (Figure 7-16), we see that while the emission is difficult to identify in the former map, it is dominating the entire Roche lobe in the latter, though the emission is not uniformly distributed. The measured $K_{\rm em,RV} \sim 111$ km s^{-1} is located near the lower radial velocity end of the emission spot, indicating that we underestimate the radial velocity amplitude for the entire Ca K emission feature. Using the Doppler map to locate the emission, we find

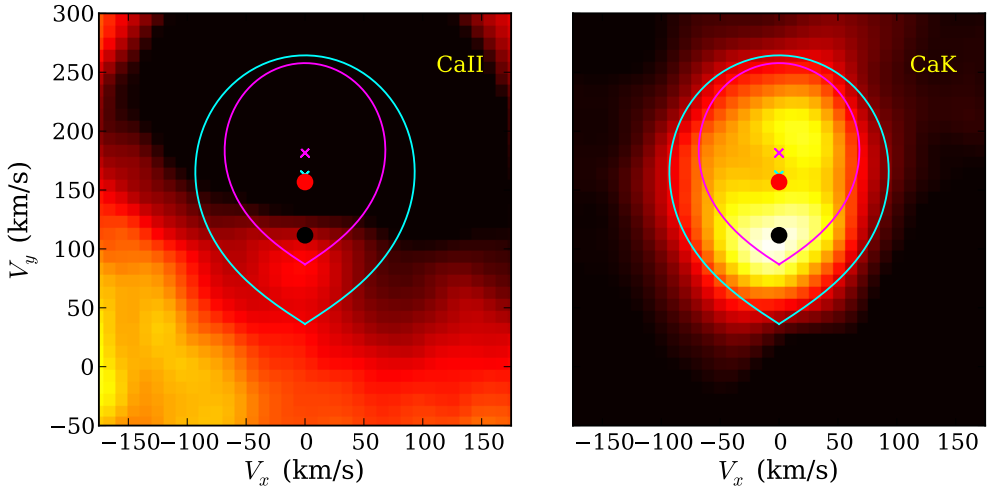

Figure 7-16: **Left:** For comparison purposes, we replot the Ca II map for SS Cyg including our best solution (magenta) and the $v \sin i$ solution (cyan). **Right:** Ca K map for SS Cyg, including the two solutions. While the emission is not clearly present in Ca II, it maps very well to the location of the donor in Ca K. The non-uniform covering of the full lobe suggest a different origin for the emission than irradiation.

$K_{\rm em} \sim 150$ km s^{-1} for the entire emission spot, which is in excellent agreement with $K_{\rm em} \sim 150$ km s^{-1} found for Hα (North et al., 2001). This high value, very close to $K_{\rm abs}$, can only be explained if the emission comes from higher latitudes on the donor than the L_1 point. If this is the case, SS Cyg is ill-represented by our light curve models, as it places the emission near the L_1 point, and the presented ΔK, q and Roche model are not a good representation of SS Cyg.

Discarding our value for $K_{\rm em}$ does not completely solve the problem, however, as even the published $q_{v \sin i} = 0.685 \pm 0.015$ solution with $K_2 = 162.5 \pm 1.0$ km s^{-1} (Beekman et al., 2000) lies close to the limit set by our $K_{\rm abs}$, which is consistent with $K_{\rm abs} = 165 \pm 1$ km s^{-1} found from absorption in the λ6300-6600Å region (North et al., 2002). Inspecting the two solutions in the Ca II Doppler map (Figure 7-16) shows that the $v \sin i$ solution covers the barely visible emission spot in Ca II and the majority of the emission in Ca K, while the Roche lobe for our best solution is too small to fit either. Figure 7-15 indeed shows that both solutions lie above the K_1, q plane span by $K_{\rm abs}$, K_1 and q. Based on our *irradprof* models, to reproduce an emission radial velocity as small as 111 km s^{-1} with $K_2 < K_{\rm abs}$, a mass ratio of $q < 0.3$ is needed.

When re-examining the Ca K trails, it is possible to identify two sources of radiation, with different strengths and different radial velocity components, that broaden the profile

(see also the discussion in Section 6.3). This broadened profile as a function of the orbital phase, translates into the Ca K Doppler map as a bimodal spread of the emission (right panel in Figure 7-16). As the highest intensity is located near L_1, is it highly unlikely that the modulation seen in the FWHM of the Ca K profile (Figure 6-2) comes from ellipsoidal modulation as would display itself as a decrease in the flux on the inner donor face.

Steeghs et al. (1996) report the presence of a slingshot prominence in SS Cyg, in which material from the donor is placed in a magnetic loop, away from the donor surface. This material finds equilibrium in the Roche lobe of the WD, near the centre of mass and hence has $K_{\rm em} \ll K_2$. Our Ca K maps display a similar spread as the Balmer and He I maps. Unfortunately, our instrumental set-up for SS Cyg did not cover the same wavelength range, which prohibits a direct comparison of the donor features. However, it does raise the possibility that most of donor emission is chromospheric with possible contamination by prominences, especially when combined with the bimodal spread seen in the flux variation.

We conclude that our method for the dynamical determination of the mass ratio for SS Cyg is not in agreement with the previously published solutions. This can be attributed to the presence of extended donor star emission with reported chromospheric activity across its entire surface. For these donors, our light curve models are a bad representation of reality as they locate the emission near the inner Lagrangian point.

GW Lib

GW Lib is the prototype for our method to constrain the mass ratio using the dynamical limits set by emission in the Ca II profiles (Chapters 3 and 4). Our best value for the mass ratio is $q_{\rm best} = 0.106 \pm 0.068$, even though the Roche lobe is rather small to fit the emission spot (right panel, Figure 7-3). Due to the low inclination ($\sim 11°$), all our measured values of $K_{\rm disc}$ are lower than ~ 20 km s^{-1}and the minimum radial velocity of the disc is $K_{\rm disc,min} = 11 \pm 7$ km s^{-1}, in good agreement with our tentative value of $K_1 = 13 \pm 2$ km s^{-1} for Mg II[3]. Our best estimate for the mass ratio is larger than the mass ratio derived from the superhump excess, $q_{\rm sh} = 0.062$. To back-up a mass ratio this small, we require the WD to have a radial velocity in the range $5 - 7$ km s^{-1}, much lower than the observed variability in the Mg II absorption line. However, to solve the system parameters for GW Lib once and for all, we require high-resolution,

[3] $q_{\rm best} = 0.125 \pm 0.006$ if we take $K_1 = 13 \pm 2$ km s^{-1}.

time-resolved spectroscopy, simultaneously covering the Mg II absorption line to trace the WD motion and the Ca II triplet lines to trace the donor motion.

We were awarded two nights to observe GW Lib with the Echelle spectrograph UVES at the VLT in May 2010. Unfortunately, bad weather and technical problems prevented any data from being obtained.

WZ Sge

Our best solution for WZ Sge is $q_{\rm best} = 0.097 \pm 0.027$, with $K_{\rm disc,min} = 48 \pm 13$ km s^{-1}, $K_{\rm em} = 402.9 \pm 0.5$ km s^{-1} and $\Delta K = 94 \pm 37$ km s^{-1}. The Roche lobe corresponding this solution fits the emission component nicely (Figure 7-5, magenta model). For comparison, a previous study found the donor in emission in Hα ($K_{\rm em} = 493 \pm 10$ km s^{-1}) which leads to $493 < K_2 < 585$ km s^{-1} (Steeghs et al., 2001) compared to our value of $K_{\rm em} = 402.9 \pm 0.5$ km s^{-1} in Ca II.

As discussed before, Patterson et al. (2005) use WZ Sge to anchor the empirical relation $\epsilon(q)$ at the extreme low mass ratio end, even though different solutions are proposed for its mass ratio. On the one hand, Steeghs et al. (2007) claim that $q = 0.092 \pm 0.008$, with $K_{\rm wd} = 47 \pm 3$ km s^{-1} and $K_2 = 493 \pm 10$ km s^{-1} (Steeghs et al., 2001). This solution (orange, Figure 7-5) agrees almost perfectly with our best solution.

On the other hand, Patterson (2001) argues for $q = 0.045 \pm 0.020$ and $K_1 < 40$ km s^{-1}. The latter constraint is simply 'added' rather than argued nor does their value for the mass ratio follow from their preceding discussion of previously published mass ratios for the system. Their value of q, combined with those on K_2, returns only a small range of possible values for K_1, i.e. $18 < K_1 < 22$ km s^{-1}. This is considerably smaller than their set limit on $K_1 < 40$ km s^{-1}. When we combine Patterson et al.'s proposed value of q with our uncorrected $K_{\rm em}$ as K_2 (at these small mass ratios the K-correction is minimal) we find $K_1 \sim 18$ km s^{-1} (bottom cyan Roche lobe in Figure 7-5). However, this solution is an poor fit to the location of the emission on the donor surface. Using their lower limit on the mass ratio, $q = 0.025$, in combination with the value of $K_1 \sim 47$ km s^{-1}, we find a $K_2 > 1000$ km s^{-1} (top cyan Roche lobe in Figure 7-5). This is an even less likely solution as the donor emission is not located within the Roche lobe surface. In addition, the Roche lobe extends past the disc emission in the Doppler map (indicated by the white dotted line), which is implausible as the distance from the donor to the WD is larger than the distance for any disc annulus to the WD.

Hence the Keplerian velocity of the donor is smaller than that of any part of the disc, placing the donor always within the disc ring in a Doppler map. The only plausible conclusion is that our best solution for the mass ratio is consistent with the mass ratio published by Steeghs et al. (2007). The low mass ratio proposed by Patterson (2001) is an unlikely solution for WZ Sge. The mass ratio is not based on directly measured system parameters, nor does this mass ratio provide a good Roche lobe fit to the donor emission in the Ca II Doppler map when combined with either $K_{\rm wd} = 47 \pm 3$ km s^{-1} or $K_2 = 493 \pm 10$ as measured by Steeghs et al. (2001), whereas both these values is consistent with our values for $K_{\rm disc}$ and K_2.

Eclipsing systems appear to validate the proposed method of using the information provided by the Ca II emission profile for short period CVs, harbouring small donor stars. In the eclipsing systems we find that $K_{\rm em} + \Delta K$ lies very close to the eclipse solution for K_2. As the same profile gives measures for both K_1 and K_2, we avoid the need to combine measurements obtained with different lines and at different epochs, which reduces the systemic errors.

We find that our final error on q is not set by the error on $K_{\rm em}$ nor on the details concerning ΔK, but comes from the large fractional error on K_1. To improve our best estimates for the mass ratio, we thus require better measures of K_1, and a more meaningful error estimate on our measurement, as derived from Doppler maps.

7.4 Ca II as tracer of q in DNe?

The main aim of this Chapter is to determine how well q can be constrained using the emission components in the Ca II lines. Our main conclusions are:

- We present dynamical mass ratios for 13 CVs. For 5 CVs this is the first ever measurement of the mass ratio.
- We find that $q_{\rm best}$ agrees with the eclipse solutions within $\sim 1\sigma$ for all 4 eclipsing systems in our survey. This gives us confidence in the validity of the mass ratios for the systems without an eclipse.
- We find that Doppler maps provide the strongest constraints on both K_1 and K_2 via respectively $K_{\rm disc}$ and $K_{\rm em}$.
- In the overall uncertainty, we find that the K-correction is not the dominant source

of error on the mass ratio q, but the dominant factor is the fractional error on K_1.

- The main improvements for the method lie in the construction of a physically meaningful error bars for K_1, as the fractional error on this parameter dominates the error on $q_{\rm best}$. Any improvement in K_1 would directly translate into a better constraint on q. This can be seen in the case of GW Lib; when we accept $K_1 = 13 \pm 2$ km s^{-1} as the best estimate for the WD motion rather than the minimum value of $K_{\rm disc,min} = 11 \pm 7$ km s^{-1} we find $q_{\rm best} = 0.125 \pm 0.006$ instead of $q_{\rm best} = 0.106 \pm 0.068$.

We can conclude that Ca II is a reliable tracer of the mass ratio.

Chapter 8

Discussion and Conclusions

8.1 Motivation

Theory predicts that a large fraction of CVs should have passed through the minimum period. The Sloan Digital Sky Survey (SDSS) sample is finally unearthing these systems in large numbers (Figure 1-5 shows a spike at short orbital periods, Gänsicke et al. 2009). But due to their faint donor stars, the orbital period is often the only measurable system parameter for most of these CVs. The easy to measure superhump period, and hence superhump excess, could potentially provide an indication of the mass ratio of the systems via the empirical relation $\epsilon(q)$. While this relation is potentially very useful for the determination of mass ratios, the large scatter in the calibrators, especially at the low mass ratio end, prohibits a direct conversion between easy to measure light curve variability and the much sought after mass ratio. To place a short period CV firmly on the evolutionary track (e.g pre- or post bounce), more direct methods to determine the mass ratio are required, as well as a better calibration and validation of the $\epsilon(q)$ relation.

We can achieve this, by constraining the mass ratios of short period CVs using dynamical constraints on the radial velocities of the binary components. The radial velocity of the WD (K_1) is only occasionally directly measurable as the WD features are typically swamped by the strong disc features. As the disc is centred on the WD, measuring the disc radial velocity can give an indication of the WD radial velocity, but these measures tend to be biased by the hotspot and other asymmetries in the disc, and generally provide only an upper limit as outer disc asymmetries tend to increase the apparent radial velocity amplitude and give a phase offset. Despite these flaws, this method is commonly used, as disc lines are normally strong and easily accessible in most CVs.

Measuring the radial velocity of the donor star (K_2) is less straightforward and normally performed by either measuring the radial velocity of the donor absorption lines for earlier type donor stars, or via emission lines associated with the donor star, if

irradiated by the disc and WD. The first method fails in short period CVs as the faint features from the late type donors in these systems are concealed in the accretion and WD dominated optical spectrum, even at very low mass loss rates. The second method comes with tight timing constraints as the irradiated donor is generally only visible on top of the double peaked disc emission shortly after outburst and data needs to be obtained via target of opportunity programs. This is easier said than done, as we require time-resolved medium-resolution spectroscopy of a minimum of one orbital period, and hence generally need a minimum of two hours of observing. An added difficulty is that for the short period systems that are of the greatest interest to us, mass transfer rates are low, and hence outbursts are few and infrequent.

In this thesis, we explored new techniques in addition to the traditional methods for the determination of the radial velocity components in short period CVs. We combined these new methods with the exploitation of the more 'exotic' Ca II triplet lines in the I-band, in addition to the commonly used Balmer lines. Our ambition was to determine the mass ratios of the short period, superhumping CVs included in our small spectroscopic survey. By simultaneously covering the Balmer lines in the blue and the Ca II triplet lines in the I-band, we hoped to find signatures of both the disc and the irradiated donor in the calcium lines and use these to dynamically constrain their mass ratios.

8.2 GW Lib as prototype

The prototype of the survey, GW Lib, has been extensively covered in this thesis and our results have been published in van Spaandonk et al. (2010b) and van Spaandonk et al. (2010a).

Time-resolved spectroscopy pre- and post superoutburst

We presented time-resolved optical spectroscopy of GW lib during a large number of epochs spanning before, throughout and after the 2007 outburst. We studied the long-term evolution of the spectral features tracking large changes in the accretion geometry and intensity. During the outburst, we initially saw the optically thick accretion disc dominate through broad absorption features. Their radial velocities did not trace the WD and showed semi-amplitudes of order 50 km s^{-1}. A peculiar sharp emission line component was found in the Balmer lines that is effectively stationary. This could be some low velocity outflow away from the orbital plane or a component near the WD,

but its mean velocity was similar to the systemic velocity γ, whereas material near the high gravity WD should have been gravitationally red-shifted. As the system faded back towards quiescence, accretion powered double-peaked emission profiles appeared. The absorption associated with the accretion disc continued to weaken until the system returned to a semi-quiescent state with strong double-peaked emission lines.

The contrast between the diagnostics of the Balmer lines versus those of the Ca II lines was particularly striking. The Ca II triplet in GW Lib showed that these much neglected lines of CV spectra were indeed an interesting window to search for signs of both the donor star and accretion disc structures even in cases where the Balmer lines show no signs of the donor star whatsoever and the disc itself is barely resolved. GW Lib was a particularly challenging object in that sense, due to its very low inclination and thus small projected velocities. The Ca II triplet in emission could be resolved into several components and the secondary star was discovered in emission moving between the sharp double-peaked emission from the accretion disc. Doppler tomography and radial velocity fits of the Ca II lines provided a semi-amplitude of $K_{\rm em} = 82.2 \pm 4.9$ km s^{-1} for the donor star feature and indicated a disc centre of symmetry at $K_{\rm disc} = 6 \pm 5$ km s^{-1}. The disc was also visible in the Hβ maps but with less detail and sharpness and no donor star contribution was seen. Contrasting these lines highlights the apparent diagnostic advantages provided by the Ca II triplet.

Based on previous studies together with our measured limits on K_1 and K_2, the allowed range of binary parameters were explored. While our dynamical limits placed a hard upper limit on the binary mass ratio of $q < 0.23$, close to the value derived by Copperwheat et al. (2010), we favoured a significantly lower value. A mass ratio near $q \sim 0.06$ was in accordance with estimates based on the detected superhump modulations, the constraints on the faintness, and thus mass, of the donor star and the indications that K_1 is very small. Given such a mass ratio, our measured $K_{\rm em}$ implied $K_2 = 100.8 \pm 7.1$ km s^{-1} for the donor star component when applying the relevant K-correction. The implied $K_1 = 6.2 \pm 0.4$ km s^{-1} was then also close to our measured disc centre of symmetry. The combination of a WD mass near the value suggested by the pulsations, and a low mass donor near the empirical sequence of an evolved CV near the period bounce, appeared to be consistent with these new dynamical constraints.

WD mass determination

We noted the presence of the magnesium II line in absorption in pre-outburst data. This offered the opportunity to measure the gravitational redshift of the Mg II absorption line in high-resolution archival Echelle spectra of GW Lib during quiescence. Assuming an origin in the photosphere of the accreting WD, we combined this redshift with non-zero temperature mass-radius relations for WDs to derive a WD mass of $0.84 \pm 0.02 M_{\odot}$. The measured Doppler shift for this line provide a cautious $K_{\rm WD} = 13 \pm 2$ km s^{-1}. Because the Mg II line was well-resolved in our data, we could also estimate the spin period of the WD to be 97 ± 12 seconds, if we assumed the width of the line to be dominated by rotational broadening.

Our mass value was significantly below the 1.02 $M_{\odot}$ lower limit derived by Townsley et al. (2004). However, their choice of preferred solution was largely driven by the WD size as implied by the measured UV flux. Additional UV spectroscopy and model fitting is warranted to try and achieve a picture consistent with the latest distance, spin period, pulsation periods and our dynamical constraints from optical spectroscopy.

Final notes on the mass ratio of GW Lib

Using the same method as for all systems in our survey to constrain the mass ratio, we derived a dynamical mass ratio for GW Lib using the dynamical constraints given by the presence of both disc and donor emission. Our maximum mass ratio was $q_{\rm max} = 0.18 \pm 0.02$ and our best estimate is $q_{\rm best} = 0.106 \pm 0.068$. An additional constraint can be added by associating the measured radial velocity of Mg II with the true radial velocity of the WD, resulting in $q_{\rm best,Mg\ II} = 0.125 \pm 0.006$. This mass ratio is twice the value suggested by the superhump excess, $q_{\rm sh} = 0.062$. This latter mass ratio, combined with our $K_2 \sim 100$ km s^{-1}, would imply a much smaller $K_1 \sim 6$ km s^{-1}, and a spectral type for the donor of $\sim$T (Knigge 2006; Knigge et al. 2011). Whereas, our preferred mass ratio, combined with our WD mass, implies a donor star of mass $M_2 = 0.105 \pm 0.006 M_{\odot}$. Knigge's empirical donor sequence predicst a donor star with a spectral type close to $\sim$M6 for this donor mass.

Our solution for the system parameters hinges on a small number of assumptions. To align all methods and unravel the systems parameters, we need to revisit the mass from asteroseismology while taking into account the effects of rotation to see if a WD model with a mass of $0.84 M_{\odot}$ at the latest distance can be fitted to the UV data with reasonable

temperatures. To be able to calculate a direct mass ratio, a positive identification of the Mg II line as fixed in the WD atmosphere, followed by a reliable measure of K_1 is needed. This should be possible through high S/N time-resolved spectroscopy. If furthermore the motion of the WD is matched with a solid ephemeris, using the emission from the donor star (giving K_2 and γ), a fully consistent and accurate WD mass for this prototypical accreting WD pulsator is entirely feasible.

8.3 Outcome of our survey

Motivated by our success with GW Lib, we initiated a spectroscopic survey to observe a sample of short period CVs, simultaneously covering the Balmer lines in the blue and the Ca II triplet lines in the I-band. We selected objects for the programme with an orbital period near the bounce period and/or with detected Ca II lines in archival or published spectra. Since we wished to test and calibrate the $\epsilon(q)$ relation, priority was given to DNe with a recent detected superoutburst followed by a detection of superhumps or a previously recorded superhump period. We included CVs with an independently determined q (e.g. via eclipse studies), alongside several systems with a longer period, to be able to validate and calibrate the proposed method. The final list of observed systems included 19 systems with orbital periods ranging between 77 minutes (GW Lib) and 396 minutes (SS Cyg), of which 18 were in quiescence state during our observations.

8.3.1 Ca II emission

We found disc emission features in the Ca II triplet lines in 90% of the quiescent systems in our survey. Donor emission features wee found in 75% of these systems, which is equivalent to an overall success rate of 2 out of 3. This reduces to 50% (and a success rate of 2 out of 5) if we limit ourselves to CVs with an orbital period of less than a hundred minutes. In two short period systems we found donor emission in the Balmer lines only. We located all donor features in their Doppler maps, which allowed us to measure their the radial velocity and determine the phase zero point by placing this emission spot at $V_x, V_y = 0, +K_2$. We also showed, using multi epoch observations of GW Lib, that potentially one could constrain the period by determining the phase zero points in the various epochs, if tradiational methods using RV fits fail due to low S/N.

At low inclinations ($\lesssim 20^\circ$), the Ca II triplet disc lines displayed more detail than the Balmer disc lines, as the double peaked profiles are intrinsically wider for calcium than for hydrogen at the same inclination. For modest inclination systems ($35 - 55^\circ$), with

strong, saturated, single peaked hydrogen profiles, the Ca II lines keep their distinct double peaked shape, whereas the Balmer lines are saturated. The Balmer features in high inclination systems ($\gtrsim 75°$) are dominated by strong central absorption, whereas the Ca II triplet lines remain free from this effect. Thus in all cases, the Ca II lines offered an improved insight into the disc emission features. This is highlighted in the cleaner and sharper Doppler maps for Ca II for all systems.

We considered various correlations between the bulk emission line properties and relevant binary parameters. We found that the ratio of Ca II EW to Balmer EW is largest at low inclinations. We found no evidence of the proposed $\cos i$ relation for the EW in our survey. Low WD temperatures ($\lesssim$ 11 000 K) seemed unable to irradiate the donor and/or disc in Ca II. At intermediate temperatures and for sufficiently short periods, the WD temperature contributed to the EW ratio of Ca II to Balmer. This effect decreased with increasing orbital period, and hence increasing orbital separation, as the WD contribution becomes less important for larger discs. No significant dependence on WD mass is found for the detection of disc and donor emission lines in Ca II. Time since outburst appeared not to be of importance for the presence of donor emission in Ca II, as we found donor emission at a broad range of since the last outburst. The ratio of Ca II EW to Balmer was EW incredibly stable in GW Lib on time scales of 2 years.

8.3.2 Measuring K_1

WD

In only two systems, we were able to detect absorption associated with the WD in the Mg II λ4481Å line. In GW Lib, we were able to track the movement of this line as a function of the binary orbit. This resulted in a measure for K_1, even though the value is close to the resolution limit of the data. Unfortunately, for UV Per, the presented data were not of sufficient resolution to positively identify the line with the WD as the poor S/N prevented us from tracking the WD motion as a function of the orbital phase.

Disc

We measured the radial velocity of the disc features in both the Balmer and Ca II profiles, using three different methods: 2-Gaussian fits to the disc profile, a diagnostic diagram and a search for the centre of symmetry in the Doppler maps. Generally, the first two methods agreed to within the error bars, whereas the latter method proved highly variable in comparison. However, the two Gaussian methods were equally distorted by

the disc asymmetries, such as the hotspot, and did not allow us to avoid these regions. In contrast, the Doppler map allowed us to deal with these asymmetries in a superior way, by permitting an easy identification of these regions, which then could be avoided for centre of symmetry searches. Tables 5-10, 5-11 and 5-12 indicated that the Ca II profiles provided a more stable solution over all three measures and thus appears to be a superior probe of K_1.

Comparisons to previous studies showed that the disc radial velocity derived using double Gaussian fits is highly variable. It is generally accepted that disc emission can by asymmetrical, distorting both the phase and, more importantly, the radial velocities of the disc. In these cases, when the previous measurement did not agree with our values, especially when different lines were used, a strong hotspot was visible and/or there had been an outburst between measurements. As these effects can potentially change the morphology of the disc profile, we conclude that the 2-Gaussian measures did not represent the radial velocity of the disc and are inadequate tracers of K_1.

8.3.3 Measuring K_2

Overall, we found donor emission in 13 out of 18 systems ($\sim 75\%$). All donor features could be located in Doppler maps, which allowed $K_{\rm em}$ to be measured, as well as the determination of a phase zero point. For 10 systems, radial velocity curve fits could be made to improve this measure. As expected, only the two longest period systems showed donor absorption lines in the covered wavelength range (IP Peg and SS Cyg). When previous measures of donor emission have been published, these agreed with our values.

As the emission originates from near the inner Lagrangian point, we needed to apply a K-correction (ΔK) to our measured $K_{\rm em}$ to find the true radial velocity of the donor star (K_2). For all these systems, we constructed model irradiation light curves and optimised for the velocity scale of the system to return the measured $K_{\rm em}$ over a range of mass ratios to determine ΔK. The true radial velocity of the donor was calculated via $K_2 = K_{\rm em} + \Delta K$. We found that these models are not the dominant error in the constraint on the mass ratio.

8.3.4 Constraining q

We presented dynamical mass ratios for 13 CVs in this thesis. For 5 CVs this is the first ever constraint on their mass ratio. We found that our $q_{\rm best}$, including a conservative

error bar, agreed with the eclipse solutions within $\sim 1\sigma$ for all 4 eclipsing systems in our survey. This gave us confidence in the validity of the mass ratios for the systems without an eclipse. We found that Doppler maps of Ca II provided the strongest constraints on both K_1 and K_2 via $K_{\rm disc}$ and $K_{\rm em}$, respectively. Irradiation models provided correction terms for the donor emission, which proved very reliable when compared to eclipse solutions. The main improvements for the method will be in the constructions of a physically meaningful error bar for K_1, as the fractional error on K_1 dominates the error on $q_{\rm best}$.

8.3.5 Period evolution combined with q

We can plot the orbital period against our best measures for the mass ratio, and compare these to the available binary evolution models for the evolution of the mass ratio as a function of the orbital period, see Figure 8-1. The first period evolution path is the initial path as calculated by Kolb & Baraffe (1999). New evolution paths are presented by Knigge et al. (2011). The first one assumes standard angular momentum loss (i.e. magnetic braking above the gap and gravitational radiation below the gap). Their second model is optimised for the available data and returns that below the gap, the fit requires an enhanced angular momentum loss rate at 2.47 $\times$ GR, where above the gap the rate is slightly reduced at 0.66 $\times$ MB. Also indicated is the location of the period spike as determined by Gänsicke et al. (2009).

For systems above the period gap, we see that SS Cyg is located far below any of the models, which is not surprising as we had already indicated that we greatly underestimate the mass ratio of this system and that for chromospherically active donor stars our irradiation models are a bad representation, and hence our method for the dynamical constraint on the mass ratio does not work. However, for IP Peg, our best estimate for the mass ratio coincides with eclipse solutions and places the system on the evolutionary tracks.

Eleven of our systems have periods that place them below the period gap. Unfortunately, the errors on the mass ratio are too large to confirm their position in respect to pre- and post bounce systems, especially for ASAS 0025, which lies exactly on the bounce location. Interestingly, all four systems with periods above 100 minutes ($P_{\rm orb} \gtrsim 0.07$ days) seem to be located below the predicted evolution trends, whereas the systems with orbital periods less 100 minutes, are located on the curves.

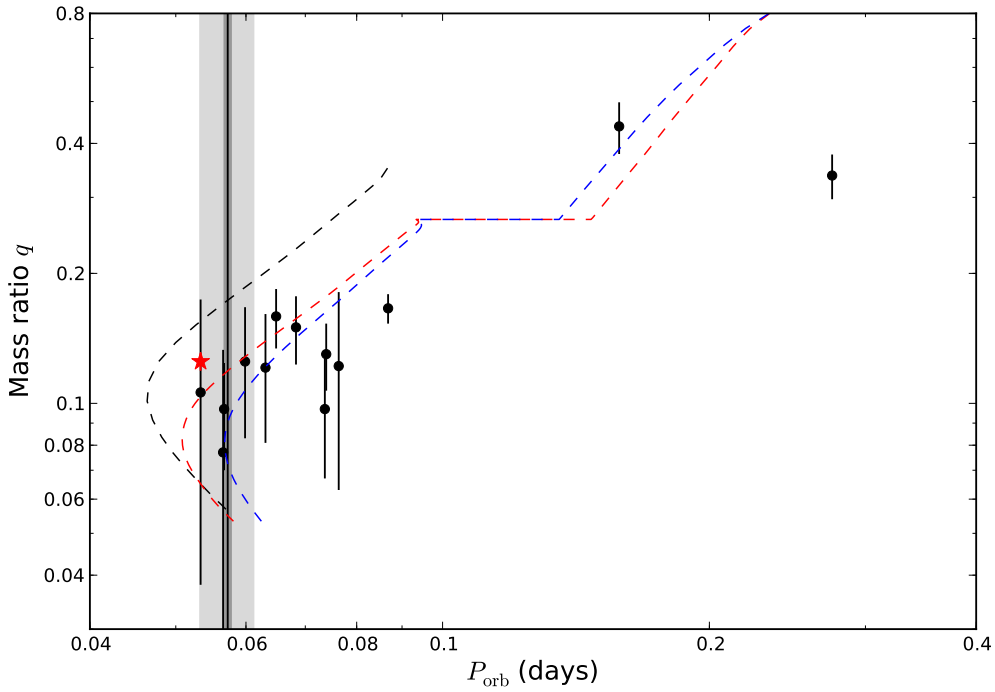

Figure 8-1: Orbital period versus our best estimates for the mass ratio ($q_{\rm best}$) as derived in Section 7.3 (black dots). Indicated by the *black dashed* line is the binary evolution model as derived by Kolb & Baraffe (1999). Knigge et al. (2011) provide two models: in *red dashed* their standard evolution track and in *blue dashed* the optimised evolution track. The *vertical black* line is the period spike as determined by Gänsicke et al. (2009), with 1σ error bars (*dark grey shaded*) and the measured FWHM of the peak (*light grey shaded*). Indicated by the *red star* is the mass ratio for GW Lib if we assume $K_1 = 13 \pm 2$ km s^{-1}.

8.4 Implications for the empirical $\epsilon(q)$ relation

One of the aims of this thesis was to identify new calibrators for the empirical relation between the superhump excess and the mass ratio, $\epsilon(q)$. With estimates for the mass ratio under our belt, we can finally attempt this.

In Figure 8-2, the old set of calibrators from Patterson et al. (2005) (top left) are plotted together with his proposed relation and the one given by Knigge (2006), see also Section 1.3.2. These calibrators are replotted with an updated superhump excess (middle left; Kato et al. 2009, Kato et al. 2010). The only drastic changes in the data points that could influence the initial $\epsilon(q)$ relation are the changes in the sumperhump excess of V2051 Oph (from $\epsilon = 0.30 \pm 0.002$ to $\epsilon = 0.0220 \pm 0.0014$) and KV UMA (black hole binary; from $\epsilon = 0.0047 \pm 0.009$ to $\epsilon = 0.0026 \pm 0.002$). The latter movement is of

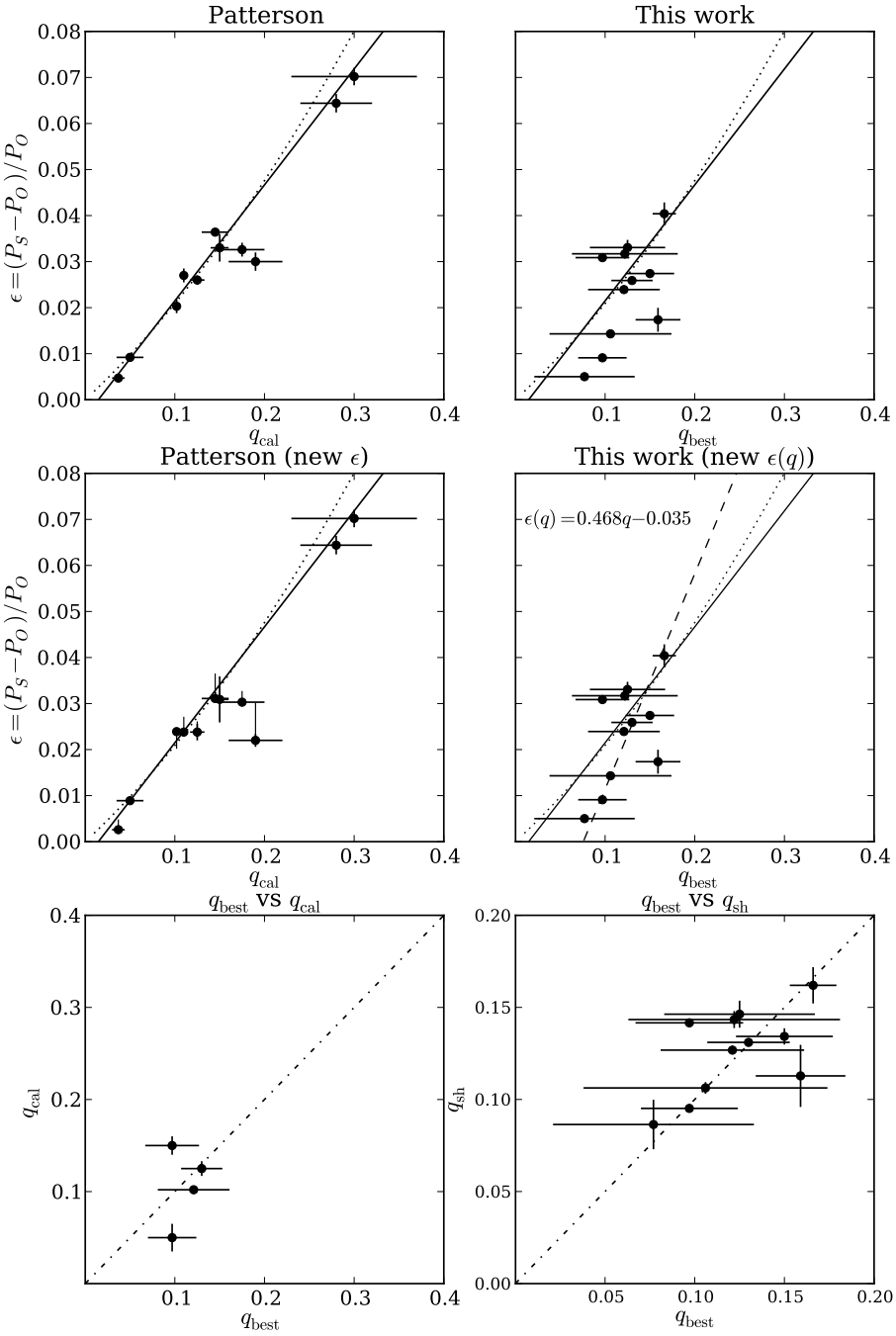

Figure 8-2: **Top Left:** Mass ratio versus superhump-excess. The $\epsilon(q)$ relation as published by Patterson et al. (2005) and refitted by Knigge (2006). In all panels, the *solid* black line denotes the $\epsilon(q)$ relation from Patterson et al. (2005), where the *dashed* line represents the relation given by Knigge (2006). **Middle Left:** Patterson's calibrators, but with an updated ϵ from Kato et al. 2009, 2010, when available. The black narrow line denotes the move from the previous location. **Top Right:** The results from this work. **Middle Right:** Our $\epsilon(q)$ relation. The *dotted* line represents our relation. **Bottom left:** Our $q_{\rm best}$ against $q_{\rm cal}$ from Patterson et al. (2005) (e.g. WZ Sge, OY Car, HT Cas and IY UMa) The *dotted-dashed* line represents the one-to-one relation. **Bottom Right:** Our best measures for the mass ratio, against the mass ratios inferred from the superhump excess combined with our empirical relation: $\epsilon(q) = 0.468q - 0.035$, with a scatter of 0.022.

importance as it serves as the low-mass anchor, especially as the use of WZ Sge (with $q = 0.050 \pm 0.015$) as a calibrator is under scrutiny.

The top right panel in Figure 8-2 shows our best estimates for the mass ratio versus the most recent published superhump excess for each system. The errors on the mass ratios are more conservative than the errors on the eclipse determined mass ratios. This is caused by the large fractional errors on K_1. In general, this panel shows that we cannot confirm nor deny the validity of the $\epsilon(q)$ relation, predominantly due to the absence of larger mass ratio systems as well as by the large scatter around the relation for the low mass ratio systems.

Using our sample of superhumping CVs, we fitted our own $\epsilon(q)$ relation (middle right panel in Figure 8-2). This panel shows our best mass ratio ($q_{\rm best}$) against the superhump excess (ϵ). The three $\epsilon(q)$ models indicated are from Patterson et al. (2005; *solid black line*) , Knigge (2006; *dotted black line*) as before and our best fit to the data (*dashed black line*):

$$\epsilon(q) = 0.468q - 0.035. \tag{8-1}$$

The bottom right hand panel of Figure 8-2 shows our $q_{\rm best}$ against the $q_{\rm sh}$ as calculated from our $\epsilon(q)$ relation. The line represents the one-to-one relation between the two values and has a scatter of 0.022.

The bottom left panel in Figure 8-2 shows the four systems (e.g WZ Sge, OY Car, HT Cas, IY UMa) that are present in both Patterson et al. and our data sets to display the difference. Other than WZ Sge, the systems remain close to the $\epsilon(q)$ relation to within the errors, as the eclipse solution agrees with our best estimates for the mass ratios. Depending on the mass ratio estimate accepted by the different parties, the location of WZ Sge changes dramatically in the plot. The only possible conclusion regarding this system is that WZ Sge should be omitted until an unambiguous mass ratio for WZ Sge is found.

However, omitting WZ Sge as a calibrator does not solve all questions regarding the validity of the proposed $\epsilon(q)$ relationship. Copperwheat et al. (2011) find that the first eclipsing AM CVn system SDSS J0926 + 3624, agrees with the relation at the very low mass ratio end ($q = 0.041 \pm 0.002$ and $\epsilon = 0.00874 \pm 0.00010$ in u'), whereas AM CVn ($q = 0.18 \pm 0.01$, $\epsilon \sim 0.021$; Skillman et al. 1999) does not. Is this because the indirectly determined mass ratio of AM CVn itself is unreliable or because the relationship in general is not valid for these hydrogen poor systems (Pearson, 2007)?

Several more questions remain in relation to the proposed correlation between ϵ and

q. How stable is the superhump period over several superoutburst cycles, see just the sheer range of superhump periods listed per object in Kato et al. (2009) and Kato et al. (2010) and how do these superhump period changes influence the empirical relation?

8.5 Conclusion

In this thesis, we present dynamically constrained mass ratios for 13 CVs, using the Ca II triplet lines in the I-band as a tracer for both the radial velocity of the disc and the donor. These donor features are visible in most systems and even provide us with a measure for the emission component of the donor in low S/N cases, when traditional methods fail. For 5 CVs, this is the first ever measure of the mass ratio. We find that our best estimate for the mass ratio ($q_{\rm best}$), including conservative error bars, agrees with the eclipse solutions within $\sim 1\sigma$ for all 4 eclipsing systems in our survey. This gives us confidence in the validity of the mass ratios for the systems without an eclipse.

We note that the difficulty for dynamically constraining the mass ratio has shifted. Previously, no measurements of K_2 could be presented while K_1 was easily accessible via the prominent disc lines in Balmer. While it suffers from some of the same systematics as the Balmer lines, we can measure K_1 better in Ca II than in Balmer, especially when exploiting the Doppler map for these measurements. More importantly, Ca II provides us with measurements of $K_{\rm em}$ for many systems. These, combined with K-correction models, provides a good measure of K_2. We find that the determination of $K_{\rm em}$ is easy in Doppler maps, and that the K-correction, via irradiation methods, is fairly reliable.

The limitation for determining the mass ratio using our methods is the to reliable measurement K_1. Any improvement in K_1 would directly translate into a better constraint on q, as noted for GW Lib. Hence, we are still limited by systematic errors in deriving mass ratio estimates using dynamical constraints, and at this point we are unable to improve the fit at the low mass ratio end of the proposed $\epsilon(q)$ relation.

We conclude that Ca II is an excellent tracer for the mass ratio.

8.6 Future projects

Follow up on GW Lib

Based on our success with GW Lib and the identification of the Mg II line in archival data, we proposed to follow up GW Lib with the high resolution spectrograph UVES

at the VLT. We were granted 2 full nights in May 2010, but unfortunately, due to bad weather, no data was obtained. We will resubmit our proposal in the next suitable proposal round at VLT/ESO.

Follow up on promising candidates

As we have covered most of the bright targets accessible from the Northern hemisphere with the WHT, we are now focusing on the Southern hemisphere. The broad wavelength coverage of X-shooter/VLT allows us to not only exploit the Ca II triplet lines, but also to simultaneously search for the traditional absorption components of the late type donor stars at long wavelengths, while still covering the traditional Balmer series at the blue end, and including Ca H/K. We are already following up ASAS 0025 with X-Shooter/VLT under program ID 086.D-0248A, as well as several other short period CVs.

Direct measures of the WD absorption lines

For low inclination systems (like UV Per), we can use the Mg II absorption line to trace the WD motion, while simultaneously tracking the donor in Ca II. For this, we require time-resolved, high spectral resolution optical spectroscopy. As UV Per is similar in brightness to GW Lib, this will require an 8-metre class telescope.

For high inclination systems, the broad disc emission profiles fill the Mg II line near the He I 4471Å line, and swamp any WD features. To resolve the WD motion, we will need to look for metal lines in the UV, in analogue WZ Sge (Steeghs et al., 2007) when optical spectroscopy fails.

We acknowledge that both of these tests are time consuming and expensive (as it needs time-resolved, high S/N spectra), but it is worth looking into for those systems that are most promising in terms of calibrating $\epsilon(q)$.

Error bars on Doppler maps

As error information is difficult to propagate into Doppler maps, the best way to determine physically meaningful errors is by doing Monte Carlo/bootstrap simulations to find the likelihood of placing the emission at the expected location ($K_{\rm em,MEM}$) and to find the error in the centre of symmetry method on the measure of $K_{\rm disc,MEM}$.

LMXB

For Low Mass X-ray binaries in quiescence, the Ca II triplet has already proven its usefulness (Casares, 1996). The Bowen blend is only strong just after outburst (Steeghs & Casares, 2002). In contrast, the Ca II triplet lines become visible during quiescence, and will aid in our attempts to constrain the black hole masses.

Now: SDSS

The SDSS spectrograph covers up to 9000Å (York et al., 2000) and combined with the many detections of short period CVs provides the capability to identify those systems that have both a short period and Ca II in emission. If, in addition, the spectra show the WD in absorption, one of the key characteristics of low accretion rates, it will open the window for the identification of both low accretion rate DNe systems and post-period bounce systems containing brown dwarfs. Up to now, SDSS has proven to be able to find a significant fraction of the missing population of CVs at short orbital periods (Gänsicke et al., 2009). With their initial spectral properties and orbital periods known, good candidates for spectroscopic follow-up can be easily identified and in combination with I-band spectroscopy on larger telescopes, might reveal the more mass ratios at the low mass rate end of the $\epsilon(q)$ relation. We have already searched the SDSS database for bright targets with promising Ca II lines when selecting targets for the observing runs reported in this thesis. However, quite a few faint systems remain with indecisive (and noisy) I-band SDSS spectra, and we should look into observing these systems in greater detail.

To test the tentative trends seen we have seen between the EW of the various emission lines as a function of the period, we can exploit the $\sim$ 300 CV spectra provided by SDSS. These spectra should be of good enough quality to measure the EWs for the Ca II lines and a few Balmer lines. Measuring these quantities would allow us to plot an additional $\sim$ 300 points in Figure 6-3, independent of selection effects. This sample size should then be sufficient to validate the proposed trends.

Near future: GAIA

Gaia is the next, large ESA mission, and is set to be launched in 2012. The mission's goal is to create a three dimensional map of the Milky Way, using accurate position and velocity measurements to map the composition, formation and evolution of our galaxy. The potential power of using Ca II lines, due to their intrinsic sharpness and location

away from telluric lines, over the traditionally used strong Balmer lines for emission line studies has been acknowledged by this astrometric mission (Perryman et al. 2001; Perryman 2005); GAIA has a high resolution spectrograph that is exactly centred on the Ca II triplet lines (Katz, 2005). One of the three main science goals is 'Stars', which has as sub science goals: 'White Dwarfs' and 'Variable stars'. Both goals will be looking for binary properties as these are vital to place the systems on their evolutionary tracks and constrain the system parameters. Hence, it is expected that many CVs will be detected and/or observed in the Ca II triplet lines. No time-resolved spectroscopy is obtained, but at a bare minimum these data will be useful for the identification of strong disc lines, and hence provide us with good candidates for the detection of donor emission lines, vital to constrain the mass ratio using the methods proposed in this thesis.

Far future: LISA

As the evolutionary pathways for ultra compact binaries, AM CVn's, double white dwarfs and CVs are all interlinked, a better understanding of the path that leads to CVs is important. This is especially true given that all these sources act as verification binaries for the Laser Interferometer Space Antenna (LISA, Bender 1998); constraining one pathway will be beneficial for the identification of all sources. CVs themselves produce gravitational wave radiation at the low frequency band that LISA is sensitive to (Meliani et al., 2000). The dimensionless parameter h - a measure of stretch, for low eccentricity binary orbits can be estimated via an equation that is dependent only on the binary masses M_1, M_2, the distance d and orbital period $P_{\rm orb}$ (Thorne, 1987). When plotted in the LISA sensitivity plot, the compact binaries are placed above the unresolved double white dwarf noise background (Nelemans et al., 2004), see Figure 8-3. Additionally, we plot the LISA verification sources as a function of their frequency and h estimate, including AM CVn stars, ultra-compact X-ray binaries, double white dwarfs and cataclysmic variables. GW Lib is also indicated in Figure 8-3 and should be detectable above the LISA horizon within a couple of years after first light. As LISA will not be able to spatially resolve sources, having complimentary data (e.g. optical spectroscopy) is crucial to distinguish and identify sources. The gravitational wave detection of a binary, combined with suitable electromagnetic data, will provide us with strong constraints (via the relation given in Thorne 1987) to resolve the system parameters, including the individual masses and the inclination angle.

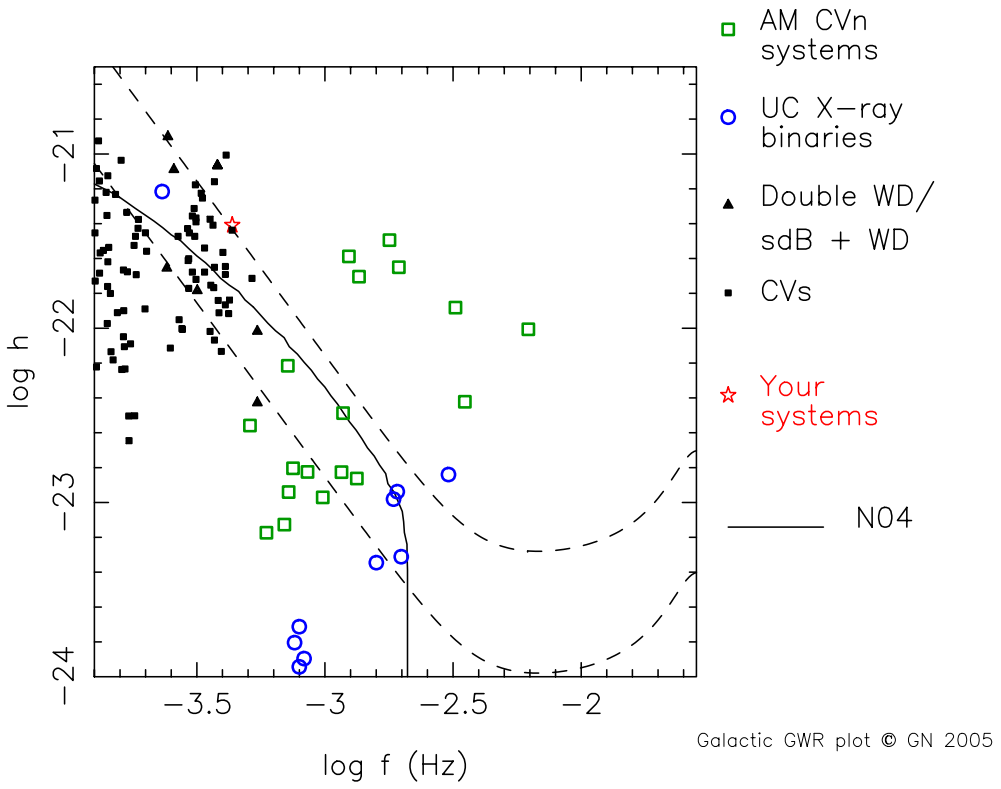

Figure 8-3: Short period binaries systems that will be resolved by the space based gravitational wave detector LISA. The *dashed* lines are the proposed LISA's sensitivity (after 1 and 5 years of operation) and the *solid* line is the unresolved double white dwarf noise background as predicted by Nelemans et al. (2004). Indicated in *red* (as 'your systems') is GW Lib, with $M_1 = 0.84 M_\odot$, $q = 0.125$, $d = 100$pc and an eccentricity of $\epsilon \sim 0$. Figure courtesy of Gijs Nelemans.

References

Araujo-Betancor, S., et al., 2005, A&A, 430, 629

Bagnulo, S., Jehin, E., Ledoux, C., Cabanac, R., Melo, C., Gilmozzi, R., The ESO Paranal Science Operations Team, 2003, The Messenger, 114, 10

Barker, J., Kolb, U., 2003, MNRAS, 340, 623

Beekman, G., Somers, M., Naylor, T., Hellier, C., 2000, MNRAS, 318, 9

Bender, P. L., 1998, in American Astronomical Society Meeting Abstracts, vol. 30 of Bulletin of the American Astronomical Society, p. 1326

Bergeron, P., Wesemael, F., Lamontagne, R., Fontaine, G., Saffer, R. A., Allard, N. F., 1995, ApJ, 449, 258

Bigelow, B. C., Dressler, A. M., 2003, in M. Iye & A. F. M. Moorwood, ed., Society of Photo-Optical Instrumentation Engineers (SPIE) Conference Series, vol. 4841 of Society of Photo-Optical Instrumentation Engineers (SPIE) Conference Series, p. 1727

Bitner, M. A., Robinson, E. L., Behr, B. B., 2007, ApJ, 662, 564

Boyle, W. S., Smith, G. E., 1970, Bell Systems Technical Journal, 49, 587+

Carroll, B. W., Ostlie, D. A., 1996, An Introduction to Modern Astrophysics, Addison-Wesley Publishing Company, inc

Casares, J., 1996, in A. Evans & J. H. Wood, ed., IAU Colloq. 158: Cataclysmic Variables and Related Objects, vol. 208 of Astrophysics and Space Science Library, p. 395

Copperwheat, C. M., Marsh, T. R., Dhillon, V. S., Littlefair, S. P., Hickman, R., Gänsicke, B. T., Southworth, J., 2010, MNRAS, 402, 1824

Copperwheat, C. M., et al., 2009, MNRAS, 393, 157

Copperwheat, C. M., et al., 2011, MNRAS, 410, 1113

Cox, A. N., 2000, Allen's astrophysical quantities, Springer-Verslag New York Inc.

Cushing, M. C., Rayner, J. T., Vacca, W. D., 2005, ApJ, 623, 1115

Dekker, H., D'Odorico, S., Kaufer, A., Delabre, B., Kotzlowski, H., 2000, in Iye, M., Moorwood, A. F., eds., Society of Photo-Optical Instrumentation Engineers (SPIE) Conference Series, vol. 4008 of Society of Photo-Optical Instrumentation Engineers (SPIE) Conference Series, p. 534

D'Esterre, C. R., 1913, Astronomische Nachrichten, 193, 281

Eddington, A. S., 1924, MNRAS, 84, 308

Efron, B., Tibshirani, R., 1994, An Introduction to the Bootstrap (Chapman & Hall/CRC Monographs on Statistics & Applied Probability), Chapman and Hall/CRC

Eggleton, P. P., 1983, ApJ, 268, 368

Fabricant, D., Cheimets, P., Caldwell, N., Geary, J., 1998, PASP, 110, 79

Fontaine, G., Brassard, P., Bergeron, P., 2001, PASP, 113, 409

Foulkes, S. B., Haswell, C. A., Murray, J. R., Rolfe, D. J., 2004, MNRAS, 349, 1179

Frank, J., King, A. R., Raine, D. J., 1992, Accretion power in astrophysics, Cambridge University Press, Cambridge

Gänsicke, B. T., 2007, in 15th European Workshop on White Dwarfs, vol. 372 of Astronomical Society of the Pacific Conference Series, p. 597

Gänsicke, B. T., et al., 2009, MNRAS, 397, 2170

Godon, P., Sion, E. M., Cheng, F., Gänsicke, B. T., Howell, S., Knigge, C., Sparks, W. M., Starrfield, S., 2004, ApJ, 602, 336

Godon, P., Sion, E. M., Barrett, P. E., Szkody, P., 2009, ApJ, 701, 1091

González, L. E., 1983, IAU Circ, 3854

Green, D. W. E., 2004, IAU Circ, 8320, 1

Greenstein, J. L., Trimble, V. L., 1967, ApJ, 149, 283

Groot, P. J., 2001, ApJ Letters, 551, L89

Hōshi, R., 1979, Progress of Theoretical Physics, 61, 1307

Hagen, H.-J., Groote, D., Engels, D., Reimers, D., 1995, A&A Supplement, 111, 195

Harlaftis, E., 1999, A&A, 346, L73
Hawley, S. L., et al., 2002, AJ, 123, 3409
Hellier, C., 2001, Cataclysmic Variable Stars, Springer
Hessman, F. V., Hopp, U., 1990, A&A, 228, 387
Hessman, F. V., Robinson, E. L., Nather, R. E., Zhang, E.-H., 1984, ApJ, 286, 747
Hiroi, K., et al., 2009, PASJ, 61, 697
Hirose, M., Osaki, Y., 1990, PASJ, 42, 135
Hoffmeister, C., 1949, Astron. Nachr. Erganzungshefte, 12, 1
Horne, K., 1995, A&A, 297, 273
Horne, K., Marsh, T. R., 1986, MNRAS, 218, 761
Horne, K., Wade, R. A., Szkody, P., 1986, MNRAS, 219, 791
Horne, K., Wood, J. H., Stiening, R. F., 1991, ApJ, 378, 271
Howell, S. B., 2000, Handbook of CCD Astronomy, Cambridge University Press
Iben, I. J., 1991, ApJ SS, 76, 55
Iben, I. J., Livio, M., 1993, PASP, 105, 1373
Ishioka, R., Sekiguchi, K., Maehara, H., 2007, PASJ, 59, 929
Kafka, S., Honeycutt, R. K., 2006, AJ, 132, 1517
Kato, T., Maehara, H., Monard, B., 2008, PASJ, 60, L23+
Kato, T., et al., 2009, PASJ, 61, 395
Kato, T., et al., 2010, PASJ, 62, 1525
Katz, D., 2005, in C. Turon, K. S. O'Flaherty, & M. A. C. Perryman, ed., The Three-Dimensional Universe with Gaia, vol. 576 of ESA Special Publication, p. 51
Kepler, J., Ptolemaeus, C., Fludd, R., 1619, Harmonices mvndi libri v. qvorvm primus geometricvs, de figurarum regularium, quae proportiones harmonicas constituunt, ortu demonstrationibus, secundus architectonicvs, SEU EX geometria figvrata, de figurarum regularium congruentia in plano vel solido: tertius proprie harmonicvs, de proportionum harmonicarum ortu EX figuris
Knigge, C., 2006, MNRAS, 373, 484
Knigge, C., Hynes, R. I., Steeghs, D., Long, K. S., Araujo-Betancor, S., Marsh, T. R., 2002, ApJ Letters, 580, L151
Knigge, C., Baraffe, I., Patterson, J., 2011, ApJ SS, 194, 28
Kolb, U., 1993, A&A, 271, 149
Kolb, U., 2010, Extreme Environment Astrophysics, Cambridge University Press
Kolb, U., Baraffe, I., 1999, MNRAS, 309, 1034
Kolb, U., Ritter, H., 1992, A&A, 254, 213
Kunze, S., Speith, R., Riffert, H., 1997, MNRAS, 289, 889
Landau, L. D., Lifshitz, E. M., 1975, The classical theory of fields, Pergamon Press, Oxford
Littlefair, S. P., Dhillon, V. S., Marsh, T. R., Gänsicke, B. T., Southworth, J., Watson, C. A., 2006, Science, 314, 1578
Littlefair, S. P., Dhillon, V. S., Marsh, T. R., Gänsicke, B. T., Southworth, J., Baraffe, I., Watson, C. A., Copperwheat, C., 2008, MNRAS, 388, 1582
Long, K. S., Gilliland, R. L., 1999, ApJ, 511, 916
Long, K. S., Sion, E. M., Gänsicke, B. T., Szkody, P., 2004, ApJ, 602, 948
Long, K. S., Brammer, G., Froning, C. S., 2006, ApJ, 648, 541
Lubow, S. H., 1991a, ApJ, 381, 259
Lubow, S. H., 1991b, ApJ, 381, 268
Lubow, S. H., 1992, ApJ, 401, 317
Maehara, H., 2007, vsnet-alert, 9530
Margon, B., 1984, Annual review of astronomy and astrophysics, 22, 507
Marquardt, D. W., 1963, SIAM Journal on Applied Mathematics, 11, 431
Marsh, T. R., 1988, MNRAS, 231, 1117
Marsh, T. R., 1989, PASP, 101, 1032
Marsh, T. R., 1990, ApJ, 357, 621
Marsh, T. R., 2001, in Boffin, H. M. J., Steeghs, D., Cuypers, J., eds., Astrotomography, Indirect

Imaging Methods in Observational Astronomy, vol. 573 of Lecture Notes in Physics, Berlin Springer Verlag, p. 1

Marsh, T. R., Dhillon, V. S., 1997, MNRAS, 292, 385

Marsh, T. R., Horne, K., 1988, MNRAS, 235, 269

Marsh, T. R., Robinson, E. L., Wood, J. H., 1994, MNRAS, 266, 137

Meliani, M. T., de Araujo, J. C. N., Aguiar, O. D., 2000, A&A, 358, 417

Mennickent, R. E., Unda-Sanzana, E., Tappert, C., 2006, A&A, 451, 613

Monaghan, J. J., 1992, Annual review of astronomy and astrophysics, 30, 543

Morales-Rueda, L., Marsh, T. R., Steeghs, D., Unda-Sanzana, E., Wood, J. H., North, R. C., 2003, A&A, 405, 249

Murray, J. R., 1996, MNRAS, 279, 402

Murray, J. R., 1998, MNRAS, 297, 323

Murray, J. R., 2000, MNRAS, 314, L1

Neilsen, J., Steeghs, D., Vrtilek, S. D., 2008, MNRAS, 384, 849

Nelemans, G., Yungelson, L. R., Portegies Zwart, S. F., 2004, MNRAS, 349, 181

North, R. C., Marsh, T. R., Moran, C. K. J., Kolb, U., Smith, R. C., Stehle, R., 2001, in H. M. J. Boffin, D. Steeghs, & J. Cuypers, ed., Astrotomography, Indirect Imaging Methods in Observational Astronomy, vol. 573 of Lecture Notes in Physics, Berlin Springer Verlag, p. 33

North, R. C., Marsh, T. R., Kolb, U., Dhillon, V. S., Moran, C. K. J., 2002, MNRAS, 337, 1215

Olech, A., Zloczewski, K., Mularczyk, K., Kedzierski, P., Wisniewski, M., Stachowski, G., 2004, Acta Astronomica, 54, 57

Osaki, Y., 1974, PASJ, 26, 429

Paczyński, B., 1971, ARA&A, 9, 183

Parsons, S. G., et al., 2010, MNRAS, 407, 2362

Patterson, J., 1979, AJ, 84, 804

Patterson, J., 2001, PASP, 113, 736

Patterson, J., 2011, MNRAS, 27

Patterson, J., Richman, H., Kemp, J., Mukai, K., 1998, PASP, 110, 403

Patterson, J., Kemp, J., Jensen, L., Vanmunster, T., Skillman, D. R., Martin, B., Fried, R., Thorstensen, J. R., 2000, PASP, 112, 1567

Patterson, J., et al., 2002, PASP, 114, 721

Patterson, J., et al., 2005, PASP, 117, 1204

Pearson, K. J., 2006, MNRAS, 371, 235

Pearson, K. J., 2007, MNRAS, 379, 183

Perryman, M. A. C., 2005, in C. Turon, K. S. O'Flaherty, & M. A. C. Perryman, ed., The Three-Dimensional Universe with Gaia, vol. 576 of ESA Special Publication, p. 15

Perryman, M. A. C., et al., 2001, A&A, 369, 339

Price, A., et al., 2004, IAU Circ, 8410, 1

Rappaport, S., Joss, P. C., Webbink, R. F., 1982, ApJ, 254, 616

Rappaport, S., Joss, P. C., Verbunt, F., 1983, ApJ, 275, 713

Ritter, H., 2008, ArXiv e-prints

Ritter, H., Kolb, U., 2003, A&A, 404, 301 (update RKcat7.15, 2011)

Rodríguez-Gil, P., Gänsicke, B. T., Hagen, H.-J., Marsh, T. R., Harlaftis, E., Kitsionas, S., Engels, D., 2005, A&A, 431, 269

Roelofs, G. H. A., Groot, P. J., Nelemans, G., Marsh, T. R., Steeghs, D., 2006, MNRAS, 371, 1231

Rolfe, D. J., Abbott, T. M. C., Haswell, C. A., 2002, MNRAS, 334, 699

Schneider, D. P., Young, P., 1980, ApJ, 238, 946

Shafter, A. W., 1983, ApJ, 267, 222

Shafter, A. W., Hessman, F. V., 1988, AJ, 95, 178

Shahbaz, T., Naylor, T., Charles, P. A., 1994, MNRAS, 268, 756

Shakura, N. I., Sunyaev, R. A., 1973, A&A, 24, 337

Sheets, H. A., Thorstensen, J. R., Peters, C. J., Kapusta, A. B., Taylor, C. J., 2007, PASP, 119,

494
Simpson, J. C., Wood, M. A., 1998, ApJ, 506, 360
Sion, E. M., Long, K. S., Szkody, P., Huang, M., 1994, ApJ Letters, 430, L53
Sion, E. M., Godon, P., Myzcka, J., Blair, W. P., 2010, ApJ Letters, 716, L157
Skidmore, W., Welsh, W. F., Wood, J. H., Catalán, M. S., Horne, K., 1999, MNRAS, 310, 750
Skillman, D. R., Patterson, J., Kemp, J., Harvey, D. A., Fried, R. E., Retter, A., Lipkin, Y., Vanmunster, T., 1999, PASP, 111, 1281
Skumanich, A., 1972, ApJ, 171, 565
Smith, A. J., Haswell, C. A., Hynes, R. I., 2006, MNRAS, 369, 1537
Smith, M. A., 1979, PASP, 91, 737
Solheim, J., 2010, PASP, 122, 1133
Southworth, J., Marsh, T. R., Gänsicke, B. T., Aungwerojwit, A., Hakala, P., de Martino, D., Lehto, H., 2007, MNRAS, 382, 1145
Southworth, J., Marsh, T. R., Gänsicke, B. T., Steeghs, D., Copperwheat, C. M., 2010, A&A, 524, A86+
Spruit, H. C., Ritter, H., 1983, A&A, 124, 267
Spruit, H. C., Rutten, R. G. M., 1998, MNRAS, 299, 768
Steeghs, D., Casares, J., 2002, ApJ, 568, 273
Steeghs, D., Stehle, R., 1999, MNRAS, 307, 99
Steeghs, D., Horne, K., Marsh, T. R., Donati, J. F., 1996, MNRAS, 281, 626
Steeghs, D., Harlaftis, E. T., Horne, K., 1997, MNRAS, 290, L28
Steeghs, D., Marsh, T., Knigge, C., Maxted, P. F. L., Kuulkers, E., Skidmore, W., 2001, ApJ Letters, 562, L145
Steeghs, D., Perryman, M. A. C., Reynolds, A., de Bruijne, J. H. J., Marsh, T., Dhillon, V. S., Peacock, A., 2003, MNRAS, 339, 810
Steeghs, D., Howell, S. B., Knigge, C., Gänsicke, B. T., Sion, E. M., Welsh, W. F., 2007, ApJ, 667, 442
Still, M. D., Quaintrell, H., Roche, P. D., Reynolds, A. P., 1997, MNRAS, 292, 52
Stover, R. J., Robinson, E. L., Nather, R. E., Montemayor, T. J., 1980, ApJ, 240, 597
Szkody, P., 1987, ApJ SS, 63, 685
Szkody, P., Mattei, J. A., 1984, PASP, 96, 988
Szkody, P., Desai, V., Hoard, D. W., 2000, AJ, 119, 365
Szkody, P., Gänsicke, B. T., Howell, S. B., Sion, E. M., 2002, ApJ Letters, 575, L79
Szkody, P., et al., 2010, ApJ, 710, 64
Templeton, M. R., 2007, AAN, 349, 1
Templeton, M. R., et al., 2006, PASP, 118, 236
Thorne, K. S., 1987, in Hawking, S. W. & Israel, W., ed., Three Hundred Years of Gravitation, p. 330
Thorstensen, J. R., 2003, AJ, 126, 3017
Thorstensen, J. R., Taylor, C. J., 1997, PASP, 109, 1359
Thorstensen, J. R., Wade, R. A., Oke, J. B., 1986, ApJ, 309, 721
Thorstensen, J. R., Patterson, J. O., Shambrook, A., Thomas, G., 1996, PASP, 108, 73
Thorstensen, J. R., Patterson, J., Kemp, J., Vennes, S., 2002, PASP, 114, 1108
Thorstensen, J. R., Lépine, S., Shara, M., 2008, AJ, 136, 2107
Tokarz, S. P., Roll, J., 1997, in G. Hunt & H. Payne, ed., Astronomical Data Analysis Software and Systems VI, vol. 125 of Astronomical Society of the Pacific Conference Series, p. 140
Townsley, D. M., Bildsten, L., 2003, ApJ Letters, 596, L227
Townsley, D. M., Arras, P., Bildsten, L., 2004, ApJ Letters, 608, L105
Tulloch, S. M., Rodríguez-Gil, P., Dhillon, V. S., 2009, MNRAS, 397, L82
Unda-Sanzana, E., et al., 2008a, MNRAS, 388, 889
Unda-Sanzana, E., et al., 2008b, MNRAS, 388, 889
Unda-Sanzana, E., et al., 2009, Journal of Physics Conference Series, 172, 012041
Urban, J. A., Sion, E. M., 2006, ApJ, 642, 1029
van Spaandonk, L., Steeghs, D., Marsh, T. R., Parsons, S. G., 2010a, ApJ Letters, 715, L109

van Spaandonk, L., Steeghs, D., Marsh, T. R., Torres, M. A. P., 2010b, MNRAS, 401, 1857
van Zyl, L., Warner, B., O'Donoghue, D., Sullivan, D., Pritchard, J., Kemp, J., 2000, Baltic Astronomy, 9, 231
van Zyl, L., et al., 2004, MNRAS, 350, 307
Verbunt, F., 1982, Space Science Reviews, 32, 379
Verbunt, F., Rappaport, S., 1988, ApJ, 332, 193
Verbunt, F., Zwaan, C., 1981, A&A, 100, L7
Voges, W., et al., 1999, A&A, 349, 389
Warner, B., 1987, MNRAS, 227, 23
Warner, B., 1995, Cataclysmic Variable Stars, Cambridge University Press, Cambridge
Warner, B., Woudt, P. A., 2002, MNRAS, 335, 84
Watson, C. A., Steeghs, D., Shahbaz, T., Dhillon, V. S., 2007, MNRAS, 382, 1105
Whitehurst, R., 1988, MNRAS, 232, 35
Wood, J. H., Horne, K., Berriman, G., Wade, R. A., 1989, ApJ, 341, 974
Wood, M. A., Montgomery, M. M., Simpson, J. C., 2000, ApJ Letters, 535, L39
York, D. G., et al., 2000, AJ, 120, 1579
Zurita, C., et al., 2002, MNRAS, 333, 791